Studying The Muon Background Component In The Double Chooz Experiment

Dissertation

der Mathematisch-Naturwissenschaftlichen Fakultät

der Eberhard Karls Universität Tübingen

zur Erlangung des Grades eines

Doktors der Naturwissenschaften

(Dr. rer. nat.)

vorgelegt von

Dipl. Phys. Dennis Dietrich

aus Esslingen am Neckar

Tübingen

2013

Tag der mündlichen Qualifikation: 28.03.2013
Dekan: Prof. Dr. Wolfgang Rosenstiel
1. Berichterstatter: Prof. Dr. Tobias Lachenmaier
2. Berichterstatter: Prof. Dr. Josef Jochum

Untersuchung des myonischen Untergrunds des Double Chooz Experiments

Das Double Chooz (DC) Reaktorneutrino-Experiment hat eine präzise Messung des dritten Neutrino-Mischungswinkel θ_{13} zum Ziel. Dieser Mischungswinkel steht im Zusammenhang mit fundamentalen Fragen, welche jenseits des gegenwärtigen Standardmodells der Elementarteilchenphysik führen. Im DC Experiment werden Neutrinos durch den inversen Betazerfall nachgewiesen, der ein von den meisten Untergründen gut zu unterscheidendes Signal hat. Da Neutrino-Wechselwirkungen im Detektor selten sind und es einen störenden Myonen-Untergrund gibt, ist ein gutes Verständnis dieses Untergrunds für dessen Reduktion zwingend. Das ist nötig, da Myonen schnelle Neutronen und βn-Emitter erzeugen, welche fälschlicherweise als Neutrino-Ereignis identifiziert werden könnten. Diese Doktorarbeit behandelt verschiedene Analysen, die mit dem kosmischen Myonenuntergrund im fernen DC Detektor zusammenhängen.

Die vorliegende Arbeit behandelt die Identifizierung von Myonen, sowie die Bestimmung der Myonenrate im Fernen DC Detektor. Unter Benutzung der Myonen-Selektion der Neutrinoanalyse wurde eine Myonenrate von $13\,\mathrm{s}^{-1}$ im Inneren Detektor (ID) und $46\,\mathrm{s}^{-1}$ im Inneren Myonen Veto (IV) gefunden. Die Myonenidentifikations-Effizienz des IV wurde gemessen und ein Wert von $> 99,97\,\%$ gefunden. Die Stabilität der Myonenraten wurde untersucht und eine jahreszeitliche Modulation gefunden. Diese ist kompatibel mit einer Änderung des Temperaturprofils der Atmosphäre. Der Koeffizient, welcher die Stärke des Zusammenhangs zwischen Temperaturänderung und Ratenänderung angibt, der effektive Temperaturkoeffizient, wurde gemessen und beträgt: $\alpha_T = 0,39 \pm 0,01(stat.) \pm 0,02(syst.)$. Dies ermöglicht die Messung des atmosphärischen Verhältnisses von Kaonen zu Pionen, dessen Wert $r(K/\pi) = 0,14 \pm 0,06$ aus den Messdaten gewonnen wurde. Eine zusätzliche Variation der Myonenrate mit dem Luftdruck wurde gefunden und der barometrische Koeffizient, der diesen Effekt beschreibt, bestimmt: $\beta_p = -0,59 \pm 0,20(stat.) \pm 0,10(syst.)\,‰/\mathrm{mbar}$. Ein weiteres zentrales Thema dieser Arbeit ist die Extrapolation des im fernen Detektor gemessenen Untergrundes zu den Reaktorneutrino-Experimenten RENO und Daya Bay. Der Untergrund von schnellen Neutronen und βn-Emittern wurde während des Shutdowns beider Reaktoren in Chooz gemessen. Da diese Untergründe von Myonen erzeugt werden, ist zur Extrapolation ein gutes Verständnis von Myonenintensität und Energie in Abhängigkeit der Tiefe des jeweiligen betrachteten Experiments zwingend. Dieser Zusammenhang wurde in der vorliegenden Arbeit untersucht. Zuletzt behandelt diese Arbeit die Überwachung und Kalibration des Detektors mit Hilfe von Myonen. Die relative Schwankung der Detektorantwort auf Myonen von $0,20\,\%_{rms}$ des Quadratischen Mittels wurde mittels des Myonenratenverhältnisses, R_μ^{IV}/R_μ^{ID}, zwischen IV und ID gemessen. Durch die Überwachung des Energieverlusts von Myonen wurde eine Schwankung der Detektoranwort von $0,70\,\%_{rms}$ im ID und $0,22\,\%_{rms}$ im IV gemessen. Eine Selektionstechnik zur Identifikation von Myonen, welche im Detektor zerfallen, wurde diskutiert. Der Energiemittelwert des resultierenden Zerfallspektrums, 35 MeV, ist kompatibel mit der Erwartung von 105/3 MeV beim Dreikörperzerfall des Myons. Als regelmäßige wöchentliche Aufgabe, wurde die relative Zeitdifferenz der Photomultiplier im IV gemessen und Kalibrationskonstanten extrahiert um etwaige Zeitdifferenzen zu korrigieren.

Studying the muon background component in the Double Chooz experiment

The reactor anti-neutrino experiment Double Chooz (DC) will measure the third neutrino mixing angle θ_{13} with very high precision. This mixing angle is connected to fundamental questions in particle physics beyond the current Standard Model. In DC neutrinos are detected via the Inverse Beta Decay reaction, which provides a clean signal distinguishable from most backgrounds. However, as neutrino interactions in the detector are very rare and an interfering muon background is present, a proper understanding and reduction of this background is mandatory. This is crucial because muons create fast neutrons and βn-emitters which lead to background capable of mimicking the neutrino interaction in the detector. This thesis covers different analysis topics related to the cosmic ray muon background at the DC far site.

The thesis covers the identification of muons, the applied rejection technique and the determination of the muon rate at DC far site. Utilizing the muon rejection cuts of the neutrino analysis a muon rate of $13\,\mathrm{s}^{-1}$ in the Inner Detector (ID) and of $46\,\mathrm{s}^{-1}$ in the Inner Muon Veto (IV) was found. The efficiency of the IV to identify and reject cosmic ray muons was measured and a value greater than 99.97 % has been found. The stability of the determined muon rates was examined and a seasonal modulation was found, compatible with a variation of the temperature profile of the atmosphere over the year. The parameter describing the strength between the relationship of temperature and muon rate change, the effective temperature coefficient was obtained: $\alpha_T = 0.39 \pm 0.01(stat.) \pm 0.02(syst.)$. This gave the opportunity to measure the atmospheric kaon to pion ratio with the DC far detector which was found to be $r(K/\pi) = 0.14 \pm 0.06$. Additional variations of muon rate with surface pressure were found and the barometric coefficient describing this effect was measured as $\beta_p = -0.59 \pm 0.20(stat.) \pm 0.10(syst.)$ ‰/mbar. Another central theme of this work was the extrapolation of the backgrounds of fast neutrons and cosmogenic βn-emitters to the other reactor neutrino experiments RENO and Daya Bay. These correlated backgrounds were measured during a period when both reactors were "shut down" for maintenance. As the production of these backgrounds by cosmic muons depends on muon intensity and energy which are a function of depth, a good understanding of these quantities is needed for the extrapolation. The relation between these quantities was studied and worked out in this thesis. The focus of the last theme lies on detector stability and the use of cosmic ray muons for calibration. A relative instability in detector response of $0.20\,\%_{rms}$ of the root mean square value has been found utilizing the muon rate ratio, R_μ^{IV}/R_μ^{ID}, of the IV and the ID. Monitoring the energy loss of muon, a relative instability of $0.70\,\%_{rms}$ has been found for the ID and a value of $0.22\,\%_{rms}$ for the IV. A technique to identify muons decaying inside the detector was discussed. The mean value of the resulting muon decay spectrum of the ID, 35 MeV is compatible with the expectation of 105/3 MeV from the three body decay of muons. In addition, as a regular duty, the relative timing of the IV photomultipliers was measured each week and calibration constants were extracted to correct for any difference in their relative timing.

Contents

List of Figures

List of Tables

Introduction

In the course of this doctoral research, the muon background in the Double Chooz far detector was analysed. Means to identify and reject this background were studied, a seasonal modulation in the muon rate was observed and quantified, and muons were utilised for detector monitoring and calibration. In this first section an introduction to the work presented in this thesis will be given.

Even not directly the focal point of this thesis, the thesis is centred around the neutrino, a particle being proposed by W. Pauli in the last century. As neutrinos play a central role in particle physics, astrophysics and cosmology their properties are of high interest. To understand this, especially the importance of the mixing angle θ_{13}, **chapter 1** will give a short introduction to Neutrino Physics and the Standard Model of particle physics. The basic mathematics of neutrino oscillations in vacuum and in matter will be explained, and a possible explanation how neutrinos masses arise will be given. The chapter will end with a short overview on how to measure neutrino oscillation and it will explain the different experimental approaches to do so.

Chapter 2 will present an overview of the various measurements of neutrino properties. This leads to the experimental observation of neutrino oscillations utilizing neutrinos from the sun, neutrinos created by cosmic rays in the atmosphere or in nuclear reactors. The observation of these oscillations leads to an extension of the Standard Model of particle physics in order to account for the flavor mixing and masses of neutrinos. This in turn opens the possibility to explore new physics beyond the current Standard Model. The chapter will close giving a summary of the parameters describing neutrino oscillations as known today.

Than the focus will shift to the Double Chooz experiment in **chapter 3**. It aims to measure the third neutrino mixing angle θ_{13} with high precision. The experimental approach will be described in detail, starting with a description of the Chooz nuclear power plant site. This will be followed by the prediction of the anti neutrino spectrum emitted from the reactor cores, coming to the experimental setup of the detector system. In addition, a short overview of Data Acquisition electronics, calibration devices and utilized software will be given.

However, different kinds of backgrounds are limiting the experiments sensitivity towards θ_{13} and a good knowledge of background rates and energy spectra is necessary for a precision measurement. The neutrino signature and the backgrounds inside the detector will be described in **chapter 4**. The most numerous source of background are muons produced by cosmic rays in the atmosphere. These muons form the main objective of this thesis.

In the following chapters the thesis concentrates on the analysis of physics data with the focal point on the muons. These particles are the most abundant cosmic ray particles and pose a potentially dangerous background for reactor neutrino experiments as they can create neutrons or cosmogenic βn-emitters via spallation. **Chapter 5** is devoted to the identification of muons with the Double Chooz detector. It will discuss different methods to determine the muon rate and extract energy and charge spectra, in addition an estimation of the muon rejection ability of the Inner Muon Veto will be given.

In **chapter 6** variations of the muon rate will be linked to temperature fluctuations of the atmosphere. These temperature variations affect the interaction of kaons and pions in the atmosphere. As these mesons can decay into muons, temperature variations also influence them. A positive correlation between muon rate and temperature is expected and thus a seasonal variation in the muon rate with maxima in summer and minima in winter. The chapter will establish the theory and analysis methods needed to proof such a seasonal variation. A Correlation Analysis will be used to quantify the strength of any correlation and the effective temperature coefficient, the parameter connecting temperature changes to muon rate changes, will be determined. The chapter will close introducing a method to estimate the atmospheric kaon to pion ratio and it will give a measurement of this ratio performed with the Double Chooz far detector.

Double Chooz is not the only experiment that wants to perform a precise measurement of the mixing angle θ_{13}. Currently two other reactor neutrino experiments, Daya Bay in China and RENO in Korea were performing this measurement. Among these experiments, Double Chooz is unique because it has the possibility to measure the backgrounds while the reactors are shutdown for maintenance. This enables the prediction and verification of the background estimates for the other two reactor experiments and also for future experiments. In **chapter 7** a data set of 7.53 days, where the reactors were shutdown, will be analyzed. This will show how to extrapolate or scale backgrounds measured with the Double Chooz far detector to the other reactor neutrino experiments.

Chapter 8 discusses the application of cosmic ray muons for monitoring and calibration purposes. Two different methods to monitor the detector response at high energies will be introduced and utilized to check the stability of the energy scale. In addition, muons are a natural calibration source via their decay and a method to identify stopping and subsequently decaying muons inside the detector will be introduced.

As a member of the Tübingen astroparticlephysics group, additional tasks were performed. This involved the design and construction phase of the Inner Muon Veto. This sub detector is devoted to the identification of cosmic ray muons. As a regular task the monitoring and calibration of this sub-detector was performed. Weekly calibration runs were analyzed and the relative timing of the Inner Muon Veto photomultipliers was extracted. The basic calibration scheme, the utilized method and the extracted calibration constants are the item of an additional chapter that can be found in the appendix.

"The most important discoveries will provide answers to questions that we do not yet know how to ask and will concern objects we have not yet imagined."

John N. Bahcall (1934-2005)

1 Theory of Neutrino Oscillation physics

This chapter aims to give an overview on the research field of neutrino oscillations and will provide motivation for the goal of the Double Chooz experiment, the measurement of the third neutrino mixing angle θ_{13}. To understand the context the Double Chooz experiment is situated in, first the Standard Model of particle physics and second, some neutrino related topics beyond it will be explained. The chapter will introduce the concept of neutrino flavor change, the so called neutrino oscillations. These are oscillating transitions $\nu_\alpha \leftrightarrow \nu_\beta$ $(\alpha, \beta = e, \mu, \tau)$ with different lepton flavor numbers $L_\alpha \neq L_\beta$. The observation of such an oscillating flavor change of neutrinos emitted from nuclear reactors is the goal of the Double Chooz experiment, leading to a θ_{13} as indicated before.

These oscillations do only happen if the masses of the three neutrino flavors are different, especially if not all neutrinos are mass less. This was first pointed out by Pontecorvo in 1959 and in the last part of this chapter light will be shed on the theoretical and phenomenological models for neutrino mass and neutrino oscillations in vacuum as well as in matter.

1.1 Standard model of particle physics

As chemistry can be understood as the physics of 3 particles (protons, neutrons and electrons) which are interacting due to the electromagnetic force, particle physics can be understood (to some extend) as the physics of two fundamental classes of particles: fermions which are interacting due to the strong force, the weak force and the electromagnetic force mediated by bosons. The Standard Model incorporates the theories of Quantumchromodynamics and Electroweak interaction. From the mathematical point of view it is a re-normalizable gauge field theory, corresponding to $SU(3) \otimes SU(2) \otimes U(1)$ in group theory, describing how fermionic particles interact with each other by exchanging bosons. This is the picture of our today's knowledge of the smallest particles and their interactions as constituted in the Standard Model of Particle Physics ($\mathcal{SM}$). Simplified, figure 1.1 shows this picture in an artists illustration.

Fermionic particles having an electromagnetic charge interact electromagnetically, those having a "weak charge" interact via the weak interaction and those with a "colour charge" via the strong interaction. At the scale of the fundamental particles gravitational interactions are not described, because at the range of energies where it is believed that the SM is valid, the gravitational interactions are negligible. However the graviton, the mediating boson for the gravitational interactions has yet not been discovered. In the following the $\mathcal{SM}$ will be

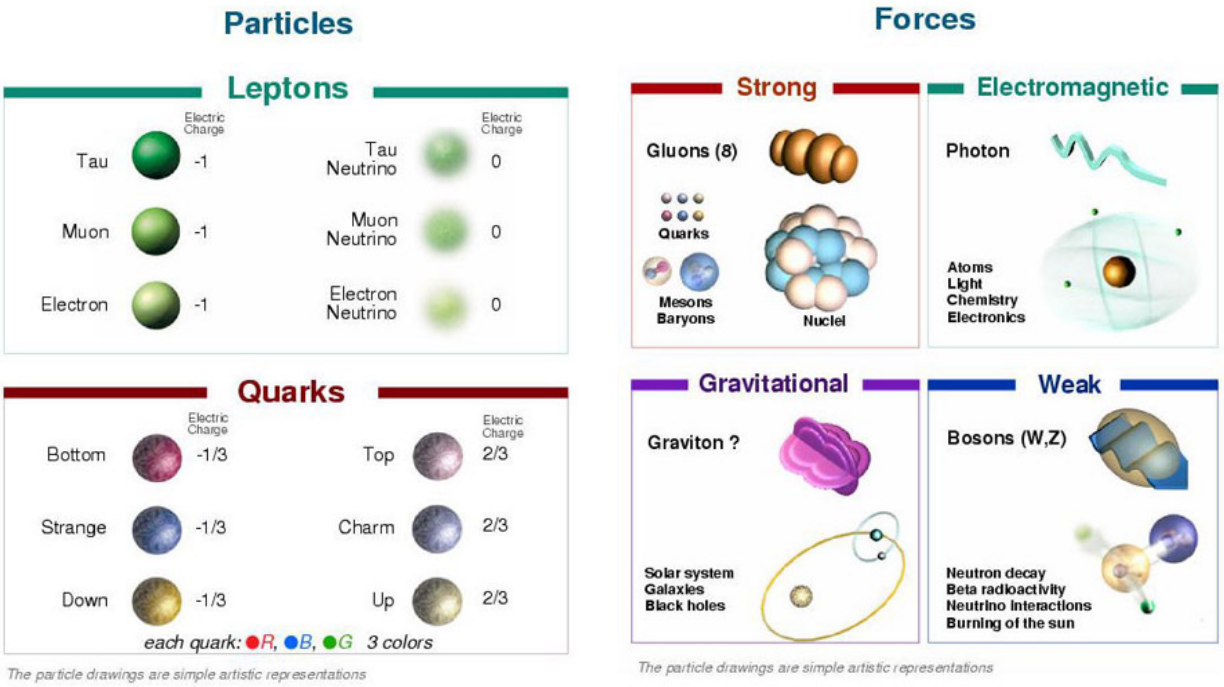

Figure 1.1: Fermions and bosons in the Standard model of particle physics. On the left the fermionic leptons and quarks are described. Interactions shown on the right are mediated by bosons. From [1].

further described in a condensed version similar to [2, 3].

1.1.1 Fermions

There are twelve spin-parity $J_P = 1/2^+$ fermions, divided in six quarks (q=u, d, c, s, t, b) and in six leptons (l=e$, \mu, \tau, \nu_e, \nu_\mu, \nu_\tau$) which constitute matter (for a summary see table 1.1). Leptons are very different from quarks as they are not interacting strongly, but via electromagnetism and the weak force. In the SM neutrinos are mass less and without electric charge being only characterized by flavor[1] during their interactions. In the weak interaction parity is maximally violated leading to neutrinos and anti-neutrinos having a fixed opposite helicity. Also the Charge-Parity symmetry (**CP**) is violated in weak interactions in a very small fraction. As a consequence quarks mix and CP violation arises from the non-diagonal elements within the Cabibbo-Kobayshi-Maskava (**CKM**) quark mixing matrix [4]. This can be described in group theory by $SU(2)\otimes U(1)$. One can group left handed quarks and leptons in doublets and right-handed particles into singlets.

$$\begin{pmatrix} u \\ d' \end{pmatrix}_L, \begin{pmatrix} c \\ s' \end{pmatrix}_L, \begin{pmatrix} t \\ b' \end{pmatrix}_L \quad , \quad \begin{pmatrix} e \\ \nu_e \end{pmatrix}_L, \begin{pmatrix} \mu \\ \nu_\mu \end{pmatrix}_L, \begin{pmatrix} \tau \\ \nu_\tau \end{pmatrix}_L$$
$$u_R,\ d_R,\ s_R,\ c_R,\ c_R \quad , \quad b_R,\ t_R,\ e_R,\ \mu_R,\ \tau_R$$

Here d', s', b' are the Cabibbo mixed states. This is because the mass eigenstates do not

[1] Flavor is the charge of the weak interaction.

conform with the flavor eigenstates. In the opposite quarks are characterized by interacting strongly and do not exist as free particles (so called quark confinement), but combined into mesons $q\bar{q}$ and baryons qqq. Thus all strongly interacting particles can be understood being composed out of quarks. Various experiments at e^+e^- accelerators showed that there three different types of strong charge, called color. As mentioned the theory describing strong interactions is Quantumchromodynamics, which is based on an invariance of rotation in the color space described by a $SU(3)$ group.

1.1.2 Bosons

Each of the interactions described before is mediated via bosons. In the $\mathcal{SM}$ there are several spin-parity $J_P = 1^-$ bosons and a single spin 0 Higgs boson. This includes the photon γ for the electromagnetic force, eight gluons g for the strong force and three $W^{\pm}$,Z^0 bosons for the weak force. The force of gravity is not included into the $\mathcal{SM}$ up to now. The photon and the gluons are mass less $m_\gamma = 0$, $m_g = 0$, whereas the mass of the carriers of the charged weak interactions the W bosons have a mass of $m_W = 80.3\,\mathrm{GeV}$. The neutral carrier of the weak interaction, the Z boson has a mass of $m_Z = 91.2\,\mathrm{GeV}$. All this is summarized in table 1.2. Simplified, one can calculate the range of the interaction assuming that it is an inverse function of the mass of the boson mediating the interaction:

$$R = \frac{\hbar}{mc} = 197\frac{\mathrm{MeV}}{mc^2}\cdot\mathrm{fm}$$

Therefore the electromagnetic interaction is endless, where as the weak interactions are limited to the size of a nucleus. Also the strong interaction would be unlimited, but as the gluons interact with themselves it is also limited within the range of a nucleus.

1.1.3 Interactions

Within the $\mathcal{SM}$ all this interaction can be described as the elementary processes $f \to f'V$, where a fermion f converts into f' with the emission of a boson V (This corresponds to a vertex in one of the interactions in figure 1.2). Processes which can be described by the same interaction are equivalent. This can be seen by exchanging a particle on one side of the reaction with its antiparticle on the other side or by reversing the direction of the arrow:

$$\begin{array}{lll} f \leftrightarrow f'V & \bar{V}f \leftrightarrow f' & f\bar{f}' \leftrightarrow V \\ \bar{f}' \leftrightarrow \bar{f}V & \bar{V}f' \leftrightarrow \bar{f} & \bar{V}' \leftrightarrow \bar{f}f' \end{array}$$

Such processes can be described via quantum field theory by a Lagrangian like:

$$\begin{aligned} \mathcal{L}(x) &= g\cdot i\bar{\psi}_{f'}(x)\Gamma_\alpha\psi_f(x)V_\alpha(x) + h.c. \\ &= g\cdot j_\alpha(x)V_\alpha(x) + h.c. \end{aligned}$$

In eq. 1.1 above, g is a coupling constant which is the strength of the interaction, ψ_f is a vector operator destroying f and creating f', $\bar{\psi}_{f'}$ creates f' and destroys $\bar{f}'$. In analogy V_α creates a boson V and destroys a boson $\bar{V}$. All these operators interact in the point $x = (\vec{x}, t)$, where the interaction takes place. Finally Γ_α is a matrix describing the interaction. The first term in the Lagrangian above is describing the 6 processes in direction

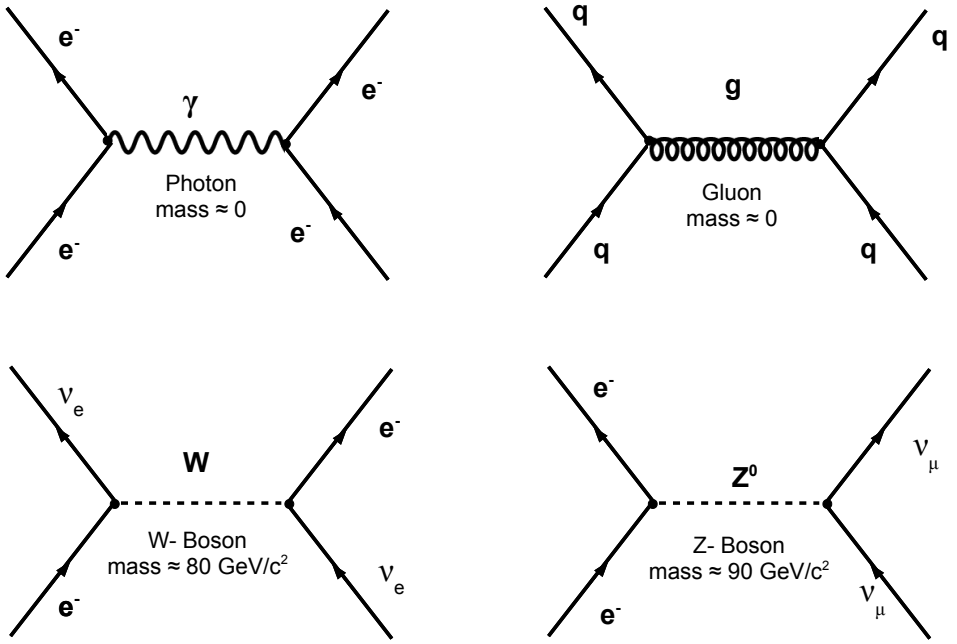

Figure 1.2: Schematic view (Feynman diagram) on the interaction between fermions mediated through bosons. In case of the electromagnetic interaction, this is the photon, for the strong interaction the gluons and for the weak interaction the W and Z bosons.

Leptons l with spin $1/2$

charge [e]	flavor	mass [GeV/c^2]	flavor	mass [GeV/c^2]	flavor	mass [GeV/c^2]
0	ν_e	$< 2.5 \times 10^{-9}$	ν_μ	$< 1.9 \times 10^{-9}$	ν_τ	< 0.018
-1	e	5.11×10^{-4}	μ	0.106	τ	1.7777

Quarks q with spin $1/2$

charge [e]	flavor	≈ mass [GeV/c^2]	flavor	≈ mass [GeV/c^2]	flavor	≈ mass [GeV/c^2]
+2/3	u	1.5×10^{-3} to 4×10^{-3}	c	1.15 to 1.35	t	174.3
-1/3	d	4×10^{-3} to 8×10^{-3}	s	0.08 to 0.13	b	4.1 to 4.4

Table 1.1: Characteristics of Leptons and Quarks sorted into three Generations. Compiled from [5].

Bosons with integer spin

electroweak	γ	W^-	W^+	Z^0	**strong**	gluon g	**gravitation**	graviton g
spin	1	1	1	1	spin	1	spin	2
charge [e]	0	−1	+1	0	charge [e]	0	charge [e]	0
mass [GeV/c^2]	0	80.4	80.4	91.2	mass [GeV/c^2]	0	mass [GeV/c^2]	0

Table 1.2: Characteristics of the exchange bosons. Today we know four fundamental interactions: electromagnetism, the weak and strong interactions and the gravitation. Compiled from [5].

left to right, the hermite conjugate term describes them in reversed direction. The operator $j_\alpha(x) = i\bar{\psi}_{f'}(x)\Gamma_\alpha\psi_f(x)$ is called current density, which induces transitions $f \to f'$. One calls the current charged if the pair ff' has a charge and due to charge conservation the mediating boson (here $V = W^\pm$) must be charged too. One calls the current neutral if the pair ff' has no charge and hence the mediating boson is also neutral ($V = \gamma, Z^0$). Beginning with a Lagrangian $\mathcal{L}(x)$ for a given interaction one is able to calculate, according to Feynman rules, all physical processes.

Based on this knowledge of particles and interactions in the 1960s, the $\mathcal{SM}$ was initiated and formulated by Glashow, Salam and Weinberg [6–8]. However there are several deficiencies of the $\mathcal{SM}$. First the question about the origin of mass, the strong CP problem, the observed asymmetry between matter and antimatter in the universe, as well as the so far not understood nature of dark matter and dark energy. All this needs theoretical developments, which can explain the observed facts. Within the $\mathcal{SM}$ neutrinos are mass less particles. However in recent years neutrino oscillation experiments showed that neutrinos do oscillate and have a non zero mass. Hence, it is time to think about physics beyond the $\mathcal{SM}$ in order to take neutrino masses into account.

1.2 Neutrino flavor change and neutrino mass

Today, due to various experiments performed so far[2], it is also well-known fact, that neutrinos and anti-neutrinos which take part in the weak interaction are of three different types or as they are also called of three different flavors e, μ, τ. Those weak interactions are described by the following Lagrangian in eq. 1.1, which consists out of two parts. First, the charged current interaction mediated via the W boson and second, the neutral current interaction mediated via the Z boson [9]:

$$\begin{aligned}
\mathcal{L}_{weak} &= \mathcal{L}_{CC} + \mathcal{L}_{NC} = \\
&- \frac{g}{\sqrt{2}} \sum_{\alpha=e,\mu,\tau} \sum_{k=1}^{3} \bar{\alpha}_L(x)\gamma_\alpha U_{\alpha k}\nu_{\alpha L}(x)W^{\alpha\dagger}(x) + h.c. \\
&- \frac{g}{2\cos\theta_w} \sum_{\alpha=e,\mu,\tau} \sum_{k=1}^{3} \nu_{kL}(x)\gamma^\alpha\bar{\nu}_{kL}(x)Z_\alpha(x) + h.c. \qquad (1.1)
\end{aligned}$$

The notion of the three different neutrino flavors ν_α, with $\alpha = e, \mu, \tau$ is dynamical. One can define the three different neutrino flavors by the decay of the W-boson, as visualized in the upper part of figure 1.3. The neutrino from the decay to an electron is named ν_e, the neutrino from the decay to a muon is ν_μ and the one in the decay to a tauon is therefore the ν_τ. For a given neutrino ν_α, the flavor L_α is a Lorentz invariant and among the different flavor neutrinos and anti-neutrinos no two are identical. Thus, within the precision of the current data the states describing different neutrino flavors are orthogonal:

[2]The experiments contributing to our today's understanding of neutrinos and neutrino oscillation will be explained in detail within the next chapter

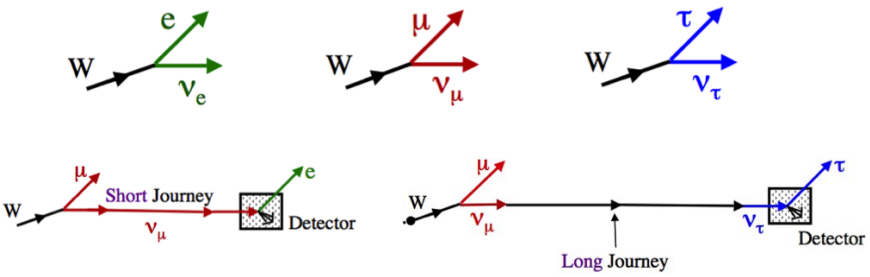

Figure 1.3: On top: Definition of the neutrino flavors from W boson decay. On the bottom: Neutrino oscillations if the decay vertex of the W boson is separated by the place of detection by a long distance. Figures taken from [10].

$$\langle \nu_\beta | \nu_\alpha \rangle = \delta_{\beta\alpha}\,, \quad \langle \bar{\nu}_\beta | \bar{\nu}_\alpha \rangle = \delta_{\beta\alpha}\,, \quad \langle \bar{\nu}_\beta | \nu_\alpha \rangle = 0 \tag{1.2}$$

$$L_\alpha |\nu_\beta\rangle = \delta_{\alpha\beta} |\nu_\beta\rangle\,, \quad L_\alpha |\bar{\nu}_\beta\rangle = -\delta_{\alpha\beta} |\bar{\nu}_\beta\rangle \tag{1.3}$$

As described before, our today's knowledge is that a change of flavor in a $\nu \to l$ interaction never occurs: This is true if the decay vertex and the place of detection are separated by a short distance. With $\alpha = e, \mu, \tau$ a ν_α only creates l_α in interactions. If one considers a larger separation distance and therefore a longer travel time for the neutrino, one can observe changes in flavor, the so called neutrino oscillations (see lower part of Fig. 1.3). These Oscillations are transitions between neutrinos $\nu_\alpha \longleftrightarrow \nu_\beta$ $(\alpha, \beta = e, \mu, \tau)$ with different lepton flavor numbers $L_\alpha \neq L_\beta$. For these oscillations two necessary conditions have to be fulfilled. First not all neutrinos have identical mass, what also means that not all neutrinos can be mass less. Second, the lepton flavor numbers are not conserved, there is a lepton-mixing. In the last decade a lot of experiments with solar, atmospheric, reactor and accelerator experiments have brought us compelling evidence for oscillations. These data imply the existence of a neutrino mixing in vacuum and non-zero neutrino masses.

But how does the neutrino mass arise? This question has not yet been answered conclusively. Within the $\mathcal{SM}$, fermions acquire mass by interaction with the Higgs field. However, these interactions involve both left- and right-handed neutrinos. This can be seen in the following way, beginning with the Lagrangian of a free fermionic particle without interaction.

$$-\mathcal{L} = \bar{\psi}\left(\gamma_\alpha \frac{\delta}{\delta x_\alpha} + m_D\right)\psi \tag{1.4}$$

Only the second term, the mass-term $-\mathcal{L} = m_D \bar{\psi}\psi$ is of interest. In order to have $\mathcal{L}$ hermitian, the Dirac mass m_D has to be real. One can decompose any fermionic wave function in chiral components using the projection operators of chirality P_L and P_R that fulfil the following relations $P_L\phi = \phi_L$,$P_R\phi = \phi_R$. Thus the second term $m_D\bar{\psi}\psi$ in eq. 1.4 can be decomposed into chiral components as well.

$$m_D\bar{\psi}\phi = m_D(\bar{\psi}_L + \bar{\psi}_R)(\phi_L + \phi_R) = m_D\bar{\psi}_L\phi_R + m_D\bar{\psi}_R\phi_L. \tag{1.5}$$

This gives a Dirac mass-term where left-handed as well as right-handed Dirac neutrinos contribute. In the $\mathcal{SM}$ only left-handed neutrinos exist, thus one has terms like $\bar{\psi}_L\phi_L$ or $\bar{\psi}_R\phi_R$. Using $P_LP_R = P_RP_L = 0$ one can get the following relations

$$\bar{\psi}_L\phi_L = \bar{\psi}P_RP_L\phi = 0\,, \tag{1.6}$$
$$\bar{\psi}_R\phi_R = 0. \tag{1.7}$$

Because of this, the Dirac mass term m_D in the $\mathcal{SM}$ has to be zero. As we do observe neutrino oscillations, the $\mathcal{SM}$ has to be revised and extended. A minimal extension incorporating a right-handed (left-handed) component for each (anti) neutrino generation, allows the construction of a Dirac mass term and a so called Majorana mass term. This means that a left-handed and a right-handed neutrino exist and both are independent of each other. Thus, in addition to a Dirac mass term, one can construct a Majorana mass term for the right-handed and the left-handed neutrinos represented by the hermitian terms $\bar{\psi}^c\psi$ and $\bar{\psi}\psi^c$ where ψ^c is the charge conjugate of ψ. The most general mass-term can than be written as

$$\begin{aligned}\mathcal{L}^{D+M} &= \mathcal{L}^D + \mathcal{L}^M_L + \mathcal{L}^M_R \\ &= -m_D\bar{\nu}_R\nu_L - \frac{1}{2}m_L\bar{\nu_L}\nu^c_R - \frac{1}{2}m_R\bar{\nu}^c_L\nu_R + h.c. \\ &= -\frac{1}{2}(\bar{\nu_L}, \bar{\nu_L}^c)\begin{pmatrix} m_L & m_D \\ m_D & m_R \end{pmatrix}\begin{pmatrix} \nu^c_R \\ \nu_R \end{pmatrix} + h.c..\end{aligned} \tag{1.8}$$

One can diagonalize this mass-matrix in eq. 1.8 above and obtain the following mass eigenvalues:

$$\tilde{m}_{1,2} = \frac{1}{2}\left[(m_L + m_R) \pm \sqrt{(m_L - m_R)^2 + 4m_D^2}\right] \tag{1.9}$$

By defining $\tilde{m}_k = \epsilon_k m_k$ with $m_k = |\tilde{m}_k|$ and $\epsilon_k = \pm 1$ one obtains positive masses. Therefore this simple addition of right-handed neutrinos into the $\mathcal{SM}$ creates neutrino masses. But still one problem remains, in comparison to the other fermionic masses, the neutrino masses are implausibly smaller (electron $m_e = 0.511\,\mathrm{MeV}/c^2$ compared to a $m_\nu < 1\,\mathrm{eV}/c^2$). A "natural" explanation to this is given by the Seesaw mechanism [11–13], which is an extension to the $\mathcal{SM}$ as well. For each lepton family in addition to the light left-handed neutrino ν_L with $m_L \approx 0$ a super-heavy right-handed neutrino ν_R with $m_R >> m_D$ is introduced. This than gives the masses of a light neutrino ν and a heavy Majorana neutrino N:

$$m_\nu = \frac{m_D^2}{m_R} << m_D \text{ and } m_N \approx m_R. \tag{1.10}$$

The mass of the light neutrino ν is suppressed by a factor of $m_D/m_R << 1$. With fixed m_D the light neutrino becomes even lighter by increasing the mass of the (hypothetical) heavy neutrino N.

1.2.1 Oscillation in vacuum

With the Lagrangian described before, one has a"three-neutrino mixing" scenario, which accommodates the experimental evidence for neutrino oscillations. The the relation between mass and flavor eigenstates can be written as a 3×3 matrix, which can be parametrized in terms of 9 parameters. Those parameters can be divided in 3 mixing angles and 6 phases. Out of these 6 phases only 3 are physical. The most common parametrization of the mixing matrix U known as the PMNS matrix (named after Pontecorvo, Maki, Nakagawa and Sakata) is [9] :

$$
\begin{aligned}
U &= R_{23} W_{13} R_{12} D(\lambda_{21}, \lambda_{31}) \qquad (1.11)\\
&= \begin{pmatrix} 1 & 0 & 0 \\ 0 & c_{23} & s_{23} \\ 0 & -s_{23} & c_{23} \end{pmatrix} \begin{pmatrix} c_{13} & 0 & s_{13} e^{-i\varphi_{13}} \\ 0 & 1 & 0 \\ s_{13} e^{i\varphi_{13}} & 0 & c_{13} \end{pmatrix} \begin{pmatrix} c_{12} & s_{12} & 0 \\ -s_{12} & c_{12} & 0 \\ 0 & 0 & 1 \end{pmatrix} \begin{pmatrix} 1 & 0 & 0 \\ 0 & e^{i\lambda_{21}} & 0 \\ 0 & 0 & e^{i\lambda_{31}} \end{pmatrix} \\
&= \begin{pmatrix} c_{12}c_{13} & s_{12}c_{13} & s_{13}e^{-i\varphi_{13}} \\ -s_{12}c_{23} - c_{12}s_{23}s_{13}e^{i\varphi_{13}} & c_{12}c_{23} - s_{12}s_{23}s_{13}e^{i\varphi_{13}} & s_{23}c_{13} \\ s_{12}s_{23} - c_{12}c_{23}s_{13}e^{i\varphi_{13}} & c_{12}c_{23} - s_{12}c_{23}s_{13}e^{i\varphi_{13}} & c_{23}1_{13} \end{pmatrix} \begin{pmatrix} 1 & 0 & 0 \\ 0 & e^{i\lambda_{21}} & 0 \\ 0 & 0 & e^{i\lambda_{31}} \end{pmatrix}
\end{aligned}
$$

With the parameters $s_{ij} = \sin\theta_{ij}$, $c_{ij} = \cos\theta_{ij}$ and θ_{12}, θ_{23}, θ_{12} are the three mixing angles. The Dirac phase is φ_{13}, the two Majorana phases are λ_{21} andλ_{31}. The matrix R_{ij} is a real rotation in the i-j plane whereas W_{13} is a complex rotation in the 1-3 plane. $D(\lambda_{21}, \lambda_{31})$ is a diagonal matrix with the Majorana phases.

In the case of Majorana neutrinos there is no difference between $\nu \neq \bar{\nu}$ and one should distinguish between states with positive and negative helicity. There is a common convention to call a neutrino a particles, if it was created together with a positive charged lepton and having almost exactly[3] negative helicity. On the opposite an anti-neutrino is the particle created together with a negative charged lepton and has almost exactly positive helicity. Within this convention Dirac neutrinos are created together with a positive charged lepton having almost exactly negative helicity. Also Dirac anti-neutrinos are created together with a negative charged lepton and having almost exactly positive helicity.

Neutrinos ν_α are created and detected with a definite flavor state in the weak charged-current interactions as described before. They are created together with charged leptons l_α^+ in processes like $A \to B + l_\alpha^+ + \nu_\alpha$, what can be seen on the left side of the diagram in figure 1.4. One can write the flavor state like

$$
|\nu_\alpha\rangle = \sum_{i=1}^{3} |\nu_k\rangle \langle \nu_k, l_\alpha^+ | j_{CC}^\rho | 0 \rangle J_\rho^{A\to B} \approx \sum_{i=1}^{3} U_{\alpha i}^* |\nu_i\rangle \qquad \alpha = e, \mu, \tau, \qquad (1.12)
$$

where one neglects the neutrino masses in the production process. The symbol j_{CC}^ρ describes the charge current in this interaction and $J_\rho^{A\to B}$ the transition from state A to B. The state $|\nu_\alpha\rangle$ describes a neutrino in the interaction point where it was created. But this creation point

[3] As neutrinos posses non-zero mass $m_\nu \neq 0$, each ν ($\bar{\nu}$) is a linear superposition of helicity -1/2 and +1/2 neutrino states, but the helicity +1/2 (-1/2) state enters into the superposition with a coefficient m_ν/E_ν and is strongly suppressed.

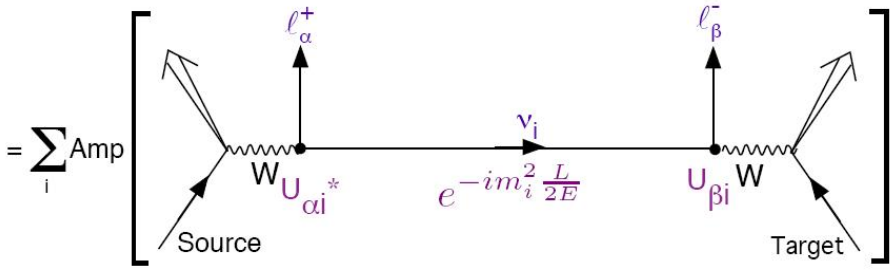

Figure 1.4: Feynman diagram describing the production of a neutrino of given flavor and the transition to a neutrino of another flavor at the detection point. Figure taken from [10].

differs from the state at the point of detection at a separation distance L at time T called $|\nu_\alpha\rangle(L,T)$. To obtain this state one uses the space-time translation operator $exp(-i\hat{E}T + i\hat{P}L)$, where $\hat{E}$ and $\hat{P}$ are the energy and momentum operators. As in experiments the propagation time T is not measured, one needs to connect the propagation time to the propagation distance L. For ultra-relativistic neutrinos this can be done easily, because the propagation time T is equal to the distance L up very small corrections in the order of the ratio of the neutrino mass and energy $\mathcal{O}(m_\nu/E_\nu)$.

$$E_k t - p_k \approx (E_k - p_k)L = \frac{E_k^2 - p_k^2}{E_k + p_k} = \frac{E_k}{m_k + p_k}L \approx \frac{m_k^2}{2E}L \tag{1.13}$$

With E_k and p_k being the energy and the momentum of a massive neutrino ν_k, as determined in the neutrino production process. E is the value of neutrino energy in the limit that the neutrino would be mass less. In this approximation the neutrino oscillation phase of ultra-relativistic neutrinos depends only on the ratio $m_k^2 L/2E$, so the oscillation probability is generally valid and not dependent on the specific production process. The resulting state $|\nu_\alpha(L)\rangle$ is

$$|\nu_\alpha(L)\rangle = \sum_{j=1}^{3} U_{\alpha k}^* e^{-i(m_k^2/2E)L}|\nu_j\rangle = \sum_{\alpha=e,\mu,\tau}\left(\sum_{j=1}^{3} U_{\alpha j}^* U_{\alpha j}^* e^{-i(m_k^2/2E)L}\right)|\nu_\beta\rangle. \tag{1.14}$$

Using the expression of $|\nu_j\rangle$ in terms of neutrino flavor states in the last step. With this the transition probability can be written as

$$\begin{aligned} P_{\nu_\alpha\to\nu_\beta}(L) &= |\langle\nu_\beta|\nu_\alpha(L)\rangle|^2 \\ &= \left|\sum_{j=1}^{3} U_{\alpha j}^* U_{\alpha j}^* e^{-im_k^2/2EL}\right|^2 \\ &= \sum_{j=1}^{3}|U_{\alpha j}|^2|U_{\beta j}|^2 + 2Re\sum_{i>j} U_{\alpha i}^* U_{\beta i} U_{\alpha i}^* U_{\beta j}^* exp\left(-i\frac{\Delta m_{ij}^2}{2E}L\right), \end{aligned} \tag{1.15}$$

making use of the definition $\Delta m^2_{ij} = m^2_i - m^2_j$. One can see that the observation of neutrino oscillations is directly connected to the fact that at least one of the neutrinos must have a non-zero mass. In addition to this, the transition probability in eq.1.15 shows, that the elements of the mixing matrix U determine Neutrino oscillations. The experimental parameters are the neutrino energy E_ν and different source-detector distance L. According to the value of L/E_ν and if one measures the survival $P_{\nu_\alpha \to \nu_\alpha}$ or transition probability $P_{\nu_\alpha \to \nu_\beta}$, different oscillation experiments can be classified as will be seen in one of the next sections.

1.2.2 Oscillations in matter

The theory of neutrino oscillations described before is only valid if these neutrinos do not travel through matter. If neutrinos propagate in matter, the oscillations are modified by coherent interactions with the medium. This was realized by Wolfenstein in 1978 [14].

In neutral current interactions all three neutrino flavors interact similar[4] in contrary to charged current interactions. In matter, electron neutrinos can interact with electrons via elastic scattering $\nu_e + e^- \to \nu_e + e^-$. This process adds an effective potential $\sqrt{2} G_F N_e$ for electron neutrinos ν_e to the Lagrangian, which is of the form $\delta\mathcal{L} = G_F N_e / \sqrt{2} \bar{\nu}_e \nu_e$. This modifies the masses as well as the mixing angles. In a two neutrino flavor scenario (ν_e, ν_μ) this leads to effective masses and an effective mixing angles:

$$m^2_{ee} \;\to\; m^2_{ee} + 2\sqrt{2} G_F N_e E_\nu \,, \tag{1.16}$$

$$\theta \;\to\; \theta_m \tag{1.17}$$

$$\sin^2 2\theta_m \;=\; \frac{\sin^2 2\theta}{\left(A/D - \cos 2\theta \right)^2 + \sin^2 2\theta}. \tag{1.18}$$

The ratio A/D is a function of the product of electron density in matter N_e and neutrino energy E_ν. One finds a resonance for $A/D = \cos 2\theta$ which gives $\sin^2 2\theta_m = 1$ or $\theta_m = 45$. This means that the probability for having ν_e or ν_μ oscillates between 0 and 1, not depending on the initial mixing angle θ in vacuum. Even small amplitudes $\sin^2 2\theta$ will be amplified to 1. This is called the MSW[5] effect which plays an important role in the sun and it is necessary to explain the results from the solar neutrino oscillation experiments. However, it does not play a significant role for reactor neutrino experiments (such as Double Chooz) and can be neglected. This is because the amount of matter traversed is comparably small, as well as the corresponding electron density compared to the one realized in the sun.

1.3 Neutrino Mass hierarchy

As will be explained in more detail in chapter 2, the measurements of neutrino oscillations have enabled the determination of the two squared mass differences being

$$\Delta m^2_{sol} \equiv \Delta m^2_{21} = 7.58 \cdot 10^{-5} \mathrm{eV}^2 \quad |\Delta m^2_{atm}| \equiv |\Delta m^2_{23}| = 2.35 \cdot 10^{-3} \mathrm{eV}^2, \tag{1.19}$$

[4] This is called the lepton universality

[5] Named after the theoreticians Mikheyev, Smirnov and Wolfenstein.

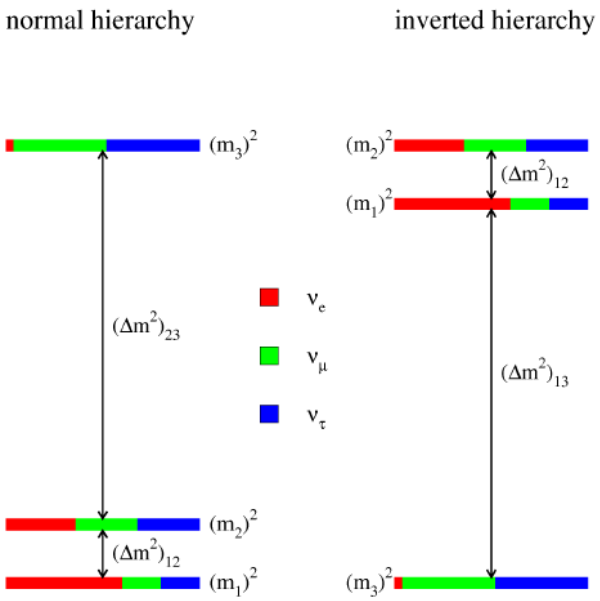

Figure 1.5: The neutrino mass hierarchy, on the left side the normal hierarchy, where the neutrino sate ν_1 with mass m_1 is the lightest and the ordering $m_3 > m_2 > m_1$holds. On the right, the inverted hierarchy, where the ordering is $m_2 > m_1 > m_3$. Plot taken from [15]

where the sign of Δm^2_{sol} was determined due to the MSW-effect. Recalling that the oscillations probabilities are, in addition to the mixing angles, determined by exponential factors where the mass squared differences between the mass states (m_1, m_2 and m_3) enter. However, only two of these three differences are independent as the following relation for the squared mass differences holds

$$\Delta m^2_{12} + \Delta m^2_{23} + \Delta m^2_{31} = 0. \tag{1.20}$$

Therefore one can calculate

$$\Delta m^2_{31} = \Delta m^2_{12} + \Delta m^2_{23} \approx \Delta m^2_{atm}. \tag{1.21}$$

Now, two possible neutrino mass hierarchies arise:

- **Normal hierarchy**: One assumes that the sign of Δ^2_{23} is positive and thus $m_3 > m_2 > m_1$. This hierarchy sees to be more "natural" since ν_e is the lightest neutrino, mainly composed of ν_1, whereas the heavier ν_μ, ν_τ neutrinos are mainly composed of the ν_2, ν_3 states.
- **Inverted hierarchy**: Now the sign of Δm^2_{23} is negative and one gets $m_2 > m_1 > m_3$.

Schematically, this can be seen in figure 1.5. Thus, in order to clarify which hierarchy is realized in nature, a measurement of the sign of the mass squared difference Δm^2_{23} is needed in the future.

1.4 Experimental view on oscillations

As described in the section before, neutrino oscillations are parametrized by the mixing angles θ_{ij} and the squared mass differences Δm^2_{ij} within the PNMS-matrix

$$U = \begin{pmatrix} c_{12}c_{13} & s_{12}c_{13} & s_{13}e^{-i\varphi_{13}} \\ -s_{12}c_{23} - c_{12}s_{23}s_{13}e^{i\varphi_{13}} & c_{12}c_{23} - s_{12}s_{23}s_{13}e^{i\varphi_{13}} & s_{23}c_{13} \\ s_{12}s_{23} - c_{12}c_{23}s_{13}e^{i\varphi_{13}} & c_{12}c_{23} - s_{12}c_{23}s_{13}e^{i\varphi_{13}} & c_{23}1_{13} \end{pmatrix}. \tag{1.22}$$

The oscillations are driven by sine or cosine functions of the mixing angles θ_{13} in addition to functions with arguments like

$$\sin\left(\frac{\Delta m^2_{ij}}{4}\frac{L}{E_\nu}\right) \quad , \cos\left(\frac{\Delta m^2_{ij}}{4}\frac{L}{E_\nu}\right). \tag{1.23}$$

The important experimental variable in these functions are the ratios L/E_ν. Each experiment able to vary and to measure this ratio can look for neutrino oscillations. However a necessary condition that has to be fulfilled is that

$$\frac{L}{E} \geq \frac{\Delta m^2_{ij}}{4} \quad \Longleftrightarrow \quad \frac{L}{E_\nu} \geq \frac{1}{\Delta m^2_{ij}}. \tag{1.24}$$

Otherwise the oscillatory term would be zero, as oscillations are not yet developed. The greater the distance L between a given ν_α source and a given ν_β detector and the smaller the neutrino energy E, the more probable it is for oscillations to develop. An experiment with a fixed L/E ratio is sensitive to squared mass differences of

$$\Delta m^2_{ij} \geq \Delta m^2_{min} \approx \frac{E_\nu}{L}. \tag{1.25}$$

If $L/E >> 4/\Delta m^2_{ij}$ many oscillations have happened and the oscillation pattern is washed out. This is the case if either L or E cannot be fixed in the experiment. For the distance L this is the case if the neutrino source is very large (like the sun or earth's atmosphere) or if the point of detection cannot be localized with high precision inside the detector. A not fixed energy E can be caused, if the source energy spectrum is not monochromatic and the energy is not measured inside the detector. All these three regions can be seen in an exemplary neutrino oscillation plot for the survival probability $P(\nu_e \to \nu_e)$ that can be found in figure 1.6 below.

In principle, a discrimination in two types of oscillation experiments is possible:

- **Appearance experiments**: One detects a different neutrino flavor $\nu_\beta \neq \nu_\alpha$ compare to the one created in the source. Therefore these experiments measure the transition probability $P(\nu_\alpha \to \nu_\beta)$. In these experiments it is very important to know the any contamination of ν_β emitted by the source, because this would otherwise fake oscillations.

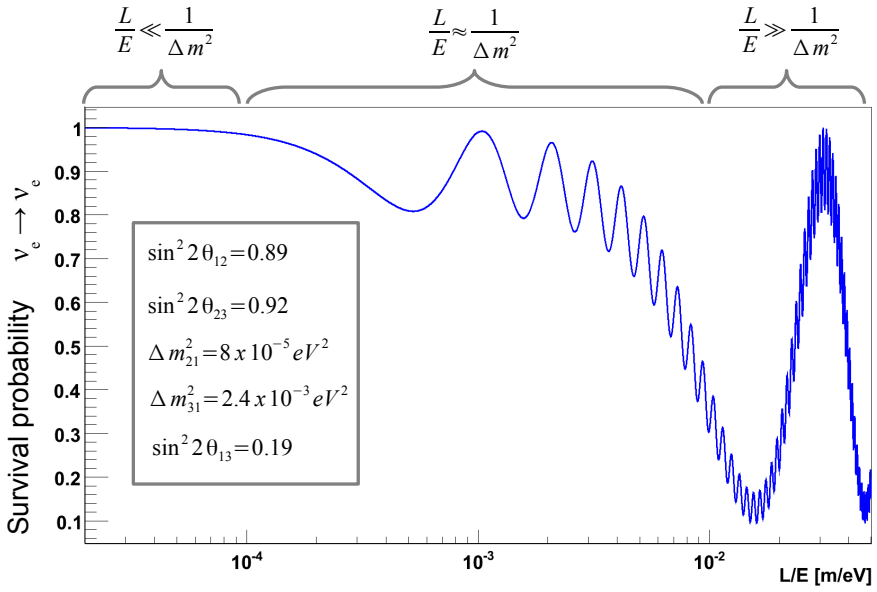

Figure 1.6: Neutrino oscillation example for $P(\nu_e \to \nu_e)$. The parameters used to draw this plot are, $\sin^2 2\theta_{12} = 0.89$, $\sin^2 2\theta_{23} = 0.92$, $\Delta m^2_{21} = 8 \cdot 10^{-5}\,\mathrm{eV}^2$ and $\Delta m^2_{31} = 2.4 \cdot 10^{-3}\,\mathrm{eV}^2$. The value $\sin^2 2\theta_{13}$ was assumed to be 0.19. In this plot of the survival probability, one is able to discriminate three regions, the first where oscillations have not yet developed for $L/E >> 4/\Delta m^2_{ij}$, the second for $L/E \approx 4/\Delta m^2_{ij}$ where oscillations do happen and the third for $L/E << 4/\Delta m^2_{ij}$ where the oscillation pattern is washed out.

- **Disappearance experiments**: The same neutrino flavor ν_α is measured inside the detector as created in the source. The survival probability $P(\nu_\alpha \to \nu_\alpha)$ is measured. This can be stated the other way round, these experiments measure $P(\nu_\alpha \to \nu_X) = 1 - P(\nu_\alpha \to \nu_\alpha)$, being the probability that a original ν_α has oscillated into a ν_X not measured by the experiment. In these type of experiments one needs exact knowledge on the flux of ν_α neutrinos, as any deficit would be interpreted as an oscillation. To avoid these absolute flux measurements, modern experiments deploy several detectors at different distances to the source and measure relative to each other.

In table 1.3 below, for both experimental approaches the neutrinos flavors created in the source, the approximate range of neutrino energy and distance between source and detector and the sensitivity to the mass difference Δm^2 is listed.

ν-**source**	ν-**flavor**	**energy [MeV]**	**distance [m]**	L/E **[MeV/m]**	**min.** Δm^2 **[eV^2]**
Reactors	$\bar{\nu}_e$	$1-10$	$10-10^2$	$1-10^2$	10^{-2}
Accelerators	ν_μ,$\bar{\nu}_\mu$	$10-10^5$	$10-10^7$	$10^{-3}-10^4$	10^{-4}
Atmosphere	$\nu_{\mu,e}$,$\bar{\nu}_{\mu,e}$	10^3	10^4	10^{-1}	10^{-4}
Sun	ν_e	1	$1.5 \cdot 10^8$	10^{-7}	10^{11}

Table 1.3: In this table the sensitivity of different oscillation experiments and the corresponding parameters classifying them are summarized. This table is compiled from [2] and [16].

1.5 Summary

The Standard Model of particle physics was introduced in this chapter, as well as the theoretical concept of neutrino flavor change and oscillations. It was stressed, that these oscillating changes in neutrino flavor do only happen if neutrinos have different masses, especially not all of them being mass less as assumed by the Standard Model. Already this theoretical observations give the conclusion that the Standard Model needs to be extended with massive neutrinos. This yields more fundamental questions regarding the particle nature of the neutrinos, being a Dirac or a Majorana particle and the origin and ordering of their mass, which is the focus of today's research interest.

An short overview on the experimental observation principle was given introducing appearance and disappearance experiments. With this theoretical background, the next chapter will put its emphasis on the measurements of neutrino characteristics performed so far. It will describe the observation of neutrino oscillation for neutrinos originating from the sun or being created in earth's atmosphere and at the end it will focus on the measurement of the third mixing angle θ_{13}.

"Physics is becoming so unbelievably complex that it is taking longer and longer to train a physicist. It is taking so long, in fact, to train a physicist to the place where he understands the nature of physical problems that he is already too old to solve them."

Eugene P. Wigner (1902-1995)

2 Measuring Neutrino Oscillations

It took quite a long time to experimentally establish the existence of the neutrino, and even longer for the first observation of neutrino oscillations. The first indication was the deficit of solar neutrinos observed by the Homestake experiment in 1968. In addition, experiments measuring neutrinos generated in the earth's atmosphere through cosmic rays did not show an agreement with expectations. Both observations lead to the so called Solar and Atmospheric neutrino anomalies that will be explained in the first part this chapter together with a brief overview of the scientific history of the neutrino.

The experimental establishment of neutrino oscillations as a solution to the solar and atmospheric anomaly will be presented in the second section. Those neutrino oscillations were first confirmed by the Super Kamiokande experiment about 30 years after the first indication in the Homestake experiment in 1998. The experiments contributing to our today's understanding of neutrino oscillations will be briefly described and their results will be listed.

Besides the search of solar or atmospheric neutrino oscillations, experiments looking for oscillations driven by with man-made neutrinos at accelerators and nuclear reactors will be explained at the end of this chapter. These experiments lead to the successful measurement of the up to 2012 unknown third mixing angle θ_{13} and lead to the picture of a three neutrino flavor mixing.

2.1 Neutrino history in brief

This first section compiles the history of neutrinos, likewise [17, 18], with the focal point on the historical events, physicists and measurements led to the present understanding of the neutrino properties, flavor oscillations and finite mass. With exception of the parts on the "Solar" and the "Atmospheric neutrino anomaly" that lead to experimental evidence for neutrino oscillations and will be described in more detail, all other items will only be shortly reviewed.

- **Paulis desperate remedy (1930)**

  The neutrino was the idea of W. Pauli. He made his neutrino proposal in a letter addressed to people attending a meeting about radioactivity in Tübingen. The primary purpose of the letter was to apologize for being unable to attend, as he was indispensable in Zurich because of a ball during the time of the meeting. His hypothetical neutrino could explain the continuous spectrum observed in β-decays. At that times

it was thought that this is a two-body decay with a fixed energy. By introducing a third, electrically neutral particle in the decay he could rescue the energy and angular momentum conservation in this decay. In the beginning few physicists liked the idea of introducing a new particle. Opinions were ranging from "wrong" to "crazy" regarding Pauli's idea. He himself wagered a case of champagne for those first detecting it.

- **Fermi's weak theory (1934)**

  In 1933 E. Fermi attended the Seventh Solvay Conference of Particle Physics in Brussels, where Pauli also presented his neutrino idea. This was a special conference, as the discoveries of the positron and of the neutron were presented. Fermi left the conference with many new ideas that he would use in the development of a theory of β-decay. He proposed that an electron and a neutrino were emitted from a neutron in the β-decay, $n \to p + e^- + \bar{\nu}_e$, similar to the emission of a photon from a radioactive decay.

  At that time the latter process was possible to be described by using Diracs theory, which he adopted and replaced the electric charge e with a new coupling constant. He named it G_F, now known as the Fermi coupling constant and came with a new force of nature, the weak force. He wanted to publish his theory in Nature, but it was refused for "containing abstract speculations too remote from physical reality to be of interest to the readers" [19]. He later published his theory in an Italian journal [20] and later in German [21].

- **Seeing the invisible (1956)**

  At the end of World War II, F. Reines thought about the possibility of neutrino detection during the explosion of an atomic bomb. During a summers visit in Los Alamos, Fermi pointed him towards nuclear reactors. C. Cowan joined him in their first experiment, Project Poltergeist, which was situated at the Hanford engineering site. But there, they were not able to shield their experiment against cosmic ray background and so they moved to the Savannah river side, where they could build a bigger detector placed underground. In 1956, nearly 25 years after Pauli proposed the neutrino, the neutrino could be detected the first time [22]. For the detection they used the inverse β-decay ($\bar{\nu}_e + p \to e^+ + n$) by measuring a coincidence of photons from the annihilation of positrons and electrons and a gamma's from the capture of neutrons on cadmium chloride ($CdCl_2$) delayed by $5\,\mu$s. Pauli was still alive at that time and they won the wagered case of champagne from him.

- **Measurement of neutrino helicity (1958)**

  In 1958 M. Goldhaber was the first in measuring the helicity[1] of the neutrino [23]. For this he used the electron capture reaction in an europium isotope, transforming it to samarium:

$$e + {}^{152}Eu \to {}^{152}Sm + \nu_e \to {}^{152}Sm + \nu_e + \gamma$$

  After the electron capture on the Eu at rest, the emitted neutrino and the excited Sm nucleus have the same, but opposite momentum. The Sm dexcites by γ emission.

[1] The helicity is the projection of a particles spin in direction of its momentum: $h = \vec{S} \cdot \vec{p}/|\vec{p}|$.

Interesting for the experiment are only those photons which are emitted in the direction of flight of the Sm nuclei. Their energy is $\vec{p}_\gamma = -\vec{p}_\nu$ and the Sm nucleus is practically at rest after the emission. For such a photon it is possible to do resonance scattering on another Sm nucleus:

$$\gamma + {}^{152}Sm \rightarrow {}^{152}Sm^* \rightarrow {}^{152}Sm + \gamma$$

Due to angular momentum conservation and to the opposite photon and neutrino momenta one ends up with $H(\nu_e) = H(\gamma)$. Goldhaber was able to measure the neutrino helicity by measuring circular polarization of photons and obtained $H(\nu_e) = -1.0 \pm 0.3$. The experiment showed that neutrinos are always left-handed.

- **Parity non conservation (1960s)**

  The experiment made by Goldhaber together with many other experiments scoping on the parity non-conservation in weak reactions in the 1950s lead to the (V-A) theory of weak interactions [24]. The parity non-conservation in weak reactions was first measured by C.S. Wu [25] with the beta-decay of polarized ${}^{60}Co$ nuclei. In charged current (anti)-neutrino $\nu, \bar{\nu}$ interactions with (anti)-leptons $l, \bar{l}$ one can calculate the probability $P(H)$ for observing a lepton l with helicity H:

$$P(H \pm 1) = \frac{1}{2}\left(1 \pm \alpha \frac{v}{c}\right) \text{ with } \alpha = \begin{cases} -1 & \text{for leptons} f \\ +1 & \text{for anti-leptons} \bar{f} \end{cases}$$

  Within the $\mathcal{SM}$, where neutrinos are assumed to be mass less one finds:

$$P_\nu(+1) = 0 \quad P_\nu(-1) = 1$$
$$P_{\bar{\nu}}(+1) = 1 \quad P_{\bar{\nu}}(-1) = 0$$

  Many experiments afterwards proofed, that neutrinos are always emitted with helicity $H(\nu) = -1$ and anti-neutrinos with helicity $H(\bar{\nu}) = +1$.

- **Different neutrinos? (1959)**

  In the year 1959 B. Pontecorvo worked on the question if the neutrino that is created together with $e^\pm$ in beta-decay is the same as the one created with $\mu^\pm$ in muonic decays of pions. He and Schwartz proposed to use high energy proton accelerators to create muon neutrinos and study their interactions. The AGS experiment at Brookhaven National Laboratory clarified this in 1962 and showed that there are different types of neutrinos [26]. In the experiment a 15 GeV proton beam was used. The beam was shot on a beryllium target and created pions and kaons. These particles traveled through a 13.5 m thick iron screen, where they decayed into muons which shortly after decayed into muon neutrinos. So after the iron screen they had only muon neutrinos and were looking for reactions in a 10 t spark chamber. The measured reactions were of type $\nu_\mu + n \rightarrow \mu^- + p$ and $\bar{\nu}_\mu + p \rightarrow \mu^+ + n$ but not one with $e^\pm$ was measured. The conclusion of the experiment was $\nu_\mu \neq \nu_e$.

- **Discovery of the tau (1975)**

  In 1975 a third charged lepton, the tauon was discovered at the Stanford Linear Accelerator Center (SLAC) [27] by Perl. They were discovered in e^+e^- annihilation processes of type:

  $$e^+ + e^- \rightarrow e^\pm + \mu^\mp + \text{missing energy}.$$

  These events were "abnormal", because except for $e^+ + \mu^-$ or $e^- + \mu^+$ no other charged particles or photons could be detected and the Lepton number seemed to be violated. Using (V-A) theory of weak interaction an explanation emerges if one considers the production of another pair of charged leptons, which in turn further decay:

  $$\begin{aligned} e^+ + e^- &\rightarrow \tau^+ + \tau^- \rightarrow e^+ + \nu_e + \nu_\tau + \mu^- + \bar{\nu}_\mu + \bar{\nu}_\tau \\ &\rightarrow \tau^- + \tau^+ \rightarrow e^- + \bar{\nu}_e + \bar{\nu}_\tau + \mu^+ + \nu_\mu + \nu_\tau \end{aligned} \quad (2.1)$$

  The new charged lepton was called tauon. The missing energy is carried away by four (anti) neutrinos.

- **Neutrinos from Supernovae (1987)**

  The Kamiokande and IrvineMichiganBrookhaven (**IMB**) experiments detected a burst of neutrinos from Supernova 1987A. This was heralding the birth of neutrino astronomy and was setting a limit on many neutrino properties (mass, charge, lifetime, number of neutrino flavors). A detailed example will be given for the number of neutrino flavors, which could be estimated using the energy spectrum of the measured neutrino events coming from supernova 1987A. It was assumed that the energy in the order of $2 \cdot 10^{53}$ erg released during core collapse is distributed equally to all neutrino flavors. The measured $\bar{\nu}_e$ events where compatible with having 1/6 of the total energy, which yields the number of neutrino flavors [28]:

  $$N_\nu^{SN1987A} = 2.5^{+4.1}_{-0.8} < 8$$

- **How many neutrino families? (1990)**

  At CERN the number of neutrino flavors N_ν was determined by a precise measurement of the Z^0 decay width. Four experiments at the LEP collidor participated in this effort, namely ALEPH [29], DELPHI [30], L3 [31] and OPAL [32]. The Z^0 boson decays into fermion anti-fermion pairs $Z^0 \rightarrow f\bar{f}$ with the partial decay widths Γ_f which can be summed up to $\Gamma_Z = \sum_f \Gamma_f$. Here f can be a quark q or a charged lepton l or a neutrino ν. So one can divided the partial decay widths into hadronic ones Γ_h, leptonic ones Γ_l and the ones from the neutrinos. As the neutrinos could not be measured, their decay with $\Gamma_{invis} = N_\nu \Gamma_\nu$ is called invisible. Otherwise this is the difference of the total decay width and the hadronic and leptonic decay widths:

  $$N_\nu = \frac{1}{\Gamma_\nu}(\Gamma_Z - \Gamma_h - 3\Gamma_l)$$

Here Γ_ν can be calculated from theory. The experiments measured $N_\nu^Z = 2.92 \pm 0.05$ [16], thus the number of neutrinos coupling to Z^0 is in accordance with three neutrino flavors.

Another determination of the number of neutrino flavors is possible via primordial nucleosynthesis. Shortly after the Big Bang protons and neutrons formed the light nuclei deuterium (**D**), ^{3}He, ^{4}He and ^{7}Li. Mostly ^{4}He was formed, so that hydrogen and ^{4}He are the most abundant elements in the universe making up the most part of baryonic matter. The mass fraction Y_p of the primordial ^{4}He is $Y_p = 0.234 \pm 0.006$, which is connected to the ratio of neutron to protons, n_n/n_p, at the time of nucleosynthesis:

$$Y_p = \frac{M_{He}}{M_{He} + M_H} = \frac{2n_n/n_p}{1 + n_n/n_p}$$

Whereas this ratio is connected to the freeze-out temperature T_F, the temperature where protons and neutrons are in thermal equilibrium, and to the Hubble expansion of the universe $H(T)$. The number of neutrino flavors is connected to this via a causal chain like:

$$N_\nu \uparrow \rightarrow H(T) \uparrow \rightarrow T_F \uparrow \rightarrow n_n/n_p \uparrow \rightarrow Y_p \uparrow$$

Thus, from the measurement of Y_p a value of $N_\nu < 3.6$ was obtained [33] which is in agreement with the LEP measurements and the rough SN1985A estimate. One should mention, that the nucleosynthesis result is complementary to the LEP measurements. In the Z^0 decay only neutrinos coupling to Z^0 are counted, whereas the nucleosynthesis result counts all neutrinos contributing to the energy density of the early universe, so also right handed (sterile) neutrinos which do not couple to the Z^0 boson via the weak interaction.

- **Discovery of the tau-neutrino (2000)**

  The first detection of the tau neutrino interaction was done with the DONUT (Direct Observation of the NU Tau, E872) [34] experiment, situated at Fermilab. The experiment confirmed the existence (four events above expected background of < 0.2 events) of the last lepton predicted by the $\mathcal{SM}$. In the experiment protons were accelerated and produced charged mesons which decay into tau neutrinos. Background was eliminated by several magnet systems and bulk matter of iron and concrete. After this, the accelerator beam passed through several sheets of nuclear emulsion. Only in very rare cases one of the produced neutrinos interact within the detector, producing electrically charged particles interaction which in turn left visible tracks in the emulsion that could be registered. Thus, as of today, we have three neutrinos ν_x with corresponding leptons l_x, where $x = e, \mu, \tau$.

2.1.1 Solar Neutrino Anomaly

Neutrinos are produced in star cores by fusion reactions of the pp chain or the CNO cycle. The neutrino spectrum emitted by the sun can be seen in figure 2.1. The sum effect of these complicated reactions chains can be written as:

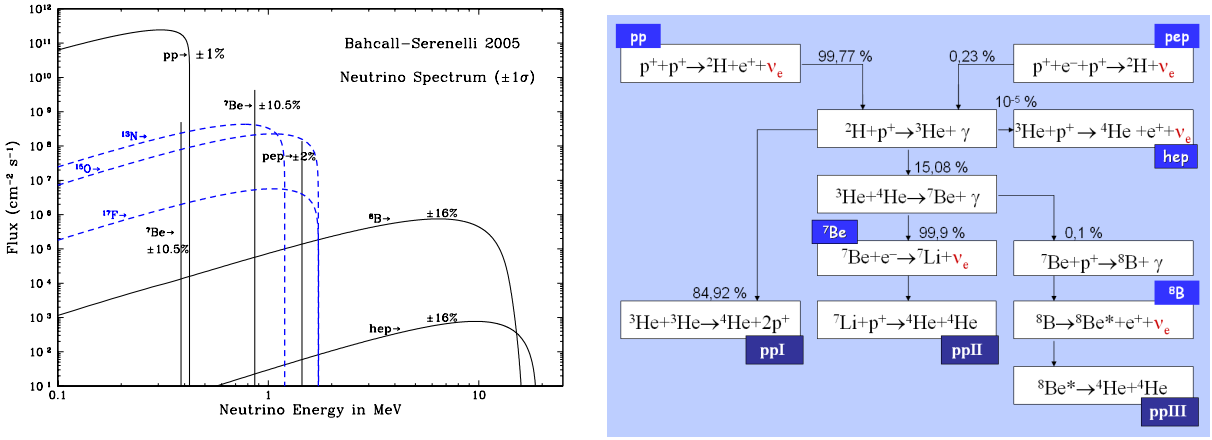

Figure 2.1: The left plot shows the neutrino spectra from proton-proton solar fusion processes as predicted by the standard solar model. Taken from the J. Bahcalls web site, http://www.sns.ias.edu/∼jnb/. The right plot shows the proton-proton chain reaction, from [35].

$$4p \rightarrow {}^4\mathrm{He} + 2e^+ + 2\nu_e$$

Since neutrinos interact only weakly with matter, they escape the star essentially unimpeded, what makes them very interesting as one can look into the stars interior. Thus if one observes neutrinos from a star, one can have a direct glimpse on the processes going on in the star core, whereas visible light emitted from surface was produced hundreds of thousands of years ago in the star core. Such an observation would directly address the theory of stellar structure and evolution, which is in turn the basis of the Standard Solar Model (**SSM**). To date solar neutrinos have been observed by several experiments using different techniques: radio chemical with chlorine (Homestake) or gallium (SAGE, GALLEX and GNO), by using water Cherenkov detectors (Kamiokande and Super-Kamiokande, SNO) or with liquid scintillation detectors (KamLAND, BOREXINO).

Radio chemical experiments

Beginning in the late 1960s R.Davis with his Homestake Experiment was the first to measure the solar neutrino flux. Because of the very low count rate, the experiment was operated in a gold mine 1500 m deep underground to protect it from cosmic rays which constitute interfering background. The experiment was based on the detection reaction

$$\nu_e + {}^{37}\mathrm{Cl} \rightarrow {}^{37}\mathrm{Ar} + e^- \quad (\text{threshold } 814\,\text{keV})$$

After typically one month, the tank was flushed with a noble gas and the few produced ^{37}Ar where extracted, a very difficult operation. The expected number of neutrinos emitted by the sun had been computed by J.Bahcall based on the SSM. The Homestake experiment found only 27 % of the predicted solar neutrino flux over the course of 30 years of operation. To solve this puzzle further experiments (GALLEX, SAGE) were started, which utilized the following detection reaction:

experiment	target	result	measured/prediction
Homestake	^{37}Cl	$2.56 \pm 0.22\,\mathrm{SNU}$	0.32 ± 0.05
GALLEX	^{71}Ga	$69.7^{+7.8}_{-8.1}\,\mathrm{SNU}$	0.53 ± 0.07
SAGE	^{71}Ga	$74 \pm 14\,\mathrm{SNU}$	0.56 ± 0.11
Kamiokande	e^-, H_2O	$(2.8 \pm 0.38) \cdot 10^6\,\mathrm{cm^1 s^{-1}}$	0.49 ± 0.10

Table 2.1: Comprehension of the solar neutrino experiments Homestake, GALLEX, SAGE and Kamiokande and comparison with the Bahcall Standard Solar Model. The discrepancy in observation versus expectation is evident and became known as the "Solar Neutrino Anomaly". The abbreviation SNU stands for solar neutrino unit and corresponds to a neutrino flux producing 10^{-36} neutrino capture reactions per target atom and per second.

$$\nu_e + {}^{71}\mathrm{Ga} \rightarrow {}^{71}\mathrm{Ge} + e^- \quad (\text{threshold } 233\,\mathrm{keV})$$

Also these experiments only found 52 % of the expected solar neutrino flux presenting a clear discrepancy to the prediction of the SSM.

Water Cherenkov experiments

The in 1987 started water Cherenkov experiment Kaimokande, later Super Kamiokande, succeeded in real-time solar neutrino observation via the neutrino electron scattering reaction:

$$\nu_e + e^- \rightarrow \nu_e + e^-$$

The threshold for this to happen was 5 MeV in Kamiokande and 7 MeV in Super Kamiokande respectively. Because of the high threshold the experiment observed pure ^{8}Be neutrinos. This was the first experiment really "seeing" the sun, because of the directional correlation between the incoming neutrino and the knock-on electron. But also only 40 % of the expected rate was measured. This discrepancies became known as the "Solar Neutrino Anomaly" and were shown in table 2.1.

The Sudbury Neutrino Observatory (**SNO**) experiment started in 1999 and convincingly confirmed the picture of solar neutrino oscillations. The water Cherenkov detector was installed deep underground and consists of 1000 tons of ultra-pure heavy water (D_2O) contained in a spherical acrylic vessel, surrounded by an water shield. SNO measured ^{8}Be solar neutrinos and was able to distinguish between elastic scattering (ES) and charged-current (CC), as well as neutral-current (NC) reactions, where $x = e, \mu, \tau$ stands for the three neutrino flavors:

$$\begin{aligned} \mathrm{ES} &: \nu_e + e^- \rightarrow \nu_e + e^- \\ \mathrm{CC} &: \nu_e + d \rightarrow p + p + e^- \\ \mathrm{NC} &: \nu_x + d \rightarrow p + n + \nu_x \end{aligned}$$

While the ν_e flux as obtained from the CC reactions is only 1/3 of the predicted flux, the total neutrino flux measured with the NC reactions is in agreement with the exceptions. The measured fluxes for CC, ES, and NC events were:

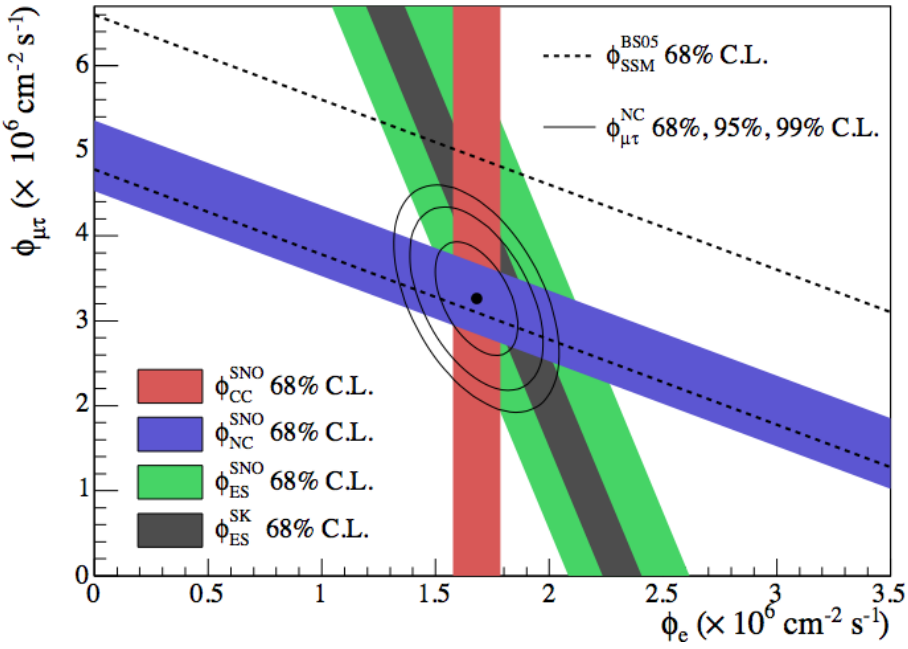

Figure 2.2: Fluxes of B solar neutrinos, $\phi(\nu_e)$, and $\phi(\mu\, or\, \tau)$ as measured with SNOs CC, ES and NC reactions and the Super Kamiokande ES flux. The SSM prediction is also shown. The drawn bands correspond to an error of 1σ.

$$\begin{aligned}
\phi_{ES}^{SNO} &= (2.35 \pm 0.22 \pm 0.15) \times 10^6\, cm^{-2} s^{-1} \\
\phi_{CC}^{SNO} &= (1.68 \pm 0.06\, ^{+0.08}_{-0.09}) \times 10^6\, cm^{-2} s^{-1} \\
\phi_{NC}^{SNO} &= (4.94 \pm 0.21\, ^{+0.38}_{-0.34}) \times 10^6\, cm^{-2} s^{-1}
\end{aligned}$$

The flux of ν_e and $\nu_{\mu,\tau}$ neutrinos can be deduced from these results via

$$\phi_{NC}^{SNO} = \phi_{\nu_e} + \phi_{\nu_{\mu,\tau}} \qquad \phi_{ES}^{SNO} = \phi_{\nu_e} + 0.1553 \cdot \phi_{\nu_{\mu,\tau}}$$

Figure 2.2 is a strong evidence for neutrino oscillations. It shows $\phi_{\nu_{\mu,\tau}}$ as a function of ϕ_{ν_e} flux. These results are consistent with those expected from the large mixing angle solution of solar neutrino oscillation in matter. At that time the possibility of other solutions could not be excluded with this data only.

Scintillator experiments

The KamLAND experiment reported its first results in 2002, which showed a clear evidence of an event deficit as it was expected from neutrino oscillations. The experiment is a 1 kton liquid scintillator detector located at the old Kamiokandes underground site in Japan. The KamLAND experiment is a long-baseline (flux-weighted average distance of ≈ 180 km) neutrino oscillation experiment using the electron anti-neutrinos emitted from all nuclear power reactors in Japan. The IBD reaction is used to detected electron anti-neutrinos. The 2002 results with 162 ton·yr exposure showed a ratio of observed to expected of

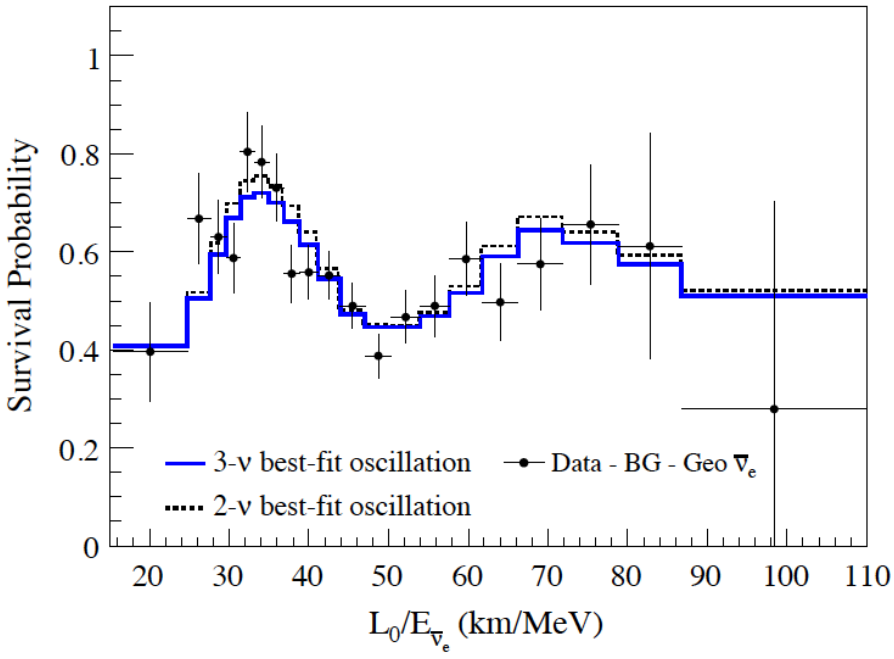

Figure 2.3: The plot shows the ratio of the background and geoneutrino-subtracted ν_e spectrum to the predicted one without oscillations as a function of L/E, where $L = 180\,\text{km}$. The curves show the best-fit expectations for ν_e oscillations.

$$\frac{N_{obs} - N_{back}}{N_{no\,Osc}} = 0.611 \pm 0.085 \pm 0.041.$$

This clear event deficit is an evidence for the neutrino oscillation hypothesis. In addition, for the first time the periodic feature of the survival probability from neutrino oscillations was measured giving a further hint. This oscillating pattern is shown in figure 2.3).

In addition to the KamLAND scintillator experiment mentioned before, the BOREXINO experiment is taking data since 2007. It measures the solar neutrinos with 300 t of ultra-pure liquid scintillator and has a very low detection threshold of 250 KeV. In this experiment the monochromatic flux of the ^{7}Be line has been measured the first time. Further measurements include the 1.44 MeV pep neutrinos and the ^{8}B neutrinos with a slightly higher threshold of 3 MeV.

2.1.2 Atmospheric Neutrino Anomaly

Neutrinos created in the atmosphere by cosmic ray particles are an annoying background if one wants to observe solar neutrinos or if one wants to do neutrino astronomy. Nevertheless they have turned out to be a very interesting physics subject. Primary cosmic ray interact in the atmosphere and create copiously neutral and charged pions. They themself decay into muons, which are also unstable and decay into electrons and neutrinos. In detail these processes will be described in chapter 5. The atmospheric neutrinos contain electron and

experiment	**ratio** R	**mass** [kt]
Kamiokande	$0.60 \pm 0.06(\text{stat}) \pm 0.05(\text{syst})$	4.5
IMB	$0.54 \pm 0.05(\text{stat}) \pm 0.12(\text{syst})$	8.0
Soudan 2	$0.64 \pm 0.17(\text{stat}) \pm 0.09(\text{syst})$	1.0
Super Kamiokande	$0.69 \pm 0.06(\text{stat})$	50

Table 2.2: Comprehension of the atmospheric neutrino experiments Kamiokande, IMB, Soudan 2 and Super Kamiokande. The discrepancy in observation versus expectation is evident and called "Atmospheric Neutrino Anomaly". Compiled from [36–38].

muon neutrinos and one would expect a ratio of:

$$\frac{N(\nu_\mu, \bar{\nu}_\mu)}{N(\nu_e, \bar{\nu}_e)} = \frac{N_\mu}{N_e} \approx 2$$

The first experiments that observed atmospheric neutrinos were the IMB and the Kamiokande, later the Super Kamiokande experiments. All experiments were massive underground nucleon decay search instruments and neutrino detectors using kilo tonnes of water as detection volume. Electron neutrinos transfer part of their energy to electrons via elastic scattering or they produce electrons in interactions $\nu_e + N \rightarrow e^- + N'$. This is different for muon neutrinos, as they only produce muons in interactions $\nu_\mu + N \rightarrow \mu^- + N'$. The electron anti- neutrinos or muon anti-neutrinos produce positrons or positive muons. These charge leptons can be detected via the Cherenkov effect in water. Because of the different acceptance of electrons and muons in a water Cherenkov detector, the ratio of muons to electrons is compared to Monte Carlo simulations. One uses the double ratio R where a value of 1 is expected if the expected interaction and propagation models hold:

$$R = \frac{(N_\mu/N_e)_{data}}{(N_\mu/N_e)_{Monte\,Carlo}}$$

Beginning in 1988, IMB [36] and Kamiokande [37] measured a ratio of R significantly lower than one. The 50 kilo tonne Super Kamiokande detector [38] also measured a clear deviation from the expectation. Table 2.2 is showing their results were on average only 2/3 of the expected atmospheric neutrino flux was measured.

This deviation from expectation was the so called "Atmospheric Neutrino Anomaly". The major breakthrough in atmospheric neutrino research was in the year 1998, when the up-down asymmetry of high-energy events generated by atmospheric neutrinos was discovered by Super Kamiokande.

Upward coming atmospheric neutrinos have to travel through the whole Earth ($\approx 12,800\,\text{km}$). Therefore, they should have a much larger probability to oscillate into another neutrino flavor compared to downward going atmospheric neutrinos, which have typically traveled a length of 20 km in the atmosphere. The Super Kamiokande result [39] for this asymmetry is

$$S_{\nu_\mu}^{up-down}(SK) = \left(\frac{N_{\nu_\mu}^{up} - N_{\nu_\mu}^{down}}{N_{\nu_\mu}^{up} + N_{\nu_\mu}^{down}}\right) = -0.31 \pm 0.04.$$

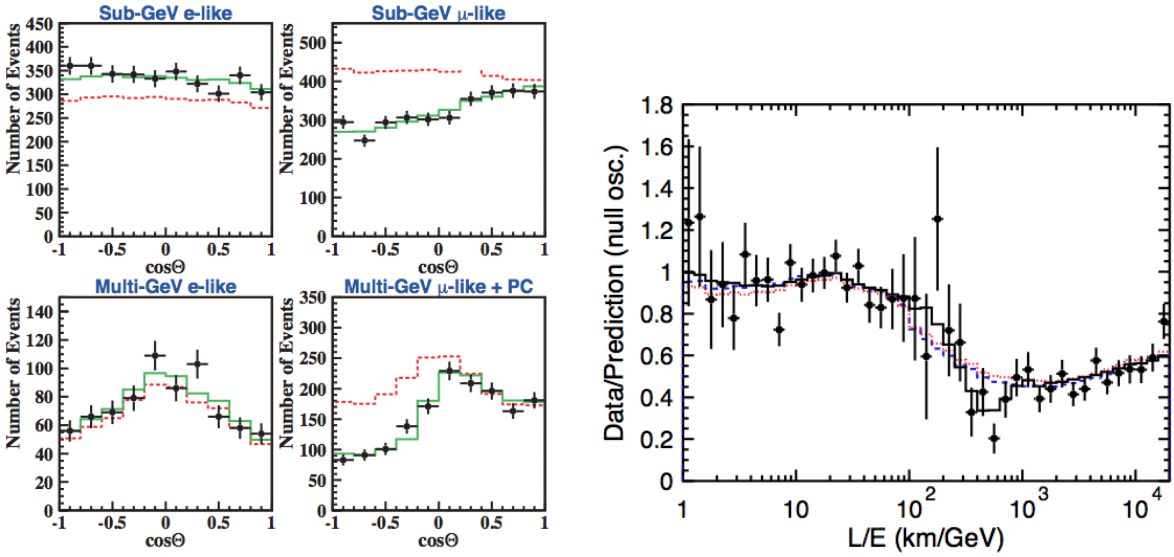

Figure 2.4: The left plot shows the zenith angle distributions of electron like and muon like events in the sub-GeV and multi-GeV region. The dotted red histograms show the non-oscillated Monte Carlo events and the solid green histograms show the best-fit expectations for $\nu_\mu \rightarrow \nu_\tau$ oscillations. The right plot shows results of the L/E analysis of Super Kamiokande atmospheric neutrino data. The points show the ratio of the data to the Monte Carlo prediction without oscillations. The solid line shows the best fit with 2-flavor $\nu_\mu \rightarrow \nu_\tau$ oscillations. The dashed and dotted lines show the best fit expectations for neutrino decay and neutrino de-coherence hypotheses, respectively.

This result was taken as a strong indication of the existence of atmospheric neutrino oscillations. The observed zenith-angle dependence in figure 2.4 of the atmospheric ν_μ and ν_μ fluxes support the $\nu_\mu \rightarrow \nu_\tau$ neutrino oscillation model. The electron events are in perfect agreement with data, whereas the muon events deviated from the no-oscillation hypothesis.

Apart from these experiments, the atmospheric Δm^2-region can also be explored by accelerator based long-baseline experiments. With a fixed baseline L of several 100 km and a narrower and a well understood neutrino spectrum of approx. $E = 1\,\text{GeV}$, these experiments have potential to constrain the atmospheric mass difference Δm^2_A and the mixing angle $\sin^2\theta_A$ with better accuracy.

The atmospheric oscillation picture was confirmed in 2002 by the K2K [40] accelerator experiment observing a disappearance of muon neutrinos. A wide-band muon neutrino beam with an average energy of $E_{\nu_\mu} = 1.3\,\text{GeV}$ was produced by protons from the KEK proton synchrotron and directed to the Super-Kamiokande detector 250 km away. The spectrum of the KEK neutrino beam was measured with a near detector located 300 m downstream from the production target. A total number of $0.92 \cdot 10^{20}$ protons on target (**POT**) were accumulated for the physics analysis. From the expected $158.1^{+9.2}_{-8.6}$ events in the Super Kamiokande detector only 112 events were detected showing a clear deviation from the no oscillation hypothesis.

The second long baseline neutrino accelerator experiment was MINOS. Here neutrinos are produced by the Neutrinos at the Main Injector (NuMI) facility at Fermilab. The far detector

is a 5.4 kton iron-scintillator tracking calorimeter located at the underground in the Soudan mine 735 km away. The near detector is of the same type as the far detector with a mass of 0.98 kton. Since 2005 a cumulative number of $7.25 \cdot 10^{20}$ POT have been accumulated, mostly in the low energy region, peaking around 3 GeV. The expectation without oscillation was 2451 events, whereas 1986 events were detected [41]. The MINOS results are consistent with the Super Kamiokande and K2K results and constrain the oscillations parameters rejecting alternative ν_μ disappearance models like neutrino decay or quantum decoherence at 7σ or 9σ respectively. In addition to ν_μ disappearance, the MINOS experiment also observed disappearance of $\bar{\nu}_\mu$, where the results are consistent with the neutrino counterparts.

The atmospheric neutrino data presented in this section are fully consistent with the $\nu_\mu \rightarrow \nu_\tau$ oscillation hypothesis. Only the appearance of ν_τ remains to be confirmed. For this purpose the OPERA experiment was constructed at the Gran Sasso underground lab, where the neutrino source in located at CERN 730 km away. The neutrino beam at CERN, CERN neutrinos to Gran Sasso (CNGS), has a average energy of 17 GeV and is produced by protons from the SPS. The OPERA experiment detects them utilizing a combination of emulsion chambers and a magnetized spectrometer. With a target mass of 1290 tons in 2008 and 2009 $5.3 \cdot 10^{19}$ POT were accumulated and one single ν_τ candidate was observed, were 1.65 signal events were expected [42, 43].

2.2 Measuring the third mixing angle θ_{13}

The goal of current neutrino oscillation experiments is to measure θ_{13} with very high precision. As introduced in chapter 1, the experimental variable in each of these experiments is the ratio L/E. Each experiment where one can measure and modify the distance L between source and detector and the neutrino energy E is capable of measuring neutrino oscillation parameters. In such an experiment one needs to know the flavor of neutrinos ν_α created in the source and needs to be able to measure the neutrino flavor ν_β in the detector after distance L. Two experimental approaches to do this θ_{13} measurement were pursued. First, accelerator based experiments can search for a appearance of ν_e and second, measurements at nuclear reactors can search for a $\bar{\nu}_e$ disappearance. In addition, solar and atmospheric neutrino experiments are sensitive to θ_{13} due to higher order oscillation effects.

2.2.1 Experiments with accelerators

In the detector one measures the appearance of another neutrino flavor $\nu_\beta \neq \nu_\alpha$ than the one created in the source. Therefore it is very important to know any contamination of ν_α in the beam. From the 1980's on, many experiments at the big proton synchrotrons (CERN, Fermilab, Brookhaven, Serpukhov) started looking for neutrino oscillations. The neutrino energies produced in the acceleration process were in the order of GeV and the distance between source and detector in the order of 1 km, thus these experiments were sensitive to mass differences $\Delta m^2 > 1\, eV^2$. In this L/E regime (10^{-6}m/eV) the search for oscillations was without success.

In the current accelerator appearance experiments, one searches for the appearance of ν_e in a fairly pure ν_μ beam as a function of a distance of several 100 km away from the neutrino

source. In this case the neutrino oscillation probability can be written as [44]:

$$\begin{aligned} P_{\nu_\mu \to \nu_e} &= \sin^2\theta_{23} 2\sin^2 2\theta_{13} \frac{\sin^2(\Delta_{31}aL)}{(\Delta_{31}aL)^2}\Delta_{31}^2 \\ &+ \cos\delta_{CP}\sin 2\theta_{23}\sin 2\theta_{12}\sin 2\theta_{13}\cos\Delta_{32}\left(\frac{\sin(\Delta_{31}\pm aL)}{\Delta_{31}\pm aL}\right)\left(\frac{\sin(aL)}{aL}\Delta_{21}\right) \\ &+ \sin\delta_{CP}\sin 2\theta_{23}\sin 2\theta_{12}\sin 2\theta_{13}\sin\Delta_{32}\left(\frac{\sin(\Delta_{31}\pm aL)}{\Delta_{31}\pm aL}\right)\left(\frac{\sin(aL)}{aL}\Delta_{21}\right) \\ &+ \cos^2\theta_{23}\sin^2 2\theta_{12}\frac{\sin(aL)^2}{(aL)^2}\Delta_{21}^2 \end{aligned} \quad (2.2)$$

The symbol Δ_{ij} is an abbreviation for $\Delta m^2_{jk}L/4E$ and matter effects are expressed in $a = G_F N_e/\sqrt{2}$ with the Fermi constant G_F and the electron density N_e. Measurements are complicated because the oscillation probability depends not only on θ_{13}, but also on the CP-violation phase δ_{CP} and the sign of Δ_{31}. Therefore a single accelerator experiment cannot determine the value of θ_{13}, but is able to establish a non-zero value for this mixing angle.

Currently two experiments are running: T2K [45] and MINOS [46]. In 2011 the T2K experiment reported a first experimental indication of a $\nu_\mu \to \nu_e$ oscillation. The experiment is located in Japan and consists out of the JPARC proton accelerator and the Super Kamiokande detector 295 km away. A narrow band ν_μ beam produced by 30 GeV protons is directed 2.5 degree off-axis to SK and thus tuned to the first oscillation maximum. Having a commutative number of $1.43 \cdot 10^{20}$ POT they reported six ν_e appearance candidate events, while the expectation for zero θ_{13} was 1.5 ± 0.3 events. As indicated before, also the MINOS experiment searched for ν_e appearance. Depending on the exact definition of the signal a typical number of 62 candidate events is observed for $8.2 \cdot 10^{20}$ POT accumulated. The expectation in this case was $49.6 \pm 7(stat.) \pm 2.7(syst.)$ disfavoring the no oscillation hypothesis with a zero θ_{13}.

2.2.2 Experiments with reactors

Neutrinos emitted from nuclear reactors are very well suited for oscillation measurements. First because they have low energies (below 10 MeV) and are therefore sensitive to low mass differences and second because of the very high neutrino flux. Apart from the explosions of nuclear weapons, nuclear reactors are the most intense man made neutrino sources. Per nuclear fission one gets on average 6 neutrinos. One can calculate the total emitted neutrino flux ϕ_ν at the reactor core by multiplying this flux ϕ_ν with the full solid angle F according to [47]

$$F\phi_\nu = 4\pi L \cdot 1.5 \cdot 10^8 \frac{P_{th}/[\mathrm{MW}]}{L^2/[\mathrm{m}^2]}[\mathrm{m}^{-2}\mathrm{s}^{-1}] = 2 \cdot 10^{18}\frac{P_{th}}{[\mathrm{MW}]}[\mathrm{s}^{-1}]. \quad (2.3)$$

The symbol P_{th} stands for the reactor thermal power and plugging in common thermal rector powers of several GW_{th} one ends up with approximately 10^{21} ν per second. The possible interactions for a neutrino in a given detector system are elastic scattering with electrons and

charged current interactions with protons, the so called inverse beta decay (**IBD**). Most reactor experiments performed so far used the IBD reaction as principle of the neutrino detection:

$$\bar{\nu}_e + p \longrightarrow n + e^+. \tag{2.4}$$

This reaction is very well suited for the detection, because it gives a very clear signature, which can be discriminated from background. The positron produced in the reaction annihilates very quickly with an electron in the detection volume and two gammas of 511 keV energy each, are produced. This is called prompt energy deposition. The neutron created in the reaction needs some time to thermalize and can get captured on hydrogen (**H**), thereby creating gammas with a total energy of 2.2 MeV. This is the so called delayed energy. In addition to the capture on hydrogen, other materials are used in reactor experiments, including lithium (**Li**), helium (**He**) and gadolinium (**Gd**). This is done in order to enhance the neutron capture reaction, as these materials have higher thermal neutron cross sections. In addition the energy they release through their de-excitation after neutron capture is higher in energy than the natural radioactivity background.

In reactor experiments one measures the same neutrino flavor as created in the source. Therefore one measures the probability $P(\bar{\nu}_\alpha \to \bar{\nu}_\alpha)$, the so called survival probability, which provides a clean measurement of θ_{13} in comparison to accelerator based experiments. Generally, one can express the electron anti-neutrino survival probability by:

$$\begin{aligned} P_{\bar{\nu}_e \to \bar{\nu}_e} &= 1 - \cos^4\theta_{13}\sin^2 2\theta_{12}\sin 2\Delta_{12} \\ &- \sin^2 2\theta_{13}(\cos^2\theta_{12}\sin^2\Delta_{31} + \sin^2\theta_{12}\sin^2\Delta_{32}) \end{aligned} \tag{2.5}$$

At distances of approximately $(1-2)$ km from a reactor, this survival probability simplifies to

$$P_{\bar{\nu}_e \to \bar{\nu}_e} = 1 - \sin^2 2\theta_{13}\sin^2\frac{\Delta m^2_{31} L}{4E}. \tag{2.6}$$

Only one additional input is needed in the evaluation of these experiments. This is the well measured value of the atmospheric mass squared difference $\Delta^2_{atm} = \Delta^2_{31} = (2.32^{+0.12}_{-0.08})\cdot 10^{-3}\,\mathrm{eV}^2$ [48] . By choosing a proper distance between source and detector, one can tune the sensitivity of the experiment towards atmospheric or towards solar neutrino mass splitting. In neutrino history nuclear reactors have already played an important role. The first neutrino detection did happen at the Savannah river nuclear power station [22] and during the 1980's and 1990's many short baseline experiments (ILL, Bugey-4, Krasnoyarsk, Goesgen, Rovno) at nuclear reactors searched for neutrino oscillations without success. Nearly a decade later nuclear reactors helped solving the solar neutrino problem in the KamLAND experiment [49] . Some years earlier the reactor neutrino experiment CHOOZ [50] provided the current best upper limits on the mixing angle θ_{13} being

$$|\Delta m^2_{13}| = 2.0\cdot 10^{-3}\,\mathrm{eV}^2 \qquad \sin^2 2\theta_{13} \leq 0.19.$$

In all these type of experiments one needs to know the reactor flux very precisely or one needs to measure the neutrino flux on two (or even more) different sites, with different distances L between source and detector. So one can discriminate between approaches with only one detector or the approach with multiple detectors.

- In the **Single detector approach** a good understanding of the reactor source spectrum is mandatory, because all reactor related uncertainties like the evolution α_k of the fissible isotopes k in time and the neutrino spectra ϕ_ν^k emitted from these isotopes propagate into the measurement of the neutrino rate and spectrum, as can be seen for the measurable neutrino rate below:

$$N(t) = \sum_i^{reactors} \frac{n_p T}{4\pi L_i^2} \sum_k^{isotopes} \alpha_k(t) \int dE_\nu \phi_\nu^{k,i}(E_\nu, t) P_{\nu_e \to \nu_e}(E_\nu, L_i) \sigma_{IBD}(E_\nu) \epsilon(E_\nu). \quad (2.7)$$

  L_i is the distance between the detector and reactor core i and ϵ the efficiency in detecting neutrinos.

- For the **Multi detector approach** the reactor dependency cancels out, with this approach one measures the relative rate between two or more detectors and looks for deviations from the simple ratio L_{ji}/L_{ki}. Now only detector dependent values enter in the equation for the measurable rate, this is the number of target protons in the detector $n_{p,j}$ and the response and efficiency of the detectors ϵ_j. Therefore one tries to built these detectors as similar as possible.

$$\frac{N_j}{N_k} = \frac{P_{\nu_e \to \nu_\mu}(E_\nu, L_{ji})}{P_{\nu_e \to \nu_e}(E_\nu, L_{ki})} \cdot \left(\frac{L_{ji}}{L_{ki}}\right)^2 \cdot \frac{n_{p,k}}{n_{p,j}} \cdot \frac{\epsilon_k(E_\nu)}{\epsilon_j(E_\nu)} \quad (2.8)$$

In addition a disappearance analysis can be done in two ways, first by measuring the ratio R of observed to predicted events (rate-analysis) and second by measuring the spectrum (shape-analysis) of the observed neutrino candidates. This gives further information on the oscillation, because the measured spectrum will deviate from a Monte Carlo simulated one assuming no neutrino oscillation.

2.2.3 Comparison between present running reactor experiments

Next to Double Chooz (**DC**), there are two other reactor neutrino experiments currently taking data. These are Daya Bay (**DB**) [53] in China and the Reactor Experiment for Neutrino Oscillation (**RENO**) in South Korea [52]. The neutrino detectors of the three experiments share the similar detection concept and thus the same design and structure; the innermost of the detectors consist out of a gadolinium doped liquid scintillator, outside this volume a gamma-catcher and surrounding all this a buffer volume filled with mineral oil (Visualized in figure 2.5). A gamma-catcher is used to avoid a loss of photons and the buffer ensures some distance between the sensitive volumes and the photomultipliers, which are itself a unavoidable source of radioactivity. The three volumes are in turn surrounded by a veto detector that is optically separated from the other volumes, which is filled with purified water (DB

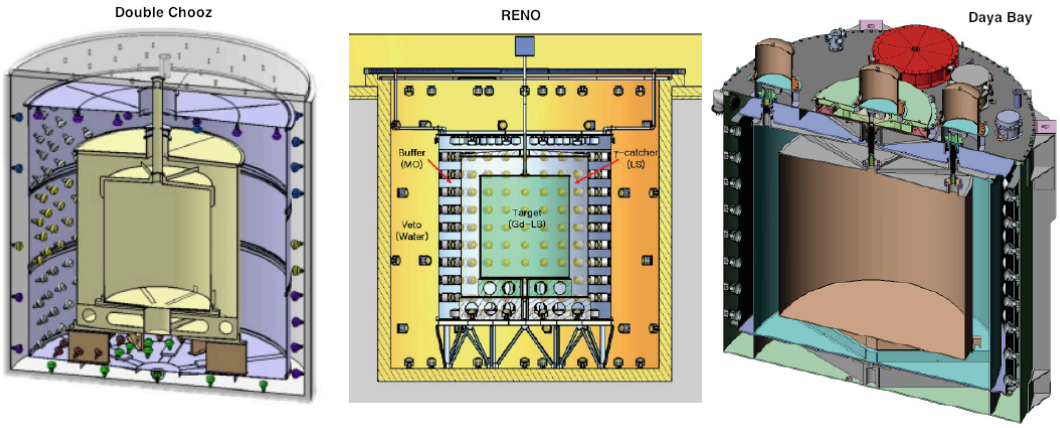

Figure 2.5: Schematic view of the Double Chooz, RENO and Daya Bay anti-neutrino detectors. All three detectors share the same, onion-like structure, having the innermost neutrino target region, surrounded by a gamma-catcher volume that again is surrounded by a buffer region. All these volumes are shielded by an additional volume acting as an veto detector. Plots of the detectors taken from [51–53].

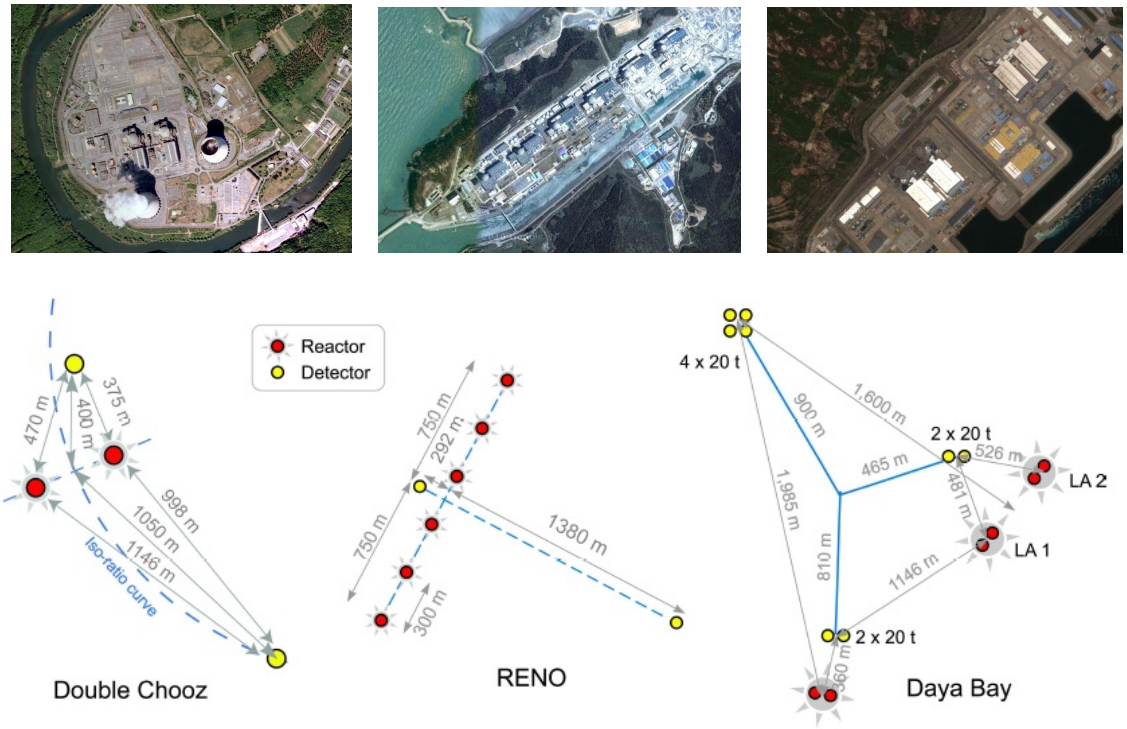

Figure 2.6: Aerial view and schematic layout of the three reactor anti-neutrino experiments Double Chooz, RENO and Daya Bay. Aerial view made with Google maps and layouts taken from [54].

experiment	Double Chooz (France)	RENO (South Korea)	Daya Bay (China)
thermal power [GW]	8.5	16.4	11.6 (17.4)
distances N/F [m]	400/1050	290/1380	363(500)/1985(1615)
depth N/F [mwe]	115/300	120/450	260/910
target mass [tons]	10/10	16/16	40·2/80
scintillator	O-PXE [$C_{16}H_{18}$]	LAB [$C_6H_5C_{12}H_{25}$]	LAB [$C_6H_5C_{12}H_{25}$]

Table 2.3: This table summarizes the properties of the Double Chooz, RENO and Daya Bay experiment. It was compiled from [51–53].

and RENO) or liquid scintillator (DC). Differences of the experiments arise from different dimensions, different target masses and the number of reactor cores and detectors. The DB experiment is located in China at the Ling Ao nuclear complex ($6 \times 2.9\,\mathrm{GW}_{th}$) utilizing six functional identical detectors being in two near halls (470 m and 576 m of flux-weighted baselines away from the reactor cores) and one far hall (1658 m) underground hall. The RENO experiment is located at the Yeonggwang reactor complex ($6 \times 2.8\,\mathrm{GW}_{th}$) in South-Korea and has a near (294 m) and a far detector (1383 m) operational since August 2011. All three experiments use gadolinium doped liquid scintillator to enhance neutron capture, only the scintillators used differ from one experiment to another. While Double Chooz uses Pheny-xylyl ethane (**PXE)** as scintillator base, the other two experiments utilize Linear alkyl benzene (**LAB**). Table 2.2.3 is summarizing the properties of the three experiments below and figure 2.2.3 is showing aerial views of the experimental sites and schematic layouts for detector and reactor positions.

At the time of writing this thesis (end of 2012) all three experiments reported their first results on reactor $\bar{\nu}_e$ disappearance. The DC collaboration presented a first oscillation result by using the far detector only [55]. It is planned to have the near detector ready in 2013. An updated result [56] measured during 33.71 GW ton years shows a disappearance of ν_e from the reactors at a 2.9σ level. With a combined analysis of the positron rate and the shape of the measured positron spectrum a value of

$$\sin^2\theta_{13} = 0.109 \pm 0.030\,(stat.) \pm 0.025\,(syst.)$$

could be obtained. The DB result [57] corresponds to 43,000 GW ton years of exposure and a rate-only analysis yields

$$\sin^2\theta_{13} = 0.092 \pm 0.016\,(stat.) \pm 0.005\,(syst.),$$

excluding a zero θ_{13} at a level of 5.2σ. Whereas the RENO result [58] from 229 days of exposure yields in a rate-only analysis

$$\sin^2\theta_{13} = 0.113 \pm 0.013\,(stat.) \pm 0.019\,(syst.)$$

excluding the zero hypothesis at a 4.9σ level. These results are compatible and establish a non-zero mixing angle θ_{13} and the three neutrino mixing scenario. With the results of all three experiments presented here, their backgrounds and different shielding situations will be the items of a more detailed discussion in chapter 7.

2.3 Reactor neutrino anomaly

As stated before, reactor neutrino experiments are disappearance experiments. One needs to have a precise prediction of the un-oscillated anti-neutrino flux emitted from the reactors to do such experiments. This is done by converting beta-decay spectra S_k of the main fissile isotopes k (^{235}U, ^{238}U,^{239}Pu and ^{241}Pu) into anti-neutrino spectra ϕ_ν^k. The technical details of the way how this prediction is done will be described in more detail in chapter 3. The original calculation [59] done in the late 1980's used a phenomenological model for this conversion.

In 2011 different independent reanalysis of the predicted beta-decay spectra S_k were performed [60–62]. The result of those studies is an overall shift in the normalization of $+(2-3)\%$ of the anti-neutrino spectra, thus yielding a higher predicted flux. All the short-baseline experiments ($< 100\,\mathrm{m}$ away from the reactor core) performed in the 1980's and 1990's had measurements consistent with the no-oscillation hypothesis so far. Taking the overall increase of the normalization into account, the ratio measured to predicted neutrino events for a rate analysis decreases. Calculating a baseline weighted mean of all the short baseline experiments with the new predication one finds a ratio of

$$R = 0.943 \pm 0.023. \tag{2.9}$$

This finding corresponds to a deviation from unity of 98.6 % C.L. and defines the so called reactor neutrino anomaly (visualized in figure 2.7). Apart from that, additional experiments report on anomalies, namely LSND and MiniBoone as well as the gallium neutrino experiments, where during calibration runs with neutrino sources a deficit was observed. These effects/anomalies could possibly be explained by a fourth sterile neutrino state driving the neutrino oscillations at very short baselines [62, 63] having the parameters

$$|\Delta m^2_{new}| \approx \mathrm{eV}^2, \quad \sin^2 2\theta_{new} \approx 0.1. \tag{2.10}$$

Future experimental programs are needed and they have to check whether there are sterile neutrinos realized by nature or not?

2.4 Neutrino Oscillation Parameters

Within this section the neutrino oscillation data will be summarised according to the latest Particle Data Group review [64]. In the used convention, $0 \leq \Delta m^2_{21} \leq \Delta m^2_{31(32)}$, the PMNS matrix-element $U_{e3} = \sin\theta_{13}$ is small, as it was shown by the previous mentioned reactor experiments. Thus it is possible to identify the mixing angles θ_{12} and θ_{23} with the solar ν_e and the atmospheric $\nu_\mu(\bar{\nu}_\mu)$ oscillations. Therefore we have $\theta_{12} \equiv \theta_{Sol}$ and $\theta_{23} \equiv \theta_A$.

The squared mass differences can also be connected: $\Delta m^2_{21} \equiv \Delta m^2_{Sol}$ and $\Delta m^2_{23} \equiv \Delta m^2_{atm}$. The data of solar neutrino oscillation experiments show that the term $\Delta m^2_{21}\cos 2\theta_{12} \geq 0$. Using the convention introduced before results in $\cos 2\theta_{12} \geq 0$. Table 2.4 gives the results of a global analysis of the existing neutrino oscillation data. From these results it follows that $\theta_{23} = \pi/4$, $\theta_{12} = \pi/5.4$ and $\theta_{13} = \pi/20$ being drastically different from the pattern of quark mixing.

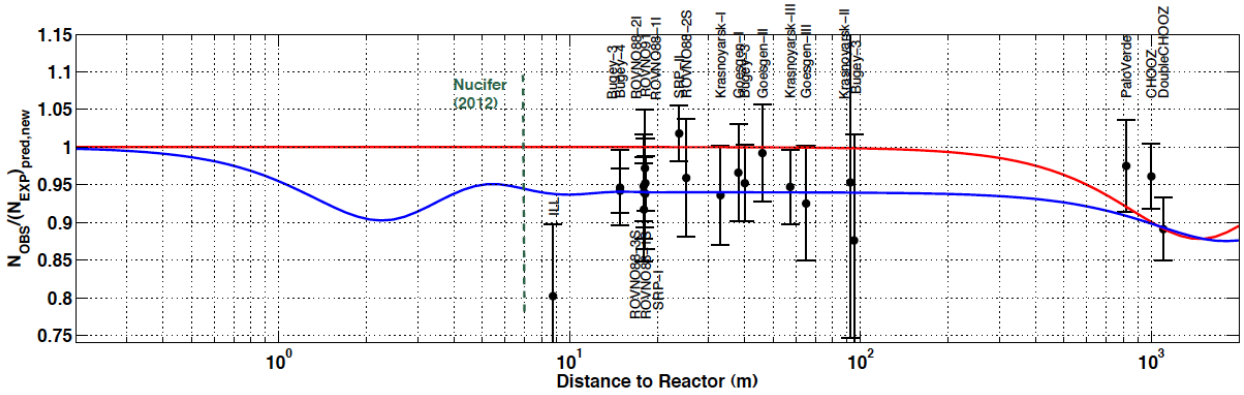

Figure 2.7: The short baseline reactor neutrino anomaly. The experimental results are compared to the prediction without oscillation, taking into account the new 2011 anti-neutrino spectra. The baseline weighted mean of all the experiments is 0.943 ± 0.023. To illustrate the 3 neutrino mixing solution the red curve was drawn assuming $\sin^2 2\theta_{13} = 0.15$. In opposite to the blue curve, illustrating the 3+1 solution with a new sterile neutrino state having the parameters $|\Delta m^2_{new}| >> 2\,\mathrm{eV}^2$, $\sin^2 2\theta_{new} = 0.12$ and $\sin^2 2\theta_{13} = 0.085$. Plot and explanation taken from [63].

parameter	best fit $\pm 1\sigma$	3σ allowed range
Δm^2_{21} $[10^{-5}\,\mathrm{eV}^2]$	$7.58^{+0.22}_{-0.26}$	6.99 - 8.18
$\lvert\Delta m^2_{23}\rvert$ $[10^{-3}\,\mathrm{eV}^2]$	$2.35^{+0.12}_{-0.09}$	2.06 - 2.67
$\sin^2\theta_{12}$	$0.306(0.312)^{+0.18}_{-0.15}$	0.259 (0.265) - 0.359 (0.364)
$\sin^2\theta_{23}$	$0.41^{+0.08}_{-0.03}$	0.34 0.64
$\sin^2\theta_{13}$	0.096 ± 0.013	-

Table 2.4: This table, compiled from [64], shows the best-fit values and the 3σ allowed range of the three neutrino mixing scenario, which are derived from a global fit of the current neutrino oscillation data [65]. These data include T2K and MINOS (but not the new reactor anti-neutrino) results. The value of $\sin^2\theta_{12}$ was obtained using the old reactor flux prediction, whereas the value in brackets utilise the new reactor flux prediction [59, 61] yielding a somewhat higher neutrino flux. The values of θ_{13} comes from a combined analysis of the T2K, MINOS and reactor experiments and can be found in [66].

2.5 Summary

This chapter introduced the history of the neutrino from its "invention" over its first detection up to the various experiments that lead to our today's picture of neutrino oscillations. Even if recent years have seen an enormous progress in neutrino oscillation research, several critical questions about the enigmatic neutrino remain without answer. An comprehensive outlook, according to [67,68], will summarize these questions. The summary will be given to motivate the further and precise measurement of neutrino oscillation parameters, being the goal of the current reactor neutrino experiments. Finding answers to these questions forms a challenging neutrino physics program for the next decade.

- Determining the nature of massive neutrino eigenstates ν_i is an important goal. The underlying question is whether the neutrino is a Dirac or a Majorana particle and the answer to this question would be important in order to make progress in the understanding of the origin of neutrino masses.
- Determining the sign of Δm^2_{atm} (Δm^2_{31}) and the mass hierarchy of the neutrino mass eigenstates.
- Determining or having more significant constraints on the absolute neutrino mass scale.
- Measurement of the neutrino mixing angle θ_{13} with high precision.
- One can ask if neutrino oscillations violate CP symmetry? So determining the status of CP symmetry in the lepton sector is an important goal. Together with the Dirac CP-violating phase δ, the third mixing angle θ_{13} determines the magnitude of CP-violation effects in neutrino oscillations.
- Is there any relation between quark and neutrino mixing?
- Driven by the reactor neutrino anomaly, one can ask if there more than the 3 active neutrinos, is there really a forth or even more sterile neutrinos driving the neutrino oscillations at very short baselines?

These riddles are still to solve and make neutrino physics still an active and very evolving field of physics. But the first step is done according to [64], were it is written:

"*With the measurement of θ_{13}, the first steps on the long road leading to a comprehensive understanding of the patterns of neutrino masses and mixing, of their origin and implications were made.*"

"Neutrino physics is largely an art of learning a great deal by observing nothing."

Haim Harari (1901-1954)

3

The Double Chooz reactor neutrino experiment

This chapter gives an overview of the Double Chooz detector and its anti neutrino detection concept. The source of the anti neutrinos to be detected in the DC experiment are the reactor cores B1 and B2 of the Chooz nuclear power station operated by EDF. Reactors produce anti neutrinos by β-decay of unstable fission products and these neutrinos are detected via the inverse beta decay reaction $p+\bar{\nu}_e \rightarrow e^+ + n$. Therefore the first part of this chapter begins with a brief description on how neutrinos are produced inside a nuclear reactor and will discuss the different steps needed to calculate the neutrino spectrum as emitted from the two reactors at the Chooz site. The second part of this chapter will focus on the used experimental setup and starts with a general explanation about the neutrino detection inside the detector. It will explain the detector design, the utilized components, calibration systems and the DC software suite DOGS. After the description of the detector system and the utilized components the chapter closes with a report of the current status of the experiment and future plans.

3.1 The general detection concept

As derived in chapter 2 the survival probability of an electron anti neutrino emitted from one of the two Chooz reactor cores to be detected inside a DC detector is

$$P_{\bar{\nu}_e \rightarrow \bar{\nu}_e} = 1 - \sin^2 2\theta_{13} \sin^2 \frac{\Delta m^2_{31} L_i}{4E_\mu}. \tag{3.1}$$

Here the experimental parameters are the neutrino energy E_ν and the distance L_i from reactor core i for a given detector. The theoretical parameters are Δm^2_{31} and θ_{13}. The mass squared difference, $\Delta m^2_{31} = (2.43 \pm 0.13) \cdot 10^{-3}\,\mathrm{eV}^2$, is provided by the measurement of the accelerator experiment MINOS [48]. Thus a measurement of the survival probability provides a clean measurement of the mixing angle in the form of $\sin^2 2\theta_{13}$.

The DC Experiment will consist of two, almost identical detectors filled with gadolinium loaded liquid scintillator. The aerial photography in figure 3.1 shows an overview of the plant and the positions of both DC detector sites are marked. In its first stage, the DC experiment performs a single-detector measurement of the anti neutrino flux at a mean distance of 1.05 km to the cores and compares this to a prediction of the anti-neutrino flux and spectra emitted from the reactor cores. This far detector is situated within a cavern in a former maintenance tunnel of the first nuclear reactor at the Chooz site that was shut down in 1991. This cavern is shielded against cosmic rays by 100 m of rock corresponding to 300 m of water

Figure 3.1: Surrounded by the meuse-river, on this aerial photography one can see the two nuclear reactors of the Chooz Nuclear Power Station. Added to this photography are the rough positions of the far and near detectors (labelled as close detector). Picture courtesy of CEA/IRFU.

equivalent (**m.w.e.**) shielding, which also hosted the former Chooz experiment. Currently a new tunnel and an underground lab are excavated for the DC near detector and will be ready for detector installation in 2014. With two detectors operational, DC will perform a relative measurement of the anti neutrino flux at different distances to the reactor cores.

This Near detector will be placed at a distance of around 400 m to both reactor cores, underneath rock corresponding to 150 m.w.e., and it measures the un-oscillated anti neutrino flux. With both detectors ready in 2014, the disappearance probability will then be measured by comparing the measured rates at the Near and Far detectors as derived in 2.8. Except of the different overburdens of rock the detectors are identical within the PMT support structure of the Inner Detector (ID) having the same dimensions, the same liquid scintillator and number of PMTs. Table 3.1 summarizes the distances to the reactor cores and the different shielding situation for DC Near and Far detectors.

3.1.1 Detection technique

The reaction used to identify the electron anti neutrinos from the reactor cores is the IBD reaction as explained before in chapter 2. This reaction has the largest cross section for MeV

detector	**distance to B1 (m)**	**distance to B2 (m)**	**shielding (m.w.e.)**
DC near	466	351	150
DC far	1114.6	998.1	300

Table 3.1: Distances of the two DC labs (Near, Far) to the reactor cores and shielding situations at the sites. The distance measurements have an accuracy of 10 cm [50].

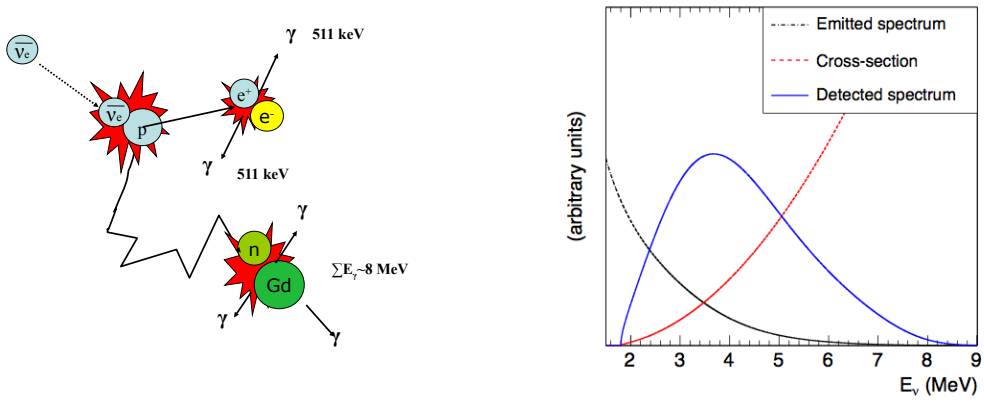

Figure 3.2: The left plot shows a sketch of the IBD reaction. The right plot schematically visualizes the emitted anti neutrino spectrum (black) of a reactor convoluted with the cross-section (red) of the IBD reaction, resulting in the positron spectrum (blue) measured at the detector site.

reactor neutrinos and it has a unique signature: $\bar{\nu}_e + p \rightarrow n + e^+$. First a positron, then a neutron is created. The positron annihilates promptly and the two resulting gamma-rays can be detected. This is followed by the delayed capture (mean time $\tau \approx 30\,\mu$s) of the neutron on hydrogen or gadolinium nuclei. The threshold for this inverse beta decay to happen is 1.806 MeV calculated using

$$E_{thr} = \frac{(m_n + m_e)^2 c^4 - m_p^2 c^4}{2 m_p c^2} \tag{3.2}$$

Thus the low energy part of the spectrum below threshold cannot be measured. Convolving the neutrino spectrum emitted from the reactors with the cross section of the IBD reaction one gets the positron spectrum as being measured in the detector. This is illustrated in the right plot in figure 3.2, where one can see the emitted neutrino spectrum from the reactors, the cross section for the IBD reaction and the resulting measurable positron spectrum. The left plot in in figure 3.2 sketches the IBD reaction, the common detection reaction to all reactor experiments. Above the threshold one can calculate the positron energy spectrum by assuming that the recoil energy of the neutron is small (typically 20 keV) and neglecting the scattering angle between positron and neutrino

$$E_{e+} = E_\nu + (m_p - m_n)c^2. \tag{3.3}$$

From this it is possible to reconstruct the deposited energy and therefore the neutrino spectrum

$$E_{vis} = E_\nu + m_p c^2 - m_n c^2 + 2 m_e c^2 \approx E_\nu - 0.78\,\text{MeV}. \tag{3.4}$$

3.2 The Chooz nuclear power plant

In the Double Chooz experiment electron anti neutrinos $\bar{\nu}_e$ are measured, being created in beta-decays of fission fragments of the four main fuel isotopes ^{235}U, ^{238}U,^{239}Pu and ^{241}Pu. These reactions take place in the two reactors cores B1 and B2, located at the Chooz nuclear power station. This power station lies within the Departement Champagne Ardennes, France, next to the border with Belgium and is operated by the French company Electricite de France **EDF** in partnership with the Belgian Utilities Electrabel. Both cores are Pressurized Water Reactors (**PWR**) of type N4 having a thermal power of $4.25\,\mathrm{GW}_{th}$ each. Both of them were built by the Areva company and use slightly enriched uranium dioxide (UO_2) as fuel. Table 3.2 summarizes the reactor properties.

core	**B1**	**B2**
thermal power	4.25 GW_{th}	4.25 GW_{th}
electric power	1.5 GW_{e}	1.5 GW_{e}
construction finished	August 1996	April 1997
commercial operation	May 2000	September 2000

Table 3.2: Summary of the properties of the Chooz nuclear power station. Both cores B1 and B2 are pressurized water reactors of type N4 and as such the two are the most powerful cores in the world.

3.2.1 Fission processes inside the reactor cores

The two nuclear reactors at Chooz produce a very high and isotropic flux of neutrinos. As mentioned in chapter 2 before, nuclear reactors produce a pure sample of electron anti neutrinos $\bar{\nu}_e$. The unstable fission products of the fuel isotopes are very neutron rich and therefore decay via beta-decay. The resulting reactor neutrino spectrum is the sum of all this individual beta-decays, which are continuous in energy up to the endpoint (Q-value) of the parent nucleus decay. The radioactive elements inside the reactor core most relevant for the neutrino flux are ^{235}U, ^{238}U,^{239}Pu and ^{241}Pu. In the fission of these isotopes on average 6 anti neutrinos are created and an average energy of 200 MeV is released. In addition neutrons are created in these decays. A fraction of them is captured by ^{238}U nuclei and forms the isotopes ^{239}Pu and ^{241}Pu. Thus, during its operational time, a reactor is burning ^{235}U and accumulating ^{241}Pu. This is the so called burn-up as can be seen in the reaction schemes below:

$$n + {}^{238}\mathrm{U} \longrightarrow {}^{239}\mathrm{U} \longrightarrow {}^{239}\mathrm{Np} \longrightarrow {}^{239}\mathrm{Pu} \qquad T_{1/2} = 24,000\,a \tag{3.5}$$

$$n + {}^{239}\mathrm{Pu} \longrightarrow {}^{240}\mathrm{Pu} + n \longrightarrow {}^{241}\mathrm{Pu} \qquad T_{1/2} = 14.4\,a \tag{3.6}$$

At the end of a fuel cycle the fission rates of (^{235}U and ^{241}Pu) become comparable. It is therefore crucial to know the time evolution of the four main fuel isotopes and the beta-spectra of their associated fission products, in order to predict the time dependent anti neutrino spectrum with high precision.

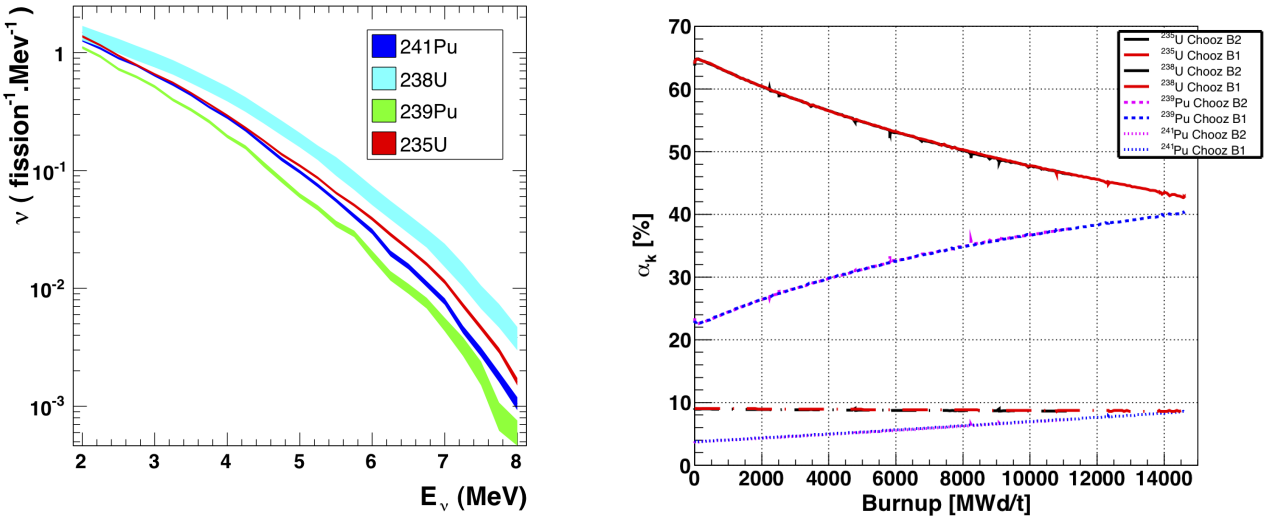

Figure 3.3: The left plot [72] shows the neutrino spectra of the four main isotopes ^{235}U, ^{238}U,^{239}Pu and ^{241}Pu with experimental error bars (one should note that the spectrum of ^{238}U is not measured yet, but the calculated spectrum is shown). The plot [73] on the right side shows the α_ks (percentual time dependent fission rate of isotopes k) during a typical fuel cycle.

This time evolution is described by the fractional fission rates α_k for isotope k. Within the Double Chooz experiment these parameters were evaluated using two different, but complementary, reactor core simulation codes: DRAGON [69] and MURE [70, 71]. These Monte-Carlo simulations include the reactor core geometry and its fuel composition at the beginning of a reactor cycle. By introducing the time dependent coefficients α_k, the fractional change in the reactor fuel composition is taken into account. These coefficients absorb the contribution of the main fissile nuclei to the total number of fissions of the k-th branch. Using this definition, one is able to calculate the mean energy released per fission being

$$\langle E_f \rangle = \sum_k \alpha_k(t) \langle E_f \rangle_k. \tag{3.7}$$

In general the neutrino flux and the associated spectrum from a nuclear reactor can be determined from the time varying fission rates $f_k(t)$, that can be expressed as

$$f_k(t) = \frac{P^i_{th}}{\sum_k \alpha^i_k \langle E_f \rangle_k} \alpha^i_k. \tag{3.8}$$

In this reformulation one needs to measure the thermal power P^i_{th} of reactor core i, the parameters α^i_k were determined by simulation. The mean energies released per fission of the different isotopes $\alpha_k(t)\langle E_f \rangle_k$ can be found in table 3.3 and were computed according to Kopeikin [74], where nuclear data from the JEFF3.1 database [75] are used. The EDF company provides data on the time-varying thermal power $P_{th}(t)$ of both reactors in steps of 30 s. If the initial fuel composition is known, the time evolution of the neutrino spectra $\alpha_k \phi^k_\nu(E_\nu)$ of the different isotopes k can be calculated with an accuracy better than 1% [76]. Thus one can call a

isotope	neutrinos emitted	energy released [MeV]	beginning	end
^{235}U	1.92±0.036	201.7±0.6	60.5 %	45%
^{238}U	2.38±0.048	205.0±0.9	7.7%	8.3%
^{239}Pu	1.45±0.030	210.0±0.9	27.2%	38.8%
^{241}Pu	1.83±0.035	212.4±1.0	4.6%	7.9%

Table 3.3: Number of neutrinos produced and energy released by each fission isotope above IBD threshold (1.8 MeV). Also shown is a typical fuel composition at the beginning and at the end of one cycle normalized to 100 %. Compiled from [76] and [51].

nuclear reactor a well calibrated neutrino source. The plots in figure 3.3 show the emitted neutrino flux and an exemplary time evolution (burn-up) of the different isotope fractions α_k.

3.2.2 Emitted anti neutrino flux

How to predict the emitted anti neutrino flux from the reactors? At the level of each beta-decay branch of a given fission isotope k, the neutrino spectrum per fission ϕ_k can be inferred from the associated beta-decay spectrum S_k. These spectra are given by

$$S_k(E) = \sum_k Y_k(t) \sum_l b_k^l P_k^l(Z_k, Q_k^l, E), \tag{3.9}$$

with the time dependent beta-decay rate $Y_k(t)$ for fission isotope k, and P_k^l the beta-decay spectrum of branch l for isotope k, where b_k^l is the branching ratio, Q_k^l the endpoint energy and Z_k the Fermi function correcting for the deceleration of electrons within the Coulomb field of the nucleus.

There are two different approaches to compute the anti neutrino spectra from these beta-decay spectra:

- **Virtual-branch**: In the first approach, called the virtual-branch approach, the anti neutrino spectra were computed by converting reference electron spectra. The spectra were precisely measured at the Institute Laue Langevin (ILL) high flux reactor in Grenoble, France [59, 77]. These beta decay spectra were measured after samples of U or Pu were irradiated for one day. One fits these spectra to a sum of virtual beta-decay branches and than converts them to the anti neutrino spectra.
- **Ab-initio:** In the second, so called ab-initio approach, the anti neutrino spectrum is directly calculated by using all available beta-decay data of P_k^l at the branch level [60]. The main source of this data is the ENSDF database where different measurements and models have been used where no data was available in the database.

With the use of these techniques, the neutrino energy spectrum per fission ϕ_ν^k for a given isotope k, the flux-weighted IBD cross section per fission, can be written as

$$\phi_\nu^k \equiv \langle \sigma_f \rangle = \sum_k \alpha_k \langle \sigma_f \rangle_k = \sum_k \alpha_k \int_0^\infty dE S_k(E) \sigma_{IBD}(E). \tag{3.10}$$

number of target protons	N_p	0.29%
baseline	L	0.038%
thermal power	P_{th}	0.460%
Bugey4 measurement	$\langle\sigma_f^{bugey}\rangle$	1.420%
energy per fission	$\alpha_k E_k$	0.157%
reference spectra	ϕ_ν^k	0.170%
fuel composition	α_k	0.872%
total		**1.745%**

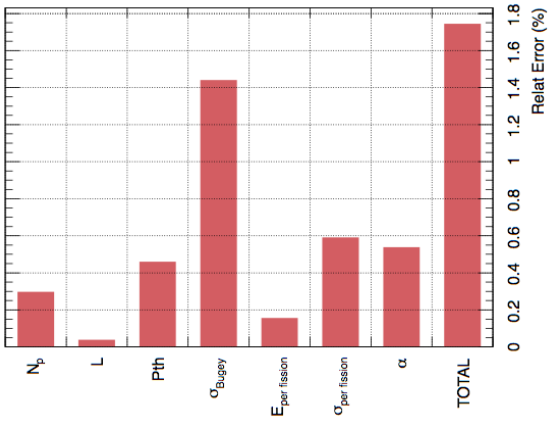

Table 3.4: The table and the bar chart give a summary of reactor related systematic errors in the first phase of Double Chooz [55, 56], where the far detector is used only. The second phase of the DC experiment will reduce these errors, because instead of relying on the accurate prediction of the reactor spectrum a relative measurement between the near and the far site will be performed.

With σ_{IBD} being the well known cross section and S_k the reference spectra as discussed before. In general the neutrino flux is dependent on the fission rates f_k changing with time. A principal limitation of the DC experiment in its current stage is that one needs to know the absolute anti neutrino flux from the reactors very precisely, as one is looking for a disappearance of neutrinos and therefore for a deviation in the spectrum. So the knowledge and prediction of reactor neutrino spectrum is the dominant source of systematic error. All these reactor related uncertainties yield a systematic error on the total neutrino flux of around 1.8% and are summarized in table 3.4.

To mitigate the impact of these reactor related uncertainties the normalization of $\langle\sigma_f\rangle$ was tied to measurements made with very short-baseline reactor neutrino experiments. Now one has the chance of using different normalizations, where DC uses the Bugey4 measurement [78] as normalization or anchor point.

$$\langle\sigma_f\rangle = \langle\sigma_f^{bugey}\rangle + \sum_k (\alpha_k^{DC} - \alpha_k^{bugey})\langle\sigma_f\rangle_k \tag{3.11}$$

This treatment makes the Bugey4 detector effectively to an near detector for DC. The second term in the formula above corrects for the different fuel compositions of the Bugey and Chooz reactors.

Now, one is able to calculate the number of expected neutrinos to be detected (under the no-oscillation assumption) via inverse beta decay at the experimental site with distance L_i to reactor i. This rate is given by

$$N_\nu^{exp} = \frac{\epsilon N_p}{4\pi} \sum_{i=\{B1,B2\}} \frac{1}{L_i^2} \frac{P_{th}^i}{\langle E_f\rangle^i} \times \left(\frac{\langle\sigma_f\rangle^i}{\sum_k \alpha_k^i \langle\sigma_f\rangle_k} \sum_k \alpha_k^i \langle\sigma_f\rangle_k \right), \tag{3.12}$$

detector	diameter [mm]	height [mm]	filled with	volume [m^3]	mass [tons]
Target	2300	2458	Gd-Ld	10.3	0.35
Gamma-Catcher	3392	3574	LS	22.3	1.1-1.4
Buffer	5516	5674	Oil	110	7.7
Inner Veto	6590	6640	LS	90	20

Table 3.5: Overview of the detector dimensions and properties. The different volumes are concentric cylindrical tanks and were noted in the table from the innermost, the target to the outermost volume, the inner muon veto.

with N_p being the number of protons within the sensitive detector volume and ϵ the sensitivity of the detector. Now, as one has an expectation of the number of anti neutrinos that can be detected and of their energy spectrum, the next section focuses on the DC detector and the experimental techniques to measure the neutrinos emitted from the reactors.

3.3 Detector design

The DC detector system consists of a main detector, composed out of four concentric cylindrical tanks filled with liquid scintillator or mineral oil. This main detector is covered with an outer veto built out of plastic scintillator strips. The detector system has been much inspired by the preceding CHOOZ experiment, where the emphasis in the new design were changes towards a higher neutrino event rate and better signal to background ratio.

The DC detector system has a concentric, onion like structure: starting with the inner volumes, the detector elements are the target, the gamma-catcher and the buffer, which form the Inner Detector (**ID**). Surrounding this is the Inner Muon Veto (**IV**). All materials used in building these detectors were chosen to match demands on radiopurity. This detector design deals with the different backgrounds of cosmic muons, fast neutrons, as well as cosmogenic isotopes created by them. Details on the backgrounds and on their measurement will be given in the next chapter. Finally, on top of this main detector there is the Outer Muon Veto (OV). Table 3.5 lists the detector dimensions[1] and properties and figure 3.4 is giving an overview.

Differences in the designs for both, near and far detectors and laboratory sites arise from the different shielding situations in these labs. For the FD the IV is surrounded by low activity steel bars (in total 250 t of 150 mm wide strips covering the full height of the detector system), which provide shielding against external radioactivity from the rock around the detector lab. The ND will differ in this point, instead of steel bars there will be an additional volume filled with water to shield against external radioactivity. Also due to the higher muon flux at the ND site, the OV will be bigger, not only covering the detector system itself but also the water pit surrounding it. Now these different detector elements will be described in more detail:

- **Target (NT)**: the neutrino target is the innermost volume and is defined by a 8 mm thick acrylic vessel with diameter of 2300 mm and a height of 2450 mm and is filled

[1] A technical drawing of the detector system can be found in A.2 in the appendix.

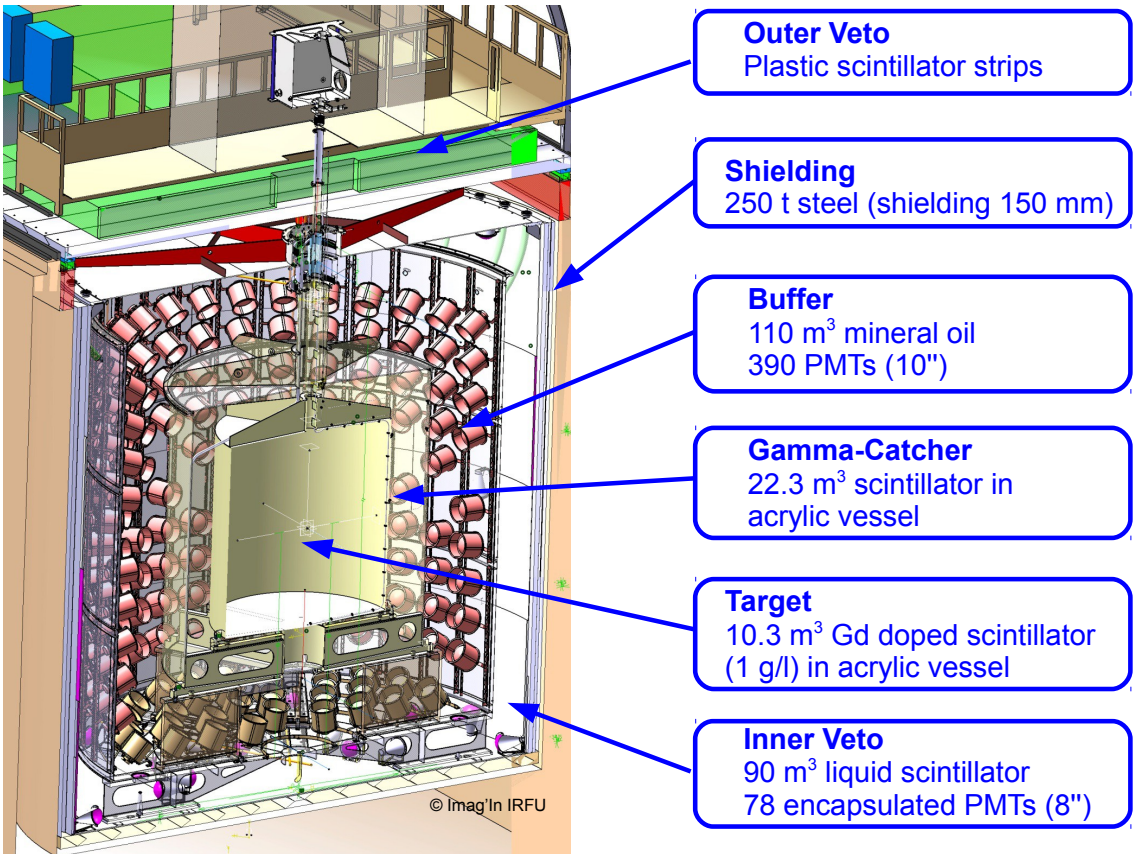

Figure 3.4: Overview of the Double Chooz detector design. The innermost volume is the neutrino target, surrounded by the Gamma-Catcher. Both volumes are made out of acrylic vessels filled with liquid scintillator. These vessels are contained within the buffer, a stainless steel vessel holding the PMTs. All this is surrounded by another active volume, the Inner Muon Veto which is also instrumented with PMTs and filled with liquid scintillator. On top of that is the Outer Muon Veto, made out of plastic scintillator strips, also read-out by PMTs. In the far detector case, the whole detector is shielded by iron bars, in the Near Detector case there will be a pit filled with water around the detector system. Picture courtesy of CEA/IRFU.

with 10.3 m^3 of gadolinium doped liquid scintillator[2]. In this volume the IBD reaction is happening. The use of Gadolinium gives a very clear experimental signature, first the "prompt" positron energy and annihilation (2 x 511 keV) and after a mean time of 30 μs the "delayed" neutron capture with an 8 MeV γ-ray cascade.

- **Gamma-Catcher (GC)**: this volume is also defined by a 12 mm thick acrylic vessel which is 550 mm in radius and surrounds the target. It contains the same liquid scintillator (22.3 m^3) as the target volume, but is not doped with Gd. Its purpose lies within the capture of electrons/positron escaping the target region and in the containment of the gamma-ray cascade following a capture on Gd. Thus the neutrino detection efficiency is increased and neutrino candidate events can be identified more reliable than without this volume.

- **Buffer**: this volume is defined by a stainless steel vessel, which also holds a support structure on which 390 10-inch PMTs are mounted. It is designed to shield the inner volumes against external radioactivity and also against radioactivity coming from the PMTs themselves. This volume is filled with non-scintillating organic liquid (110 m^3).

- **Inner muon veto (IV)**: the IV is the outermost volume containing the buffer vessel, its purpose lies within the identification and tagging of cosmic muons and spallation neutrons, created by them. It is a steel vessel, which is optically separated through the steel buffer vessel against the T and GC volumes. In total 78 8-inch PMTs are mounted on support structures on the veto vessel. These PMTs were previously used in the IMB and Super-Kamiokande experiments and carefully tested and modified for their use within DC [79]. The IV is filled with an organic liquid scintillator based on LAB (Linear Alkyl Benzene). Therefore all the PMTs are encapsulated in a stainless steel cone with a PET window in front. To match the optical properties of the IV scintillator, the interior of the encapsulation is filled with mineral oil.

- **Outer muon veto (OV)**: In addition to the IV there is another detector within DC to tag atmospheric muons. This is the OV which consists of multiple layers (currently two layers: X and Y) of staggered strips of plastic scintillator covering an area of 13 m x 11 m. It is assembled from modules containing 64 scintillator strips with the dimension 5 cm x 1 cm x 320 cm. These modules are 1.625 m wide and 3.6 m long. Each strip has a wavelength shifting fiber in its the center which is connected to a single channel of a Hamamatsu H8804 multi-anode photomultiplier tube. Cosmic ray muons will travel through the strips and produce scintillation light which is collected by the fibers and than transported to the PMTs. Hits in geometrically overlapping strips define precisely muon entry points and will be used to reconstruct muon tracks in combination with the ID/IV more accurately than with the ID/IV alone.

3.3.1 The used liquid scintillators

Within the DC experiment a liquid scintillator is used to detect the IBD reaction. These organic scintillators typically consist of aromatic hydrocarbon atoms composed of benzene ring structures. The scintillation mechanism is based on the excitation of molecular states by

[2]A mixture of the chemicals n-dodecane, PXE, PPO, bis-MSB and 1 g/l gadolinium as a beta-diketonate complex.

Figure 3.5: View inside the Inner Muon Veto. The surface of the IV vessel are painted with highly reflective white paint, also the encapsulated PMTs are visible.

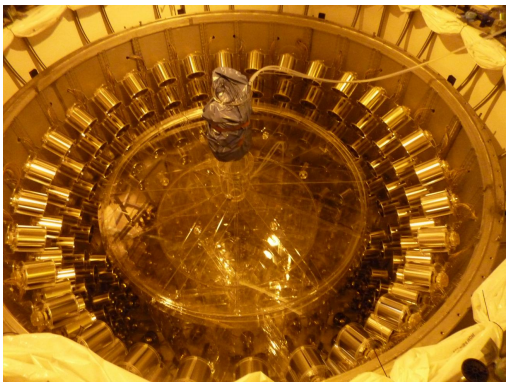

Figure 3.6: View inside the Buffer. Both acrylic vessels, the Target as well as the Gamma-Catcher are visible in addition to the PMTs of the ID mounted on the buffer wall.

Figure 3.7: View of the steel shielding on top of the main detector. This cover is made from 15 cm thick demagnetized steel bars in order to suppress external, environmental gamma-rays from reaching the detector setup.

Figure 3.8: View of the Outer Muon Veto covering an area of 13 m x 11 m above the main detector centered at the position of the chimney. A small region of 110 cm x 30 cm is left open to access the chimney.

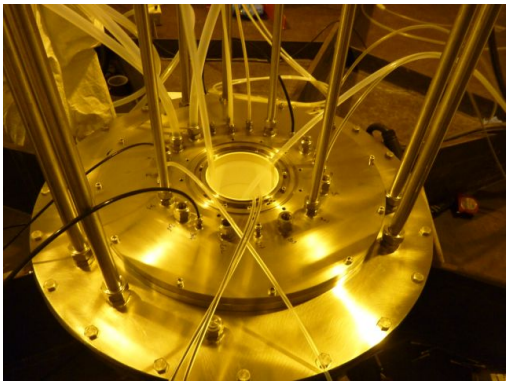

Figure 3.9: Picture of the upper part of the chimney, mounted in the z-axis of the detector. The various pipes and tubes used to fill liquids and to deploy radioactive sources inside the detector are visible.

Figure 3.10: This picture shows civil works inside the near detector cavern. It is expected that the lab will be ready for detector installation in the middle of 2013 and ready for data taking early 2014.

scintillator	component	chemical name	concentration
Neutrino Target	Dodecane	n-dodecane	80 $\%_{vol}$
	PXE	ortho-Phenylxylylethane	20 $\%_{vol}$
	PPO	2,5-Diphenyloxazole	7 g/l
	bis-MSB	4-bis-(2-Methylstyryl)benzene	20 mg/l
	Gd-(thd)3	Gd(III)-tris-(2,2,6,6-tetramethyl -heptane-3,5-dionate)	4.5 g/l
	Oxolane	tetrahydrofuran	0.5 $\%_{wt}$
Gamma-Catcher	Shell Ondina 909	mineral oil	66 $\%_{vol}$
	Dodecane	n-dodecane	30 $\%_{vol}$
	PXE	ortho-Phenylxylylethane	4 $\%_{vol}$
	PPO	2,5-Diphenyloxazole	2 g/l
	bis-MSB	4-bis-(2-Methylstyryl)benzene	20 mg/l
Buffer	Shell Ondina 909	mineral oil	53.5 $\%_{vol}$
	Cobersol C70	n-dodecane	46.5 $\%_{vol}$
Inner Veto	LAB	linear alkyl benzene	50.5 $\%_{vol}$
	Cobersol C70	n-dodecane	49.5 $\%_{vol}$
	PPO	2,5-Diphenyloxazole	2 g/l
	bis-MSB	4-bis-(2-Methylstyryl)benzene	20 mg/l

Table 3.6: Double Chooz liquid scintillator composition and properties. The table is taken from [81].

charged particles. During the de-excitation of these states UV photons are emitted. Responsible for this are the non-localized π-bonds within the sp- or sp^2-hybrid orbitals along the benzene ring. In addition the used scintillators are loaded with wavelength shifters, because the scintillator absorption spectrum partly overlaps with its emission spectrum. These will shift the wavelength to higher values were the scintillator is more transparent. In addition, the emitted wavelength can be matched to the sensitivity of the utilized photomultipliers.

As the predecessor Chooz experiment was limited due to the time-stability of their scintillator, one of the main efforts was to develop a new gadolinium loaded liquid scintillator that is stable over the lifetime of the experiment. This goal was achieved resulting in a Gd beta-diketonate loaded liquid scintillator, that is used for the first time in a neutrino detection experiment, within the DC [80] target volume.

In DC the used scintillators are ortho-Phenylxylylethane (**PXE**) for NT and GC volumes and linear alkyl benzene (**LAB**) for the IV. In addition the two wavelength shifting flours 2,5-Diphenyloxazole (**PPO**) and 4-bis-(2-Methylstyryl)benzene (**bis-MSB**) are added to the composition of NT, GC and IV scintillators. This leads to a very efficient energy transfer as the emission spectrum of PXE as well as the emission spectrum of LAB overlaps with the absorption spectrum of PPO. The emission spectrum of PPO in turn overlaps with the absorption spectrum of bis-MSB. In the end most of the scintillation light is emitted by the bis-MSB. The scintillator compositions can be found in Table 3.6 and it should be mentioned that all the liquids were matched to the same density of $(0.804 \pm 0.001)\,\mathrm{kg/l}$ at $15\,^{\circ}\mathrm{C}$ to avoid mechanical stress on the acrylic vessels which might otherwise be ruptured.

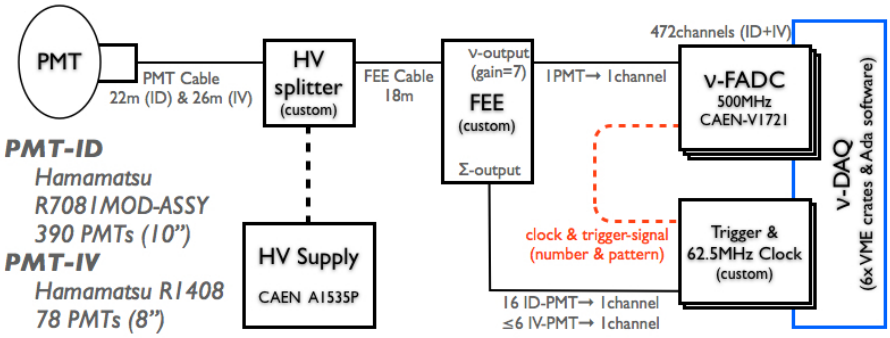

Figure 3.11: Overview on the Data Acquisition System, from [82]. Each PMT (either ID or IV) is connected to a splitter module, where signal and high voltage are divided, the signal is further given to custom made frontend (FEE) modules, that distribute the signal to the FADC modules and the trigger.

3.3.2 Data Acquisition and Processing

The main goal of the Data Acquisition System (**DAQ**) is to provide an accurate (time and charge) measurement of the PMT pulse waveforms. An overview on the DAQ system is given in figure 3.11. Photons created inside the detector are converted by PMTs to an electronic signal. Each of the 390 ID PMTs as well as the 78 IV PMTs is connected to custom made splitter modules via a single cable. This cable carries the signal and the high voltage which are separated by the splitter modules. The signals enter custom made analogue devices (Front End Electronics, **FEE**) which handle baseline restoration, filtering and pre-amplification or attenuation of the PMT pulses. Their main purpose is to match the measured signal to the dynamic range of the FADC cards.

Afterwards the signals are splitted and either entering a Flash ADC (labelled ν-FADC in F figure 3.11) where the waveform of the PMT pulse is digitized or the Trigger board. In the experiment there are two DAQ systems, the ν-DAQ and the μ-DAQ. The ν-DAQ consists of 60 FADC cards (Model VX1721) that were developed within the DC collaboration together with the CAEN company. These cards were designed to handle the low energy events from neutrinos (up to 15 MeV) and are virtually dead time free. Each of these cards is a 8 channel waveform digitizer with a timing resolution of 2 ns and a sampling rate of 500 MHz. The μ-DAQ in turn receives the attenuated pulses from the FEE modules, corresponding to high energy events presumably being muons. This system is designed to measure the high energy signal from muons without any distortion or truncation of the pulse due to the high amplitude exceeding the FADC dynamic range. It should be noted, that during the data taking period considered in this thesis, the system was not yet deployed and operational and will therefore not be described below in the general data taking scheme. The FADC is continuously taking data and stores it in a round buffer able to save the previously recorded 2048 ns and is read out if a valid trigger is issued.

The ID PMTs are divided into two groups A/B and the custom build Trigger system creates the analogue sum of the two groups. This Trigger system consists of four units: three Trigger boards (2 for ID and 1 for IV) and a Trigger Master Board. In these groups mentioned

before, each A PMT is surrounded by B PMTs and vice versa. The reason for this grouping is that after the summing of all A or B PMTs respectively, each Trigger Board can take a trigger decision for the whole detector and to have the possibility to monitor one board with the other. In addition all input signals of the IV will also be summed. A valid trigger signal is sent out by the Trigger Master Board to the FADC cards, if any of the three sums is above a given threshold. In this case a 256 ns time window is recorded for ID and IV PMTs. The threshold of the ID is set at a value of 400 keV being well below the minimum energy of a positron created by an anti-neutrino in the IBD reaction. The threshold of the IV is set at approximately 4 MeV corresponding to around 36,000 digital units of charge (**DUQ**), as will be seen in chapter 5. The OV has a separate DAQ system, where the triggers are later synchronized off-line.

If a valid trigger is issued, read out processors read the data from the FADC cards and transfer them to the event builders, where in turn a binary file for each event is created. Afterwards all data files for one given run (typically 1 hour long) are converted into ROOT format and transferred to the "Centre de Calcul de l'IN2P3" computing center in Lyon, France.

3.3.3 Calibration devices

In order to monitor the detector response and to establish the overall energy scale, several calibration devices and sources are used within the DC experiment. A schematic overview is shown in figure 3.12. All these systems (except the Light Injection ones) are connected to an air and light tight glove box directly positioned above the chimney. This box is continuously flushed with nitrogen and used to deploy sources (AmBe, ^{60}Co, ^{68}Ge, ^{252}Cf and ^{137}Cs) inside the detector.

- **Light Injection (LI)**: the first system to be mentioned is a multi wavelength LED fiber system, which is used to inject LED light into the ID (IDLI) and into the IV (IVLI) at a set of fixed points. These fibers are routed from the outside of the detector and each end is attached to one PMT. With these systems the PMT gains, as well as the relative timing of each PMT to another were measured every week.

- **Source Tubes**: the system comprises two thin stainless steal tubes running next to the NT and GC acrylic vessels. The first one (red) is the Buffer Tube, the second one (blue) the Guide Tube. Small radioactive sources can be deployed and moved through the detector inside these tubes. This offers the possibility to have sources near the outer surface of NT and GC an to move them along the z direction of these vessels.

- **Z-axis and Articulated Arm**: in order to access other regions of the detector volume the z-axis system is currently used. Here the sources were simply lowered inside the detector from the chimney region on along the z-axis. In addition a diffuser ball, having a blue ($\lambda = 470$ nm) and a UV ($\lambda = 380$ nm) LED, can be deployed in order to determine PMT gains and charge likelihoods. The Articulated Arm system is currently not operational, but once installed, sources can be mounted on a tip at the very front of the arm and virtually every position inside the detector volume is reachable as the device is moveable in 3D.

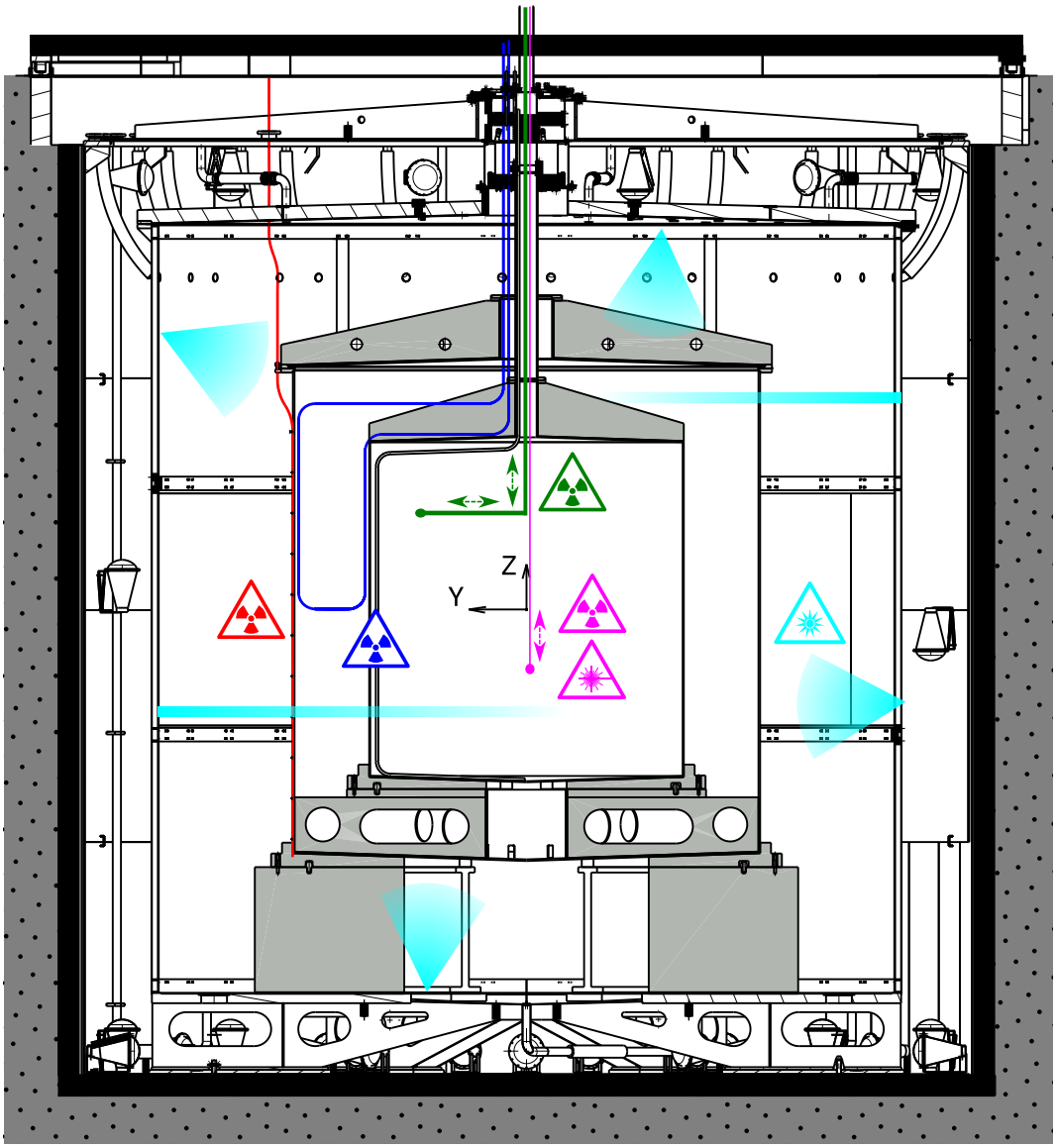

Figure 3.12: Schematic overview of the used calibration devices. In red and blue the Buffer and Guide Tube systems are shown running next to the outer surface of the NT and GC acrylic vessels. Right on the z-axis of the detector, the Z-Axis System is visible in pink. The Articulated Arm, able to deploy radioactive sources within the whole detector volume, is shown in green. Also displayed are the various fibers of the IDLI and IVLI systems that are connected to LEDs outside the detector. Picture taken from [83].

3.4 The DC software package DOGS

A dedicated software suite was developed within the DC collaboration named Double Chooz Offline Group Software (**DOGS**) to process, store, analyse or even simulate the data. This is a software framework with external dependencies on ROOT (Data Analysis software)[3], GEANT4 (High Energy Physics Simulation)[4] and MySQL (database)[5]. As explained before, if a valid trigger is issued by the Trigger System the data is read from the FADC cards and transferred to event builders, which in turn create a binary file for each event. Afterwards these data files for one given run of typically 1 hour length are converted to ROOT format, the so called DOGSification Process. Afterwards they are transferred to the "Centre de Calcul de Institut National de Physique Nuclaire et de Physique des Particule" (**in2p3**) computing center in Lyon, France were they are stored.

This "DOGSified data" is further processed up to a common level including the reconstruction of the PMT pulse form, the application of calibration constants as well as the reconstruction of event vertices and muon tracks. This processing step is the so called common trunk (**CT**) and this data is permanently stored on a band drive at the in2p3 computing center in Lyon were it is accessible for analysis. The three software packages responsible for pulse (RecoPulse), vertex (RecoBama) and muon track reconstruction (RecoMuHam) will be briefly explained now:

- **RecoPulse:** the aim of this reconstruction algorithm [84] is to provide the charge and the exact timing of each PMT pulse waveform. First the software estimates the baseline B_{mean} of the pulse waveform and its associated root mean square value, B_{rms}, for each PMT over the full readout window of 256 ns using a fixed external trigger issued every second. The measured charge is defined as the integral of each digital ADC count for a given waveform after the baseline has been subtracted. To improve the charge resolution a sliding 122 ns sub-sample of the readout window is used and the algorithm searches for the window maximizing the reconstructed charge. To ensure that a reconstructed pulse is actually from a signal and not a baseline fluctuation two thresholds are applied: the first one requesting that the maximum bin has more than 2 ADC counts, the second applies to the reconstructed charge that has to be bigger than

$$Q - B_{mean} \geq Q_{min} \equiv B_{rms}\sqrt{N_S}, \tag{3.13}$$

  where N_s is the number of integrated waveforms samples. For each reconstructed pulse the start time, defined as the time where the pulse reaches 20% of its maximum, is calculated. These start times are later corrected by the relative PMT to PMT offsets that were measured with the IDLI and IVLI systems.

- **RecoBama:** the software package performing the vertex reconstruction inside the ID. The software was used in the calibration campaign and for the visualization of event vertices. However, it should be noted, that it was not used in the neutrino selection.

[3]ROOT analysis software: http://root.cern.ch/.
[4]GEANT4 simulation software: http://geant4.cern.ch/.
[5]MySQL databse: http://www.mysql.com/.

Thus no fiducial volume cut is applied in the neutrino analysis. The fiducial volume here is given by the acrylics vessel of gadolinium doped scintillator within the NT. The RecoBama algorithm is based on a charge and/or time likelihood function, which is defined as

$$\mathcal{L}(X) = \prod_{q_i=0} f_q(0, \mu_i) \prod_{q_i>0} f_q(q_i, \mu_i) f_t(t_i, t_i^{pred}, \mu_i). \tag{3.14}$$

The first product multiplies over all PMTs that have not been hit, whereas the second one multiplies all remaining PMTs that have been hit. Under the assumption that the events are point-like , they can be characterized by the set $X = (x_0, y_0, z_0, t_0, \Phi)$ of initial coordinates, event time and light strength. From this set, the amount μ_i of light measured at PMT i and the photon arrival time t_i^{pred} can be calculated. The functions f_q, f_t are the charge, time probability functions which are determined from MC simulation. They have been carefully checked using calibration data. The reconstruction algorithm tries to find the set of parameters X_{min}, that minimizes the event likelihood $F(X)$

$$F(X) = -l \ln \mathcal{L}(X) = -\sum_i \ln f_q(q_i, X) - \sum_{q_i>0} f_t(t_i, X) = F_q(X) + F_t(X). \tag{3.15}$$

This set X_{min} defines the reconstructed event vertex. Using calibration sources at known positions along the z-axis of the ID and off-axis within the guide tube, the spatial resolution was found to be around 22 cm.

- **RecoMuonHam:** is the muon track reconstruction algorithm used in the ID. The software chooses the first PMT hit inside a given gate as a first guess for the muon entry point, EP. Afterwards it searches for the most likely muon exit point, XP, which is found by comparing the first hit times of each individual PMT i with the muon time of flight: $\Delta t_i = t_{hit,i} - t_{tof,i}$.

  The coordinates of the PMT with the lowest Δt_i is then chosen as preliminary XP. Using these two points, the most likely first photon arrival times are computed for all other PMTs, which are then compared to the observed ones [85]. The difference between the observed and the calculated arrival times is then χ^2-minimized by varying the muon entry and exit points, EP and XP. The lateral resolution was tuned on MC data. A comparison with OV hits in the X-Y stips yielded an overall lateral resolution of 350 mm.

3.5 Summary

The construction of the DC far detector ended in autumn 2010, it was filled during winter 2010/2011 and was comissioned in early 2011. The detector is actively taking data since April, 13th 2011.

With the first 101 days of data and only the far detector active, a first indication of a non-zero mixing angle θ_{13} could be achieved: $\sin^2 2\theta_{13} = 0.086 \pm 0.041(\text{stat.}) \pm 0.031(\text{syst.})$. In summer 2012, with more than double the statistics and an exposure of 33.71 GW ton years and a better understanding of systematic effects in the detector response, a more robust result of $\sin^2 2\theta_{13} = 0.109 \pm 0.030\,(stat.) \pm 0.025\,(syst.)$ could be achieved. The data set used for this second neutrino analysis will be the item of investigation in this thesis regarding the identification, measurement and rejection of cosmic ray muons.

The Near Detector lab is currently under construction and will be ready for detector installation in 2013. The Near Detector itself is expected to be ready for data taking in early 2014. At this time the DC experiment will have two detectors operational and will perform a relative neutrino flux measurement between the two sites.

"If you cannot, in the long run, tell everyone what you have been doing, your doing has been worthless."

Erwin Schrödinger (1887-1961)

4 Backgrounds and neutrino signal

This chapter gives an overview of the discrimination of anti neutrino from background events. It emphasises the importance of muons, as they create secondary particles which can mimic the neutrino signature. To motivate the studies of cosmic muons performed in this thesis, the first section starts with a short description of the anti neutrino detection in DC and the applied selection cuts. Following this, a general background classification in accidental and correlated backgrounds is introduced, orienting itself at the the measurements of the predecessor Chooz experiment. In addition to these two types of background, the intrinsic detector background of light noise is explained. After this first, general part, the focus of the chapter is put on muons.

Even by placing the detectors shallow underground, there is still an interfering cosmic muon background present. As stressed before, these muons are potentially dangerous as they induce background events by creating secondary particles which can mimic a neutrino coincidence. The processes creating secondary particles like fast neutrons and cosmogenic βn-emitters will be described. Because of the importance of muons, a detailed description of cosmic ray muon production in the atmosphere and the propagation of muons through rock to the detector setup underground will be given. This includes analytical descriptions as well as the summary of the results of a dedicated Monte Carlo simulation of muon flux and energy loss at the DC far site.

These detailed descriptions are given in anticipation to studies performed later in this thesis. In chapter 6 the perturbation of muon production in the atmosphere caused by seasonal temperature fluctuations is studied. In chapter 7 the extrapolation of muon flux and mean energy values with depth based on the DC Far detector site to other depths of interest will be discussed.

4.1 The neutrino signal

Anti neutrinos from the two nuclear reactor cores at Chooz are detected via the inverse beta decay reaction and are selected by the coincidence of two triggers within a given energy and time window. The choice of the energy and time windows is governed by the neutrino energy spectrum and the capture of neutrons on gadolinium. The resulting selection of neutrino candidates is done on a sub sample of recorded triggers, where triggers have been rejected if they are identified as light noise, if they are of external origin[1] or if they are below a visible

[1] External triggers Include the fixed rate trigger of 1 Hz or the ID and IV light injection triggers.

energy of 0.5 MeV where the trigger efficiency is below 100 %. Light noise events originate from the sporadic glowing of some PMT bases inside the ID vessel. More details on this will be given later in a dedicated subsection 4.3.

Based on this pre-selection, all triggers are rejected if they follow within 1000 μs after an identified cosmic muon traversing the ID or the IV. The application of this muon rejection leads to an effective dead time. The reason for this muon veto is to reject fast neutrons and other secondary particles produced by cosmic ray muons. The specific choice for the veto time window and the applied cuts to identify and reject muons will be the topic of the next chapter 5. In addition an isolation cut is applied, which rejects some of the fast neutrons produced by muons. This can be done because of the small amount of detectable neutrinos of around 50 d^{-1}. This results in a very small probability of an accidental coincidence of a neutrino event with other triggers and thus one can expect that neutrino events show up isolated in time. The neutrino selection scheme is visualized in figure 4.1. To summarize, the following cuts are applied to select neutrino candidates:

- **1). prompt trigger**: 0.7 MeV$< E_{\mathrm{prompt}} <$ 12.2 MeV
- **2). delayed trigger**: 6 MeV$< E_{\mathrm{delayed}} <$ 12.2 MeV
- **3). time difference prompt-delayed**: $2\,\mu\mathrm{s} < t_{\mathrm{pd}} < 200\,\mu\mathrm{s}$
- **4). isolation cut to previous trigger**: $(t_{\mathrm{prompt}} - t_{\mathrm{trig}}) > 100\,\mu\mathrm{s}$
- **5). isolation cut to following trigger**: $(t_{\mathrm{trig}} - t_{\mathrm{delayed}}) > 400\,\mu\mathrm{s}$

4.2 General background classification

The delayed coincidence of the positron and the neutron in the IBD reaction is very helpful to discriminate real anti-neutrino events from background events. However, every pair of events within the requested energy and time window can mimic both, the prompt and the delayed part of a neutrino coincidence. In order to be sensitive to the disappearance of electron anti-neutrinos from the nuclear reactors, one must have a good understanding of the background and its behavior.

As explained in chapter 3, the Double Chooz detector design was inspired by the predecessor Chooz experiment [50] and influenced by their knowledge of the observed backgrounds. The Chooz experiment was located at the DC Far underground detector site and thus the backgrounds can be considered nearly identical[2]. The experiment had the advantage that it was able to measure the background directly in a phase lasting around 138 days, were both nuclear reactors at the Chooz nuclear power station were shut down. During the DC data taking period this happened twice so far, leading to a total of 7.3 days of background measurement in 2011 and 2012 as will be explained in chapter 7.

[2]The Chooz detector is not fully comparable to the and DC Far detector, as the shielding situations are different. The Chooz detector was surrounded by sand, whereas there is a steel shielding for DC Far detector.

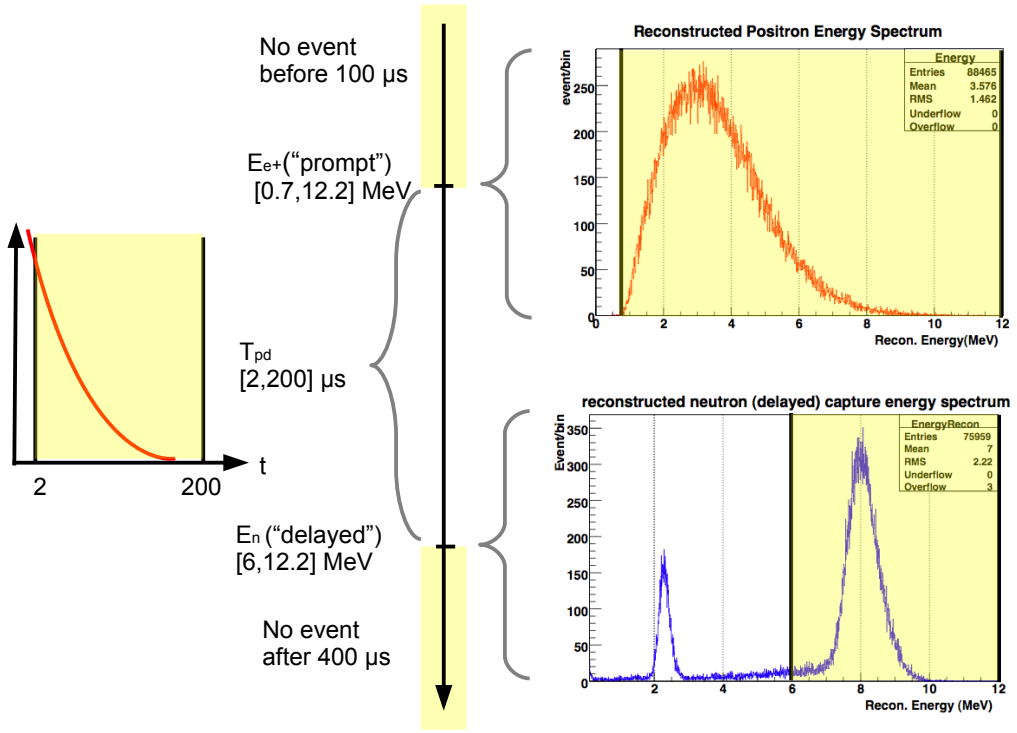

Figure 4.1: Schematic visualization of neutrino candidate selection: a prompt and a delayed event within a specific time window isolated in time from other events. Plot taken from [83] and modified.

In the reactor on and off data of the Chooz experiment, two different classes of background events could be distinguished: First accidental coincidences of uncorrelated background events and second correlated background events. This can be seen from figures 4.2 and 4.3 where the energy plane of positron and neutron-like events is shown, as well as the time delay between these two event types. Four categories have been introduced named A-D, where categories A and D show a flat time delay distribution indicating an origin in otherwise uncorrelated events. This accidental coincidence is formed by a low energy radioactive decay event coincident with another one (category D) or with a high energy event most likely being a proton recoil (category A). The events in category C show a clear peak of 8 MeV in the neutron-like energy, the typical energy of neutron capture on gadolinium. This events are still persisting in the reactor off data and can be interpreted as correlated background, associated with high energy spallation neutrons produced by cosmic ray muons. The neutron delay distribution with a mean time of $\approx 30\,\mu$s confirms this interpretation. These neutrons enter the detector, are slowed down to thermal velocities and scatter off protons, which give a positron-like proton recoil signal until they are finally captured on gadolinium faking the neutron-like signal. In addition there are βn-emitters produced by muons contributing to the correlated background. At last, the events in category B are events compatible with the decay of muons at rest due to the exponentially distributed lifetime of $\approx 2\,\mu$s. Thus these events are cosmic muons entering the detector, being stopped and decaying therein.

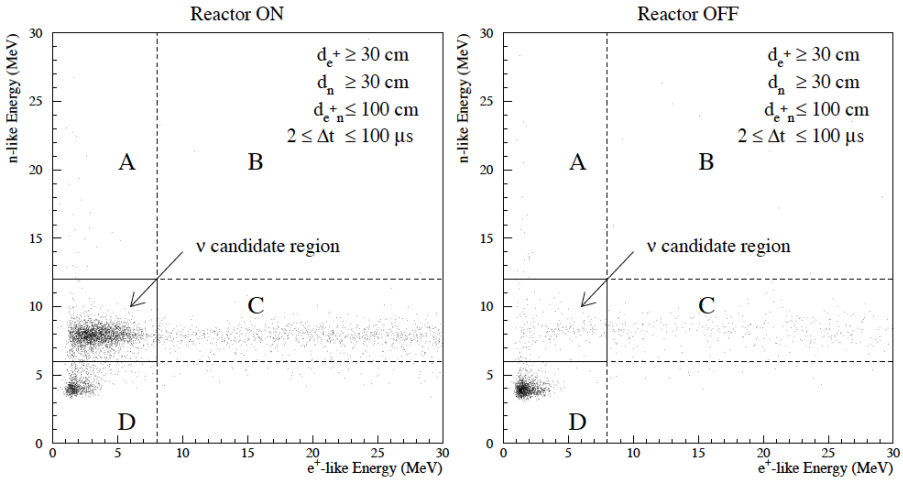

Figure 4.2: Plot of the energy plane of positron versus neutron-like events in the Chooz experiment. The left plot shows data collected during reactor on, whereas the right plot shows data collected during both reactors being off. One distinguishes four categories in these plots, namely A-D, surrounding the neutrino candidate energy region. The neutron-like energy distribution shows a peak at 8 MeV indicating its origin from neutrons being captured on gadolinium. Plot taken from [50].

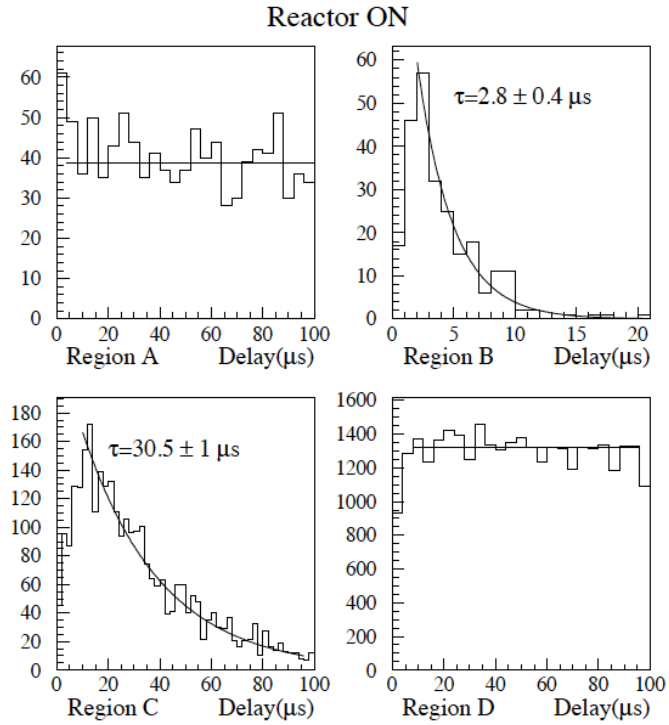

Figure 4.3: Time delay between positron and neutron-like events in the Chooz experiment for the four different categories A-D. The time delay of $\tau \approx 30\,\mu$s confirms the neutron capture on gadolinium. The events in categories A and D show a flat time distribution therefore indicating an accidental coincidence of two uncorrelated signals. Finally the time delay distribution of the events in B of $\tau \approx 2.8\,\mu$s is compatible with the decay of muons. Plot taken from [50].

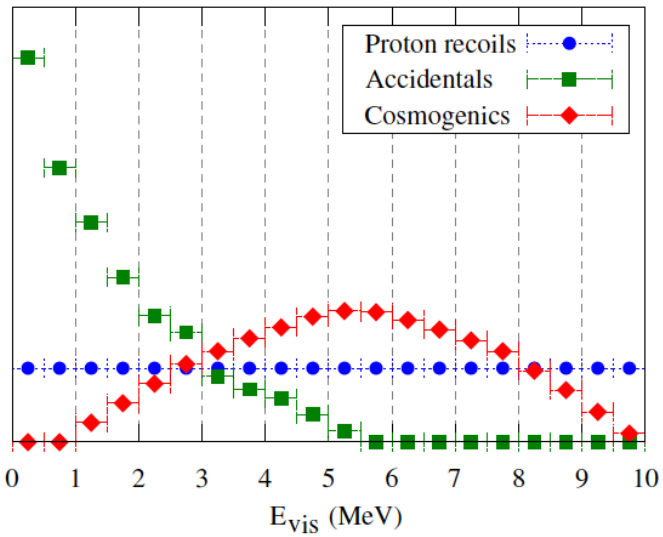

Figure 4.4: Expected backgrounds. Accidental background is shown in green, fast neutrons in blue and cosmogenic βn- emitters in green. Plot and explanation taken from [54].

Figure 4.4 schematically visualizes the spectra of these background components, being either accidental or correlated background. The accidental background (green) is expected to decrease exponentially with energy, whereas the fast neutron background (blue) is assumed to be flat. The βn-emitter spectral component (red) is based on nuclear database information.

4.2.1 Accidental background

Just by chance, any pair of events within the neutrino time window having the correct energy can form accidental background. One can calculate such an accidental rate by

$$R_{acc} = \tau_\nu \cdot R_e R_n, \tag{4.1}$$

where R_e is the positron-like event rate and R_n the neutron like event rate and τ_ν the coincidence time window. The spectrum of these positron-like events is shown in figure 4.5 measured during the data taking period considered in this thesis. These events mostly originate from natural radioactivity from Uranium, Thorium and Potassium within the used construction and detector materials, the scintillator itself and the glass windows of the PMTs. In addition to this, single neutrons contribute to so called single events. Whereas alpha decays do not contribute as their typical energy is quenched below 1 MeV in LS and is therefore below threshold.

During the design and construction phase of the DC Far detector, high priority was given to cleanliness and radio pure materials were chosen to keep the overall accidental rate below critical values [51]. All parts used in the experiment have been screened before their use by direct gamma spectroscopy with germanium detectors. In addition to this, a neutron activation analysis has been carried out for dedicated parts of the ID, namely the used

acrylics and the wavelength shifter PPO. The design goal was to have a rate of accidental neutrino-like coincidences less than 0.8 events per day.

4.2.2 Correlated background

In comparison to accidental background, the correlated one is more problematic. It occurs if a single physical source can mimic both, the prompt positron-like event as well as the delayed neutron-like event. This category includes fast neutrons (**FN**), stopping muons (**SM**) and cosmogenic βn-emitting isotopes created by cosmic muons. The spectra of these correlated background events are shown in figure 4.6 and 4.7 as measured in the considered data taking period.

FN created inside the detector can easily be identified and rejected by the identification of the preceding muon creating them. However, neutrons created by muons in the vicinity of the detector are more dangerous, as their large interaction length enables them to cross the full detector volume and there is no handle to identify them as the parent muon is not crossing the detector volume. The recoils of FN on protons can mimic the positron-like event whereas their capture after thermalisation on gadolinium can mimic the neutron-like event.

Also a subset of SMs belongs to this category. These muons enter the detector via the chimney and do not create enough detectable light in the IV to be identified. Their energy loss via ionization can mimic the positron-like event, while their subsequent decay can mimic the neutron-like event.

At last cosmogenic $\beta-$n emitters will be discussed. These are radioisotopes created via cosmic muon spallation having lifetimes in the order of several 100 ms. Because of the relatively long lifetimes they cannot easily be rejected by a veto time window following a detected muon because the introduced dead time would be unacceptably high. Regarding this cosmogenic background the most problematic source is ^{9}Li which has a lifetime of 250 ms and decays via beta-decay accompanied by a neutron in 50.8 % of all decays.

4.3 Instrumental light noise

Intrinsic background is caused by the instrumental light noise originating from a sporadic discharge in the passive electronics of the PMT's socket. As these events do not happen inside the scintillator their pulse shape is different from physics events inside the scintillator. The events caused by this discharge are spread out in time and the measured charge is very localized to a few PMTs.

Making use of these attributes, a discrimination between light noise and real physics events is possible. In this distinction two variables are used, first the ratio Q_{max}/Q_{tot}, where Q_{max} is the maximum charge recorded in one PMT for this event and Q_{tot} the total measured charge for this event and second $rms(t_{start})$ which is the standard deviation on the starting times t_{start} of each PMT within an event. The cut values [56] to identify and reject light noise used in this thesis are:

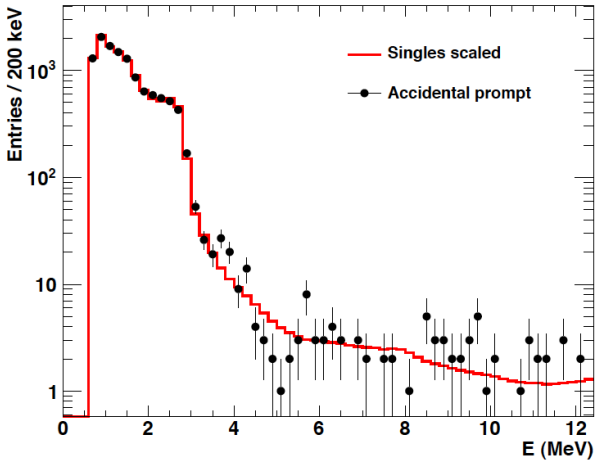

Figure 4.5: Prompt positron-like spectrum (black circles) of accidental events. The measured events are shown superimposed on the radioactivity energy distribution (red) measured in the DC Far detector normalized to have the same number of entries. Plot and explanation taken from [56].

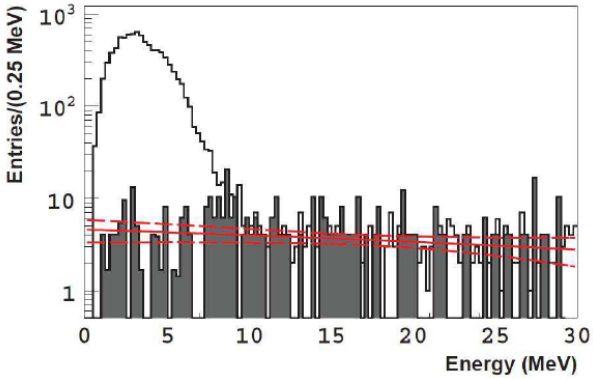

Figure 4.6: The Plot shows the combined spallation neutron and stopping muon contribution to the correlated background (gray histogram) superimposed on the spectrum of inverse beta-decay. The dashed red line corresponds to a range of $\pm\sigma$ uncertainty in this background. Plot and explanation taken from [56].

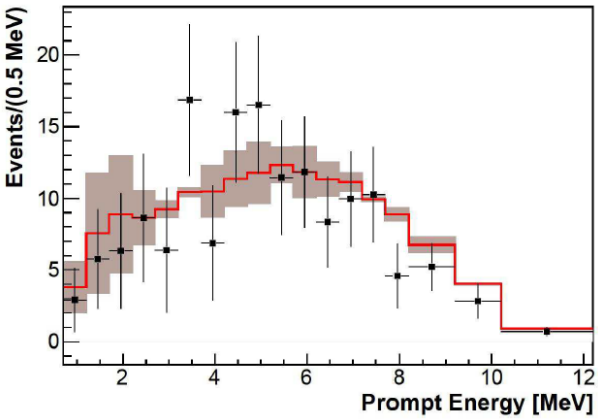

Figure 4.7: The plot shows the positron-like prompt spectrum of the βn-emitter ^{9}Li (black squares) superimposed on a Monte Carlo simulation of this isotope (red line). Plot and explanation taken from [56].

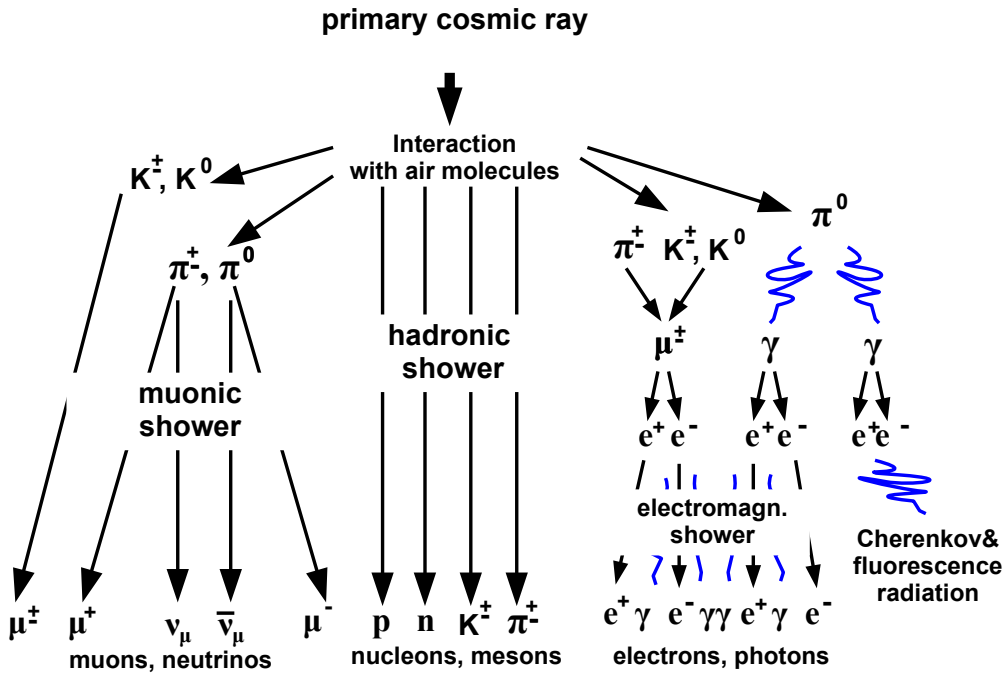

Figure 4.8: A primary cosmic ray particle hits the atmosphere and creates a lot of secondary particles, a particle shower is created.

- $Q_{max}/Q_{tot} < 0.09$
- $rms(t_{start}) < 40\,\text{ns}$

4.4 Cosmic ray muons

This section gives a detailed description of cosmic ray muon production in the atmosphere. As cosmic rays interact with air molecules in the atmosphere, it is not possible to detect them on earth's surface, only products of the reactions can be measured, which can be seen in figure 4.8. At high energies ($> 10^9\,\text{eV}$) such interactions do not happen with the whole nucleus of the atom or molecule, but instead with single nucleons within the nuclei. Most likely these are nuclei of oxygen and nitrogen, which produce predominantly pions, but also kaons and anti-nucleons.

$$X + N, O \longrightarrow \pi^{\pm,0} + Y$$

These particles undergo reactions and create further particles, a hadronic shower is born. The neutral pions π^0 decay within $8.4 \cdot 10^{-17}\,\text{s}$ [64] into two photons, which in turn create electron-positron pairs. These pairs annihilate and create, if the parent pion energy E_π is high enough, the starting point of an electromagnetic shower. In contrast, the charged pions π^+, π^- have a much longer lifetime ($2.60 \cdot 10^{-8}\,\text{s}$ [64]) and decay into muons μ^+, μ^- and muon neutrinos $\bar{\nu}_\mu, \nu_\mu$. The same happens for the decays of kaons. For muon energies E_μ higher than the critical value of $10^9 eV$ around 100 per square meter and second arrive at sea level.

Below this critical energy their decay with a lifetime of $\tau = 2.2 \cdot 10^{-6}\,\mathrm{s}$ [86] plays a major role. One ends up with a particle shower containing an electromagnetic component ($e^{\pm}$, γ), a muon component ($\mu^{\pm}$, ν_μ, $\bar{\nu}_\mu$) and a hadronic one p, n, $K^{\pm}$, $\pi^{\pm}$).

$$\begin{aligned} \pi^0 &\longrightarrow 2\gamma \longrightarrow 2e^- + 2e^+ \\ \pi^-, \pi^+ &\longrightarrow \mu^+, \mu^- + \nu_\mu, \bar{\nu}_\mu \\ \mu^-, \mu^+ &\longrightarrow e^-, e^+ + \bar{\nu}_e, \nu_e + \nu_\mu, \bar{\nu}_\mu \end{aligned}$$

The biggest fraction (ca. 80%) of particles one can measure at sea level is taken up by muons. Depending on their energy, they can either reach sea level or decay in flight. The ones being detected are highly relativistic particles (99.875 % of c), produced at altitudes of approximately 10 km in the decay of parent pions and kaons. These muons are energetic enough to penetrate several 100 m.w.e. and can still be measured underground.

4.4.1 Cosmic ray muons at sea level

Within this section the cosmic ray muon spectrum at sea level will be derived. This energy spectrum as well as the flux of muons at sea level is a direct consequence of meson production by hadronic interactions of primary cosmic rays with air molecules in the upper atmosphere as explained in the section before. A valid assumption is that the meson production falls off exponentially like e^{X/Λ_N}, where X is the primary cosmic ray track within the atmosphere and Λ_N the cosmic ray mean free path. In addition it is assumed that the produced mesons have the same direction as their progenitors, making the calculation 1-dimensional. This is justified as the cosmic ray flux is isotropic in solid angle in the upper atmosphere. The meson production through primary cosmic ray particles N is described by the meson production function $\mathcal{P}_M$ [87, 88]

$$\mathcal{P}_M = \frac{Z_{NM}}{\Lambda_N} N_0(E_M) e^{-X/\Lambda_N}, \tag{4.2}$$

with the spectrum weighted inclusive cross-section moment [89]

$$Z_{NM} = \int_0^1 x^\gamma \frac{dN_{NM}}{dx} dx \tag{4.3}$$

and the meson production spectrum

$$N_0(E_M) = A \times E_M^{-(\gamma+1)}, \tag{4.4}$$

where $x = E_M/E_N$ stands for the meson to primary particle energy ratio and γ is the differential primary spectral index. After considering meson production one has to look at processes reducing the number of mesons. Two processes of meson absorption compete with each other depending on the meson energy E_M. The first process to note are further hadronic

interactions $dX/d\Lambda_M$, where $M = \pi, K$ either stands for a pion or a kaon. The second process is the meson decay into a muon $M \to \mu\nu_\mu$.

$$\frac{d\tau}{\tau} = \frac{m_M c^2}{E_M \tau_M} \frac{dX}{\rho c} \tag{4.5}$$

where $d\tau = dX/(c\rho)^{-1}$ is the time to travel the distance X in the atmosphere and $\tau = \tau_M E_M / m_M c^2$ is the meson lifetime in a coordinate system fixed to the earth. Now, having terms for production and loss of mesons M, one can write the differential equation for the meson intensity as

$$\begin{aligned} d\mathcal{M} &= \mathcal{P}_M dX - \mathcal{M}\left(\frac{dX}{\Lambda_M} + \frac{d\tau}{\tau}\right) \\ &= \frac{Z_{NM}}{\Lambda_N} N_0(E) e^{-X/\Lambda_N} dX - \mathcal{M}\left\{\frac{dX}{d\Lambda_M} + \frac{m_M c^2}{E_M \tau_M} \frac{dX}{\rho c}\right\}, \end{aligned} \tag{4.6}$$

This equation is equivalent to the equation of radioactive decay where a constant activation term is present, like $dN = Pdt - \lambda N dt$. In the equation above the first term represents the meson production through primary cosmic rays, the second and third term represent meson losses through further hadronic interactions or decay respectively. One can define the so called critical meson energy

$$\epsilon_M = \frac{m_M c^2}{c\tau_M} \frac{X \cos\theta}{\rho} = \frac{m_M c^2 H(T)}{c\tau_M} \tag{4.7}$$

which separates further hadronic interactions from decays. Taking into account the known values of pion and kaon masses and lifetimes one calculates the values of $\epsilon_\pi = 114 \pm 3\,\mathrm{GeV}$ and $\epsilon_K = 851 \pm 14\,\mathrm{GeV}$ respectively. The function $H(T)$ is the atmospheric scale height, which is related to the air density via $\rho = X\cos\theta/H(T)$, having a value of around 6.5 km. At this point it should be noted that the critical energy introduces a dependence on density and temperature to the differential meson intensity. Rewriting the differential meson intensity in eq. 6.14 and using the definition of the critical ϵ_M yields

$$\frac{d\mathcal{M}}{dX}(E_M, X, \cos\theta) + \mathcal{M}(E_M, X, \cos\theta)\left\{\frac{dX}{d\Lambda_M} + \frac{\epsilon_M}{E_M X \cos\theta}\right\} = \frac{Z_{NM}}{\Lambda_N} N_0(E_M) e^{-X/\Lambda_N}, \tag{4.8}$$

which is an ordinary differential equation, that can be solved using the integrating factor $\beta(X) = exp\int dX(1/\Lambda_M + \epsilon_M/(EX\cos\theta))$. Defining $1/\Lambda'_N = 1/\Lambda_N - 1/\Lambda_M$ and integrating both sides of eq. 4.8 yields the solution of this differential equation

$$\begin{aligned} \mathcal{M}(E_M, X, \cos\theta) &= \frac{1}{\beta(X)} \int \frac{Z_{NM}}{\Lambda_N} N_0(E_M) e^{-X/\Lambda_N} \beta(X) \\ &= \frac{Z_{NM}}{\Lambda_N} N_0(E_M) e^{-X/\Lambda_M} X^{-\epsilon_M/E_M \cos\theta} \int_0^X X'^{\epsilon_M/E_M \cos\theta} e^{X'/\Lambda'} dX'. \end{aligned} \tag{4.9}$$

This function describes the production of mesons through cosmic ray primary particles at the top of the atmosphere and also their propagation through the atmosphere towards earth, during which further hadronic interactions or decays can happen. The function $\mathcal{M}$ will now be used to calculate the corresponding function $\mu(X)$ for muons, assuming that the direction of muon propagation is about the same as the direction of meson propagation:

$$\mu(X)dX = \frac{d\tau}{\tau}\mathcal{M} = \frac{m_M c^2}{E_M \tau_M}\mathcal{M}\frac{dX}{\rho c} = \frac{\epsilon_M}{E_M X \cos\theta}\mathcal{M}dX \tag{4.10}$$

The generated muons will be distributed homogeneously in the energy interval $r_M E_M \leq E_\mu \leq E_M$, here $r_M = m_\mu^2/m_M^2$ is the squared mass ratio of muon to meson. The muon production function from eq. 4.10 above needs to be folded with the two-body decay kinematics $M \to \mu\nu_\mu$ of the parent mesons decay. Because of the smallness of the neutrino mass, it can be neglected in this decay and one can write the differential flux per unit cross section as

$$\frac{dn}{dE_M}dE_M = \frac{B_M m_M}{2pE_M}dE_M = \frac{B_M dE_M}{E_M(1-r_M)}, \tag{4.11}$$

with B_M being the branching ratio of the decay [90]. Therefore muons will be generated by meson decay with energies from E_μ up to E_μ/r_M. Convolving eq. 4.11 and the muon production function eq. 4.10 yields

$$\begin{aligned}\mathcal{P}_\mu(E_\mu, X, \cos\theta)dX &= \sum_{M=\pi,K}\int_{E_\mu}^{E_\mu/r_M} dE_M \frac{dn}{dE_M} f_\mu \qquad (4.12)\\ &= \sum_{M=\pi,K}\frac{\epsilon_M}{X\cos\theta(1-r_M)}\int_{E_\mu}^{E_\mu/r_M}\frac{dE_M}{E_M}\frac{\mathcal{M}(E_M, X, \cos\theta)}{E_M}dX.\end{aligned}$$

Taking into account that muons can decay via $\mu \to e\nu_\mu$ one gets an additional exponential multiplication factor to eq. 4.12 above stating the probability of a muon to pass from the atmospheric layer of creation X' to the layer of detection X without decay [87]

$$\varphi_\mu(E_\mu, X, X') = exp\left(-\frac{m_\mu c}{\tau_\mu}\int_X^{X'}\frac{dL}{\rho(L)}\frac{1}{E_\mu - \alpha(L-X)}\right) \tag{4.13}$$

Here α corresponds to the energy loss of the muon passing through $1\,\mathrm{g/cm^2}$ of air. As muons are not created at one particular depth within the atmosphere, but from the boundary of the atmosphere X up to the level of observation, the production spectrum has to be integrated over the whole atmosphere:

$$\frac{dN_\mu}{dE_\mu d\Omega} = \int_0^\infty dX \mathcal{P}_\mu(E_\mu, X, \cos\theta)\varphi_\mu(E_\mu, X, X') \tag{4.14}$$

The propagation of mesons and muons in the atmosphere depends strongly on the considered energy range, as further interactions are competing with decay of the particles. The relative

importance of the two processes depends on the energy, using the definitions of the critical energies ϵ_M, ϵ_μ one is able to distinguish three different energy regions in eq. 4.14 representing the muon spectrum [89] :

- $E_\mu >> \epsilon_M$: at these high energies further hadronic interactions are dominating and the meson production spectrum has the same power law dependence as the primary cosmic ray spectrum. This is also the typical energy range for muons measured deep underground.
- $\epsilon_\mu \leq E_\mu \leq \epsilon_M$: In this intermediate region nearly all mesons decay. Below the critical muon energy ϵ_μ, having a value of 1 GeV muon decay and energy loss become important.
- $E_\mu \leq \epsilon_\mu$: In this energy region muons are more likely to decay. Because of their low kinetic energy, processes in the atmosphere leading to an energy loss cannot be neglected. Therefore these low energetic muons do not reach a detector lab underground.

The mean muon energy at the far detector lab is 63.7 ± 0.8 GeV [91], being in the intermediate energy region, where one has to consider both meson reduction terms (interactions or decay) and one can safely neglect muon decay and energy loss in good approximation. Making use of these assumptions, the integration yields the differential muon spectrum at a particular depth (e.g. at sea level):

$$\begin{aligned}
\frac{dI\mu}{dE_\mu} &= \int_0^\infty \mathcal{P}_\mu(E, X, \cos\theta) dX \\
&= \sum_{M=\pi,K} \int_0^\infty dX \frac{\epsilon_M}{X \cos\theta (1 - r_M)} \int_{E_\mu}^{E_\mu / r_M} \frac{dE_M}{E_M} \frac{\mathcal{M}(E_M, X, \cos\theta)}{E_M} \\
&\approx AE^{-(\gamma+1)} \left\{ A_{\pi\mu} \frac{1}{1 + 1.1 E_\mu \cos\theta / \epsilon_\pi} + 0.635 A_{K\mu} \frac{1}{1 + 1.1 E_\mu \cos\theta / \epsilon_K} \right\}, \qquad (4.15)
\end{aligned}$$

where the factor A incorporates some numerical values and one defines

$$A_{M\mu} = Z_{NM} \frac{1 - r_M^{\gamma+1}}{(1 - r_M)(\gamma + 1)}. \qquad (4.16)$$

Calculating the ratio of $A_{k\mu}/A_{\pi\mu}$ yields

$$\eta = \frac{A_{k\mu}}{A_{\pi\mu}} = \frac{Z_{nK}}{Z_{n\pi}} \frac{1 - r_\pi}{1 - r_K} \frac{1 - r_K^{\gamma+1}}{1 - r_\pi^{\gamma+1}}. \qquad (4.17)$$

By solving the integrals and using the definitions from eq. 4.16 and eq. 4.17 one obtains the differential muon spectrum at sea level [92]:

$$\frac{dI_\mu}{dE_\mu} \approx \frac{0.14\, E_\mu^{-(\gamma+1)}}{\mathrm{cm}^2\,\mathrm{s}\,\mathrm{sr}\,\mathrm{GeV}} \left\{ \frac{1}{1 + 1.1 E_\mu \cos\theta / \epsilon_\pi} + \frac{\eta}{1 + 1.1 E_\mu \cos\theta / \epsilon_K} \right\} \qquad (4.18)$$

4.4.2 Cosmic ray muons underground

As mentioned before in the introduction of this chapter, a way to reduce this cosmic ray muon background is to place the detectors underground, which is done in the DC experiment. The earth above the laboratory will function as a shielding against cosmic ray muons. The range of muons is only limited due to energy losses. These losses can be summed up in losses due to ionization, bremsstrahlung, pair creation and nuclear interactions, which are all functions of the muon energy. One defines the parameter $\epsilon = a/b$, which divides the energy into a range being dominated by ionization losses and a region dominated by radiation losses [93]. Here x stands for the muon track length in matter, so the amount of material traversed, and $a(E_\mu)$ for the losses due to ionization and $b(E_\mu)$ for the losses due to radiation

$$-\frac{dE_\mu}{dx} = a(E_\mu) + b(E_\mu)E_\mu. \tag{4.19}$$

By integration of the muon energy loss dE_μ/dx over all muon energies E_μ one finds the range R of muons in matter. This range defines a muon threshold energy E_{th}, being the energy required for a muon to survive to depth R. With the knowledge of the sea level cosmic ray muon spectrum and the energy loss processes of muons in mater, one is in principle able to calculate the muon spectrum underground

$$\begin{aligned} I_\mu &= \int_{E_{th}}^{\infty} dE_\mu \frac{dN_\mu}{dE_\mu d\Omega} \\ &\approx BE_{th}^{-\gamma}\left\{\frac{1}{1+1.1E_{th}\cos\theta/\epsilon_\pi} + \frac{\eta}{1+1.1E_{th}\cos\theta/\epsilon_K}\right\} \end{aligned} \tag{4.20}$$

However this is only possible analytically, if one assumes a and b to be constant[3] and having flat overburdens, where one can safely integrate over the solid angle and does not have to take any hill profile of the site into account. In addition, this term is only valid if the material composition along the muon track is homogeneous. Due to the topology of the experimental sites (the overburden of the lab sites is not flat) both conditions are not fulfilled and one needs to step away from the pure analytical approach and look for an accurate and efficient numerical method to calculate spectra, flux and rate underground.

The numerical method used with the DC experiment uses the MUSIC code [91], which simulates the 3-dimensional transport of muons through a given material of slant depth $D(\theta, \phi)$, taking into account the energy loss mechanisms. The software is composed of a Monte Carlo simulation of muon energy loss and a simulation of angular deviation and lateral displacement. Without going into detail one defines a probability function $P(E_\mu, D(\theta, \phi))$, which is the survival probability of a muon traveling a track D through matter at a zenith angle θ and the azimuthal angle ϕ with initial energy E_μ. This is evaluated using a topological map of the hill profile above and surrounding the DC experimental sites also taking into account the measured chemical composition of the rock at the Chooz site. The hill profile is shown in figure 4.9 where the coordinate (0,0,0) indicates the location of the DC far detector.

[3]For the considered muon energy range the parameters a, b vary moderately with $\ln(E_\mu)$.

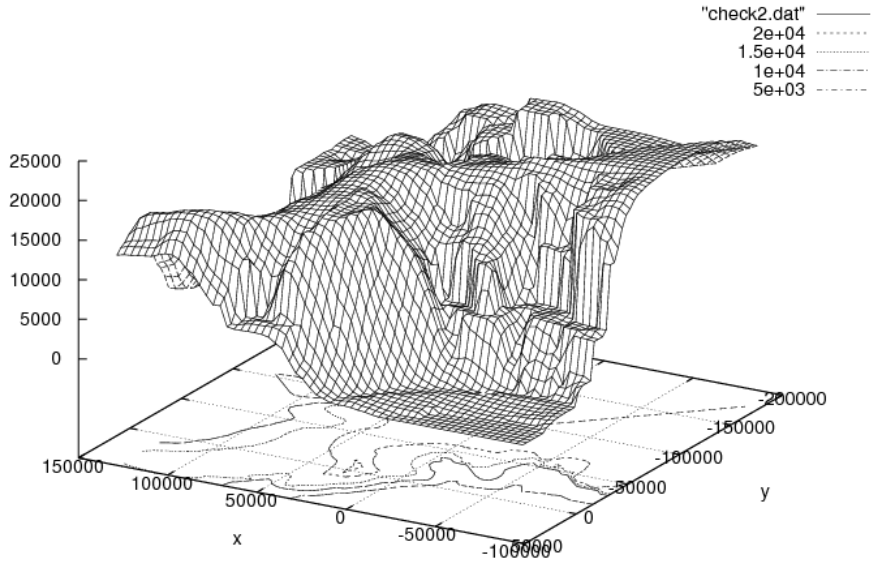

Figure 4.9: This figure shows a 3-dimensional map of the hill topology of the DC far site. The coordinate (0,0,0) indicates the position of the DC far detector. Plot taken from [94].

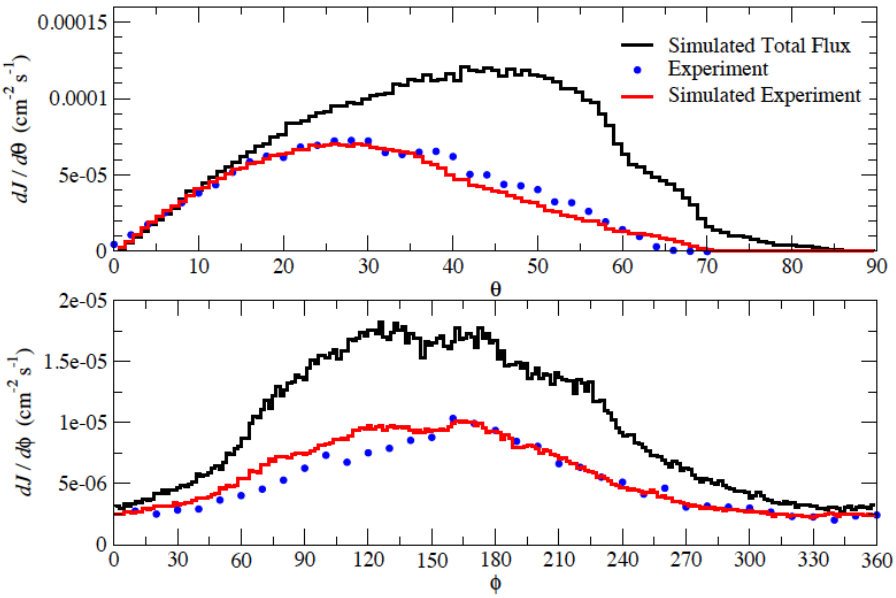

Figure 4.10: Angular distribution of muons at the DC far underground site. Plot taken from [91] where a MUSIC simulation was performed. The simulated total flux (black) refers to the simulated muon flux integrated over the entire hemispherical solid angle and was binned to generate the angular distributions. The simulated experiment (red) is the simulated muon flux integrated over a limited range of solid angle described by the geometry of the RPC plates used in a cosmic ray experimental setup (blue) at the DC far site.

Within the MUSIC simulation program one propagates muons through the hill profile and stores the values of P in order to integrate the observables (flux Φ_μ, rate R_μ and mean energy $\langle E_\mu \rangle$) underground numerically:

$$\Phi_\mu(D(\theta,\phi)) = \int_\Omega d\Omega \int_0^\infty dE_\mu P(E_\mu, D(\theta,\phi)) \frac{dN_\mu}{dE_\mu d\Omega} \quad (4.21)$$

$$R_\mu(D(\theta,\phi)) = \int d\mathbf{A}\cdot\hat{r}\Phi_\mu = \int d\mathbf{A}\cdot\hat{r} \int_\Omega d\Omega \int_0^\infty dE_\mu P(E_\mu, D(\theta,\phi)) \frac{dN_\mu}{dE_\mu d\Omega} \quad (4.22)$$

$$\langle E_\mu \rangle (D(\theta,\phi)) = \frac{1}{\Phi_\mu} \int_S d\Omega \int_0^\infty dE_\mu \frac{dN_\mu}{dE_\mu d\Omega} \int_0^\infty dE_\mu E_\mu P(E_\mu, D(\theta,\phi)) \quad (4.23)$$

Details on this can be found in previous work [83], where also a comparison between GEANT4 and MUSIC was made. Table 4.1 shows the results obtained from a MUSIC simulation for the DC far site [91], using detailed maps on the topology of the mountain sites at Chooz and geologic surveys done prior to the Double Chooz experiment. The values for the Near site are extrapolated from the far site values using empirical formulas given in [95, 96]. In chapter 7 the extrapolation or scaling will be further introduced and also used to extrapolate muon flux and mean energy to the depths of the reactor neutrino experiments RENO and Daya Bay. Figure 4.10 shows the angular distribution of muons at the DC Far underground site resulting from a MC simulation. The angular distribution is not uniform in azimuth angle ϕ and is not following a $\cos^2\theta$ distribution for the zenith-angle θ. Basically these angular distributions resemble the hill topography of the experimental site, which influences the number of muons from a given direction because of the energy loss of these muons depending on the amount of rock shielding they have to cross to reach the detector underground.

	near site	**far site**
depth (m.w.e.)	**150**	**300**
Φ_μ ($s^{-1}m^{-2}$)	3.5 ± 0.3	0.75 ± 0.01
R_μ^{ID} (s^{-1})	61.7 ± 5.2	13.2 ± 0.2
R_μ^{IV} (s^{-1})	228.7 ± 19.6	49.2 ± 0.7
$\langle E_\mu \rangle$ (GeV)	23.2 ± 0.2	63.7 ± 0.8

Table 4.1: Comparison of depth, mean muon energy $\langle E_\mu \rangle$ and expected muon rates in ID, R_μ^{ID}, and IV, R_μ^{IV} at the near site and the far site. The quoted values for the far site are from [91], scaled from the former Chooz experiment dimensions, whereas the flux and mean energy values for the near site were scalded from the far site using extrapolation formulas that can be found in [95, 96].

4.5 Fast neutrons created by muon spallation

Fast neutrons are created in the following interaction processes of muons:

- **Nuclear disintegration**: a muon interacts with a nucleus via the exchange of a virtual photon and the nucleus is subsequently emitting neutrons. This process is also called muon spallation.
- **Elastic scattering**: Muons scatter elastically with neutrons bound in the nucleus, in turn kicking these neutrons out of the nucleus.

- **Photo nuclear interactions**: neutron production by photons in electromagnetic showers initiated by muons.
- **Secondary neutron production**: Neutron production following any of the three described processes above.

In addition to the described processes, muons can stop and get captured on a nucleus resulting in highly excited states emitting one or more neutrons. All these processes are quite fast and happen close to the muon track, thus the production mechanism enables their rejection. In order to do so, one needs to identify cosmic muons crossing the detector or passing through rock nearby as good as possible. After identifying a muon a veto time window is set and all events within this time window are rejected in order to sort out these muons and the possibly created neutrons. Problematic are neutrons created outside the detector setup. Because of their high kinetic energies these neutrons have a mean free path of a couple of meters and they can still reach the detector.

In opposite to charged particles a neutron cannot be easily detected until it gets captured on a nucleus, mimicing one part of a neutrino coincidence. Occasionally these neutrons scatter off nuclei in the detector, depositing considerable amounts of energy. For non-relativistic neutron energies the recoil energy transferred to a nucleus can be expressed as

$$E_{rec}(\theta) = \frac{4A}{(1-A)^2}\cos^2\theta E_n, \tag{4.24}$$

where A is the atomic mass of the target and θ the scattering angle. For $\theta = 180$ the maximum energy can be transferred. A proton can receive the full energy of the neutron, whereas the main constituent of organic liquid scintillators regarding mass, a carbon nucleus will get approximately 30 % of the neutron's kinetic energy. The recoiling nucleus in turn will excite the scintillator which produces detectable light.

Compared to the light output of electrons, the light output of the nucleus is quenched to lower energies. As indicated before, a FN can loose energy via elastic scattering off nuclei in the scintillator, where the most efficient energy transfer is reached for scattering off a proton. This happens until its kinetic energy reaches the thermal regime ($E_{kin} \approx 0.025\,\mathrm{eV}$), where it can be captured by a nucleus. This nucleus enters an excited state emitting a cascade of gamma rays with the sum energy of the excitation in turn. For the DC scintillators these nuclei are hydrogen (20 %) and gadolinium (80 %).

4.6 Cosmogenic βn-emitters created by muons

Muons can produce various isotopes by interacting with carbon atoms in the liquid scintillator. Most of these isotopes are unstable and decay via beta-decay contributing single events which can lead to accidental background. A potentially more dangerous background, are the isotopes ^{8}He and ^{9}Li which undergo beta-decay followed by neutron emission. Therefore each of these isotope can create a positron-like event followed by a neutron-like event,

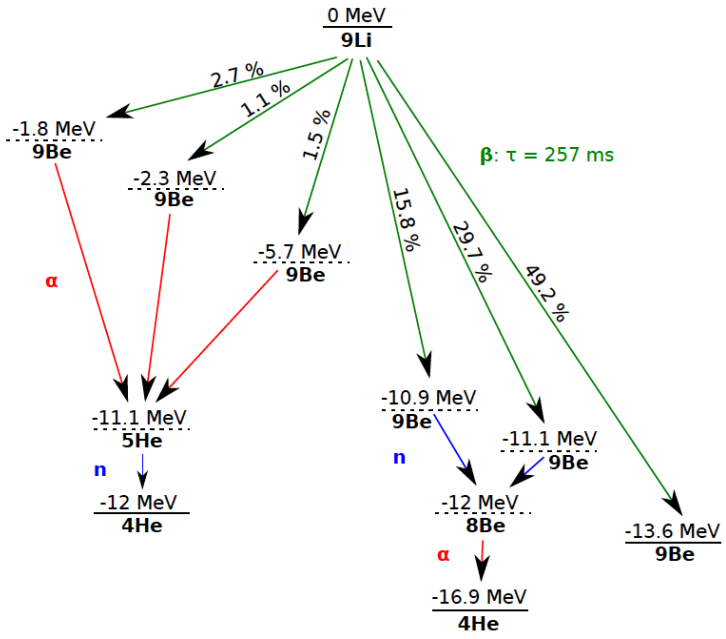

Figure 4.11: Visualization of the ^{9}Li decay scheme. The largest decay fraction goes to the ground state of ^{9}Be, whereas the rest goes to an excited state of ^{9}Be. This excited state decays into ^{8}Be and a neutron or ^{4}He and a neutron in the end. Scheme taken from [83].

faking a neutrino coincidence. As they have half-lifes in the order of several 100 ms they cannot simply be rejected by a veto-time window after each muon because of the high muon rate.

As the isotope ^{8}He is less abundantly produced, the dominating isotope is ^{9}Li [97], which will be considered in the following. It has a half-life $\tau_{Li} = 178$ ms, undergoes beta-decay which can go to the ground state in 49.2 % of all cases or to various excited stated of ^{9}Be in 50.8 % of all cases. The ground state of ^{9}Be is stable, however the excited states quickly break up. This can happen either due to a decay into ^{8}Be followed by subsequent neutron emission or via alpha-decay into ^{5}He emitting a neutron in turn to become ^{4}He. This combination of a beta-decay followed by the neutron emission mimics the anti-neutrino event. The overall endpoint (Q-value) of the ^{9}Li beta-decay is at 13.6 MeV, thus covering the full energy window for the prompt event. The decay scheme of this isotope is visualized in figure 4.11.

4.7 Conclusion

The neutrino selection and the backgrounds to the neutrino analysis of the DC experiment have been presented and the role of cosmic muons in producing these background events was stressed. A detailed description of the cosmic muon production in the atmosphere and the expectation of muon rate, flux and mean energy at the DC far and near shallow underground sites was given. With this theoretical background the next chapter will focus on how to identify and reject cosmic muons and following muon correlated events reliably.

"Physics is, hopefully, simple. Physicists are not."

Edward Teller (1908-2003)

5

Identification and rejection of the cosmic ray muon background

At sea level muons are the most abundant cosmic ray particles. As they have a small interaction cross section the high energetic muons can penetrate earth and are still present underground, whereas the less energetic ones have already been absorbed. In order to reduce the cosmic muon background both Double Chooz detectors will be placed shallow underground. Even in shallow depth, a few tenth of meters beneath soil a considerable muon reduction can be achieved. In the case of the DC far detector the muon flux is reduced from around $200\,\mathrm{m^{-2}s^{-1}}$ at sea level to $0.8\,\mathrm{m^{-2}s^{-1}}$ in a depth of 300 m.w.e. as pointed out in the last chapter.

Regardless, the residual muons underground are still a potentially dangerous background. They create neutrons via spallation of carbon in the used organic liquid scintillator and through muon capture in the detector. In addition to the overburden provided by building the detectors underground a veto detector (the IV) is used to further reduce the residual muon background rate. Cosmic muons and events correlated to muons can be identified by the amount of energy they deposit, as their track intersects the detector. In addition there could also be the case, that neutrons are created by muons passing the detector in the nearby rock which can reach the detector. These neutrons deposit energy in the detector via proton recoil in the IV, or their capture on H or Gd . To identify fast neutrons any threshold should be set as low a possible in terms of energy, so that their small energy depositions via proton recoil can also be detected. As fast neutrons are correlated in space and in time to the muon creating them, a veto window after each muon is applied to reject them. In addition muon generate the unstable isotopes ^{8}He and ^{9}Li by spallation in the organic liquid scintillator. These isotopes undergo beta decay followed by neutron emission faking a neutrino interaction. As these background events are produced by muons, it is mandatory to have a proper understanding of the cosmic muon background and the measures to identify it.

This chapter will give an overview on the identification of the muon background at the DC far underground site and it will introduce the general concept to veto muons and correlated background events induced by muons. The chapter will compare muon spectra and rates using different logical combinations of the muon tag that will be introduced in the following. Utilizing these different combinations and different methods to extract the muon rate, a handle on muon sample purity is given. In addition the stability of the muon thresholds in ID and IV will be studied to have an estimation of a systematic error in the muon rate

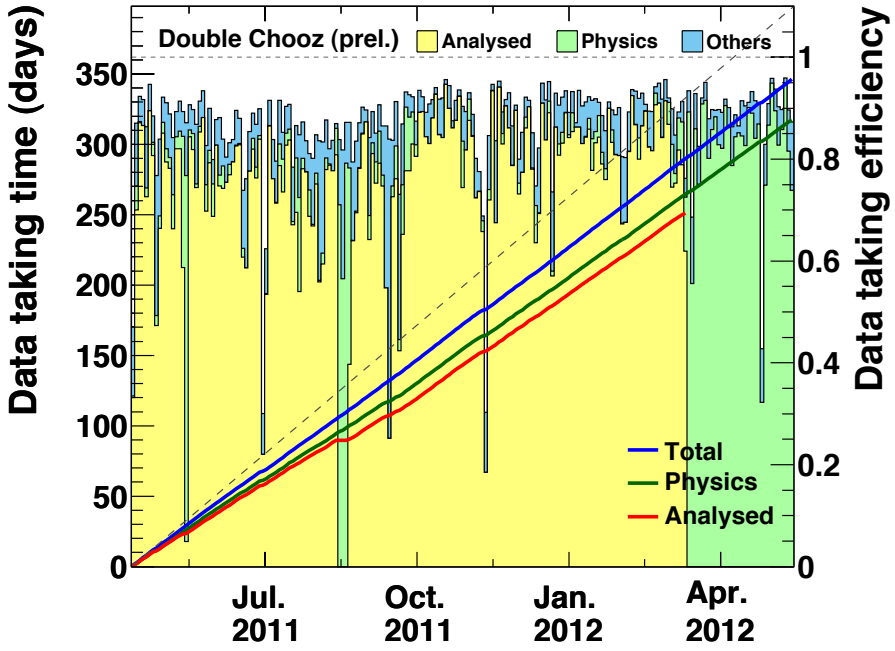

Figure 5.1: Visualization of the data taking statistics, left ordinate shows integrated data taking days, whereas the right ordinate shows the efficiency of data taking versus calender day. The blue color indicates the time where the DAQ system was actively taking data, the green color visualizes the physics data taking and yellow the analyzed data after quality cuts for the considered time period from 2011/04/13 till 2012/05/11. This data sets is the same as the one used in [56] for neutrino analysis. Plot and numbers taken from *http://dchooz.titech.jp.hep.net/components/online/DC_ ONLY/DataTaking/neutrino2012.php*.

determination. Utilizing the rate measurements in the different sub-detectors, ID and IV, the efficiency of the IV to identify and reject cosmic muons will be determined.

5.1 Run selection

The data considered in this thesis were collected from 13th of April 2011 till 11th of May 2012, corresponding to a total span of 394 days without data quality cuts (Visualized in Fig. 5.1). From these data a set of runs was taken, where the detector was running under stable conditions, rejecting calibration and test runs. In addition runs having a duration of less than 5 minutes were rejected. The remaining "physics" runs devoted to neutrino analysis presented in [56] and used in the following in this thesis corresponds to 6322 runs of approximately 1 hour each. Figure 5.1 shows the efficiency of the data taking as well as the analyzed runs with the integrated data taking superimposed. The left ordinate shows the integrated days of data taking, whereas the right ordinate shows the data taking efficiency, which is the time fraction where the DAQ system was actively taking data. Light blue visualizes the overall taken data, whereas green indicates the physics data taking and yellow the analyzed runs. For the considered period, the average data taking efficiency was 87 %, for physics data it was about 80 %.

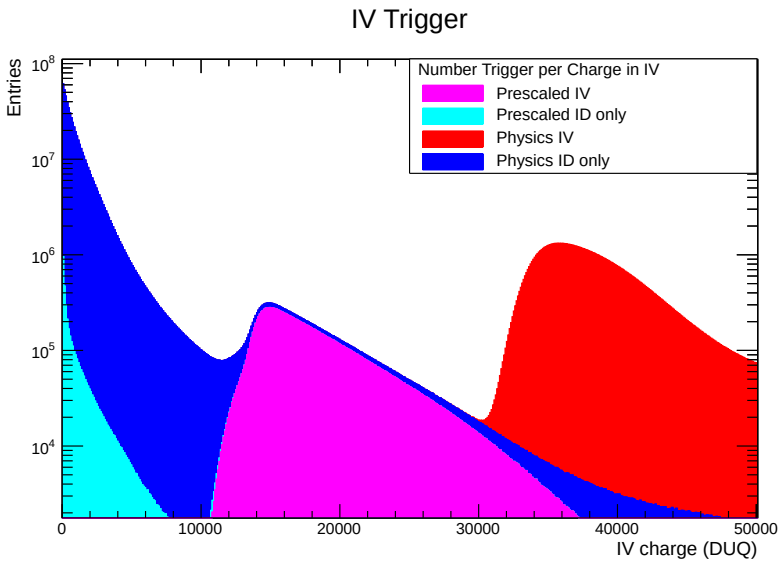

Figure 5.2: Charge region below 50 kDUQ in the IV. Shown in colors are the different trigger conditions forcing a readout of the IV, being an event triggered at pre-scaled threshold in the ID, at nominal threshold in the ID or being triggers of the IV. The shown distributions are scaled to each other. The first inflection point around 10 kDUQ was misinterpreted during commissioning time to be the self-triggering threshold, whereas the actual value is around 35 kDUQ. Plot by courtesy of M. Röhling.

5.2 Identifying muons

In order to distinguish neutrino events from reducible background, several selection criteria are applied. As motivated before, a general selection criterion is imposed by the rejection of cosmic muons. The cuts presented in the following are not only used to identify and reject cosmic muons going through the detector, but also FN, SM and any cosmogenic background created by muons in the detector or in its vicinity. After each event being identified as muon a veto window will be applied and the following events within this veto window are rejected. This is done because the backgrounds mentioned before are correlated to a preceding muon in space and time and thus can be rejected by this to some extent. This event rejection is applied off-line in the data analysis and leads to an effective dead time, which must be considered in the neutrino rate analysis. This section will give an outline on the studies performed to decide on the energy and charge cut values in ID and IV to be used for the applied muon identification, following an extensive description of the different steps that can be found in [98].

5.2.1 Inner Veto muon tagging

During commissioning the self-triggering threshold of the IV was thought to be set around 8.5 kDUQ. At this point one can discriminate two regions in the IV charge spectrum. The region below this self-triggering threshold is dominated by events originating from natural radioactivity and the region above by cosmic muons. In addition this was the lowest possible threshold value that the DAQ could withstand in terms of trigger rate, being approx. 45 triggers/s. for the configuration at that time. Below this self-triggering threshold value,

energy depositions in the IV are only recorded if there was also an energy deposition above threshold in the ID within the previous 256 ns. The trigger caused by such an event will also force a readout of the IV.

However, later studies [99] showed that the self-trigger threshold of the IV was actually set at 35 kDUQ. As indicated before, smaller charges were recorded if there was a valid trigger of the ID or a pre-scaled trigger of the IV. This is visualized in figure 5.2 where the charge range below 50 kDUQ in the IV is shown. The first inflection point was misinterpreted as distinction between natural radioactivity and muon events. The impact of this is yet unclear and dedicated studies evaluating this will be made in future, likely the muon threshold will be increased as already proposed in [100].

At commissioning time a dedicated study was performed based on this misinterpretation in order to identify the optimal choice of the IV muon identification threshold [98, 101]. To do so the number of neutron captures on hydrogen and gadolinium was counted as a function of different charge ranges recorded in the IV. Here a valid capture event has to follow a muon within 70 μs up to 150 μs and has to have the right energy of $1.5 - 2.5$ MeV for hydrogen and $6.0 - 10.0$ MeV for gadolinium. Figure 5.3 shows the number of neutron captures within the right energy and time window versus the given charge range of the IV. For the low charge range of $10 - 11$ kDUQ the highest number of caption events is observed. Integrating this plot yields a monotonic increase in the number of capture events with IV charge. As a consequence the threshold of the IV should be placed as low as possible in order to reject those neutrons in the ID, as they can fake the delayed event of a neutrino event otherwise. With the result of this study it was decided to use a value as close as possible to the self-trigger threshold of the IV. A slightly higher value of 10 kDUQ for the IV muon threshold was chosen in order to avoid position dependent variations in the IV response caused by the buffer support structure and the different number of PMTs on the veto vessel walls, bottom and top.

5.2.2 Inner Detector muon tagging

The detector geometry leaves the possibility that a muon enters the ID through the chimney not being identified by the IV. In order to identify these muons the ID itself needs a handle to identify muons. In addition, a cut value in the ID should be chosen in a way that FN not identified by the ID can be identified in the IV. In the following the choice of 30 MeV for the muon cut value of the ID will be motivated.

Muons entering the ID through the chimney are stopping muons, which can be understood by the following arguments. If a muon enters the ID through the chimney and leaves the ID afterwards it should be identified by the IV. Muons crossing large portions of the ID should deposit a huge amount of energy and can therefore easily be identified. The muon cut value of the ID of 30 MeV was chosen for two reasons. First, to be higher in energy than the typical energy of ≈ 8 MeV of a delayed gadolinium capture event. Second it was chosen to cover part of the michel electrons originating from the decay of SM. A SM can either be tagged by it's track length within the scintillator (> 30 MeV approx > 15 cm) or by the subsequent decay into a michel electron. Second, the energy region from 15-30 MeV is used to moni-

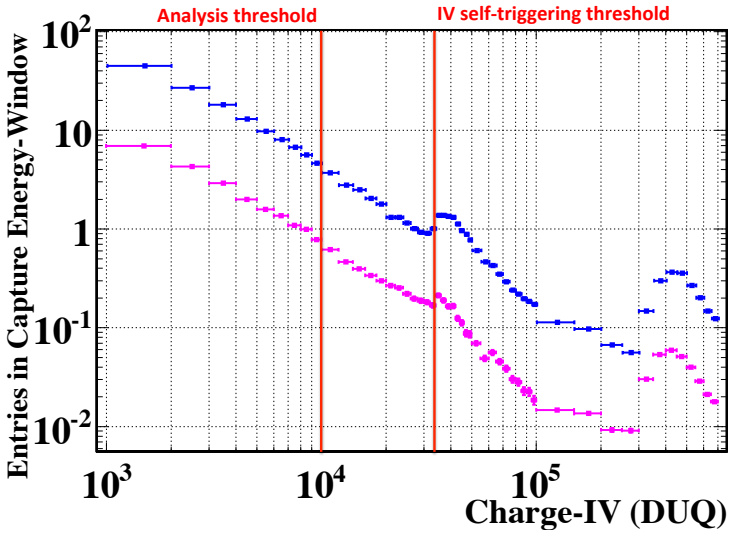

Figure 5.3: Number of neutron capture on hydrogen (blue) and gadolinium (magenta) in the ID as a function of different IV charge ranges. The definition of neutron capture are an energy deposition of $1.5 - 2.5\,\mathrm{MeV}$ for hydrogen or $6.0 - 10.0\,\mathrm{MeV}$ for gadolinium, respectively. The capture events are integrated in a time window of 70 to $150\,\mu\mathrm{s}$ after an identified muon event. Energy depositions in the IV below the self-triggering threshold of 35 kDUQ were only recorded if there was an energy deposition above threshold in the ID which in turn forces the IV to be readout as well. Currently the muon identification threshold is set to be at 10 kDUQ. Plot and explanation taken from [101].

tor the FN background, especially the shape of the FN spectrum in order to extrapolate it to lower energies. Not neutrinos are expected in this energy range, because the energy of reactor neutrinos is not exceeding 15 MeV and any correlated event showing up at higher energies could either a FN, a SM or a βn-emitter produced by a cosmic muon. Thus the IDs muon threshold has to have a higher value as the upper value of this monitoring energy range.

The only muons not being identified with this threshold are the ones stopping after less than 15 cm track length in scintillator, as well as muon decays which release less than 30 MeV energy. As result of this one expects small contamination of SM piling up below the lower end of the chimney. These chimney muons are actually observed and lead to a correlated background. Several studies were performed to identify this background [102–105] and its now well understood and is rejected in off-line data analysis.

5.2.3 Tagging of showering muons

As explained in chapter 4 before, β-n emitters produced by cosmic muons constitute a correlated background to the neutrino search. Because of their relatively long lifetimes a simple veto window of several lifetimes for each muon is not possible, as it would introduce an unacceptable large dead time. To handle this background a partial veto was introduced affecting neutrino candidates. Each neutrino candidate within up to 0.5 s after a high energetic muon is vetoed.

The basis of this rejection is the observation that cosmogenic radioisotopes are mostly produced by high energetic, so called showering muons. In DC Far a showering muon is defined to have an energy E_μ bigger than 600 MeV. This threshold value as well as the veto window of 0.5 s were chosen to maximize the reduction of βn-emitters while making sure that the loss in neutrino statistics is less than 5 %. The use of this high energy muon cut and the determined rates of cosmogenic isotopes will be discussed in chapter 7.

5.3 Veto time window after muon

Muons traversing the detector setup or passing the surrounding rock can create FN through spallation processes. These neutrons can be detected via their captures on hydrogen and gadolinium which happen correlated to the preceding muon in space and time. To reject them, a veto time window after each event identified as muon is applied.

A dedicated study [101, 106] showed, that there is an excess of neutrino candidate events as one gets closer in time to the preceding muon. This analysis was made under the assumption that the number of neutrino candidates scales exponentially with the veto time, whereas the number of correlated background events scales somehow different. Utilizing the standard neutrino cuts presented in chapter 4, the number of neutrino candidate events was counted for different veto time values. Parametrizing the region which is thought to be signal dominated, being more than 2000 μs away from the last muon, one is able to calculate the excess of neutrino candidate events with respect to the exponential expectation in the background dominated region. Figure 5.4 shows the calculated excess of neutrino candidates. It can be seen that there is an increase in the correlated background below 800 μs, which is believed to be caused by FN being created by one of the previous muons. This analysis justifies the chosen value of 1 ms, as in analogy to the predecessor experiment Chooz. In addition this value was chosen because it is long compared to the mean neutron capture times on hydrogen ($\approx 30\,\mu$s) and gadolinium ($\approx 180\,\mu$s).

5.3.1 Definition of run and live time

The run time is defined as the time were the DAQ system has been taking data and is measured by a 1 Hz clock within the trigger. Each time a muon-like event is tagged, a veto time window of 1 ms is opened and therefore a correction to the run time should be applied. This correction defines the live time, which is the run time corrected for the muon veto time window and effectively the time which can be used to search for neutrino candidates

$$\text{live time} = \text{run time} - \text{veto time}. \tag{5.1}$$

In the formula above the veto time is calculated for each run by counting the number of triggers N_μ that fulfill the ID or IV muon threshold, multiplied by the 1 ms veto time window

$$\text{veto time}^{\text{uncorrected}} = N_\mu \times 1\,\text{ms}. \tag{5.2}$$

However a small correction to this scheme has to be applied. Considering the time between two consecutive muons $T_{\mu\mu}$, veto time windows can overlap in the sense that the time difference between them is shorter than 1 ms. For muons coming earlier in time to the previous

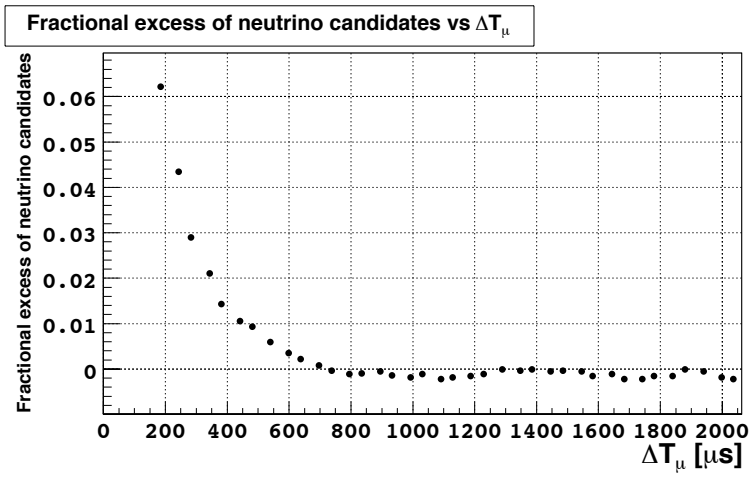

Figure 5.4: Fractional excess of neutrino candidates as a function of the time difference to last identified muon ΔT_μ. The excess, with respect to an expected exponentially scaling law with veto time, below 800 μs can be attributed to muon-correlated background being FN and to some extent to cosmogenic βn-emitters. Plot taken from [106].

muon than 1 ms, the veto time window of the previous muon is truncated, being only the time difference between those two muons $T_{\mu\mu}$. By this the muon veto time can be calculated like

$$\text{veto time}^{\text{corrected}} = N_\mu^{T_{\mu\mu}>1\,\text{ms}} \times 1\,\text{ms} + \sum_{T_{\mu\mu}<1\,\text{ms}} T_{\mu\mu}^i \tag{5.3}$$

for a given muon candidate i. This correction is small for the far detector (2.9 % in the veto time and 1.4 ‰in the live time), but will be significantly bigger for the near detector, because the muon rate is expected to be 10 times higher, leading to a much steeper $T_{\mu\mu}$ distribution, therefore yielding more muon candidates below the 1 ms border and less above. Table 5.1 summarizes the basic information about the data set[1] used in [56] and in this thesis.

	run time [d]	**veto time [d]**	**live time [d]**
simple calculation	251.27	11.44	239.83
with correction	251.27	11.11	240.17

Table 5.1: Comparison of run, veto and live time for the utilized data set. Numbers computed with and without the correction for overlapping muons. Considering overlapping veto time windows, the correction to the veto time is about 2.9 % and about 1.4‰ for the live time.

5.4 Muon rate and spectra in ID and IV

Having proper cut definitions for the ID and the IV, one can think about different logical combinations of these cut values in order to get further insight in the energy and charge

[1]The data set used in this thesis covers a span of 322 days from 2011/04/13 till 2012/03/11 after quality cuts.

distributions of muons. This has two sides, first for the neutrino analysis one wants to identify and reject muons and muon correlated events with very high efficiency. Second, having studies with cosmic muons in mind, pure muons samples are needed. In the following the different logical combinations, their associated energy, charge spectra and their rates in the considered data taking period will be discussed.

The muon identification used in the neutrino analysis is a logical *or* between the ID and the IV cut value (ID$\vee$IV). This combination will identify muons traveling through the whole detector setup or through the IV only. As pointed out in the last section one expects a small contribution of FN and SM depositing less than 30 MeV in the ID and less than 10 kDUQ in the IV, piling up directly below the lower end of the chimney. In addition, some high energetic light noise is expected to leak into the selected muon sample in the energy range below 100 MeV.

The logical *and* of the ID and the IV cut value (ID$\wedge$IV) should select muons traveling through the whole detector system yielding a purer muon sample, as only muons are expected to deposit the high amounts of energy and charge deposited in ID and IV as required by the thresholds. Apart from this combination, events only detected in one of the detectors, either ID and not IV or vice versa, could be of interest. A selection on muon candidate event only identified in the ID (ID$\wedge(\neg$IV)) should in principle select SM below the chimney, FN and high energetic light noise. Actually this is the first step for an analysis of the FN/SM background as discussed in the last chapter leading to a sub-threshold analysis for the IV. Opposite to this a selection of muon candidate events only identified by the IV (IV$\wedge(\neg$ID)) should select muons passing through the IV, but not crossing the ID or only clipping the ID's corners. Thus the relevant logical possibilities are:

- ID: $E_{vis} > 30\,\mathrm{MeV}$
- IV: $Q_{IV} > 10\,\mathrm{kDUQ}$
- ID$\wedge$IV: $E_{vis} > 30\,\mathrm{MeV}$ and $Q_{IV} > 10\,\mathrm{kDUQ}$
- ID$\vee$IV: $E_{vis} > 30\,\mathrm{MeV}$ or $Q_{IV} > 10\,\mathrm{kDUQ}$
- ID$\wedge(\neg$IV): $E_{vis} > 30\,\mathrm{MeV}$ and $Q_{IV} < 10\,\mathrm{kDUQ}$
- IV$\wedge(\neg$ID): $E_{vis} < 30\,\mathrm{MeV}$ and $Q_{IV} > 10\,\mathrm{kDUQ}$

5.4.1 Muon energy and charge spectra

Figures 5.5 and 5.7 show the energy and charge spectra of all events satisfying the different logical combinations of the muon thresholds for ID or IV described before. In addition figure 5.6 shows two-dimensional plots in the plane of energy deposition in the ID and collected charge in the IV.

Starting with the energy spectrum of events identified as muon in the ID, three features are visible in the spectra. First an exponentially decreasing shape at low energies up to 100 MeV. Second an enhancement at intermediate energies $400 < E_\mu < 500\,\mathrm{MeV}$ and third, a cut off

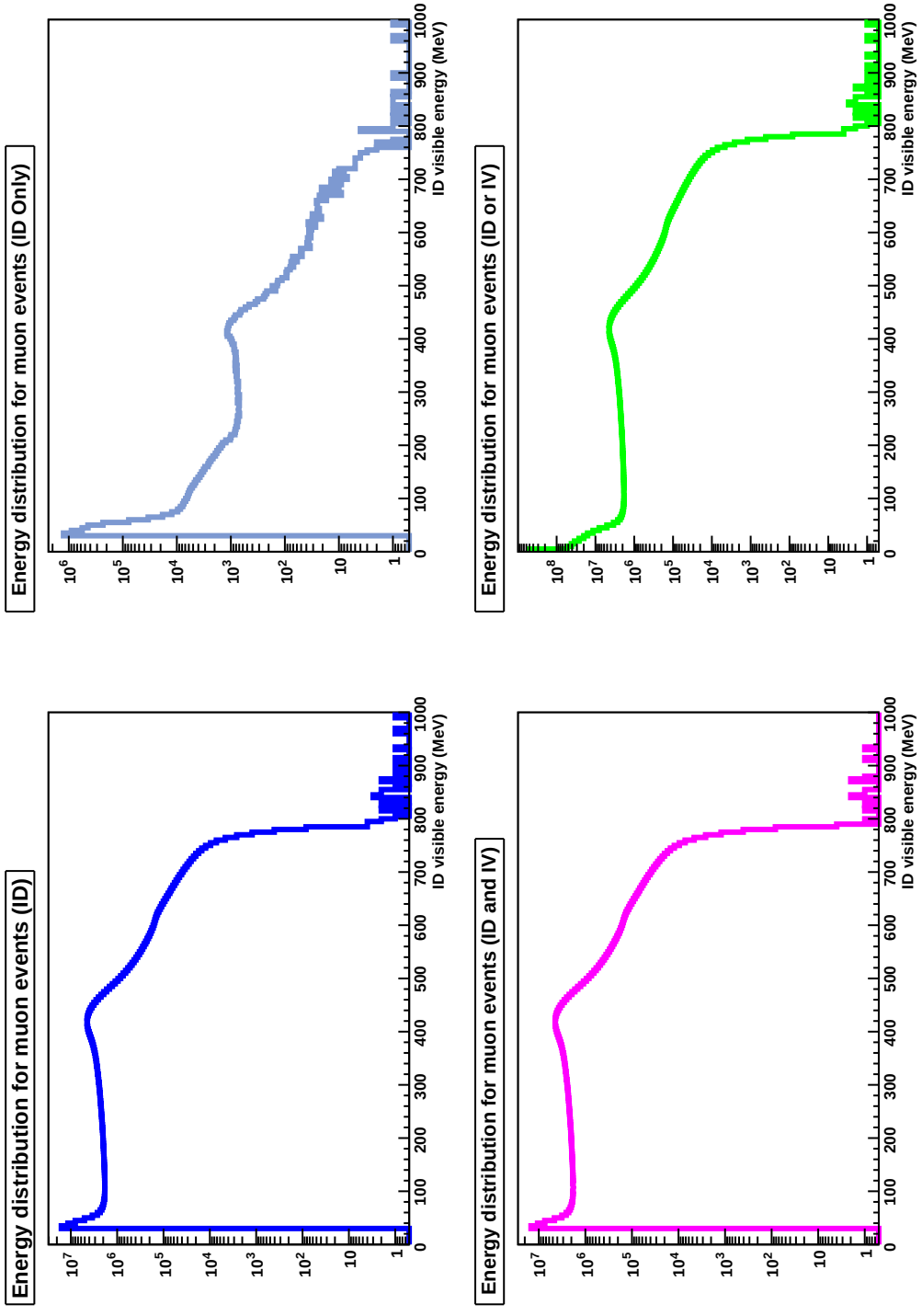

Figure 5.5: Muon energy spectra in ID. In clockwise direction, first for muon events in the ID in blue, muon events only identified in the ID, ID∧(¬IV) in light blue. Than muon events identified in both detectors, ID∧IV, in magenta or muon events identified in one of the detectors, ID∨IV, in green.

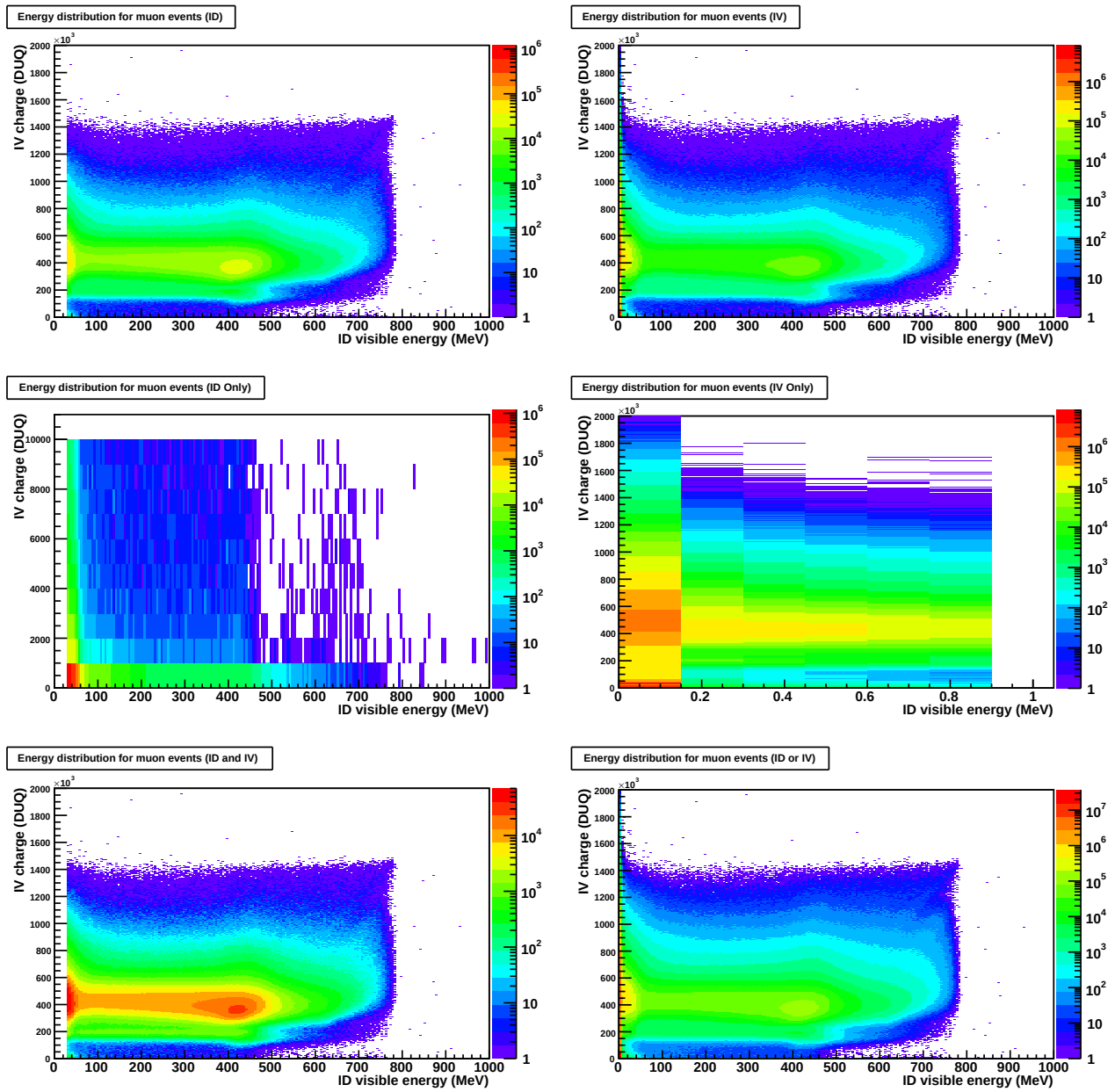

Figure 5.6: Muon energy spectra in ID versus muon charge response in IV. In clockwise direction first for muon events identified in the ID, than in the IV. Followed by events only identified in one of the detectors, first only in the ID, than only identified in the IV. At last the logical *and* combination of the muon thresholds for the ID and the IV is shown in addition to the logical *or*.

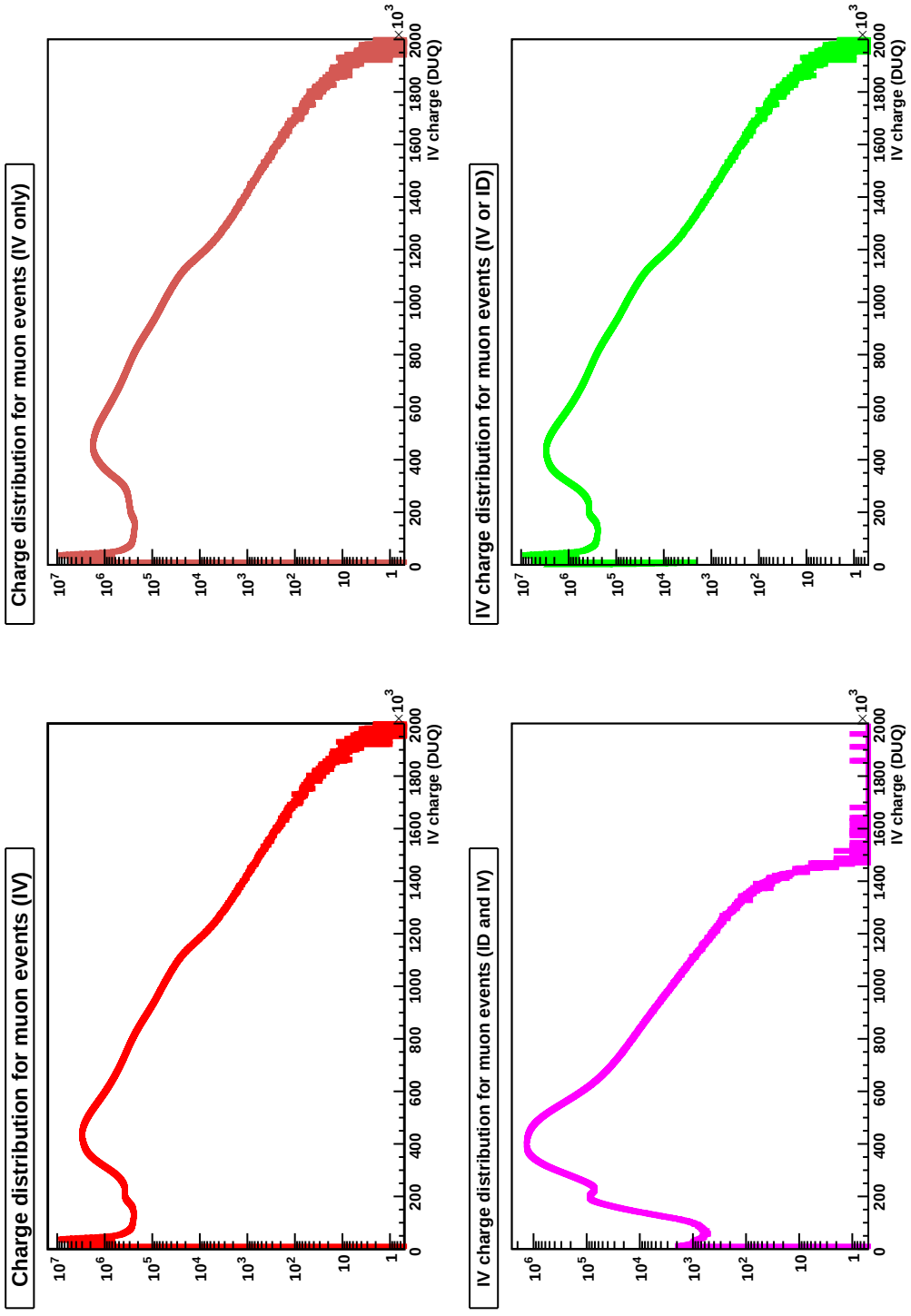

Figure 5.7: Muon charge spectra in IV. In clockwise direction, first for muon events in the IV in red, muon events only identified in the IV, IV∧(¬ID) in light red. Than muon events identified in both detectors, ID∧IV, in magenta or muon events identified in one of the detectors, ID∨IV, in green.

at very high energies around 800 MeV. These structures can be understood using the RecoMuonHam track reconstruction algorithm by combining muon track length with spectral information [85]. The exponentially decreasing part of the energy spectrum has muon tracks of up to 7 m and a relatively slow increase of deposited energy with increasing track length. This corresponds to an energy loss being smaller than the one expected through the scintillation process in LS, thus these are muons crossing only the buffer volume creating light via the Cherenkov effect. Within the buffer muons can travel up 7 m straight trough the volume, creating less detectable light compared to the same track length in LS. The enhancement in the middle of the energy spectrum corresponds to track lengths around $5 - 6$ m crossing NT and GC. Thus this is the energy distribution of minimum ionizing muons in these volumes, which is supported by the observed linear dependence between deposited energy and muon track length. The higher energy depositions are due to high energetic muons in the NT and GC volumes, which lose energy mainly through radiative processes, less through ionization. Such muons are called showering muons as they produce showers of electrons/positrons and gammas in the detector, creating excess light compared to muons loosing energy via ionization.

In addition two independent MC simulations yield the same conclusions for the origin of the observed spectral features and support this understanding of the spectra. First in [107] a simple MC was performed based on a $\cos^2\theta$ angular distribution of muons and assuming a constant muon energy loss not accounting for effects of the DAQ and readout electronics. This MC reproduces the shape at low and intermediate energies, but as the energy loss is assumed constant it fails to explain the high energy part believed to be due to showering muons. The second simulation [108] uses a detailed MUSIC simulation of the DC far site. A simulation of the readout electronics was performed to make this MC comparable to the measurement. The spectral shape of the ID is reproduced except for the cut off at high muon energies. This is because the saturation of the PMTs is not implemented in the code.

Focusing now on the IV spectra, they show a lot more features, three peaks for charges below 50 kDUQ. These peaks are not present in both MC simulations and actually correspond to dedicated pre-scaled triggers[2] of the ID and IV, thus being induced by the DAQ and readout electronics. Actually requesting a high energy deposition in the ID and the IV these structures vanish. At higher charges values, an enhancement is visible at around 200 kDUQ corresponding to IV track lengths of around 78 cm. A second structure at 435 kDUQ is visible corresponding to IV track lengths of around 156 cm. These structures correspond either to muons crossing the IV volume once entering the ID and stopping therein, or crossing the IV volume twice. The very high charges correspond to muons traveling only through the IV. This is supported by the spectrum of the logical combination of ID and IV (ID$\wedge$IV), where the high charges are not populated in the spectrum. It should be noted that a tracking algorithm for the IV is currently under development in the DC Collaboration [85] to have an energy track length correlation for the IV as well. The conclusions for the IV presented here are thus based on MC information only.

The plots in the plane of energy in the ID versus charge in the IV shown in figure 5.6

[2]Pre-scaled triggers are recorded below the actual threshold of the detector, but only 1 event out of a 1000. This gives some information about the spectra and rates below the applied threshold.

support these conclusions. The features in the ID spectrum are correlated to charges in the IV of either 200 kDUQ or 435 kDUQ, corresponding to the expected energy loss for muons crossing the IV once or twice. Requesting the ID to trigger as well, the very high charges regime above 1.4 MDUQ is not populated, whereas it is in the case of $IV \wedge (\neg\text{ID})$ with small energy deposition in the ID. This supports the conclusion that these high charge depositions in the IV correspond to muons crossing the full length of the IV. Considering the opposite condition, $ID \wedge (\neg\text{IV})$, the full ID energy range is populated by events, whereas there is only a small charge deposition in the IV indicating SM entering the ID through the chimney or FN. However, the region below 100 MeV is correlated with charge deposition of up to 10 kDUQ and is contributing a large fraction of the events identified only by the ID. This can be explained by the accidental coincidence of high energy light noise in the ID and natural radioactivity events in the IV.

5.4.2 Muon rates

This section will focus on the determination of the muon rates for the different logical muon threshold combinations. The muon rates are quantities interesting for many studies, like the search for an expected seasonal modulation in the muon signal[3], to obtain the efficiency of the IV to identify or reject muons. Also the evolution of the muons rates with time can be used to monitor the detector performance and stability.

Different methods can be used to extract the muon rates from data. At first a simple method is presented which counts the number of events above the given threshold and dividing this number by the duration of the run. As second method the distribution of time differences $T_{\mu\mu}$ between consecutive muons can be fitted with an exponential function to obtain the rates. The third method uses the statistical properties of the expected exponential distribution of the muon time differences. In the following the simple counting method is used to determine muon rates, as this method provides reliable and precise results. The other two methods, taking into account the poissonian distribution of $T_{\mu\mu}$ are used as a cross-check and as estimators to determine the purity of the selected muon samples.

- **Counting method:** One simply needs to count the events $N_\mu(E_{vis}, Q_{IV})$ above the given threshold in the ID, E_{vis}, and the IV, Q_{IV}, and to calculate the duration of the data taking t_{run}:

$$R_\mu = \frac{N_\mu}{t_{run}}, \qquad \Delta R_\mu = \sqrt{\left(\frac{\sqrt{N_\mu}}{t_{run}}\right)^2 + \left(\frac{N_\mu}{t_{run}^2}\Delta t_{run}\right)^2} \tag{5.4}$$

  For DC, data are normally taken in runs of around one hour duration. This duration is calculated using the fixed rate trigger, a special trigger that is emitted from the Trigger Master Board every 62,499,841 clock ticks corresponding to 0.999997456 s for a 16 ns clock period. A negligible systematic error is introduced using 1.000 ms for the fixed rate trigger. Using this to extract muon rates is easy and fast to do with small errors, but a crucial point is missing. This method has no ability to check whether the identified events are muons or if there is any contamination from non-muon events.

[3]Seasonal modulation in muon rates is well known since the 1960s and will be discussed in detail in chapter 6.

- **Fitting method:** The muon rates are determined utilizing the distribution of time differences $T_{\mu\mu}$ between two consecutive identified muon candidates. As the production of muons through the decay of kaons and pions is a possonian process, the time between two consecutive muons is exponentially distributed. Figure 5.8 shows the distribution of time differences and an exponential fit for each of the different logic muon tagging combinations. The muon rate can be extracted from the fit as the inverse value of the slope:

$$R_\mu = \frac{1}{\text{slope}}, \qquad \Delta R_\mu = \frac{1}{(\text{slope})^2}\Delta\text{slope} \tag{5.5}$$

  Usually fitting is more time consuming and error prone than simple event counting, but it offers the possibility to check for any non-exponential deviation of the distribution indicating a contamination by events not following the exponential behavior. This could be fast neutrons or additional triggers caused by one single muon, because the baseline was not restored and the sum signal of all PMTs was above threshold. In addition using the time difference $T_{\mu\mu}$ one can take consecutive overlapping muons in the veto time window into account according to eq. 5.3 presented before.

- **Statistical method:** Using the characteristics of the exponential distribution, which is defined as $f(X,\lambda) = \lambda e^{-\lambda X}$ for X values bigger than zero, the muon rates can be extracted. The mean of the exponential distribution is defined as $E[X] = \lambda^{-1}$ and the variance as $V[X] = \lambda^{-2}$. The standard deviation can be computed from the variance being $\sqrt{V[X]} = \lambda^{-1}$. Hence, if $\sqrt{V[X]} = E[X]$ for the given measured distribution one has a perfect exponential behavior. The rate R_μ is given by the parameter λ, which is $1/T_{\mu\mu}$ in this case.

$$R_\mu = \frac{1}{\mathrm{T}_{\mu\mu}}, \qquad \Delta R_\mu = \frac{1}{(\mathrm{T}_{\mu\mu})^2}\Delta\mathrm{T}_{\mu\mu} \tag{5.6}$$

  The mean and the standard deviation are equal within less than 1% for the whole data sample, indicating a nearly exponential distribution of $T_{\mu\mu}$. This method offers the possibility to check the muon sample purity. It can give an estimation of how much the muon sample is contaminated by events different from muons.

Figure 5.8 shows the distribution of time differences $T_{\mu\mu}$ between consecutive muons for the six considered logical threshold combinations. Except for the ID-only (ID$\wedge(\neg$IV)) combination the time distributions follow the expected exponentially behavior. This behavior is a visual cross-check that the utilized threshold values of $E_{vis} > 30\,\text{MeV}$ for the ID and $Q_{IV} > 10\,\text{kDUQ}$ for the IV really select muons in the corresponding detector volumes.

In order to determine the muon rates all three methods have been utilized. As said before, the simple counting method is expected to give the most accurate results and the other two methods are used as a cross-check. To calculate the overall rates for the whole data set, the

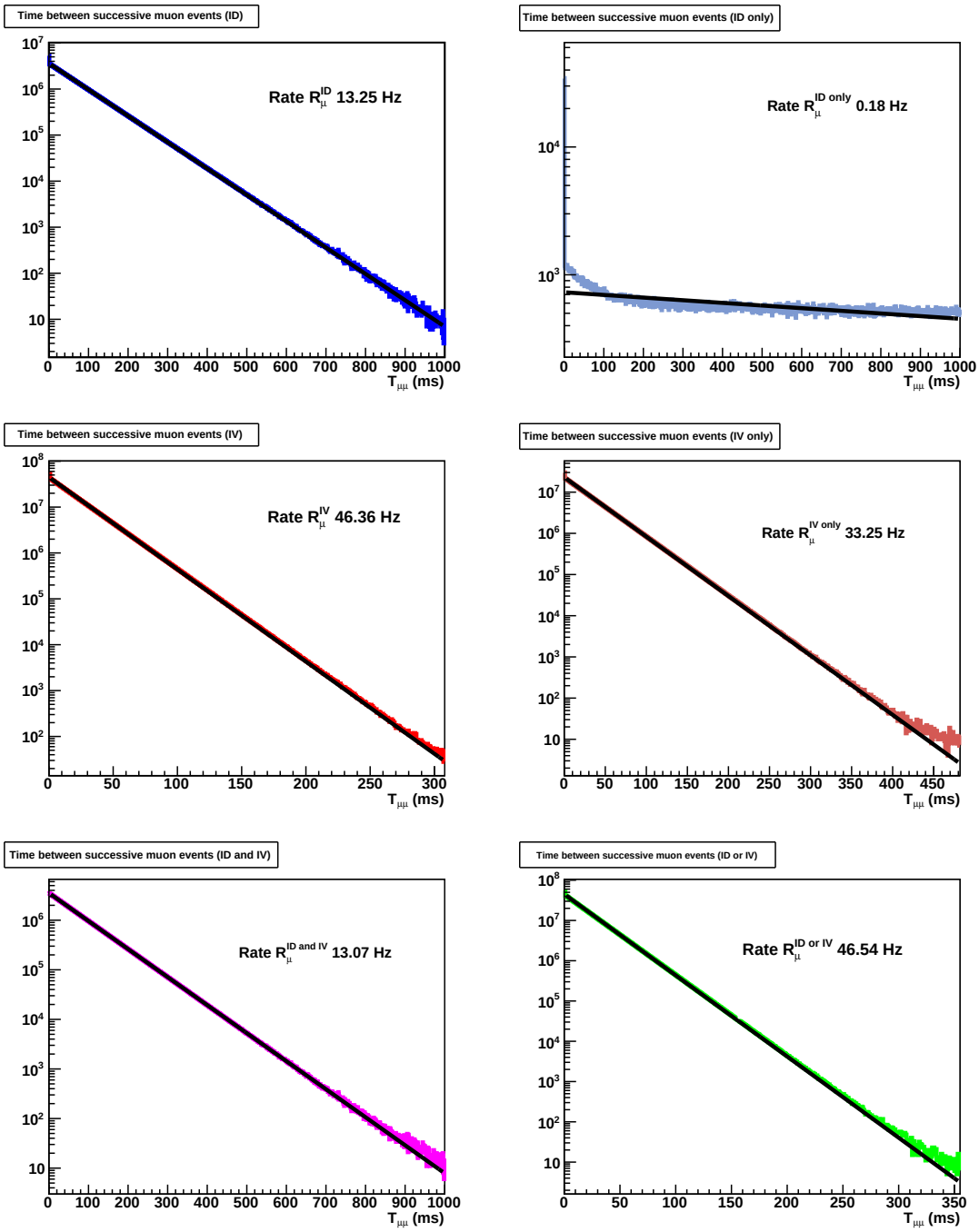

Figure 5.8: Distribution of time differences between consecutive muons $T_{\mu\mu}$. From upper left to bottom right: ID, ID∧(¬IV), IV, IV∧(¬ID), ID∧IV, ID∨IV tagged events. As the ordinate is plotted logarithmically, one expects a linear slope for the exponential time distribution. This is true for all logical muon threshold combinations under investigation except for the ID only threshold (ID∧(¬IV)). Here most of the events accumulate around 1 ms right after a muon. The rest of the timing difference distribution is approximately flat, indicating for most of these events no strong correlation to a previous muon tagged event.

weighted mean rates (s^{-1})	**ID**	**IV**	**ID∧IV**	**ID∨IV**	**ID∧(¬IV)**	**IV∧(¬ID)**
method 1	12.924	45.405	12.750	45.578	0.166	32.612
method 2	13.193	46.340	13.015	46.513	0.807	33.287
method 3	13.194	46.350	13.017	46.527	0.174	33.292
difference [%]	**ID**	**IV**	**ID∧IV**	**ID∨IV**	**ID∧(¬IV)**	**IV∧(¬ID)**
method 1 : method 2	2.02	2.01	2.03	2.00	89.39	2.02
method 1 : method 3	2.03	2.03	2.03	2.03	2.19	2.03
method 2 : method 3	0.01	0.02	0.01	0.03	328.91	0.02

Table 5.2: Comparison of three different methods to extract the muon rate. In method 1 the number of events fulfilling the tag was counted and this number was than divided by the run-time. In method 2 the $T_{\mu\mu}$ distribution of time differences between consecutive muons was fitted with an exponential function. In method 3 the characteristics of the expected exponential distribution of the time differences $T_{\mu\mu}$ was utilized. Methods 2 and 3 agree well within $(1-2)\,‰$, whereas the difference to method 1 is about $2\,\%$ in both cases. This difference is expected to originate from non muon events contaminating the selected samples.

run-wise muon rates values were averaged. A weighted average was used for each run k and for each method i. The reason for this weighting is to reduce the influence of short runs with low statistics. The weight ω_k is given by the statistical error $\Delta R_{\mu,k}$ of the rate determination for each run k. Thus the average muon rate for method i can be calculated according to:

$$\langle R_\mu \rangle^i = \frac{\sum_{k=1}^{n} R^i_{\mu,k}/\omega_k}{\sum_{k=1}^{n} 1/\omega_k}, \tag{5.7}$$

Differences in the utilized methods can be hints on the sample purity in terms of muons. This is possible because the methods 2 and 3 implicitly assume the selected events to follow the exponential distribution expected from muons. This is not the case for method 1 which simply counts the number of events above threshold. Table 5.2 lists the mean muon rate values for the different logical muon cut combinations and compares these values for all three utilized methods.

From the tabulated values, it can be seen that methods 2 and 3, taking into account the expected exponential distribution of $T_{\mu\mu}$, agree very well within $(1-2)\,‰$. The differences to method 1 is much bigger and has a value of about $2\,\%$. The only exception showing a disagreement of all three methods is the rate for muon candidate events only identified in the ID (ID∧(¬IV)). As stressed before, methods 2 and 3 intrinsically use the assumption that the candidate events are muons. As the deviation to method 1 is big, it can be assumed that a large fraction of the muon candidate events only identified in the ID, but not in the IV are actually not muons. Another observation is that methods 2 and 3 yield higher rate values of about $2\,\%$ than method 1. As method 1 simple counts the number of events above threshold to obtain the muon rate it defines an upper limit- there cannot be more physical events than the number of counted triggers above threshold. The cause of the difference is the contamination of non-muon events in the selected samples. This creates a deviation from the exponential $T_{\mu\mu}$ distribution and drags the fit to higher values for method 2 or creates a deviation between the mean and the variance of the distribution for method 3.

weighted mean rates (s^{-1})	**ID**	**IV**	**ID∧IV**	**ID∨IV**	**ID¬IV**	**IV¬ID**
lower threshold	12.977	45.416	12.798	45.594	0.170	32.649
nominal threshold	12.924	45.405	12.750	45.578	0.166	32.612
higher threshold	12.871	45.393	12.701	45.562	0.162	32.575
variation [‰]	**ID**	**IV**	**ID∧IV**	**ID∨IV**	**ID¬IV**	**IV¬ID**
lower threshold	+4.1	+0.3	+3.9	+0.3	+22.8	+0.4
higher threshold	-4.1	-0.3	-3.7	-0.3	-22.3	-1.1

Table 5.3: This table shows the influence of a 1 % variation of the muon identification thresholds. For the lower threshold ($E_{vis} > 29.7\,\text{MeV}$, $Q_{IV} > 9.9\text{k}\,\text{DUQ}$) and the higher threshold ($E_{vis} > 30.3\,\text{MeV}$ and $Q_{IV} > 10.1\,\text{kDUQ}$) the variations have the same order of magnitude and being sometimes numerically the same. The reason for this is the relative flatness of the spectral shapes around the normal muon tag values, so that a linear relation around this points is approximately valid.

5.4.3 Influence of a threshold variation

The stability of the energy scale can influence the determination of the muon rates and therefore has to be considered. Changes in energy scale can arise if the light yield of the LS, the gain of the FEE modules or the PMT gain or high voltage changes with time. A drift in detector response was measured and found to be a monotonic 2.2 % increase per year at an energy of 8 MeV. This was measured by monitoring the stability of the mean of the energy distribution originating from neutron capture on gadolinium. The definition of the detected visible energy E_{vis} used in DC will be explained in more detail later. It takes care of the correction of this monotonic increase. It is known[4] that the E_{vis} energy and Q_{IV} charge scale are stable within 1 % in the muon energy range. As the energy varies events can be shifted above or below the actual threshold values.

To determine the effect of these changes on the muon rate, the data set was analyzed with two slightly different muon thresholds, being off from the nominal values by 1 %. The results of both analysis, being either obtained from the lower threshold ($E_{vis} > 29.3\,\text{MeV}$ or $Q_{IV} > 9.9\,\text{kDUQ}$) or the higher threshold ($E_{vis} > 30.3\,\text{MeV}$ or $Q_{IV} > 10.1\,\text{kDUQ}$) can be found in table 5.3.

All logical threshold combinations show a variation below 1 %, except for $ID \wedge (\neg\text{IV})$, the muon candidates only identified in the ID. For this sample the difference is about 2 % for a variation of 1 % in the muon threshold values. This is caused by events populating the energy region around 30 MeV in the ID, not being presented if one requires a charge deposition in the IV. Most likely the events originate from high energetic light noise.

Utilizing the energy and charge spectra discussed in the last section, cumulative energy and charge distributions for the different logical combinations of the muon thresholds can be constructed. The cumulative distributions can be found in figures 5.9 and 5.10. They visualize the effect of a change in muon threshold in E_{vis} or Q_{IV} on the muon rate R_μ. Essentially these distributions resemble the spectra, as they are constructed out of the integral of the spectra. These distributions from data are consistent with those obtained from the simple

[4]For details see chapter 8

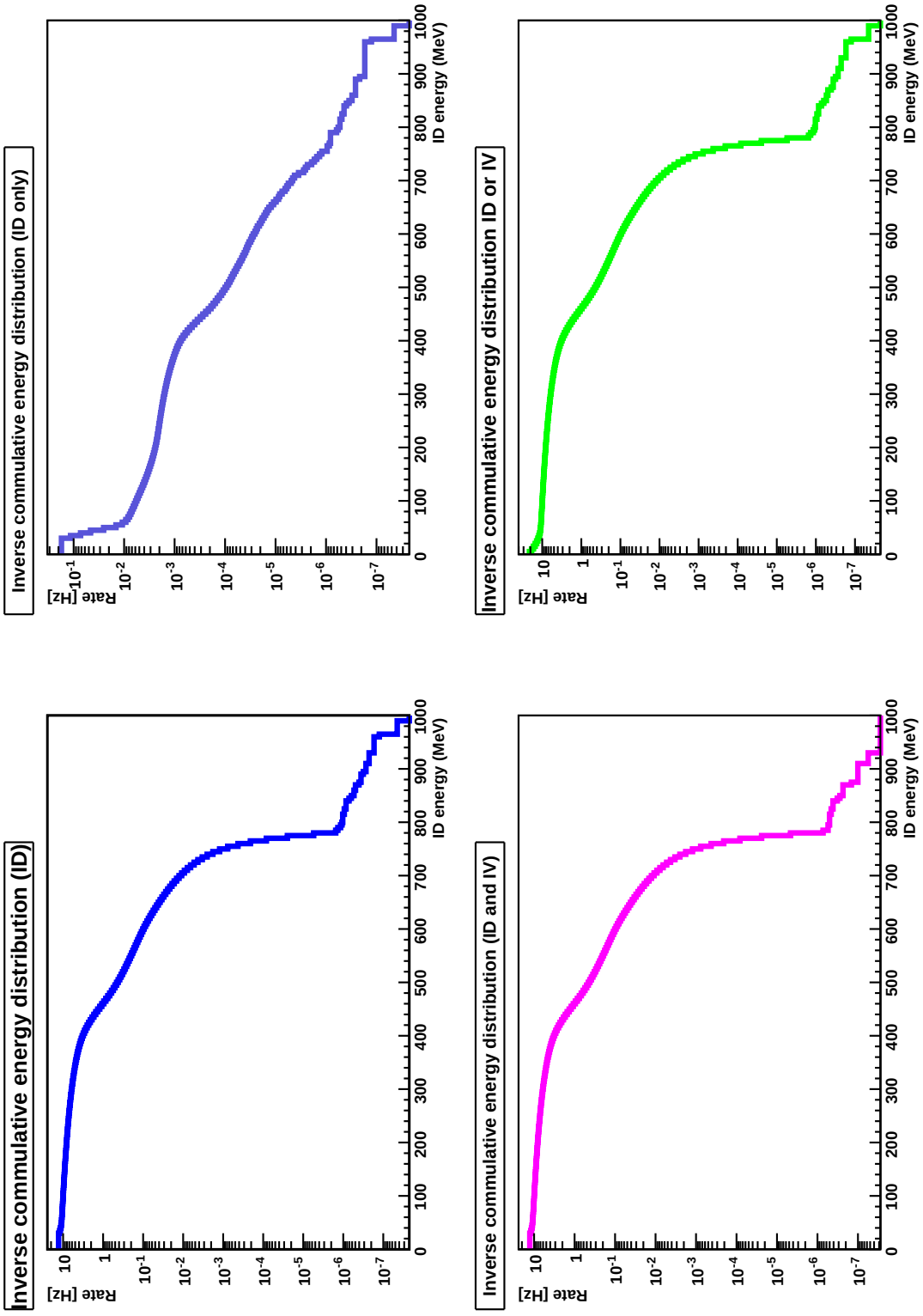

Figure 5.9: Inverse cumulative muon energy spectra in ID. From left to the right, ID, ID and IV, ID or IV and ID only.

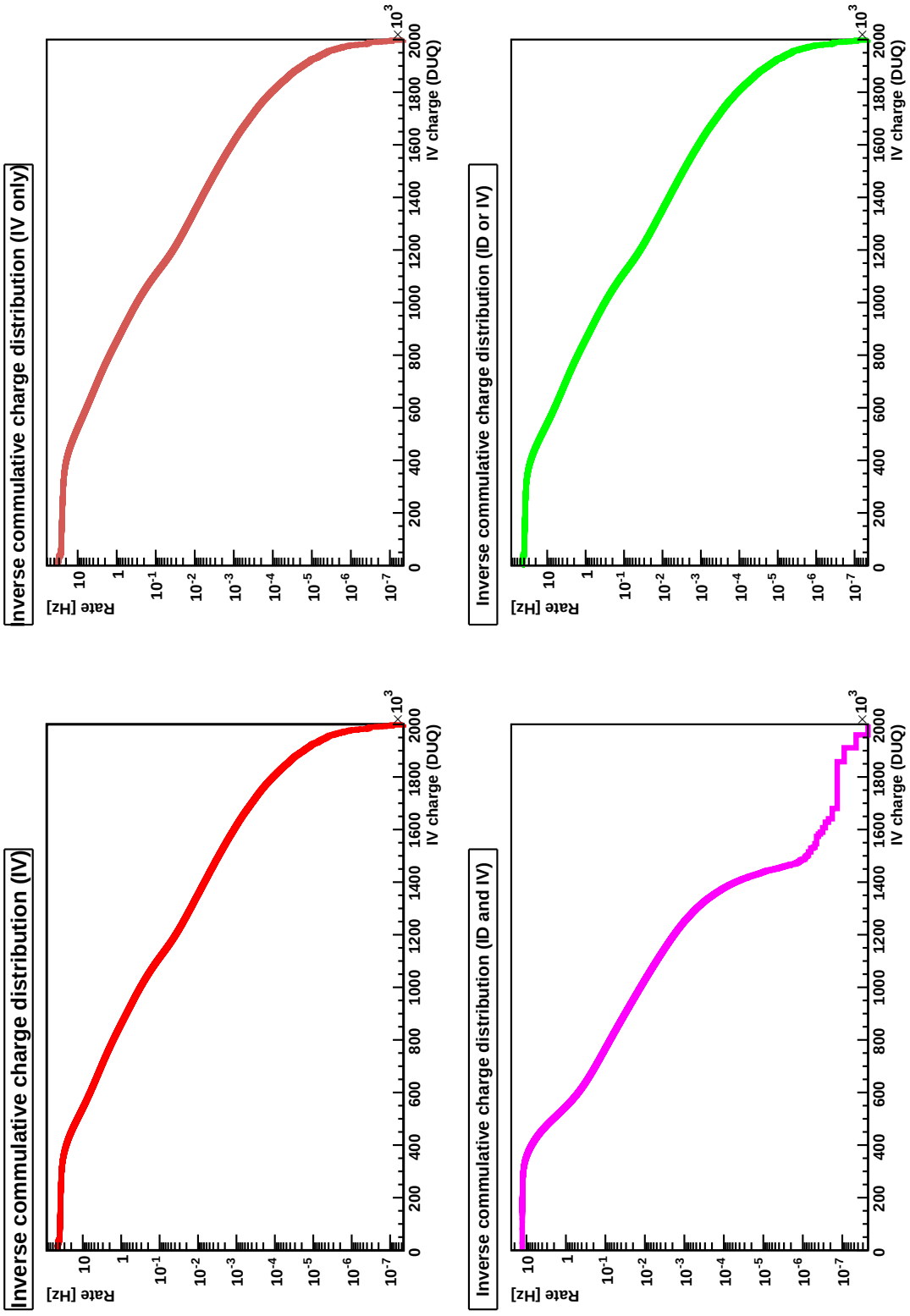

Figure 5.10: Inverse cumulative muon charge spectra in IV. From left to the right, IV, ID and IV, ID or IV and IV only.

MC presented in [107]. From these distributions and the values presented in table 5.3 it follows that a variation of 1 % of the nominal muon threshold values changes the muon rate in the order of a few permil, and this fractional changes will be used in the following as a systematic error in the muon rate determination.

5.5 Determination of the IV Muon Rejection Efficiency

Extensive Monte Carlo studies were performed in order to design the IV to identify and reject muons and correlated events produced by cosmic muons with very high efficiency [51,83,109]. Having measured the muon rates defined by the different logical combinations of the muon thresholds, these rates can be used to determine the muon rejection efficiency of the IV from data. This determination will depend on the chosen threshold values of E_{vis} and Q_{IV}. The efficiency can be obtained from the rate $R_\mu(ID \wedge (\neg IV))$, thus the number of muon like events identified by the ID, but not by the IV and the rate of muon events in ID and IV $R_\mu(ID \wedge IV)$. With this rates a definition of the muon rejection efficiency of the IV can be made:

$$\mu_R^{IV} = \frac{R_\mu(ID \wedge (\neg IV))}{R_\mu(ID \wedge IV) + R_\mu(ID \wedge (\neg IV))}. \tag{5.8}$$

This definition is chosen in analogy to [109], where the muon rejection efficiency of the IV was determined from a dedicated Monte Carlo simulation and was found to be 99.978 %. Using the rate values obtained from the simple counting method in table 5.2, this leads to a muon rejection efficiency of 98.691 %, being significantly lower than the Monte Carlo prediction. This deviation can be examined studying the time series of daily averaged muon rates, which enables the calculation of muon rejection efficiency μ_R^{IV} per day. This time series of $\mu_R^{IV}(t)$ is visualized in figure 5.11 below.

The mean of this time series is 98.711 % compatible with the value of around 98.691 % that was calculated from the tabulated rates in 5.2 for method 1. The obvious jumping behavior of μ_R^{IV} is directly connected to the rate of muon candidates detected only in the ID, $R_\mu(ID\neg IV)$, as the time periods where the efficiency decreases correspond to time periods were the rate of these events increases. Such a hopping behavior in the rate is not expected to originate from muons and does not show up in the rates for the other logical threshold combinations. Thus these events must have a non-muon origin, not even being correlated to a muon as indicated in the section before. As this behavior only shows up in the ID, the origin of this is thought to be high energetic light noise (**HELN**) faking a muon event, as first observed in [110] and mentioned in the sections before.

This light noise assumption is further supported by calculating μ_R^{IV} as a function of visible energy E_{vis} in the ID, which shows how different energy ranges contribute to the efficiency. Figure 5.12 shows $(1 - \mu_R^{IV})$, being the inefficiency in muon detection. Thus values different from zero indicate a deviation from the full efficiency. This plot is obtained from the inverse cumulative distributions of the ID∧IV and ID∧(¬IV) threshold combinations by calculating the rate ratio per energy bin k in analogy to eq. 5.8. It can be seen that the energy range

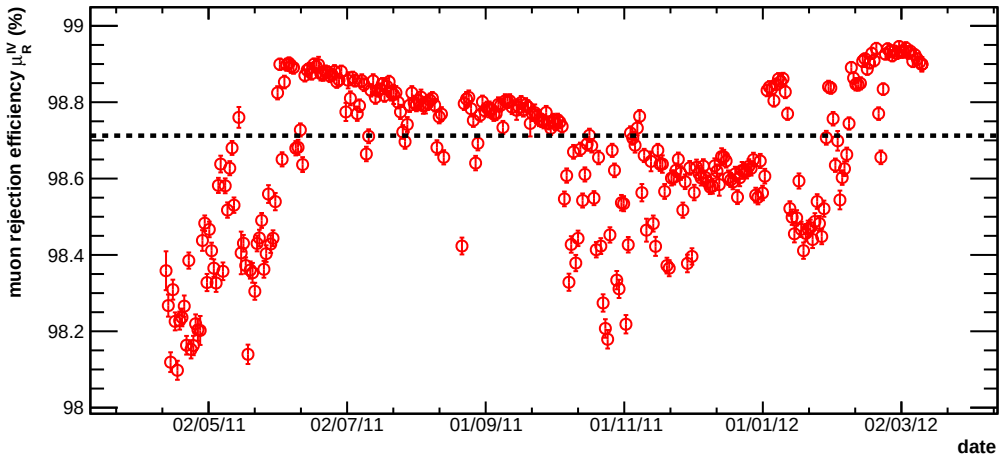

Figure 5.11: Time series of muon rejection efficiency $\mu_R^{IV}(t)$ of the IV with the utilized muon threshold values of $E_{vis} = 30\,\text{MeV}$ and $Q_{IV} = 10\,\text{kDUQ}$. A jumping behavior of the IV's efficiency for a couple of days can be observed. Periods of decreased μ_R^{IV} correspond to time periods of increased rate $R_\mu(ID \wedge (\neg IV))$ of muon like events detected only in the ID. The average value of 98.711 % is indicated by the dotted line.

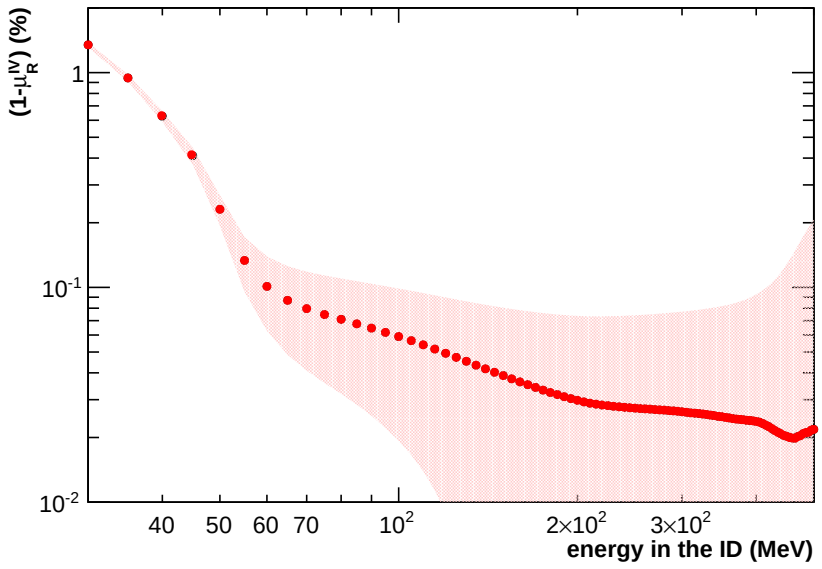

Figure 5.12: Inefficiency $(1 - \mu_R^{IV})$ of the IV to identify and reject muons as a function of visible energy E_{vis} in the ID. The shaded region indicates the statistical error of the inefficiency. The inefficiency of the IV is mainly dominated by events having an energy below 100 MeV.

$30 - 100\,\mathrm{MeV}$ contributes the most to the inefficiency in μ_R^{IV} being on the level of some permil, whereas the inefficiency decreases (efficiency increases) for higher energy supporting the light noise origin assumption. The decrease for higher energies is slow, practically being constant after 200 MeV. At very high energies the inefficiency increases again, but this is due to very poor statistics in the high energy regime, consisting of a dozen of events. The shaded region indicates the statistical error in the determination of this inefficiency.

The assumption, that these events do only originate from light noise in the ID can be checked using OV hit information. Changing the definition of the muon rejection efficiency μ_R^{IV} in eq. 5.8 to incorporate the OV leads to

$$\mu_R^{IV'} = \frac{R_\mu((ID \wedge IV) \wedge OV)}{R_\mu((ID \wedge IV) \wedge OV) + R_\mu((ID \wedge OV)\neg IV)}. \tag{5.9}$$

This definition should neglect all non muon events in the ID, as they should not have a hit in the OV[5] similar to the one in [111]. The sample selected should virtually have no contamination from non-muons events, as only muons deposit enough energy in all three sub detectors. A very high efficiency is expected, as the only possibility for a muon to create a hit in the OV and enter the ID unseen by the IV is through the chimney. Since only a very small fraction of all muons fulfill these conditions a very small inefficiency in the muon identification is expected.

Figure 5.13 shows the inefficiency $(1 - \mu_R^{IV'})$ as a function of E_{vis} in the ID for all events depositing enough energy in the IV and having created a hit in the OV. This inefficiency is very small compared to the one obtained without the OV, being in the range of $(0.1 - 0.4) \cdot 10^{-4}\,\%$. This inefficiency practically stays constant over a wide energy range in the ID, decreasing slightly for high muon energies. This is expected, as the primary source of inefficiency should be SM entering the ID through the chimney and their subsequent decay. As muons deposit more energy in the ID, their corresponding track length in the ID vessel should also increase, at one point resulting in inclined tracks going through the IV as well. Thus with increasing muon energy one expects an increase in muon rejection efficiency, or in this case a decrease in the inefficiency.

Indeed the average value obtained with this definition of the muon rejection efficiency is 99.977 % being even better than the MC prediction. The time series of $\mu_R^{IV'}(t)$ averaged per day is shown in figure 5.14. It is more stable than the time series utilizing the definition without the OV and has a deviation on the permil-level. Some days show an efficiency around 1, this is the case when the rate $R_\mu((ID\neg IV) \wedge OV)$ is nearly zero. As the data taking with the OV started in July 2011, the first months of data set are not covered by this definition of the muon rejection efficiency in this plot.

[5] Accidental coincidences can be calculated according to $R_{acc} = R^{ID} R^{IV} R^{OV} \times \tau^2 \approx 13\,\mathrm{Hz} \cdot 45\,\mathrm{Hz} \cdot 2.5\,k\mathrm{Hz} \times 256^2\,\mathrm{ns}^2$ being less than 1 per day in a coincidence time window τ of 256 ns and can thus be neglected.

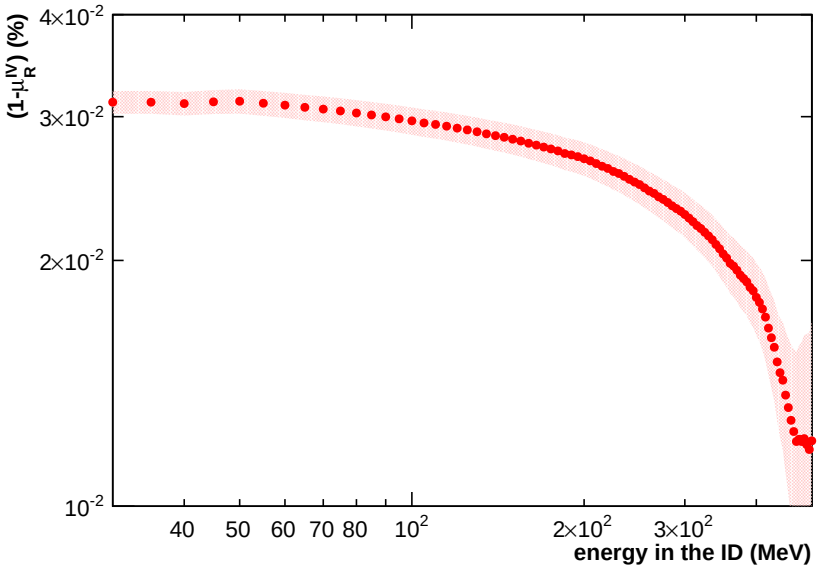

Figure 5.13: Inefficiency $(1 - \mu_R^{IV})$ of the IV to identify muons and reject muons as a function of visible energy E_{vis} in the ID. The shaded region indicates the statistical uncertainty of the inefficiency. In contrast to the definition without the OV, the inefficiency is much smaller (10^{-4} % compared to 10^{-1} %) and a big contribution of the energy bins below 100 MeV is not obvious any more.

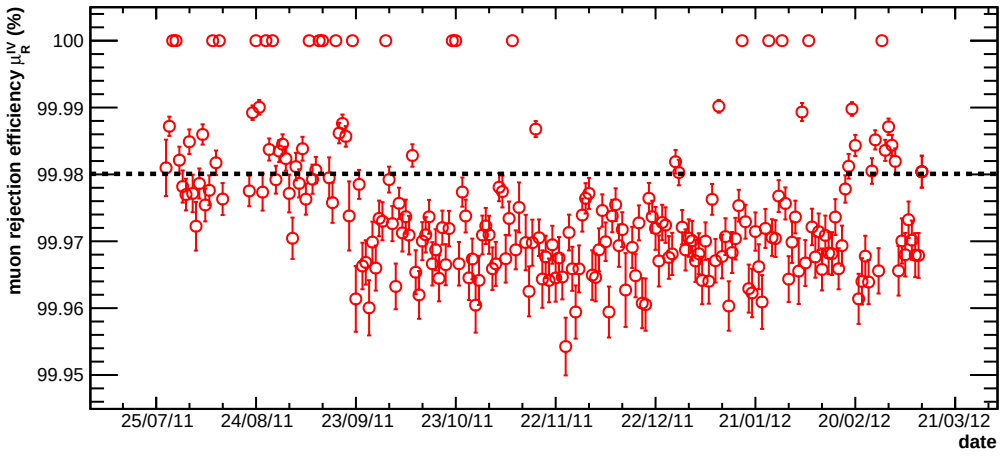

Figure 5.14: Time series of muon rejection efficiency of the IV with the utilized muon tag values. As the data taking with the OV started in July 2011, the first months of the used data set are not covered. The average value of 99.977 % is indicated by the dotted line.

5.6 Summary

In this chapter the cut conditions to identify and reject muons utilized in the neutrino analysis were introduced and the chosen values of $E_{vis} > 30\,\mathrm{MeV}$ for the ID and $Q_{IV} > 10\,\mathrm{kDUQ}$ for the IV were motivated. It was shown that these cut conditions identify cosmic ray muons and muon correlated events like FN and cosmogenic βn-emitters very efficiently. As all triggers within a veto time window of 1 ms after such an identified cosmic muon event are rejected, a dead time is introduced. This dead time or veto time was found to be 11.11 days for the investigated data sample from 2011/03/14 to 2012/03/15. The run time of the experiment has to be corrected for this veto time, where the resulting value is the live time, which was determined to be 240.17 days.

Different logical combinations of the muon thresholds values in ID and IV were used to get a further insight into the efficiency and muon sample purity of this selection. The muon rates for each of the logical threshold combinations have been extracted using three different methods. This comparison has given a hint of a contamination of high energetic light noise leaking into the selected muon sample in the ID. The influence of a threshold variation of 1 % of the nominal threshold values was studied to determine systematic errors on the muon rate measurement. The resulting averaged rates for the different logical combinations obtained with the simple counting method will be listed in the following. The statistical errors were estimated from the sample standard deviations and the systematic errors were found by varying the muon threshold.

$$
\begin{aligned}
R_\mu^{ID} &= 12.92 \pm 0.15\,(\mathrm{stat}) \pm 0.05\,(\mathrm{syst})\,\mathrm{s}^{-1} \\
R_\mu^{IV} &= 45.41 \pm 0.44\,(\mathrm{stat}) \pm 0.01\,(\mathrm{syst})\,\mathrm{s}^{-1} \\
R_\mu^{\mathrm{ID}\wedge\mathrm{IV}} &= 12.75 \pm 0.17\,(\mathrm{stat}) \pm 0.05\,(\mathrm{syst})\,\mathrm{s}^{-1} \\
R_\mu^{\mathrm{ID}\vee\mathrm{IV}} &= 45.58 \pm 0.44\,(\mathrm{stat}) \pm 0.01\,(\mathrm{syst})\,\mathrm{s}^{-1} \\
R_\mu^{\mathrm{ID}\wedge(\neg\mathrm{IV})} &= 0.17 \pm 0.03\,(\mathrm{stat}) \pm 0.01\,(\mathrm{syst})\,\mathrm{s}^{-1} \\
R_\mu^{\mathrm{IV}\wedge(\neg\mathrm{ID})} &= 32.61 \pm 0.39\,(\mathrm{stat}) \pm 0.03\,(\mathrm{syst})\,\mathrm{s}^{-1}
\end{aligned}
$$

These rates are consistent with the Monte Carlo prediction from [91]. A detailed comparison and the determination of the muon flux from these rates will be made in chapter 7. It should be noted that the statistical error from the sample standard deviation in the order of 1 % is caused by a periodic variation of the muon rates in time, following a seasonal pattern. This variation and its explanation will be the topic of the next chapter.

Utilizing these different rate measurements, the efficiency of the IV to identify and reject cosmic muons could be measured. This was done by determination of the fraction of muon events identified in the ID, that were not identified in the IV. However, a severe difference to the expected value was found. Studying the muon rejection efficiency in different muon energies ranges, again a contamination by high energy light noise was found. Rejecting those light noise events by additionally requesting a valid hit in the OV purified the selected muon sample and the muon rejection efficiency was determined to be 99.977 %. This number is compatible with the result of a detailed MC simulation of muons in the IV [109].

Preparing further muon related studies with the DC far data set, this chapter showed that one needs to modify the threshold values to identify a muon. This needs to be done as the focus in the following will shift from identifying and rejection muons towards selecting them with high purity. Indeed, for future neutrino analysis [100], stricter threshold values were envisaged, as well as the inclusion of the OV in the muon selection scheme. Going to higher values of visible energy E_{vis} in the ID should reject more and more high energy light noise. In addition using the logical threshold combination of ID$\wedge$IV should select a very pure sample of muon events, as only muons are expected to deposit the high amount of energy requested by the threshold values in both detector volumes. Going to higher cut values is easily possible by increasing the energy or charge values for the muon identification in the ID or the IV respectively and will be considered in the next chapter.

"There are children playing in the streets who could solve some of my top problems in physics, because they have modes of sensory perception that I lost long ago."

Robert J. Oppenheimer
(1904-1967)

6

Seasonal modulation of muon rate

The muons observed at the DC far site arise mostly from the decay of charged pions and to a small fraction from the decay of kaons. These mesons are produced by interactions of primary cosmic rays with air nuclei in the upper atmosphere and their subsequent decay produces muons. Before reaching the detector, muons loose energy as they traverse through the atmosphere and through the rock overburden above the laboratory. Only muons above a certain threshold energy $E_{thr}(h)$, at surface will be able to reach a given depth h. Muons below that threshold energy will be stopped. This was the basic picture of muon production in the atmosphere as described in chapter 4.

This chapter covers temporal variations in the rate of detected cosmic ray muons per day. These variations can be related to temperature fluctuations in the stratosphere changing the air density, which in turn affect the fraction of mesons (π,K) decaying into muons. In opposite to the temperature of the troposphere, which changes considerably during a day, the temperature of the stratosphere changes very slowly over longer time scales such a seasons. As the average air temperature increases during summer, the average gas density decreases. Due to the less dense medium the mean free path of mesons is longer, increasing the fraction of mesons decaying instead of having an interaction. Additionally the height of the primary cosmic ray interaction increases. As net effect, a rise in the temperature of the stratosphere should result in a higher muon rate. This leads to a positive correlation between muon rate and the average air temperature and to maxima in summer and minima in winter. In addition one expects short term effects, like a correlation with the surface pressure which perturbs this seasonal variation. These effects are known since the early 1950's [88] and were studied by many experiments since then [112, 113].

In this chapter the theory and analysis methods needed to show a seasonal modulation of the muon rate measured at the DC far detector location will be established. It will start by searching for periodic variations in the measured muon rates and discusses the Lomb Scargle analysis method, that was performed to search for periodicities in the daily time series of muon rates. Then, the theoretical connection between muon rate and atmospheric conditions will be investigated and quantified using a correlation analysis of the daily muon rates, the temperature and pressure values. This correlation is related to the relative contribution of π and K to the muon intensity detected underground. By measuring the correlation it was possible to estimate the atmospheric K/π ratio. The chapter will then conclude giving a summary of the observations, the performed measurements and results.

6.1 Observation of a temporal variation in muon rate

During the DC data taking period from 2011/04/13 to 2012/03/11 the measured muon rates per run were averaged daily using a weighted mean. The rates were obtained with the nominal muon selection of the neutrino analysis, $E_{ID} > 30\,\text{MeV}$ and $Q_{IV} > 10\,\text{kDUQ}$. The resulting data set is comprised of 320 days of muon data. Figure 6.1 shows the time series of daily muon rates and a variation is clearly visible. This daily muon rates $R_\mu(t)$ was fitted with the following cosine function

$$R_\mu = R_{\mu,0} + \delta R_\mu \cos\left(\frac{2\pi}{T}(t - t_0)\right), \tag{6.1}$$

where $R_{\mu,0}$ are average muon rates, δR_μ variations of this average and T, t_0 the variation period and phase respectively. The motivation to use a fit of this form is that one expects a seasonal variation of the measured muon rate resembling the seasonal temperature change of the atmosphere. Thus having a maximum in summer, where the temperature is higher and a minimum in winter, where the temperature is lower.

As can be seen in the upper panel of figure 6.1, the time series of the daily muon rates in the ID, $R_\mu^{\text{ID}}(t)$, does not follow the cosine pattern in the beginning and at the end of the data taking period. The daily IV muon rates, $R_\mu^{\text{IV}}(t)$, matches the cosine pattern much better as can be seen in the panel below. The bad χ^2/NDF listed in table 6.1 indicate that the seasonal modulation of these rates is only a first approximation to the time series data. The muon rate of the logical and combination, $R_\mu^{\text{ID and IV}}(t)$, shows the same behavior as the ID muon rate at the start and the end of the data taking period. Considering the rate of muon events only identified in the ID, $R_\mu^{\text{ID-only}}(t)$, a hint on muon sample purity is given, as these events do not follow the expected cosine pattern of a seasonal variation. The rate of muon events in ID or IV, $R_\mu^{\text{ID or IV}}(t)$, resembles the cosine pattern much better. However, from the rate of muons only identified in the IV, $R_\mu^{\text{IV-only}}(t)$, it can be seen that the measured rate is higher compared to the cosine pattern in the first 20-30 days. Still, apart from these issues in the time series of the muon rates, $R_\mu(t)$, they are showing the expected seasonal variation with higher muon rates in summer and lower rate values in winter. The parameters obtained from the cosine fits of the various logical combinations can be found in table 6.1.

One of last chapters' conclusions was that the event sample selected by ID muon threshold of 30 MeV is polluted with high energy light noise events. Thus the bad cosine fit can be understood and the fitting was repeated using higher cut values of 100 MeV for the ID and 40 kDUQ for the IV, which should select a cleaner muon event sample. The time series of the muon rates obtained with these cut values can be seen in figure 6.2. The fit results can be found in the lower part of table 6.1. The values emphasize the conclusion made before, the spread in the amplitudes of ID and IV is smaller and the period matches the expected seasonal modulation better.

Except for the time series of muon rates identified only in the ID, $R_\mu^{\text{ID-only}}(t)$, which is rather flat, a qualitatively better agreement between the cosine fit and the data could be achieved

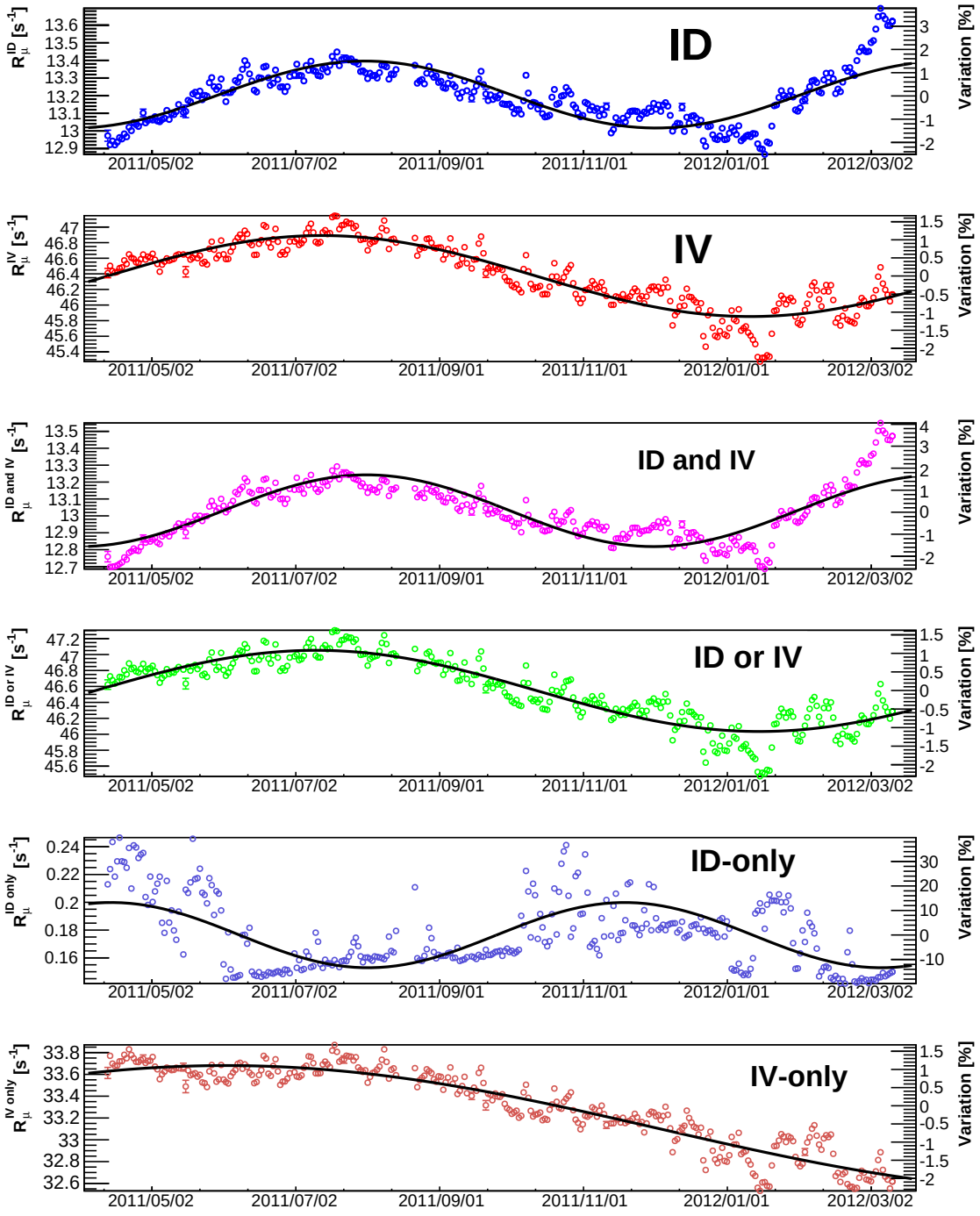

Figure 6.1: "Nominal" selection $E_{vis} > 30\,\text{MeV}$ and $Q_{IV} < 10\,\text{kDUQ}$: Panels from top to bottom show the time series of muon rates for the different logical combinations of the neutrino analysis muon threshold being ID, IV, ID∧IV, ID∨IV, ID∧(¬IV) and IV∧(¬ID). One observes a variation of the muon rates, matching the cosine pattern and the expectation to have a higher muon rate in summer compared to a lower muon rate in winter. The exception to this are the time series of ID∧(¬IV) and IV∧(¬ID), where the rate of events only identified by the ID eventually shoots up not showing a periodic behavior and the IV only pattern seems to be too high at the beginning and too low at the end of the data taking period compared to the other selections.

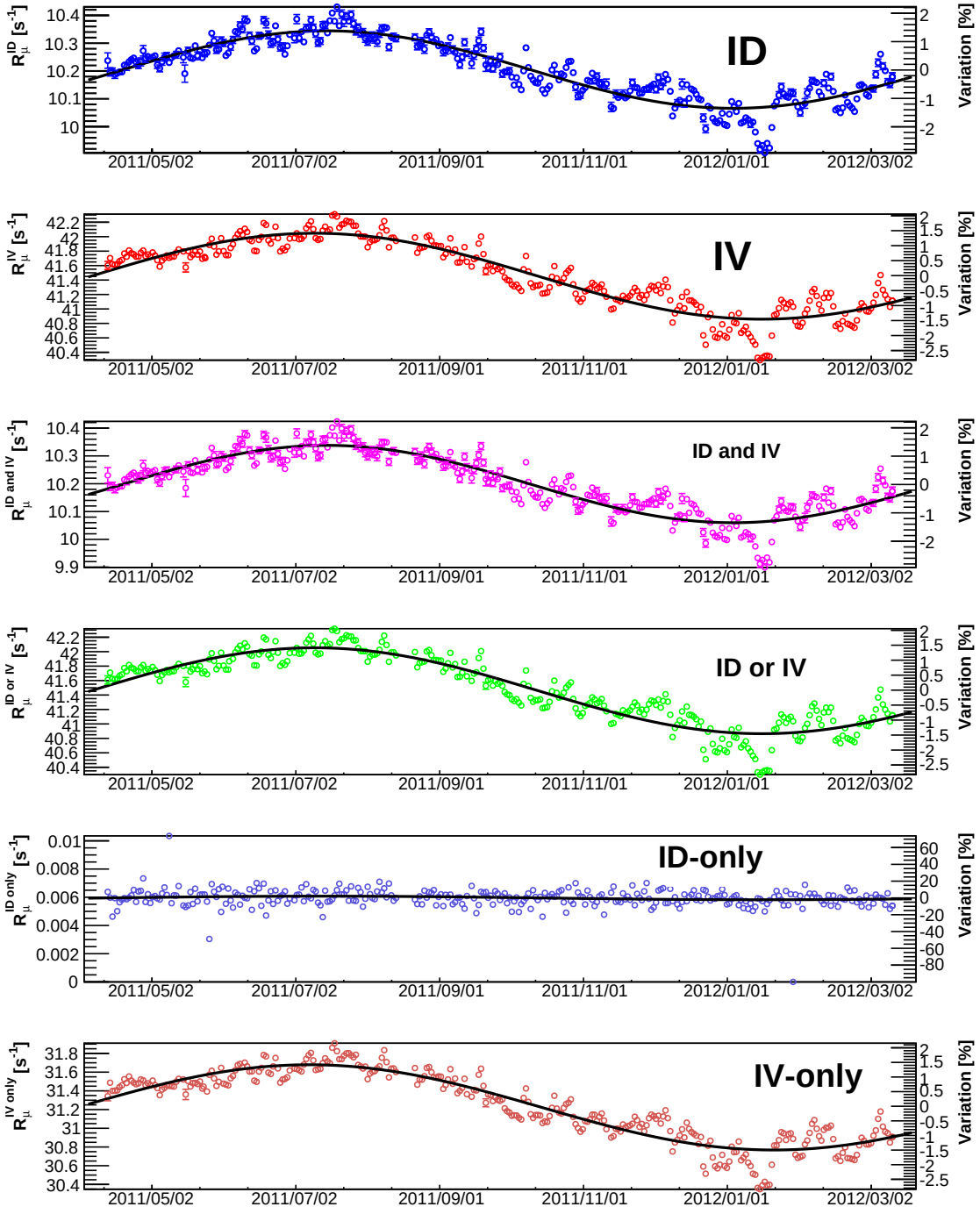

Figure 6.2: "Medium" selection $E_{vis} > 100\,\text{MeV}$ and $Q_{IV} > 40\,\text{kDUQ}$: Panels from top to bottom show the time series of muon rates for the logical muon threshold combinations ID, IV, ID∧IV, ID∨IV, ID∧(¬IV) and IV∧(¬ID). Compared to the nominal selection ($E_{vis} > 30\,\text{MeV}$, $Q_{IV} > 10\,\text{kDUQ}$), the time series of muon rates follows the cosine better. Still the event sample selected by the ID only threshold combination ($E_{vis} > 100\,\text{MeV}$ and $Q_{IV} < 40\,\text{kDUQ}$) shows no seasonal variation, being rather constant in time indicating a non muon origin.

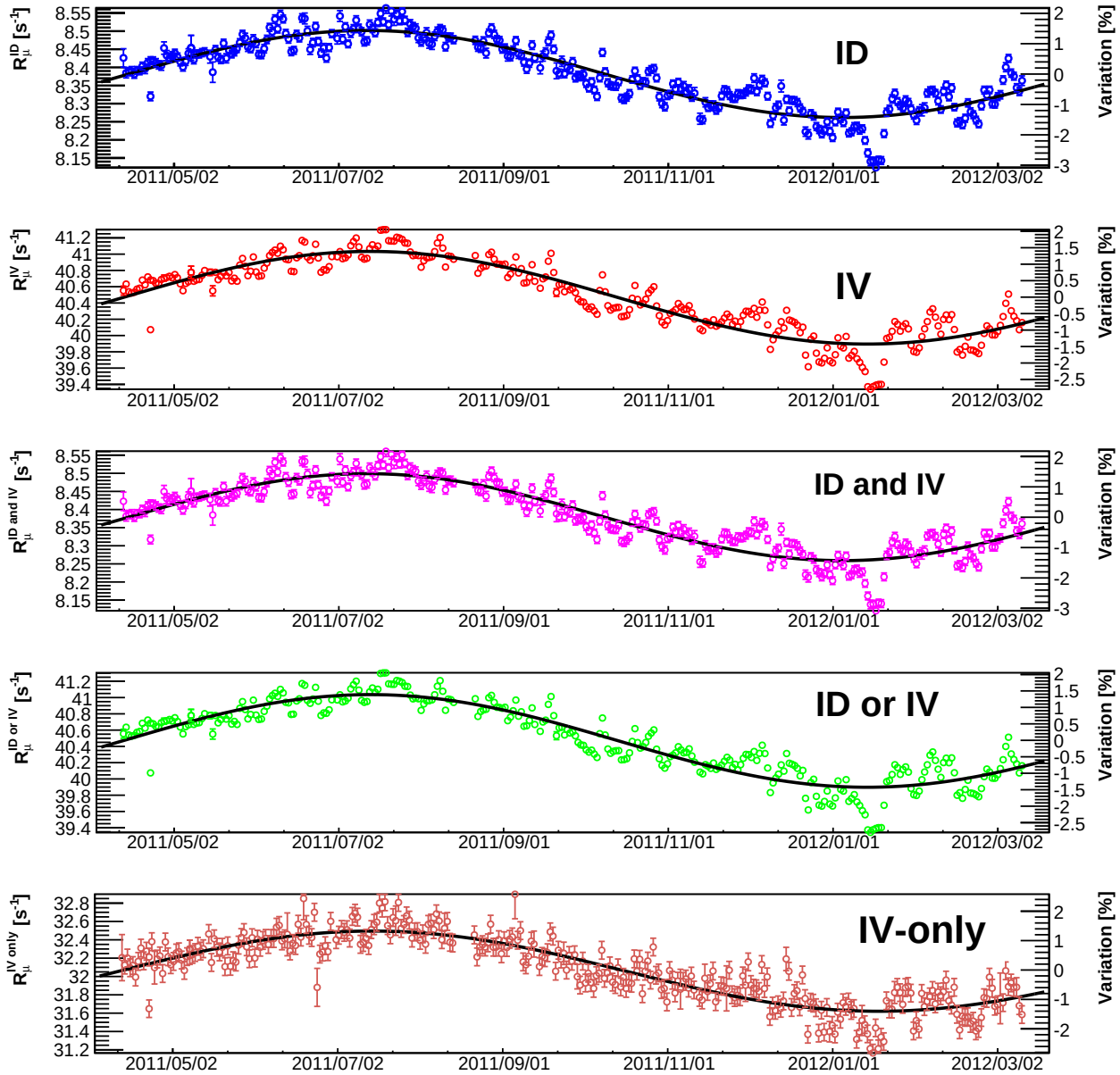

Figure 6.3: "Stricter" selection $E_{vis} > 200\,\mathrm{MeV}$ and $Q_{IV} > 50\,\mathrm{kDUQ}$: Panels from top to bottom show the time series of muon rates for the different logical combinations of the "stricter" muon thresholds being ID, IV, ID∧IV, ID∨IV and IV¬ID. The ID¬IV muon rate is not shown, as virtually no event fulfills this logical condition.

nominal muon thresholds: $E_{ID} > 30$ MeV, $Q_{IV} > 10$ kDUQ					
threshold combination	**average muon rate [s^{-1}]**	**variation amplitude [s^{-1}]**	**percentual change [%]**	**period [days]**	χ^2/NDF
ID	13.21	0.19	1.44	246.2	11,740/320
IV	46.37	0.52	1.12	362.5	12,110/320
ID∧IV	13.02	0.21	1.61	242.8	12,470/320
ID∨IV	46.54	0.51	1.09	375.1	12,420/320
ID∧(¬IV)	0.17	N/A	N/A	N/A	85,110/320
IV∧(¬ID)	33.10	0.58	1.75	732.9	8666/320
medium muon threshold: $E_{ID} > 100$ MeV, $Q_{IV} > 40$ kDUQ					
threshold combination	**average muon rate [s^{-1}]**	**variation amplitude [s^{-1}]**	**Percentual change [%]**	**period [days]**	χ^2/NDF
ID	10.21	0.14	1.27	343.9	3876/320
IV	41.45	0.59	1.42	378.4	14,350/320
ID∧IV	10.20	0.14	1.37	343.8	3070/320
ID∨IV	41.46	0.59	1.42	378.4	14,390/320
ID∧(¬IV)	0.04	N/A	N/A	N/A	N/A
IV∧(¬ID)	31.22	0.46	1.47	392.9	10,860/320
strict muon threshold: $E_{ID} > 200$ MeV, $Q_{IV} > 50$ kDUQ					
threshold combination	**average muon rate [s^{-1}]**	**variation amplitude [s^{-1}]**	**percentual change [%]**	**period [days]**	χ^2/NDF
ID	8.38	0.12	1.43	351.4	3376/320
IV	40.46	0.57	1.41	366.7	14,210/320
ID∧IV	8.38	0.12	1.43	351.4	3070/320
ID∨IV	40.46	0.57	1.41	366.7	14,260/320
ID∧(¬IV)	N/A	N/A	N/A	N/A	N/A
IV∧(¬ID)	32.06	0.44	1.37	373.5	815/320

Table 6.1: Parameters obtained from cosine fit to time series of daily muon rates. The top shows the parameters obtained using the "nominal" muon threshold values of $E_{vis} > 30$ MeV for the ID and $Q_{IV} < 10$ kDUQ for the IV which are used to identify muons in the general neutrino analysis. The middle table shows the parameters for different thresholds, called "medium" muon thresholds having the values $E_{vis} > 100$ MeV and $Q_{IV} > 40$ kDUQ. The last table shows the parameters for the "strict" muon threshold being $E_{vis} > 200$ MeV and $Q_{IV} > 50$ kDUQ which lead to much purer event samples in terms of muons. This can also be seen from the amplitudes which match better and the periods getting closer to the yearly expectation.

by using the higher cut values. This indicates that, to some extent, non-muon events could be rejected by going to higher deposited energies. In addition, one can conclude that the high energy light noise populates the energy region up to 100 MeV as no sporadic increase or bursts in rate are visible anymore. The remaining events in the ID-only sample could be fast neutrons entering the ID and depositing energy therein via proton recoil, being unseen by the IV.

A stricter selection to the muon data was applied, with $E_{vis} > 200$ MeV for the ID and $Q_{IV} > 50$ kDUQ for the IV. The time series of the muon rates selected with these higher muon thresholds can be seen in figure 6.3 for the different logical combinations. The rate of muons only identified in the ID, $R_{\mu}^{\text{ID-only}}$, is not shown, as virtually no event fulfills the combination depositing a high amount of energy in the ID on the one hand, but only depositing a low amount of energy in the IV on the other hand. The parameters resulting from the cosine fit can again be found in table 6.1, at the very bottom. The seasonal variation pattern persists,

yielding better agreement between amplitudes and periods with respect to the cosine fit. This indicates that a cleaner muon sample can be selected applying a stricter threshold. The resulting event samples follow the expected cosine pattern: a period around 350 to 370 days matching roughly the seasonal modulation. These stricter muon cut values will be used for further analysis of seasonal variation and correlation with atmospheric effects.

6.2 Lomb-Scargle Analysis

To verify the assumption of a seasonal variation in the measured muon rates and to have a complementary method to the simple cosine fits done before, a Lomb-Scargle (**LS**) analysis was performed. The LS analysis is a method [114, 115] estimating a frequency spectrum, based on a least squares fit of sinusoids to a given data sample. It has a close connection to Fourier Analysis, however the latter is restricted to data sets of equally spaced samples. Initially Lomb derived this method for usage in astronomy, where it is often necessary to analyze unevenly spaced data, especially in the field of variable sources. Nowadays it is commonly used to uncover unknown periodic components of type

$$N(t) = N_0(1 + A \cdot \sin(2\pi t/T + \varphi)) \tag{6.2}$$

in any unequally spaced data set. In this formulation, $N(t)$ is the expected time-varying event rate, N_0 represents the mean rate and A is the amplitude of a given periodic modulation. T stands for the period of this modulation and φ its phase relative to the beginning of the measurement. One defines the power P for a particular modulation period T according to

$$P(T) = \frac{1}{2\sigma^2}\left(\frac{\left[\sum_{i=1}^{n}\omega_i(N(t)-N_0)\cos\tau_i\right]^2}{\sum_{i=1}^{n}\omega_i\cos^2\tau_i} + \frac{\left[\sum_{i=1}^{n}\omega_i(N(t)-N_0)\sin\tau_i\right]^2}{\sum_{i=1}^{n}\omega_i\sin^2\tau_i}\right). \tag{6.3}$$

This power P is the weighted difference of the expected number of events N_i in every data bin i and the weighted mean number of events N_0, multiplied with sine and cosine functions that oscillate with the investigated period T, where n stands for the number of bins and τ_i for the phase in bin i. The value σ^2 stands for the weighted variance of the data.

Each bin i is weighted with, $\omega_i = \sigma_i^{-2}/\langle\sigma^{-2}\rangle$, the inverse squares of the statistical uncertainties of individual bins divided by their average value. The phase τ_i of the sine and cosine functions is defined according to BOREXINO [113] and SNO [116], where analysis were performed to search for periodic modulation in the detected muon rate or to search for periodicities in the ^{8}B solar neutrino flux respectively. The phase is defined as

$$\tau_i = 2\pi \cdot \frac{t_i - t_p}{T}, \quad t_p = \frac{T}{4\pi} arctan\left(\frac{\sum_{i=1}^{N}\omega_i\sin(4\pi t_i/T)}{\sum_{i=1}^{N}\omega_i\cos(4\pi t_i/T)}\right). \tag{6.4}$$

The result of such an LS analysis is a periodogram showing the LS powers P for a range of periods T. A peak in this periodogram indicates a period with a significant power. However, it should be noted that the resulting LS power P is not correct for modulation periods T

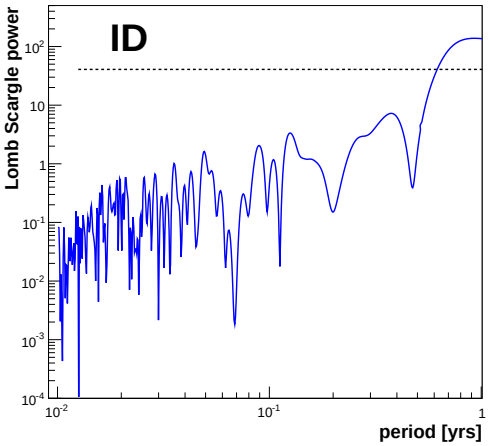

Figure 6.4: LS periodogram of ID muon rate.

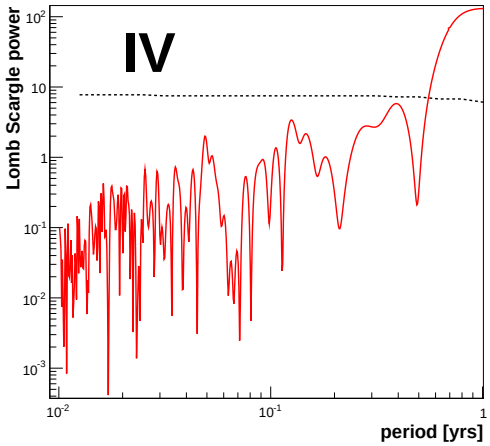

Figure 6.5: LS periodogram of IV muon rate.

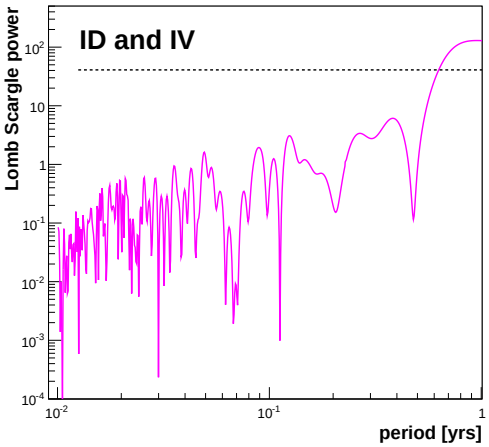

Figure 6.6: LS periodogram of ID∧IV muon rate.

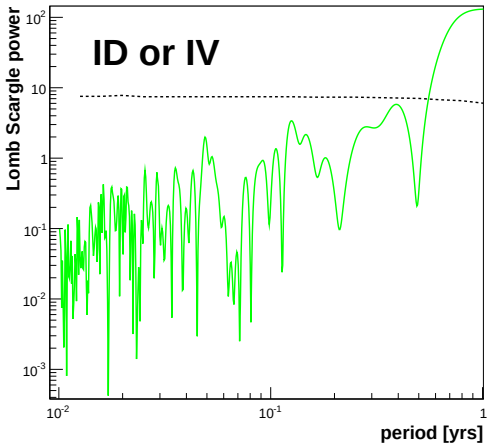

Figure 6.7: LS periodogram of ID∨IV muon rate.

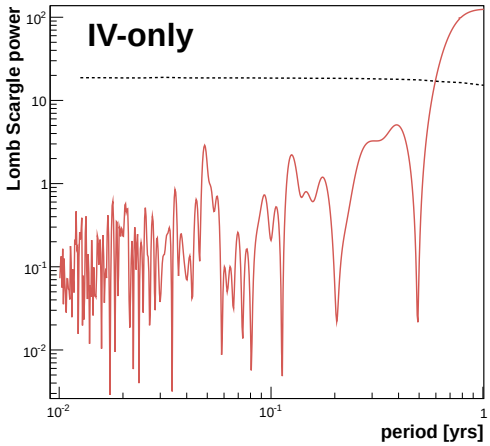

Figure 6.8: LS periodogram of IV∧(¬ID) muon rate.

extending the measurement time of the observed data. The same is true for periods which are small compared to the width of one bin, which is one day in the considered case. For this analysis, the muon rates extracted from one hour long DAQ runs were averaged daily and the uncertainty σ_i is given by the combined statistical and systematic error on the averaged rate measurement per day. However, due to DAQ crashes not all runs have a length of one hour. In addition, during the calibration campaign in summer 2011 no muon data were taken resulting in a one week gap in the data set. The resulting unevenly spaced data set justifies the application of the LS method instead of a Fourier analysis. The periodograms for the DC muon rate using the different logical combinations of the "stricter" muon thresholds discussed before, can be seen in figures 6.4 - 6.8. This corresponds to threshold values of 200 MeV for the ID and 50 kDUQ for the IV, which were used to reject some of the high energy light noise events in order to obtain a purer muon sample.

One has to carefully check the significance of a periodical modulation, because statistical fluctuations within a bin will alter the maximum P generated by white noise and also the actually observed value for the modulation [113]. Therefore one has to evaluate the statistical fluctuation of the signal height and the white noise level. This is done the same way as in [113] by performing a Monte Carlo calculation of muon sample time distributions[1]. This MC utilizes the known muon rate distribution over time, where the average rate is calculated from this data set. The calculated average is smeared using a Gaussian distribution, where the width of the distribution is given by a randomly chosen error out of the data set. Based on this, the resulting output data sample is without any modulation. Any deviation from the average of the data set is simply white noise. These MC white noise data sets were used to evaluate thresholds to discriminate between a statistical modulation and a true signal. To do this, for each period T the corresponding LS power P was calculated. For a given period T, the 3σ-threshold $P_{thr}(T)$ was set so, that 99.7 % of all white noise samples feature a lower value of P. This 3σ threshold is indicated by the dotted line in figures 6.4-6.8.

In all five periodograms a significant LS power is visible, rising just before a period of one year. This indicates the expected seasonal modulation in the muon data. Once the length of the data set increases, for example from currently 320 days to 2 or even 3 years, the LS analysis is expected to perform much better and if the assumption of the yearly modulation is true, the peak indicating itself at $T = 1$ year should be more prominent and the LS power should decrease for higher periods. For all other periods T no significant LS power P is visible, thus no significant modulation in the muon rates is observed.

6.3 Connection to atmospheric conditions

As stated in the introduction of this chapter, variations of the cosmic ray muon flux are possible due to changes in earth's atmosphere. The trend of the muon rate time series to follow the cosine pattern is a first hint for a seasonal variation of muon rates at the DC far site. This hypothesis is supported by the results of the LS periodicity analysis. Thus the theoretical connection between changes in the atmosphere and changes in muon intensity will

[1] The code to perform this LS analysis as well as the MC to generate random, white noise data sets was kindly provided by M. Wurm.

be discussed. One distinguishes several sources of muon rate modulation, for example a variation of surface pressure or variation in the atmospheric temperature profile. This changes the interaction height of incident primary cosmic rays which in turn affects the production altitude of pions and kaons decaying to muons. In the following a brief theoretical description will be given following the monographs of Gaisser and Dorman [87,90], ending in a more detailed description of the barometric effect, the change of muon intensity with a change in surface pressure and the temperature effect, the change in muon intensity caused by changes in the atmospheric temperature profile.

First recalling the definition of the muon intensity from chapter 4, taking into account muon decay and energy loss in the atmosphere, one gets the following term

$$\begin{aligned} I_\mu &= \int_{E_{th}}^{\infty} dE_\mu \frac{dI_\mu}{dE_\mu} \int_0^\infty dX \mathcal{P}_\mu(E_\mu, X, \cos\theta)\varphi_\mu(X) \\ &= \sum_{\mathcal{M}} \int_{E_{th}}^{\infty} dE_\mu \int_0^\infty dX \frac{\epsilon_M}{X\cos\theta(1-r_M)} \int_{E_\mu}^{E_\mu/r_M} \frac{dE_M}{E_M} \frac{\mathcal{M}(X, E_M, \cos\theta)}{E_M} \\ &\times \; exp\Big(-\frac{m_\mu c}{\tau_\mu} \int_0^X \frac{dX'}{\rho(X')} \frac{1}{E_\mu - \alpha(X'-X)} \Big). \end{aligned} \tag{6.5}$$

Using the definition above, one can account for these effects by varying the variables that depend on meteorological conditions, being the threshold energy E_{th}, the slant depth X and the air density ρ. By doing this one ends up with the following terms according to [87] describing several meteorological effects:

$$\frac{\Delta I_\mu}{I_\mu} = \left(\frac{\Delta I_\mu}{I_\mu}\right)_{\text{snow}} + \left(\frac{\Delta I_\mu}{I_\mu}\right)_{\text{grav.}} + \left(\frac{\Delta I_\mu}{I_\mu}\right)_{\text{wind}} + \left(\frac{\Delta I_\mu}{I_\mu}\right)_{\text{barom.}} + \left(\frac{\Delta I_\mu}{I_\mu}\right)_{\text{temp.}} \tag{6.6}$$

The effect of snow, wind and gravitation are small and can be neglected. Thus, only the barometric and the temperature effect remain. The complicated dependency on the integrals over different atmospheric layers and meson and muon energies in eq. 6.6 is aborbed into effective parameters β_p, α_T. This yields a more simple term describing both meteorological effects. Thus, one ends up with a term describing the change in muon intensity caused by a change in surface pressure Δp (mbar) at pressure level X (g/cm^2) and a term describing the change in muon intensity caused by changes of the atmospheric temperature profile $\Delta T(X')$ at level X' [117]:

$$\Delta\{lnI_\mu(E_{th}, X, \theta)\} = \beta_p(E_{th}, X, \theta)\Delta p + \int_0^X dX' \alpha_T(X, E_{th}, X', \theta)\Delta T(X') \tag{6.7}$$

The first term on the right hand side represents the barometric effect, whereas the second represents the temperature effect. The next two sections, 6.3.1 and 6.3.2, will explain these effects and the choice of this empirical parametrisation with β_p and α_T. The rest of this chapter is devoted to the investigation of these two effects at the DC far site.

6.3.1 Barometric effect

Phenomenological studies of the barometric effect can be found in [117–119]. A simple and overall negative correlation between the fractional change of muon intensity ΔI_μ and changes in surface pressure Δp is found:

$$\Delta\{lnI_\mu\} = \frac{I_\mu - \langle I_\mu \rangle}{\langle I_\mu \rangle} = \beta_p \cdot (p - \langle p \rangle) = \beta_p \cdot \Delta p \tag{6.8}$$

Detailed studies [119] showed that the barometric effect actually consists of three different kinds of effects. Pressure changes induce density changes in the atmosphere: an increase in pressure increases the density and leads to additional energy loss of muons (negative effect, less muons). In addition, the muon survival probability φ_μ is decreased (negative effect). Also the production of muons through pions and kaons is affected, because with a denser atmosphere more mesons are produced which can eventually decay into muons (positive effect).

If one takes into account that a detector counts a discrete number of muons N_μ in a given time t one can relate the muon rate $R_\mu(t)$ to the intensity I_μ by considering the detection efficiency of muons ϵ, A the surface area and Ω the solid angle.

$$R_\mu = N_\mu/t = \int d\Omega I_\mu(\Omega)\epsilon(\Omega)A_{tot}(\Omega) \tag{6.9}$$

Thus eq. 6.8 is valid for the muon rate as well yielding

$$\frac{R_\mu - \langle R_\mu \rangle}{\langle R_\mu \rangle} = \beta_p \cdot (p - \langle p \rangle) = \beta_p \cdot \Delta p, \tag{6.10}$$

with $\langle R_\mu \rangle$, $\langle p \rangle$ being the averages of muon rate and pressure for the considered data set. A simple prediction for the magnitude of the effect of surface pressure on muon rate is possible by assuming that the pressure p simply scales linearly with the height of the atmosphere [118]. Approximately there is a dependence of the form

$$R_\mu = R_{\mu 0} \cos^2 \theta \tag{6.11}$$

of the rate R_μ over zenith angle θ at sea level, where $R_{\mu 0} = R_\mu(\theta = 0)$. The effective atmospheric thickness at zenith angle θ is given by X, whereas X_0 is the vertical depth. Utilizing this for small zenith angles θ yields

$$R_\mu/R_{\mu 0} = (X_0/X)^2. \tag{6.12}$$

Calculating the differential in R_μ of eq. 6.12 and dividing it by R_μ yields

$$\frac{dR_\mu}{R_\mu} = -\frac{2dX}{X} = -\frac{2dp}{p} \equiv \beta_p dp, \tag{6.13}$$

taking into account that the pressure p at vertical depth X is simply defined by $p = X$. Hence, the barometric coefficient β_p is $-2/p$. For a pressure change of several mbar, this leads to a change in muon rate of several per mil. In addition, the negative sign is predicted by this simple approximation, yielding a negative effect on muon rate for a pressure change. Eq. 6.13 also defines the dimension of the barometric coefficient β_p as ‰/mbar.

6.3.2 Temperature effect

Regarding the temperature effect the relation is more complicated as the changes in temperature occur not uniformly in the atmosphere. In addition, neither muon nor meson production happens at one specific height in the atmosphere. Thus no simple model like in the case of the barometric effect exists. Instead, one has to carefully choose atmospheric weights that can be used to approximate the temperature profile of the whole atmosphere leading to an effective temperature. In order to calculate this effect, one needs to consider the production of π and K mesons by hadronic interactions of primary cosmic rays and nuclei of air molecules in the atmosphere. Recalling the differential equation of the meson intensity that can be found in chapter 4

$$\frac{d\mathcal{M}}{dX}(E, X, \cos\theta) = \frac{Z_{NM}}{\Lambda_N} N_0 e^{-X/\Lambda_N} - \mathcal{M}(E, X, \cos\theta)\left(\frac{1}{\Lambda_M} + \frac{\epsilon_M}{EX\cos\theta}\right), \tag{6.14}$$

with the parameters defined according to [88, 90]. The critical meson energy ϵ_M separates the interaction from the decay regime for a given meson species M

$$\epsilon_M = \frac{m_M c^2 H(T)}{c\tau_M}. \tag{6.15}$$

The values m_M, τ_M are either meson mass and lifetime respectively. $H(T) = RT/Mg$ is the temperature dependent atmospheric scale height with gas constant R, molar mass M and gravitational acceleration g. Thus the critical meson energies are temperature dependent.

One defines the terms $\eta(X) \equiv (T(X) - T_{eff})/T_{eff}$ and $\epsilon_M = \epsilon_M^0(1 + \eta)$ in a way that ϵ_M^0 is the constant value of ϵ_M at $T(X) = T_{eff}$. In this case T_{eff} is the temperature that would cause the observed muon intensity I_μ if the atmosphere was isothermal. Thus the function $\eta(X)$ is a measure of any deviation from this effective temperature for a given pressure level X. To quantify the effect of a temperature change on meson intensity, one has to replace ϵ_M with the term $\epsilon_M^0(1 + \eta)$ in eq. 6.14

$$\frac{d\mathcal{M}}{dX}(E, X, \cos\theta) = \frac{Z_{NM}}{\Lambda_N} N_0 e^{-X/\Lambda_N} - \mathcal{M}(E, X, \cos\theta)\left(\frac{1}{\Lambda_M} + \frac{\epsilon_M^0(1 + \eta(X))}{EX\cos\theta}\right). \tag{6.16}$$

Finding an analytical solution is difficult as η is an arbitrary function of X, however a solution is given by expanding the exponential in a power series as presented in [120]. The solution of this can be written as $\mathcal{M} = \mathcal{M}^0 + \mathcal{M}^1$, where $\mathcal{M}^0(E, X, \cos\theta)$ is the solution with $\epsilon = \epsilon_M^0$ at

temperature $T(X) = T_{eff}$ and $\mathcal{M}^1(E, X, \cos\theta)$ being the first order in η of the power series. The function $\mathcal{M}^1(E, X, \cos\theta)$ is given by

$$\begin{aligned}\mathcal{M}^1(E, X, \cos\theta) &= \frac{Z_{NM}}{\Lambda_N} N_0 e^{-X/\Lambda_M} \left(\frac{X}{\Lambda_M}\right)^{-\epsilon_M^0/E\cos\theta} \frac{\epsilon_M^0}{E\cos\theta} \\ &\times \int_0^X dX' \frac{\eta\Lambda_M}{X'} \left(\frac{X'}{\Lambda_M}\right)^{\epsilon_M^0/E\cos\theta+1} \sum_{k=0}^{\infty}(-)^k \frac{1}{k!} \frac{(X'/\Lambda'_M)^k}{(\epsilon_M/E\cos\theta + (k+1))^2}.\end{aligned} \tag{6.17}$$

In the high energy region, $E\cos\theta \gg \epsilon_M^0$, where interactions dominate over decay, the integrand $(X'/\Lambda_M)^{\epsilon_M/E\cos\theta} \to 1$ and $\eta(X') \approx \eta(X)$ according to [88]. This is because high energy mesons can travel a large distance in the atmosphere before decaying. In the low energy region, $E\cos\theta \ll \epsilon_M^0$, where meson decay dominates, the integrand is only large when X is close to X'. Thus $\eta(X) \approx \eta(X')$ and can be taken out of the integral as before.

By defining $\Delta\mathcal{M} = \mathcal{M}^0 - \mathcal{M}^1$, a description for changes in meson intensity caused by temperature changes is found

$$\Delta\mathcal{M} = \frac{Z_{NM}}{\Lambda_N} N_0 e^{-X/\Lambda_M} \frac{\epsilon_M^0 \eta X}{E\cos\theta} \times \sum_{k=0}^{\infty}(-)^k \frac{1}{k!} \frac{(k+1)(X/\Lambda'_M)^k}{(\epsilon_M^0/E\cos\theta + (k+1))^2}. \tag{6.18}$$

Applying this term to eq. 7.7, a description for the change of the differential muon intensity dI_μ/dE_μ with temperature is found

$$\begin{aligned}\Delta\left(\frac{dI_\mu}{dE_\mu}\right) &= \int_0^\infty dX \frac{\epsilon_M^0}{X\cos\theta(1-r_M)} \int_{E_\mu}^{E_\mu/r_M} \frac{dE_M}{E_M^2} N_0(E_M) e^{-X/\Lambda_M} \frac{\epsilon_M^0 \eta X}{E\cos\theta} \\ &\times (-)^k \frac{1}{k!} \frac{(X'/\Lambda'_M)^k}{(\epsilon_M^0/E\cos\theta + (k+1))^2}.\end{aligned} \tag{6.19}$$

This can also be written as

$$\Delta\left(\frac{dI_\mu}{dE_\mu}\right) = \frac{Z_{NM}}{\Lambda_N} \left(\frac{\epsilon_M^0}{E_\mu\cos\theta}\right)^2 \frac{E_\mu^{-(\gamma+1)}}{(1-r_M)} \int_0^\infty dX e^{-X/\Lambda_M} \eta I_M(z), \tag{6.20}$$

where the function $I_M(z)$ [90] is given by the integral

$$I_M(z) = \int_1^{1/r_M} dz \frac{1}{z^{-(\gamma+2)}} \sum_{k=0}^{\infty}(-)^k \frac{1}{k!} \frac{(k+1)(X/\Lambda_M)^k}{(\epsilon_M^0/E_\mu\cos\theta + z)^2}, \tag{6.21}$$

with $z = E/E_\mu$, being the ratio of parent meson to muon energy. A solution of this integral can be found considering the two energy regimes divided by ϵ_M^0. First the high energy regime, $E_\mu \gg \epsilon_M$, with the high energy solution I_M^H and the low energy regime, $E_\mu \ll \epsilon_M$, with the low energy solution I_M^L:

$$I_M^H = \frac{1}{\gamma+3}(1-r_M^{\gamma+3})(1-e^{-X/\Lambda'_M})\frac{\Lambda'_M}{X}, \quad (6.22)$$

$$I_M^L = \frac{1}{\gamma+1}(1-r_M^{\gamma+1})\left(\frac{E_\mu\cos\theta}{\epsilon_M^0}\right)^2(1-X/\Lambda'_M)e^{-X/\Lambda'_M}. \quad (6.23)$$

A good approximation [120] that preserves the physics of the system and that is valid for all energies, incorporating both the high I_M^H and the low energy I_M^L solutions, is given by

$$\Delta\left(\frac{dI_\mu}{dE_\mu}\right) = \frac{E_\mu^{-(\gamma+1)}}{1-Z_{NM}}\int_0^\infty \frac{dX(1-X/\Lambda'_M)^2 e^{-X/\Lambda_M}\eta(X)A_M^1}{1+B_M^1K(X)(E_\mu\cos\theta/\epsilon_M^0)^2}, \quad (6.24)$$

with the parameters defined in the following way

$$A_M^1 = \frac{Z_{NM}}{1-r_M}\cdot\frac{1-r_M^{\gamma+1}}{\gamma+1}, \quad (6.25)$$

$$B_M^1 = \frac{\gamma+3}{\gamma+1}\cdot\frac{1-r_M^{\gamma+1}}{1-r_M^{\gamma+3}}, \quad (6.26)$$

$$K(X) = \frac{(1-X/\Lambda'_M)^2}{(1-e^{-X/\Lambda'_M})\Lambda'_M/X}. \quad (6.27)$$

The A_M^1 represent the amount of inclusive meson production, the parameter B_M^1 represents the relative atmospheric attenuation length of the mesons in the atmosphere. The values of these parameters can be found in table 6.2, together with all other input parameters used in the following calculations. These definitions allow to define the temperature coefficient $\alpha(X)$ as following

$$\alpha(X) = \int_{E_{th}}^\infty dE_\mu \frac{A_M^1 E_\mu^{-(\gamma+1)}}{1+B_M^1(E_\mu\cos\theta/\epsilon_M^0)^2}. \quad (6.28)$$

The variation in the integral muon intensity ΔI_μ can be written as

$$\Delta I_\mu = \int_{E_{th}}^\infty \Delta\left(\frac{dI_\mu}{dE_\mu}\right)dE_\mu = \int_0^\infty dX\alpha(X)\frac{\Delta T(X)}{T_{eff}}e^{X/\Lambda_M}. \quad (6.29)$$

The range of the energy integral is from the threshold energy E_{thr} up to infinity. Considering every pressure layer X in the atmosphere and recalling that M applies independently to pions and kaons one can write

$$\begin{aligned}\Delta I_\mu &= \int_0^\infty dX\alpha(X)\frac{\Delta T(X)}{T_{eff}}e^{X/\Lambda_\pi} + \int_0^\infty dX\alpha(X)\frac{\Delta T(X)}{T_{eff}}e^{X/\Lambda_K} \\ &\equiv \int_0^\infty dX W_M(X)\Delta T(X). \end{aligned} \quad (6.30)$$

parameter	value	Unit
γ	1.7±0.1	-
m_π	139.57018±0.00035	MeV/c^2
τ_π	26.03±0.05	ns
m_k	493.677±0.0013	MeV/c^2
τ_K	12.385±0.025	ns
$r(K/\pi)$	0.149±0.006	-
m_μ	105.6583693±0.0000003	MeV/c^2
$H(T)$	6.4±0.1	km
ϵ_π	114±3	GeV
ϵ_K	851±14	GeV
A_π^1	1	-
A_K^1	0.38×$r(K/\pi)$	-
B_π^1	1.460±0.007	-
B_K^1	1.740±0.028	-

Table 6.2: Input parameters with associated errors for the calculation of the effective temperature coefficient α_T. Values taken from [121].

In the last step, the -up to now- arbitrary constant T_{eff} was set in such a way, that for $T(X) = T_{eff}$, the critical energy is $\epsilon_m = \epsilon_M^0$. Therefore ΔI_μ is zero and T_{eff} cannot be arbitrary as it determines the weighting of the various atmospheric levels in such a way that the approximation of a isothermal atmosphere can be made. Now a definition of the effective temperature can be given

$$T_{eff} = \frac{\int_0^\infty dX T(X)\alpha^\pi(X) + \int_0^\infty dX T(X)\alpha^K(X)}{\int_0^\infty dX \alpha^\pi(X) + \int_0^\infty dX \alpha^K(X)}. \tag{6.31}$$

As the atmospheric temperature is measured at discrete pressure levels X_n, the integration is done numerically over the atmospheric layers ΔX_n

$$T_{eff} = \frac{\sum_{n=0}^N \Delta X_n \cdot T(X_n)(W_\pi(X_n) + W_K(X_n))}{\sum_{n=0}^N \Delta X_n (W_\pi(X_n) + W_K(X_n))}. \tag{6.32}$$

In this case $W(X)$ corresponds to the altitude dependence of the muon production, which can be written as the sum $W_\pi(X) + W_K(X)$, representing the contribution of pions and kaons.

$$W_M(x) = \frac{(1 - X/\Lambda'_M)^2 e^{-X/\Lambda_M} A_M^1}{\gamma + (\gamma+1) B_M^1 K(X) (E_{thr}\cos\theta/\epsilon_M^0)^2} \tag{6.33}$$

The value $E_{thr}\cos\theta$ corresponds to the minimum energy a muon must have to reach an underground detector at a given depth h under a zenith angle θ. It can be calculated using the empirical formula of [122]:

$$E_{thr}(h) = \frac{e^{h/p_0} - p_1}{p_2}. \tag{6.34}$$

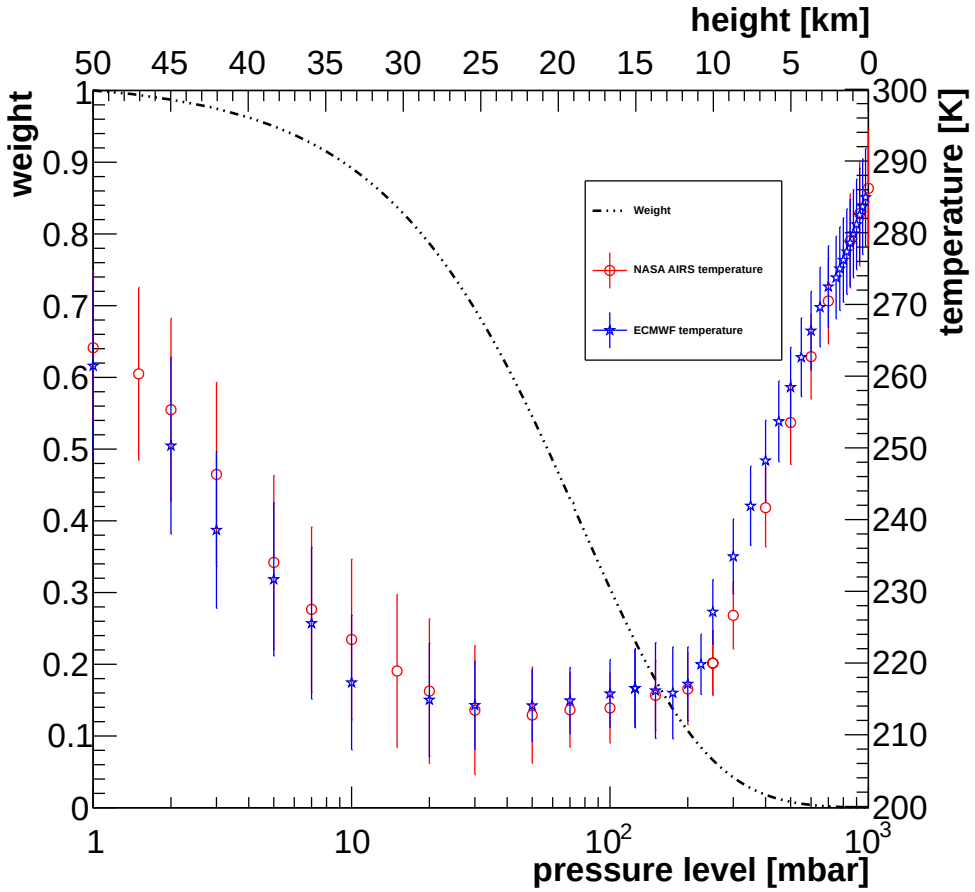

Figure 6.9: Sum of pion and kaon weight functions $W_\pi(X) + W_K(X)$ normalized to one. Shown in red and blue is the temperature profile $T(X)$ of the atmosphere above Chooz averaged per pressure level X for the considered data taking period from 2011/04/13 to 2012/03/11. The x-axis range is from 1000 mbar near sea level up to 1 mbar corresponding to approximately 50 km altitude near the top of the stratosphere.

With the parameter values being $p_0 = 2298.2\,\text{m.w.e.}$, $p_1 = 0.99809\,\text{GeV}^{-1}$ and $p_2 = 0.00192$. The calculation for the minimum 300 m.w.e. shielding of the DC far site, assuming a flat hill topology, yields a threshold energy of $E_{thr} = 74\,\text{GeV}$.

The zenith angle distribution of muons is reconstructed utilizing the RecoMuonHam muon track reconstruction algorithm. The mean of the resulting distribution is $\langle\cos\theta\rangle \approx 0.621$. Assuming that the minimum shielding of 300 m.w.e. corresponds to the direction of highest muon intensity under zenith-angle θ, the approximation $\langle E_{thr}\cos\theta\rangle \approx \langle E_{thr}\rangle\langle\cos\theta\rangle$ can be used and one finds the value of $\langle E_{thr}\cos\theta\rangle \approx 46\,\text{GeV}$. However, it should be noted that the assumption of a flat overburden is only a first order approximation and the detailed hill topology should be considered in future. This can be done by a detailed simulation of muon propagation and energy loss through the actual DC far site hill profile (see fig. 4.9).

Figure 6.9 shows the sum of both weight functions, $W_\pi(X) + W_K(X)$ normalized to 1 as a function of the pressure level X_n. This curve is superimposed with two average temperature profiles of the temperature above Chooz for the data taking period considered in this thesis.

With the definition of the effective temperature, an effective temperature coefficient α_T can be defined

$$\alpha_T = \frac{1}{I_\mu^0}\int_0^\infty dX \int_{E_{th}}^\infty dE_\mu \frac{A_M^1 E_\mu^{-(\gamma+1)}}{1 + B_M^1 (E_\mu \cos\theta/\epsilon_M^0)^2}. \tag{6.35}$$

With the definition of effective temperature T_{eff} and temperature coefficient α_T a relation between atmospheric temperature fluctuation and muon rate variation can finally be given and will be used in the analysis of the experimental data:

$$\frac{\Delta I_\mu}{I_\mu^0} = \int_0^\infty dX \alpha(X) \frac{\Delta T(X)}{T_{eff}} = \alpha_T \frac{\Delta T_{eff}}{T_{eff}}. \tag{6.36}$$

For a detector counting a number N_μ of discrete particles in time t one gets the rate $R_\mu = N_\mu/t = \int d\Omega I_\mu(\Omega)\epsilon(\Omega)A_{tot}(\Omega)$, with ϵ being the detection efficiency, A the surface area and Ω the solid angle. The constant intensity I_μ^0 corresponds to the mean rate $\langle R_\mu \rangle$ of the data set, as well as the mean effective temperature $\langle T_{eff} \rangle$ corresponds to T_{eff}. Thus one obtains an equation relating a change in the effective temperature of the atmosphere to a change in the measured muon rate

$$\frac{\Delta R_\mu}{\langle R_\mu \rangle} = \alpha_T \frac{\Delta T_{eff}}{\langle T_{eff} \rangle}. \tag{6.37}$$

6.4 The atmospheric temperature and surface pressure data

For this studies four independent environmental data sets have been used to calculate the correlation between muon rate and effective temperature and surface pressure. The measurement of the environmental data and their source will be explained in the following and in addition a LS analysis, as performed for the muon data before, will be done to search for an periodic modulation.

6.4.1 Temperature data

To calculate the effective temperature, one needs the temperature profile of the atmosphere. Two different data sets were used for this purpose. First, the temperature of the atmosphere $T(X_N)$ were obtained from the European Center for Medium-range Weather Forcasts[2] (**ECMWF**) at 37 discrete pressure level X_N corresponding to specific heights in the atmosphere. These levels are provided in the range 1-1000 mbar (1000, 975, 950, 925, 900, 875, 850, 825, 800, 775, 750, 700, 650, 600, 550, 500, 450, 400, 350, 300, 250, 225, 200, 175, 150, 125, 100, 70, 50, 30, 20, 10, 7, 5, 3, 2, 1). Four measurements are provided per day at 00:00h, 06:00h, 12:00h and 18:00h.

These data include different kinds of measurements, e.g. land or sea based surface measurements, air soundings, balloon and aircraft measurements which were taken at different

[2] http://www.ecmwf.int/

locations around the planet. ECMWF uses a global model to interpolate to a specific location, as in our case to 50.09N, 4.78E the longitude and latitude of the DC far site. Using this data set, the effective temperature was calculated with the help of the weighting functions $W_{\pi,K}$ as defined in 6.33 before

$$T_{eff} = \frac{\sum_{n=0}^{N} \Delta X_n \cdot T(X_n)(W_\pi(X_n) + W_K(X_n))}{\sum_{n=0}^{N} \Delta X_n (W_\pi(X_n) + W_K(X_n))}, \tag{6.38}$$

where ΔX_n is the difference between two adjunct pressure levels. The four measurements were averaged per day, and the error for the daily effective temperature was estimated to be $\sigma_T = \sqrt{\langle T_{eff}^2 \rangle - \langle T_{eff} \rangle^2}$, the standard deviation.

The second data set used to obtain the effective temperature at the DC far site is measured by the Atmospheric Infrared Sounder[3] (**AIRS**) instrument on NASA's[4] AQUA satellite[5]. This instrument measures the infrared and microwave brightness coming from Earth's surface and from the atmosphere in different atmospheric layers. Since this effect is temperature dependent, the AIRS instrument is able to provide accurate temperature data in different atmospheric layers. The satellite measures these data two times a day, either during descending (equatorial crossing north to south @1:30 AM local time) or ascending (equatorial crossing south to north @1:30 PM local time) orbit. In comparison to ECMWF data only 24 pressure levels (1000, 925, 850, 700, 600, 500, 400, 300, 250, 200, 150, 100, 70, 50, 30, 20, 15, 10, 7, 5, 3, 2, 1.5, 1) are being measured. Again, the measurements were averaged daily and the error is estimated by the standard deviation of the two measurements. The time series of both effective temperature data sets can be seen in figure 6.10, where the ECMWF data were plotted in blue and the NASA AIRS data in red. Both temperature data sets agree well and a variation pattern similar to the ECMWF data is apparent. This is supported by the comparison of the mean effective temperatures for the ECMWF, $\langle T_{eff} \rangle^{ECMWF} = 218.9\,\mathrm{K}$ and for the NASA AIRS data set, $\langle T_{eff} \rangle^{AIRS} = 217.1\,\mathrm{K}$, which agree within 1 %.

6.4.2 Pressure data

The surface pressure data were obtained from the National Climate Data Center[6] (**NCDC**), where meteorological data from several weather stations worldwide can be accessed. The closest of these weather stations is the military airbase at Florennes in Belgium (50.24N,4.64E). An additional weather station to cross-check the obtained surface pressure values is in the French town Charlesville-Meziers (49.78N,4.63E) roughly 40 km away from Chooz. Figure 6.11 shows a map of the Chooz location's surrounding, where both weather stations are marked as well.

The pressure data at Florennes are usually taken every hour, but there are several days were this was done less frequently. Analogue to the temperature measurements, the surface pressure was calculated as daily average with the error given by the standard deviation

[3] http://airs.jpl.nasa.gov/

[4] National Aeronautics and Space Agency

[5] The Aqua (EOS PM-1) satellite studies the precipitation, evaporation, and cycling of water. The name Aqua comes from the Latin word for water.

[6] http://www.ncdc.noaa.gov/

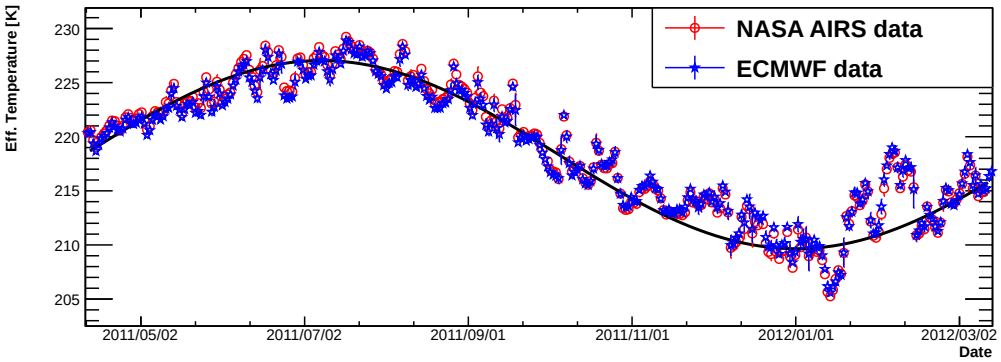

Figure 6.10: Effective temperature calculated from ECMWF (blue) and NASA AIRS (red) data in the period of interest beginning 2011/04/13 and ending 2012/03/11. The time series of effective temperatures from both data sets agree on the absolute scale and follow the same variation where slight differences in amplitude are visible. Superimposed in black is a sinusoidal fit to indicate the yearly modulation.

$\sigma_p = \sqrt{\langle p^2 \rangle - \langle p \rangle^2}$ over all measurements. The Charlesville measurements however are only collected four times a day and the value available for download at the NCDC database is already the daily average. As this is the only information provided by the weather station in addition to number of performed measurements, the error is assumed to be the same as for the Florennes data. Figure 6.12 shows the time series of both surface pressure data sets in the period of interest. The average value of around 1020 mbar is indicated by the dotted black line. Both data sets show the same time variation and agree well, also justifying the use of the Florennes error estimates for the Charlesville data. The mean values are $\langle p \rangle^{Char} = 1019.6$ mbar for Charlesville and $\langle p \rangle^{Flo} = 1020.5$ mbar for the Florennes data set.

6.4.3 LS analysis of environmental data

The LS analysis utilized before to search for periodicities in the muon data will now be used for the temperature or pressure data sets. The period of 1 year should have a significant LS power as the main time variation is given by the yearly temperature change. The periodograms for both effective temperature and surface pressure data sets can be seen in figures 6.13 - 6.16. As for the muon data, the 3σ detection threshold for a modulation is indicated by the dotted lines. Both periodograms of effective temperature show a significant LS power P, which is peaking at a period of roughly one year. However, for both pressure data sets the LS analysis yields no significant modulations above the 3σ detection threshold.

6.5 Correlation Analysis

In order to quantify any variation of muon rate with effective temperature or surface pressure, a correlation analysis was performed to measure if there is a linear dependence between the two quantities. Within this section the details of this analysis will be explained starting with an explanation of correlation and significance, which will be followed by a detailed description of the performed correlation analysis using the atmospheric data sets.

Figure 6.11: Map of the area surrounding Chooz. The red markers indicate the position of the experimental site in Chooz and the location of both weather stations. One in the city of Charlesville in France. The other located in Belgium at the Florennes military airbase. Plot made with Google maps: http://maps.google.com/.

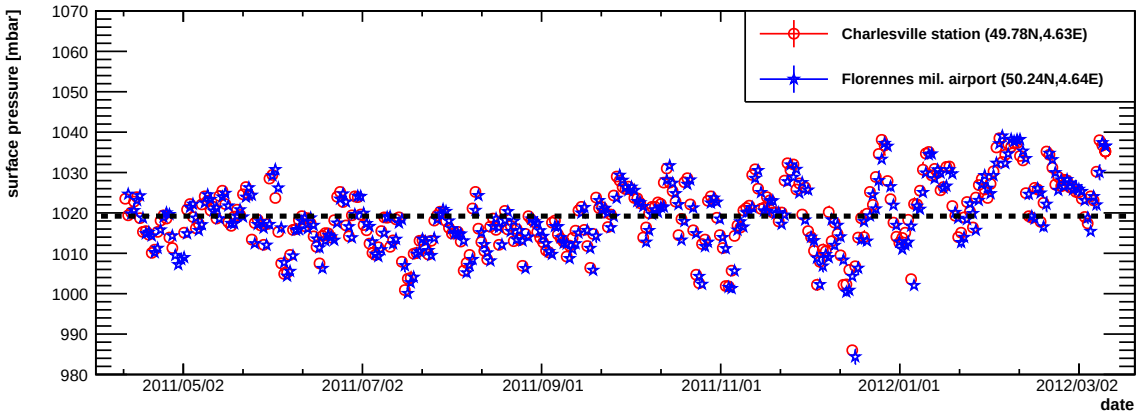

Figure 6.12: The plot shows the daily time series of the surface pressure data from the Florennes (red) and Charlesville (blue) weather stations in the period of interest.

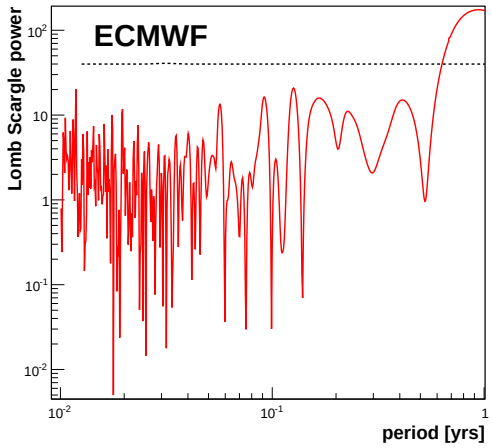

Figure 6.13: LS periodogram for the ECMWF effective temperature data.

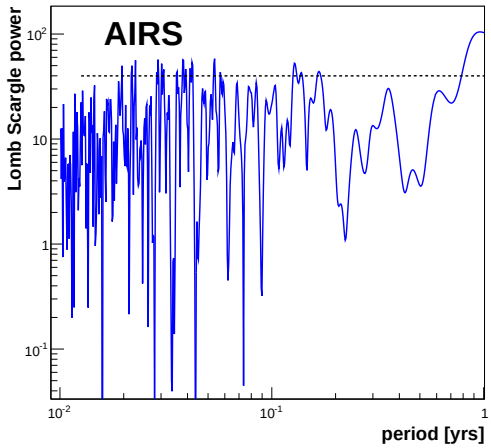

Figure 6.14: LS periodogram for the NASA AIRS effective temperature data.

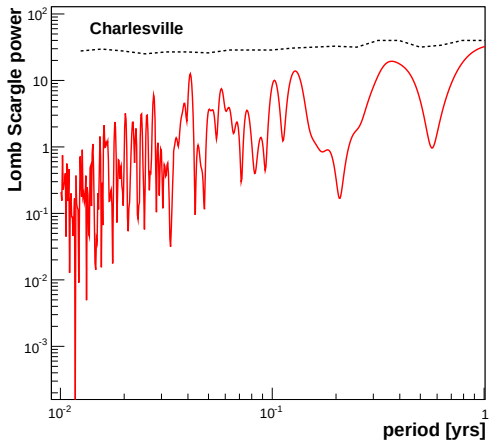

Figure 6.15: LS periodogram for the Charlesville surface pressure data.

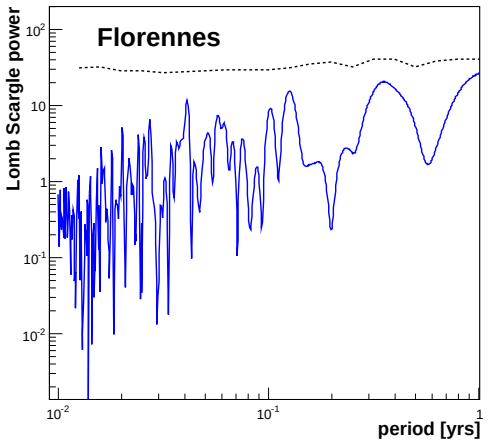

Figure 6.16: LS periodogram for the Florennes surface pressure data.

6.5.1 Correlation coefficient

Having a series of $i = 1...N$ measurements of muon rates $R_{\mu,i}$ and pressure or temperature values $X_i = \{p_i, T_i\}$ a measure for the strength of any correlation between the two values is given by the linear correlation coefficient:

$$C(R_\mu, X) = \frac{\sum_{i=1}^{N}(R_{\mu,i} - \langle R_\mu \rangle)(X_i - \langle X \rangle)}{\sqrt{\sum_{i=1}^{N}(R_{\mu,i} - \langle R_\mu \rangle)^2 (X_i - \langle X \rangle)^2}} = \frac{\sum_{i=1}^{N} R_{\mu,i} X_i - N\langle R_\mu \rangle \langle X \rangle}{(N-1)\sigma_{R_\mu}\sigma_X}. \quad (6.39)$$

The value C is called the Pearson's correlation coefficient and is calculated by dividing the covariance of the two variables by the product of their standard deviations σ_{R_μ} and σ_X. This is the so called Pearson's correlation coefficient, which is +1 if there is a perfect positive

(means increasing) linear relationship between the two variables and -1 if there is a perfect negative (decreasing) linear relationship (anti correlation). Any other degree of linear dependence is indicated by some value between -1 and $+1$.

One should note that if the variables are independent and there is no correlation the coefficient $C(R_\mu, X)$ is zero. However the opposite is not true, because only linear dependence can be quantified by this coefficient. It fails if there is a non-linear dependence.

6.5.2 Significance of correlation

In addition to the measurement of any linear dependence between two variables with the correlation coefficient C, one has to test for the significance of this relationship between the variables. This is necessary because a relationship can be strong, but not significant and conversely it can be weak but significant. For small data sets it is easy to achieve a strong correlation coefficient C just by chance, but the significance may be low. Whereas the opposite is true for big samples, where a high level of significance can easily be achieved, but the value of the correlation coefficient may be low.

The key factor is the sample size N of the data set and the value of the correlation coefficient C. The significance can be expressed in probability levels and this will tell how unlikely a specific correlation coefficient C will randomly occur given no relationship in the observed data set. Practically, this is done assuming normal distributed values of R_μ and X, being independent of each other, thus $C(R_\mu, X) = 0$, the so called null hypothesis. A test value, t, can be calculated, which follows a t-distribution with $N - 2$ degrees of freedom, where N is the number of observed couples R_μ, X [123]:

$$t = C(R_\mu, X)\sqrt{\frac{N-2}{1-C(R_\mu, X)^2}} \tag{6.40}$$

Using this test value, a p-value p describing the level of significance can be set. This determines the percentile $\alpha = 1 - p$ of the t-distribution for $M = N - 2$ degrees of freedom. The percentile is defined as the value below which a certain percent of observations fall. Depending on M and α a critical value $t(\alpha; M)$ can be calculated. If $|t| < t(\alpha; M)$ the correlation is not significant and the null hypothesis, in this case the hypothesis of no correlation cannot be rejected. The opposite is true for $|t| \geq t(\alpha; M)$, where a correlation at a significance level p is observed. This simple test mechanism was used in the following to determine the significance of any observed correlation of R_μ and X, being either T_{eff} or Δp.

6.5.3 Effective Temperature: Correlation analysis

As one of the last chapter's conclusions was the fact, that the muon data set using the normal muon tag is contaminated by events different from muons, higher cut values were chosen for this analysis. This is necessary as other event types (especially the high energetic light noise in the ID) do not follow the temperature or pressure trend. Therefore the following "strict" muon threshold was used:

- ID: $E_{vis} > 200\,\mathrm{MeV}$

	ECWMF		AIRS	
item	Cor. $C(R_\mu, T_{eff})$	α_T	Cor. $C(R_\mu, T_{eff})$	α_T
ID	0.959	0.415 ± 0.011	0.958	0.395 ± 0.011
IV	0.965	0.411 ± 0.010	0.965	0.391 ± 0.009
ID∧IV	0.959	0.415 ± 0.011	0.958	0.395 ± 0.011
ID∨IV	0.965	0.411 ± 0.010	0.965	0.391 ± 0.010
IV∧(¬ID)	0.906	0.399 ± 0.017	0.907	0.380 ± 0.016

Table 6.3: Correlation analysis of muon rates and effective temperature yielding the effective temperature coefficient α_T as a result. The left tab shows the results from the ECMWF data set, the right tab the results for the NASA AIRS data set.

- IV: $Q_{IV} > 50\,\mathrm{kDUQ}$

To quantify any correlation between the muon rate R_μ and the effective temperature T_{eff}, the rate was plotted as a function of effective temperature $R_\mu(T_{eff})$. Figures 6.17 and 6.18 show the variation of the effective atmospheric temperature $\Delta T_{eff}/T_{eff}$ for the ECMWF and NASA AIRS data sets respectively. From the plots R_μ vs T_{eff} the correlation is obvious, a strong correlation coefficient of around 0.96 for both the ECMWF and the NASA AIRS data sets is found. Utilizing the test of significance introduced before, a test value of $t \approx 61.31$ is obtained. Setting a significance level of 3σ ($99.73\,\%$, $\alpha = 0.0027$ a tabulated t-value of $t(0.0027; 320) \approx 2.81$ is found. As $t(0.0027; 320) < t$ this yields the conclusion that the observed correlation between R_μ and T_{eff} is statistically significant at more than 3σ.

Performing a linear regression between the temperature and rate values, one can obtain the temperature coefficients α_T from the data. For this the "total least square" regression method was used, which takes errors in both variables into account. The values obtained from the regression can be found in table 6.3. An error for this method can be determined by calculating a test-value t_{α_T} estimating the difference between the "true" effective temperature coefficient α_T and the value from the regression a [123]:

$$t_{\alpha_T} = (a - \alpha_T)\frac{\sigma_T\sqrt{N-2}}{\sigma_R\sqrt{1 - C(T_{eff}, R_\mu)^2}}. \tag{6.41}$$

Under the assumption that the errors in T_{eff} and R_μ are normal distributed, this test-value t_{α_T} is a random variable following a t-distribution with $N-2$ degrees of freedom. Using this, one can construct a confidence interval for α_T being

$$|a - \alpha_T| < t(\alpha; N-2)\frac{\sigma_R\sqrt{1 - C(T_{eff}, R_\mu)^2}}{\sigma_T\sqrt{N-2}}. \tag{6.42}$$

for a given confidence level $1 - \alpha$. For 322 data points and a 1σ confidence level ($\alpha = 0.05$) a critical value of $t(0.05; 320) = 1.6496$ was found and utilized to estimate the statistical error on the effective temperature coefficient found in the regression.

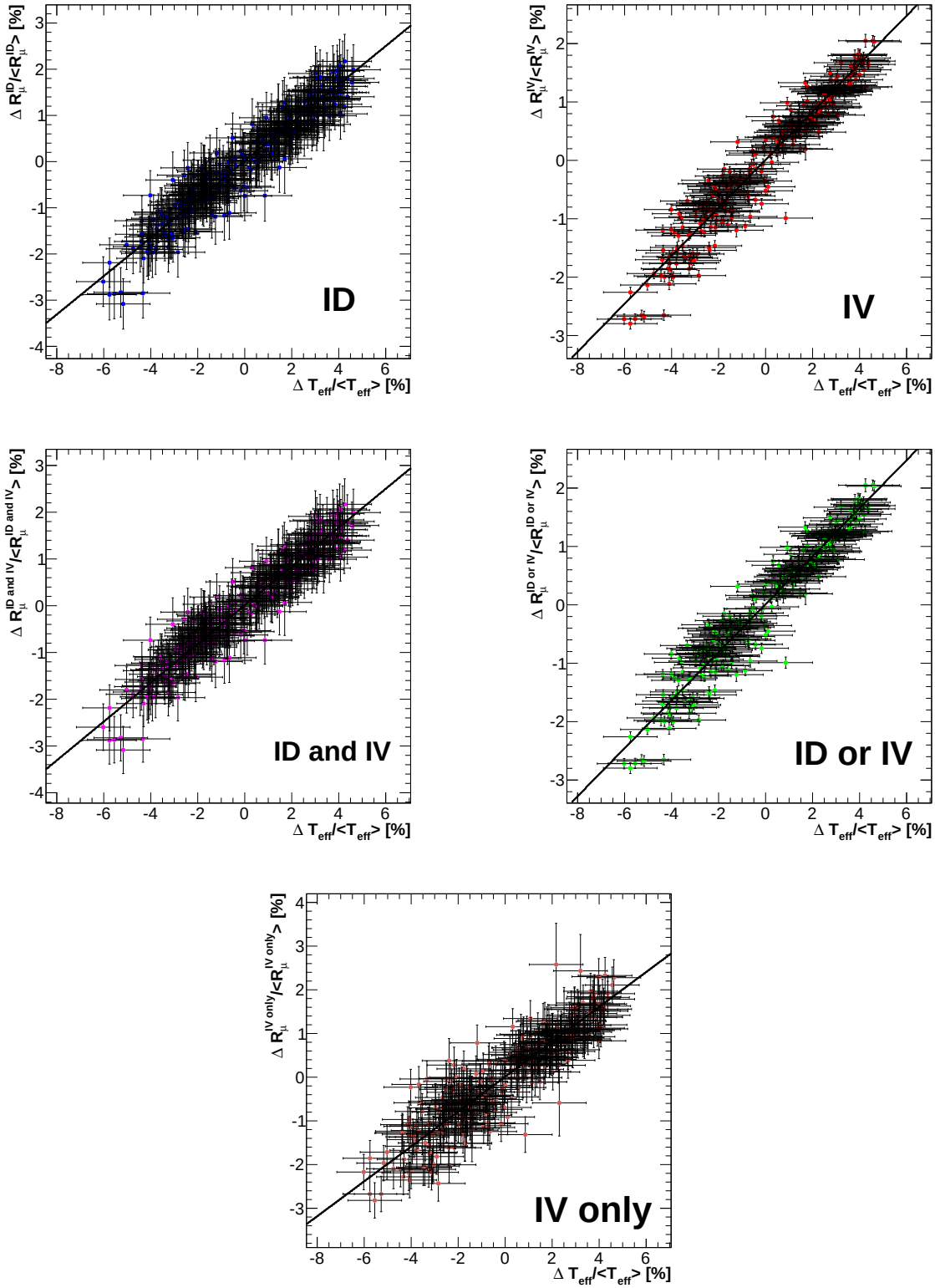

Figure 6.17: Correlation of muon rate and effective temperature for the ECMWF data set. From left to right and top to bottom the plots show the correlation for ID, IV and for the logical muon threshold combinations ID∧IV, ID∨IV and IV∧(¬ID).

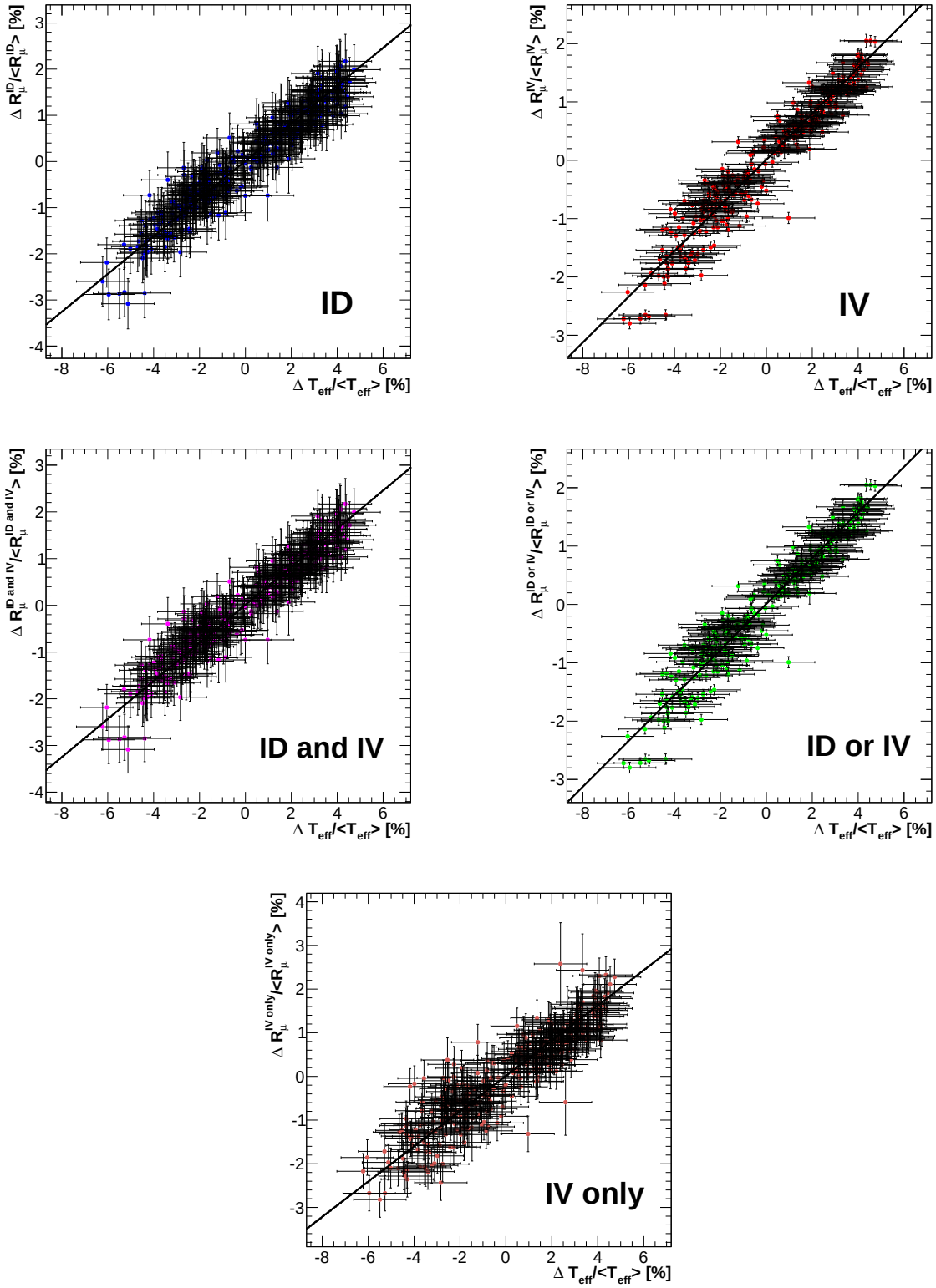

Figure 6.18: Correlation of muon rate and effective temperature for the NASA AIRS data set. From left to right and top to bottom the plots show the correlation for ID, IV and for the logical muon threshold combinations ID∧IV, ID∨IV and IV∧(¬ID).

parameter	value	error contribution
$E_{th}\cos\theta$	46 ± 10 GeV	0.6%
γ	1.7 ± 0.1	0.5%
ϵ_π	114 ± 3 GeV	0.8%
ϵ_K	851 ± 14 GeV	$< 0.1\%$
r_K	0.149 ± 0.06	$< 0.1\%$
B_π^1	1.460 ± 0.007	0.2%
B_K^1	1.740 ± 0.028	$< 0.1\%$
NASA AIRS/ECMWF	-	5.02%
total		5.15%

Table 6.4: Compilation of systematic error sources for the determination of the effective temperature coefficient.

The observed difference between the ECMWF and the NASA AIRS data sets in the values of α_T is of the order of 5 %. This could be due to the ECMWF data set, where the temperature profile of the atmosphere is actually not measured at the Chooz site, but extrapolated. For ECMWF, the measurements were taken several kilometers away and were extrapolated or calculated from a model to the detector site whereas the AIRS satellite data are actually measured in a $1^\circ \times 1^\circ$ area, where the Chooz site falls in. In addition a difference in the correlation coefficients is found, where the coefficient is smaller for ID, ID$\wedge$IV in comparison to the correlation correlation coefficient for IV, ID$\vee$IV. An example is the correlation coefficient of muon candidate events identified in the IV only, where the difference is much bigger. This could be due to a contamination from non-muon events including radioactivity from the PMTs itself or FN.

As only muons are expected to deposit the high amount of energy requested by the logical and combination of both thresholds in both detector volumes, the ID and IV correlation should be the one having the least contribution from non-muon events. Thus, this value will be taken as the measurement of α_T obtained with AIRS temperature data, where the difference to the ECMWF data is taken as systematic error regarding the used temperature data set. Additional parameters that induce systematic errors are the threshold energy $E_{thr}\cos\theta$, and the parameters $\gamma, \epsilon_\pi, \epsilon_K, r_K, B_\pi^1$ and B_K^1 used in the calculation of the effective temperature. To estimate the systematic error to the effective temperature coefficient α_T, each input parameters was varied within it's error bounds to calculate a new effective temperature T_{eff}^*. Than a correlation analysis between R_μ and T_{eff}^* was performed and the resulting parameter α_T^* was extracted. The fractional changes of the effective temperature coefficient with changes in the input parameters can be found in table 6.4. These systematic errors were added in quadrature and thus the DC far measurement of the effective temperature coefficient is

$$\alpha_T = 0.39 \pm 0.01(stat.) \pm 0.02(syst.),$$

in very good agreement with the expected calculated number of 0.387 for $E_{thr}\cos\theta = 46\,\text{GeV}$ from theory (see also fig. 6.21).

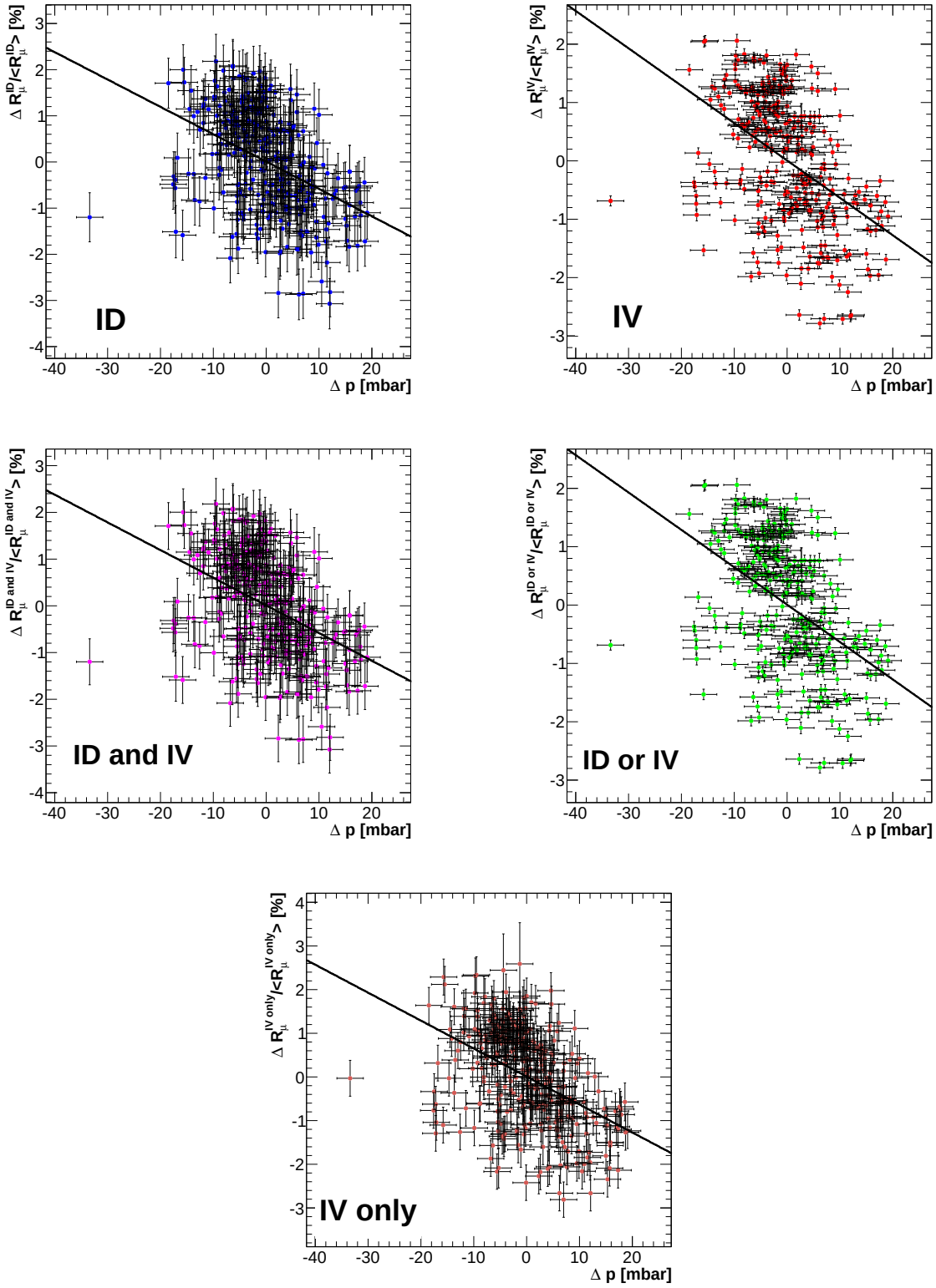

Figure 6.19: Correlation of muon rate and surface pressure for the Charlesville data set. From left to right and top to bottom the plots show the correlation for ID, IV and for the logical muon threshold combinations ID∧IV, ID∨IV and IV∧(¬ID).

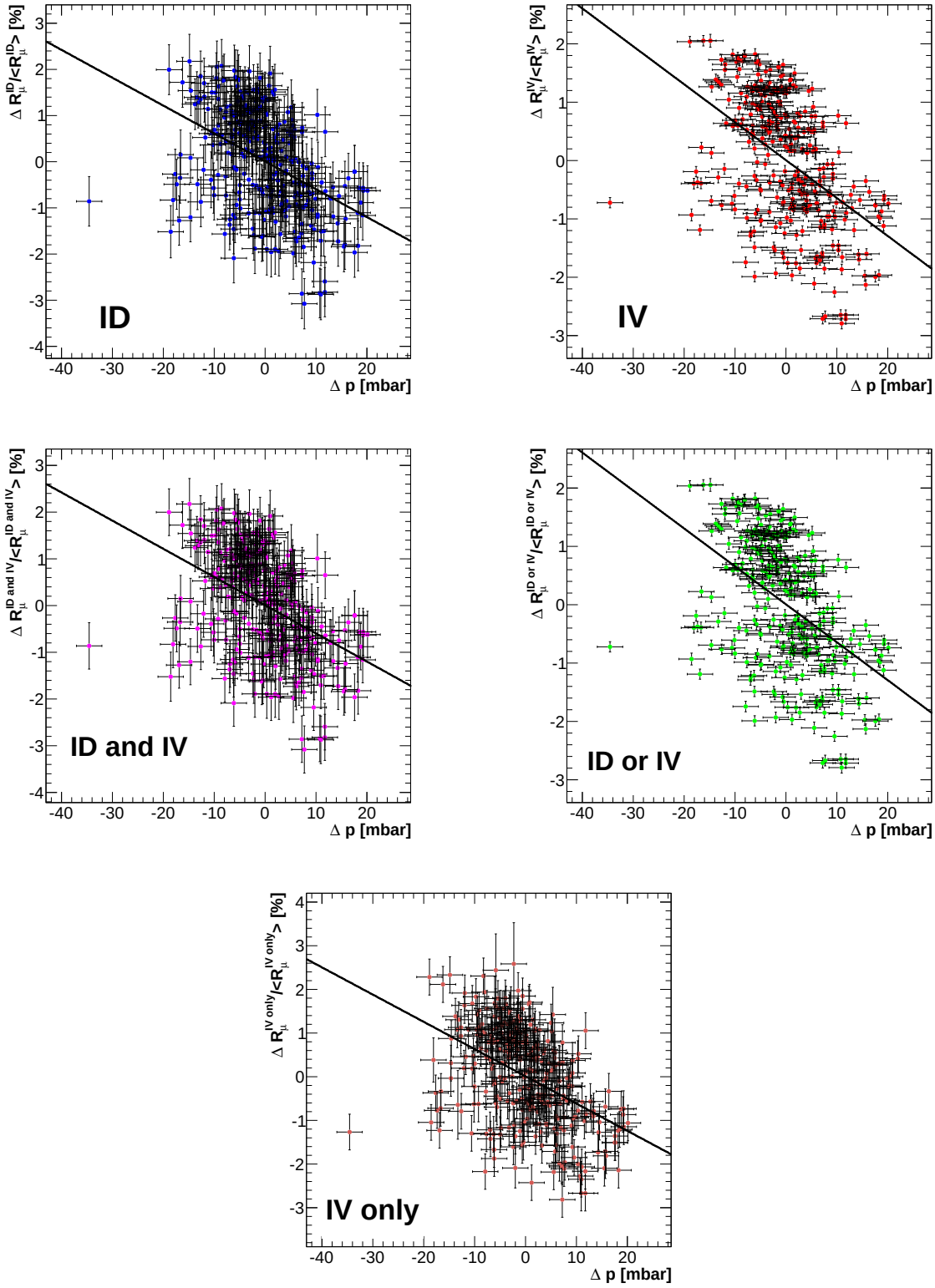

Figure 6.20: Correlation of muon rate and surface pressure for the Florennes data set. From left to right and top to bottom the plots show the correlation for ID, IV and for the logical muon threshold combinations ID∧IV, ID∨IV and IV∧(¬ID).

6.5.4 Surface pressure: Correlation analysis

As it was done in the correlation analysis before, the relative change in muon rate $\Delta R_\mu/\langle R_\mu\rangle$ was plotted versus the values of pressure change Δp. This was done for both pressure data sets taken at either Charlesville or Florennes. These plots can be found in figures 6.19 and 6.20 for the logic combinations of the muon tags. The obtained correlation coefficients can be read from table 6.5, being in the range of -0.42 to -0.48. The corresponding test values t are in the range of 8.28 to 10.06, varying much more between the different logical threshold combinations than in the case of the effective temperature. However, as these test-values are bigger than the critical value of $t(0.0027; 320) = 2.81$, the observed correlations are still significant at a 3σ level.

Again, a linear relation is expected between both values and a linear regression is performed in order to extract the pressure coefficient β_p. As before in the effective temperature case, a Total Least Squares approach is used taking into account errors in p and R_μ. As for α_T in eq. 6.41, a confidence interval for β_p was constructed:

$$|\beta_p - b| < t(\alpha; N-2)\frac{\sigma_R\sqrt{1-C(p,R)^2}}{\sigma_p\sqrt{N-2}}, \tag{6.43}$$

estimating the difference between the regression value b and the "true" barometric coefficient β_p. For the 325 (320) data points of the Florennes (Charlesville) data set and a 1σ confidence level ($\alpha = 0.05$) a critical value of 1.6497 (1.6496) was found and utilized to estimate the statistical error on the barometric coefficient obtained from the regression.

The results of this analysis, as well as the associated errors can be found in table 6.5. As for the effective temperature coefficient α_T there is a difference between the two used pressure data sets and again a difference regarding the logical combinations of the muon thresholds. The value taken for the measurement of the barometric coefficient β_p is the one with the combination ID$\wedge$IV, as only muons are expected to deposit enough energy required by the tag in both detector volumes. The difference between both data sets is taken as a systematic error, where the value obtained with the Florennes data is used, as this site is much closer to the detector than the weather station at Charlesville. Thus, the measured barometric coefficient is found to be

$$\beta_p = -0.59 \pm 0.20(stat.) \pm 0.10(syst.)\,‰/\text{mbar},$$

matching the order of magnitude of the simple prediction that was made in Section 6.3 of this chapter. This prediction yields $-2‰/\langle p\rangle = -2‰/1017\,\text{mbar} \approx 1.97\,‰/\text{mbar}$ being off by a factor of 3.

6.6 Measurement of the atmospheric pion/kaon ratio

Having quantified the effect of a atmospheric temperature change of the muon rate measured in the DC far detector, it is possible to determine the atmospheric K/π ratio. This is possible because the production, propagation and decay of pions and kaons are differently

	Florennes		Charlesville	
item	Cor. $C(R_\mu, p)$	β_p (mbar)	Cor. $C(R_\mu, p)$	β_p (mbar)
ID	-0.438	-0.60±0.11	-0.419	-0.59±0.20
IV	-0.479	-0.65±0.11	-0.460	-0.64±0.19
ID∧IV	-0.438	-0.60±0.11	-0.419	-0.59±0.20
ID∨IV	-0.479	-0.65±0.11	-0.460	-0.64±0.19
IV¬ID	-0.453	-0.63±0.11	-0.453	-0.64±0.20

Table 6.5: Correlation analysis of muon rates and surface pressure yielding the barometric coefficient β_p as a results. The left tab showing the results from the Florennes data set, the right tab the results for the Charlesville data set.

affected by atmospheric temperature variations. Such measurements were performed first by MINOS [121] and later by ICECUBE [124] using cosmic ray muons. In this case, the basic reaction is the interaction of a primary cosmic ray proton with an air nucleus, $p + A_{atm}$. Previous measurements at accelerators used the reactions $p + p$, $p + \bar{p}$, p+Pb and Au+Au collisions. The nominal value of $r(K/\pi) = 0.15 \pm 0.06$ is taken from [90], which is based on this laboratory measurements below 100 GeV center of mass energy.

The theoretical prediction for the effective temperature coefficient α_T^{th} can be written as a temperature derivative of the muon intensity [88]

$$\alpha_T^{th} = \frac{T}{I_\mu}\frac{\partial I_\mu}{\partial T} = -\frac{E_{th}}{I_\mu}\frac{\partial I_\mu}{\partial E_{th}} - \gamma. \tag{6.44}$$

This can be calculated with the help of the muon intensity given by eq. 7.7

$$\alpha_T^{th} = \frac{1}{D_\pi}\frac{1/\epsilon_K + A_{K\mu}(D_\pi/D_K)^2/\epsilon_\pi}{1/\epsilon_K + A_{K\mu}(D_\pi/D_K)/\epsilon_\pi}. \tag{6.45}$$

In the form of α_T^{th} in eq. 6.45 above, the D_M functions for meson species $M = \{K, \pi\}$ are defined as

$$D_M = \frac{\gamma}{\gamma + 1} \cdot \frac{\epsilon_M}{1.1 E_{th} \cos\theta} + 1, \tag{6.46}$$

with ϵ_M being the critical meson energy. This is the theoretical prediction incorporating both, pions and kaons contributing to the measured muon intensity. If only pions contribute to the measured seasonal effect, $A_{K\mu} = 0$ is set to zero, and this defines the pion scaling limit $(\alpha_T)_\pi$. If, however, only kaons contribute, $A_{\pi\mu} = 0$ must be set to zero instead and the kaon scaling limit $(\alpha_T)_K$ can be obtained. Writing down the scaling limits for both meson species results in

$$(\alpha_T)_\pi = 1/\left[\frac{\gamma}{\gamma+1}\frac{\epsilon_\pi}{1.1 E_{th}\cos\theta} + 1\right], \quad (\alpha_T)_K = 1/\left[\frac{\gamma}{\gamma+1}\frac{\epsilon_K}{1.1 E_{th}\cos\theta} + 1\right]. \tag{6.47}$$

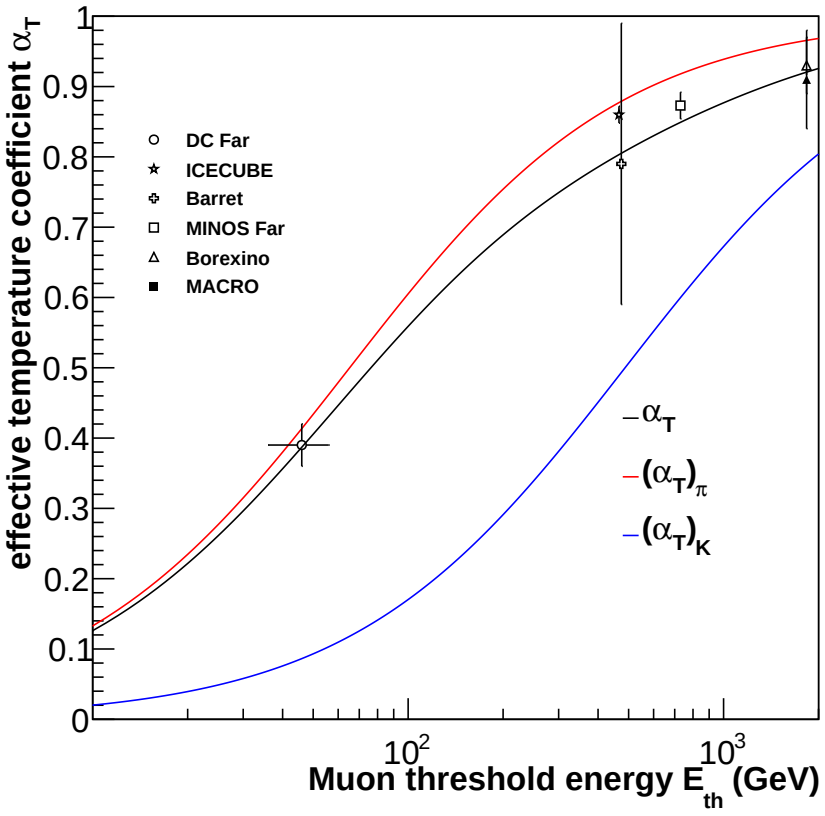

Figure 6.21: Plot of the theoretically expected α_T as a function of E_{thr} in black, where the limit for pions is given in red $(\alpha_T)_\pi$ and the limit for kaons $(\alpha_T)_K$ in blue. Various measurements of the effective temperature coefficient including the result of this work present in the last section are shown as well.

The theoretical expectation of the limits, $(\alpha_T)_\pi$ and $(\alpha_T)_K$, as well as α_T^{th} can be seen in figure 6.21, where also the result of this work and other experiments is shown.

The atmospheric kaon to pion ratio $r(K/\pi)$ enters the calculation of α_T^{th} implicitly via the parameter $A_{K\mu}$ in eq. 6.45. By calculating the effective temperature coefficient as a function of the ratio, $\alpha_T^{th}(r(K/\pi))$, and comparing it with the measured experimental value α_T^{exp}, one can actually determine the ratio for the interaction of protons with air nuclei $p + A_{atm}$. The experimental value α_T^{exp} is a weak function of $r(K/\pi)$ as pions and kaons have different critical energies ϵ_M and attenuation lengths Λ_M. These values enter the calculation of T_{eff}. The dependence of α_T^{exp} on the ratio $r(K/\pi)$ was evaluated by taking a specific value of $r(K/\pi)$ in the calculation of the effective temperature which was than used to perform a correlation analysis to extract α_T. Now, this α_T is the value of the effective temperature coefficient at the specific kaon to pion ratio. By plotting the theoretical calculation, α_T^{exp}, versus the measured one, α_T^{exp}, and varying the kaon to pion ratio in both cases, the ratio itself can be determined from the intersection point of both curves. This is shown in figure 6.22.

The intersection point and the error of this measurement can be obtained assuming gaussian

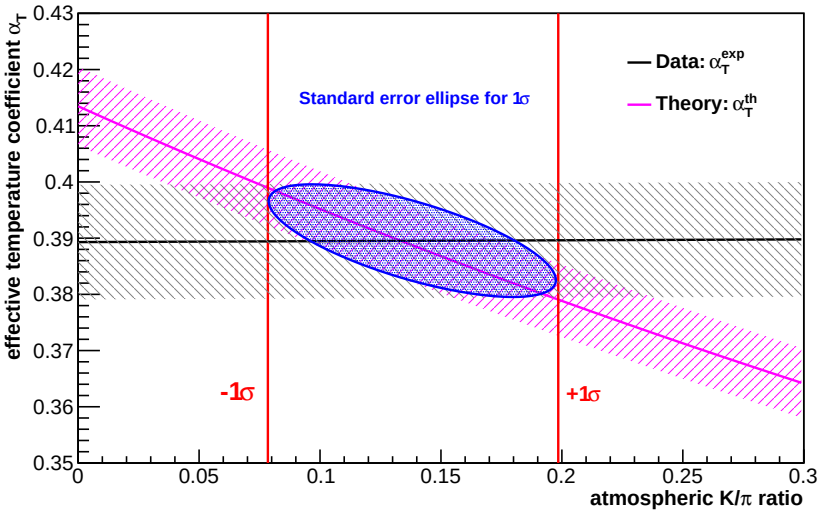

Figure 6.22: Determination of kaon to pion ratio. The experimental α_T^{exp} at the DC far site is plotted in grey as a function of the kaon to pion ratio. This curve is superimposed with the theoretical prediction α_T^{th} in magenta. The intersection happens at 0.14, the 1σ range on the x-axis is indicated by the red lines, the 1σ standard error ellipse drawn in blue centered at the intersection point of theoretical expectation and measured values.

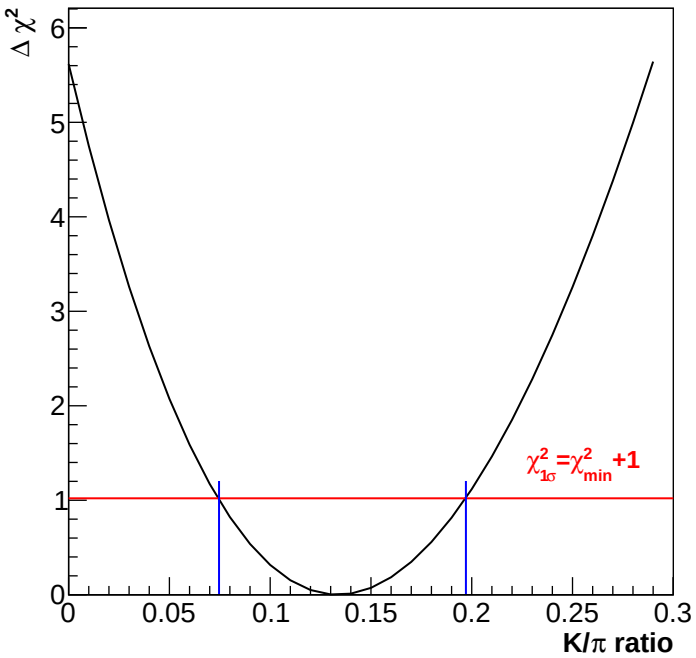

Figure 6.23: Determination of intersection point and 1σ confidence interval of the kaon to pion ratio. The minimum of the χ^2 function, χ^2_{min}, defines the intersection point. This is shown by the red line, corresponding to the values $\chi^2_{min}+1$. The intersection of this line with the parabolic χ^2 function yields the 1σ range for the kaon to pion ratio measurement. The projection of these points on the x-axis is shown in blue and defines the error for the kaon to pion ratio measurement.

distributed errors for the measured α_T value, neglecting the systematic error given by the difference between ECMWF and NASA AIRS data. For each considered value of the kaon to pion ratio $r(K/\pi)$ a χ^2 function is computed according to

$$\chi^2(r(K/\pi)) = \frac{(\alpha_T^{exp} - \alpha_T^{th})^2}{\sigma_{exp}^2 + \sigma_{th}^2}. \tag{6.48}$$

The resulting χ^2 is a quadratic function of the kaon to pion ratio $r(K/\pi)$ having a minimum at the intersection point of the theoretical and experimental curves. This point is found by fitting with a simple parabola and determining the minimum, χ^2_{min}, of the resulting function. To estimate the influence of the statistical errors, the line defined by all points fulfilling $\chi^2_{min} \rightarrow \chi^2 + 1$ is calculated. The intersection of this line with the parabolic χ^2 function defines the one sigma (68 %) confidence interval for the determined value of $r(K/\pi)$. This is indicated by the blue lines in figure 6.23. Coming back to figure 6.22, the ellipse in blue defines the 1σ contour around the intersection point. Thus a 1σ confidence interval for the measured kaon to pion ratio measurement is obtained, leading to a value of

$$r(K/\pi) = 0.14 \pm 0.06.$$

Figure 6.24 shows the comparison of this measurement with measurements made at accelerators (NA49, E735, STAR) [125–128] and with cosmic ray muons (MINOS, ICECUBE) [121, 124]. The result of this analysis is directly comparable to the two results obtained from seasonal variations of cosmic muons, whereas they are not directly comparable to the accelerator based measurements. This is because the energy of the primary cosmic ray proton, E_0, is not very well known unlike in accelerator experiments, where the center of mass energy is well known.

However, a lower limit for the primary proton energy can be estimated according to $E_0 \geq 37 \cdot E_{thr}$ [90]. This includes the assumption that the primary proton must have had at least the minimum energy a muon needs to reach the DC far detector, which it had transferred to the muon via it's parent mesons. Nevertheless, all measurements of the ratio are presented on the same energy axis to have a broad overview and enable comparison to some extent.

6.7 Conclusion

A seasonal variation in the measured muon rates at the DC far underground site was found. A simple cosine fit to the data yielded a first clue of a seasonal variation pattern with a period of roughly 340-370 days. Applying "stricter" cut values of $E_{vis} > 200\,MeV$ in the ID and $Q_{IV} > 50$ kDUQ in the IV for the muon selection, variations in the order of 1.4 % for both detectors, the ID and the IV were found. The period of 351/366 days (ID/IV) is compatible with yearly changes in the temperature in the atmosphere yielding a maximum in summer and a minimum in winter. A measurement of the effective temperature and barometric coefficients, α_T and β_p was performed, which represent the strength of the connection between a change in temperature or pressure with a change in muon rate. The values obtained are

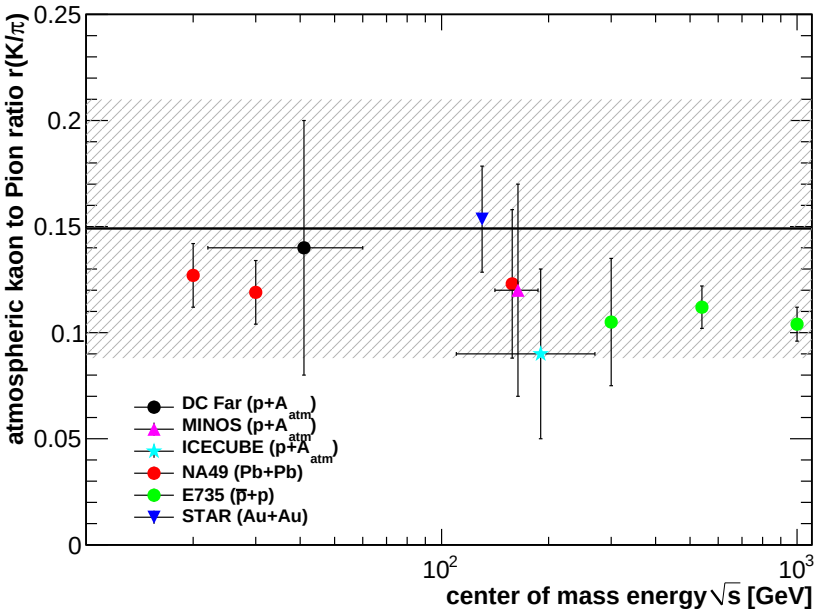

Figure 6.24: Compilation of various kaon to pion ratio measurements. The black line corresponds to the theoretical expectation of 0.149, where the uncertainty in the order of 40 % is indicated by the shaded region in grey. The measurements are taken from [121, 124–128]. However, it should be noted that the accelerator measurements are not directly comparable to the measurements utilizing the seasonal modulation method. Nevertheless they are plotted on the same energy axis for comparison.

$$\begin{aligned} \alpha_T &= 0.39 \pm 0.01(stat.) \pm 0.02(syst.), \\ \beta_p &= -0.59 \pm 0.20(stat.) \pm 0.10(syst.)\,‰/\text{mbar}. \end{aligned}$$

With the determination of the effective temperature coefficient α_T, it was possible to obtain the atmospheric kaon to pion ratio from the seasonal variation of the muon rate:

$$r(K/\pi) = 0.14 \pm 0.06.$$

This value is compatible with various accelerator measurements of the channels $p+p$, $p+\bar{p}$, Pb+Pb and Au+Au. It is also compatible with other measurements of the channel $p+A_{atm}$ performed by the MINOS and ICECUBE experiments using the same indirect method by analyzing the seasonal variation of muon rate.

It should be noted that the values of α_T and $r(K/\pi)$ moderately depend on the chosen value of $E_{th}\cos\theta$, which was found in the approximation of a flat hill topology. For future studies, a detailed Monte Carlo simulation of muon transport through matter, taking into account the detailed hill profile of the DC far site should be performed with the aim to calculate the mean threshold energy. The tools (MUSIC and MUSUN) for such a simulation are ready and were already used to calculate the mean muon energy as a function of depth underground in the next chapter.

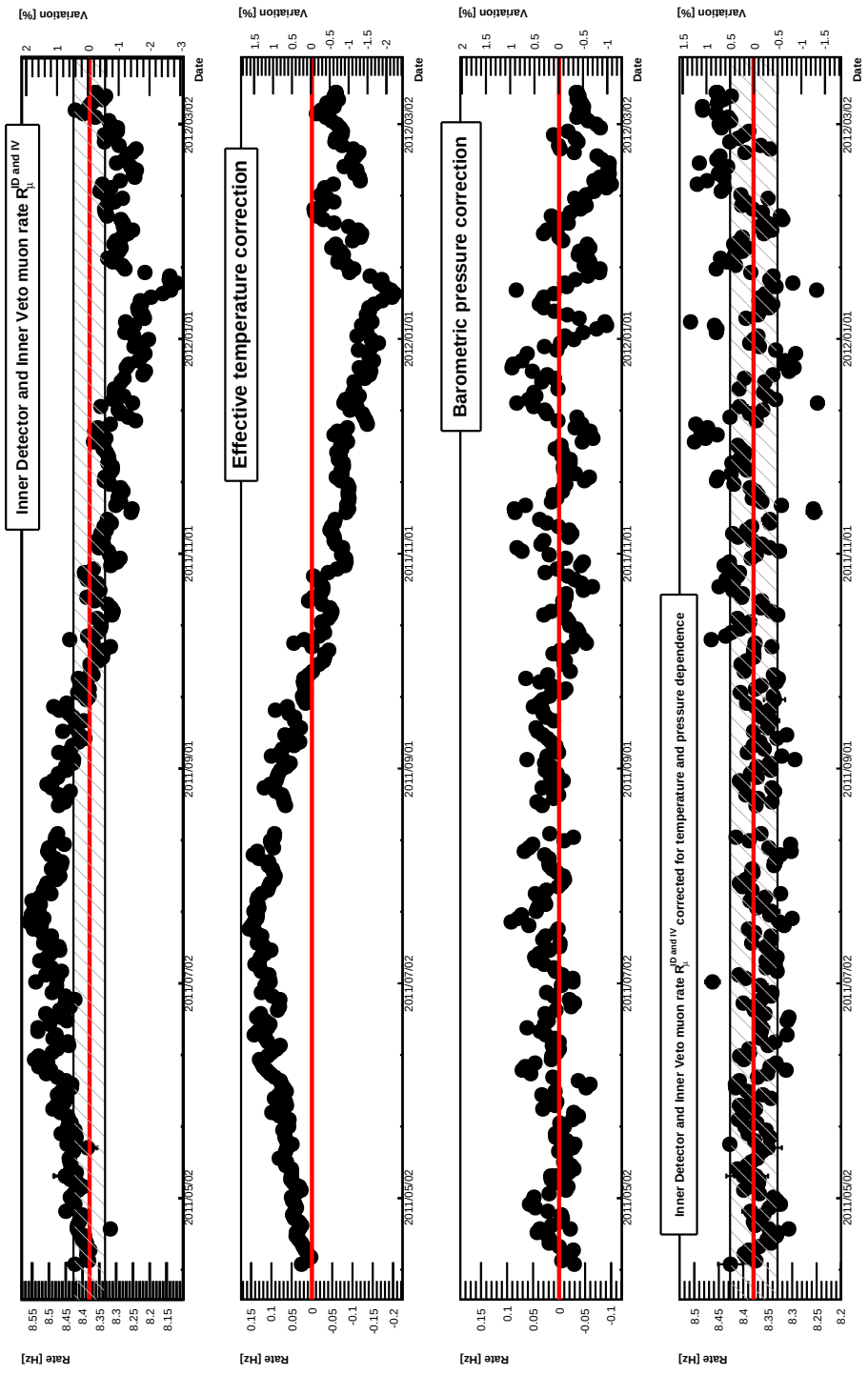

Figure 6.25: The upper panel shows the uncorrected rate for the logical and combination of the muon, $R_\mu^{ID\,and\,IV}$, obtained by the application of the "strict" cut values $E_{vis} > 200\,\mathrm{MeV}$ in the ID and $Q_{IV} > 50\,\mathrm{kDUQ}$ in the IV. The rms muon rate value, 8.38 Hz, is indicated by the red line and $\pm 0.5\,\%$ variation by the grey hatched band. The panels below show the rate corrections, first the correction for effective temperature with coefficient α_T and then for barometric pressure with coefficient β_p. The panel at the bottom shows the residual muon rate after being corrected for both effects. The remaining variation is around $0.5\,\%_{rms}$ and could be due to detector effects or an under/overestimation of the atmospheric coefficients α_T and β_p.

Having measured the strength of the atmospheric effects described by the effective temperature and barometric coefficients it is possible to correct for them. This was done for each day d were muon, $R_\mu^{\text{meas.}}(d)$, effective temperature, $T_{eff}(d)$, and surface pressure data, $p(d)$, were available. For the barometric effect, as the coefficient β_p is measured in permil, the coefficient is divided by 10 and the mean muon rate is divided by 100 % to match dimensions.

$$\begin{aligned} R_\mu^{\text{ID and IV}}(d) &= R_\mu^{\text{meas.}}(d) - \langle R_\mu \rangle \alpha_T \times \left\{ \frac{T_{eff}(d) - \langle T_{eff} \rangle}{\langle T_{eff} \rangle} \right\} \\ &- \left(\frac{\langle R_\mu \rangle}{100\,\%} \right) \left(\frac{\beta_p}{10} \right) \times \Big\{ p(d) - \langle p \rangle \Big\} \end{aligned} \tag{6.49}$$

Figure 6.25 shows the uncorrected muon rate $R_\mu^{\text{ID and IV}}$ in the uppermost panel. The rms muon rate value of 8.38 Hz is indicated by the red line and the hatched grey area visualizes a fluctuation of ± 0.5 %. This is followed by the rate corrections with effective temperature and surface pressure. The lowest panel shows the muon rate corrected for both effects. Correcting the temperature dependence leaves a (seasonal) un-modulated muon rate having fluctuations around the mean of $+0.5$ % and -1 % indicating a stable muon rate at this level. Applying the pressure correction, the residual muon rate variation is found to be $0.5\,\%_{rms}$. The remaining fluctuations could be due to detector effects matching the fluctuation of the energy scale of $0.61\,\%_{rms}$[7]. In addition there could be an under/over estimation of the temperature and pressure effects. Having an extended data set in the future could help to assess the latter.

[7]The energy scale utilized in this thesis will be explained in chapter 8.

"Science never solves a problem without creating 10 more."

George Bernhard Shaw
(1856-1950)

7

Extrapolation of the backgrounds measured by Double Chooz to Daya Bay and RENO

Among the currently running three reactor neutrino experiments, the DC experiment is unique because it can measure the backgrounds to the neutrino signal when both reactors at the Chooz nuclear power plant are shutdown for maintenance. For the other experiments, Daya Bay and RENO, this situation is highly unlikely, as they are located at nuclear power stations with five or even six cores. Therefore the DC data set collected during the period were both reactor are shutdown gives a singular opportunity to check and verify the background estimates and predictions for the other reactor experiments and also for future experiments. The input is a data set of 7.53 days in total, taken in October 2011 and in June 2012 where both reactors at the Chooz nuclear power station were shut down.

Dedicated work [129] was done to extract the spallation neutron and βn-emitter backgrounds for this periods, whereas this chapter only briefly summarizes this work in its first section. The main focus of this chapter is an analysis that was done as part of a special working group within DC aiming to extrapolate or scale these background rates to obtain predictions for the other reactor neutrino experiments. As these backgrounds are produced by cosmic muons, the second part of this chapter concentrates on the aspects of the determination of the muon flux at the DC far site. This is followed by the extrapolation of the DC far muon flux and mean muon energy to the specific depths of the RENO and Daya Bay (DB) detectors. Having obtained these scaling functions, the middle of this chapter concentrates on the derivation of the general extrapolation formula that can be used to calculate the background rates of neutrons and βn-emitters for the other experimental sites. With the muon related numbers as an input, the spallation neutron and βn-emitter rates were calculated and compared to published values at the end of the chapter .

The work that will be presented in the following was condensed into an internal technical note [130] and its results became the second part of a dedicated paper [131] on the measurement of the reactor off-off background rates in the DC experiment and the extrapolation of these backgrounds to the other reactor neutrino experiments Daya Bay and RENO. The first part of this paper concentrates on the extraction of these background values using the same cuts as in the general DC neutrino oscillation analysis.

7.1 How to measure correlated backgrounds

This first section will introduce the applied selection to extract the fast neutron **FN** and cosmogenic βn-emitter backgrounds from the combined 7.53 days reactor shutdown data set. These measurements are important as they provided the DC Far "anchorpoints" that will be used in the extrapolation to the other reactor neutrino experiments Daya Bay and RENO. For both backgrounds two different selections will be presented, the one named first selection used in the first published analysis [55], and the second selection used in the most recent analysis [56]. First, this accounts for the better knowledge of background behavior gained between the two published analysis, and second, because the results of first selection are more comparable to the RENO experiment, whereas the results obtained with the second selection are more comparable to Daya Bay measurements.

Fast neutrons

The rate of FN was estimated using the same cut conditions as for the IBD analysis, namely the neutrino selection cuts 1-5 as discussed in chapter 4, but extending the prompt energy window from 12.2 MeV to 30 MeV. In the first analysis, the FN event rate measured in this energy region was extrapolated to the neutrino signal region (0.7 MeV$< E_{prompt} <$ 12.2 MeV) assuming a flat energy spectrum. In the following this type of FN selection will be referred as "**DC I**'. The OV was not used in this analysis, as it was partially not ready for the full analysis period.

However, the FN sample obtained with this selection is not pure. It includes a contribution of stopping muons (SM). In the second selection, FN/SM were separated using the time difference between the neutrino like coincidence and the preceding muon $\Delta T_{\mu\nu}$. Cutting on $\Delta T_{\mu\nu} < 10\,\mu$s yields mostly SM, whereas a cut on $\Delta T_{\mu\nu} > 10\,\mu$s yields mostly FN. Instead of simple extrapolation of the measured rate in the $12.2-30$ MeV energy window to the neutrino energy region, assuming a flat energy spectrum, the shape of FN/SM energy spectrum was measured using the IV and the OV. The IV is sensitive to FN via proton recoils or captures on H. A sub threshold analysis was performed[1] demanding at least two IV PMTs to be hit to reject a FN/SM. For the data-taking period were the OV was available, it was used as a veto for the prompt trigger of the neutrino like coincidence. This type of analysis will be called "**DC II**" analysis in the following.

Cosmogenic βn-emitters

Considering cosmogenic βn-emitters, the first selection uses the triple coincidence of a high energy cosmic muon ($E_\mu > 600$ MeV) and a neutrino like, coincidence (cuts 1-5). In the following this type of analysis will also be called "**DC I**", whereas the second selection scheme used in the most recent analysis will called be"**DC II**", in analogy to the FN case. In this second selection several energy regimes and different parts of the ID were considered. A cut of $E_\mu > 600$ MeV selects muons crossing the NT, whereas a energy window of $275 < E_\mu < 600$ MeV selects muons crossing the NT and GC. To remove uncorrelated pairs, a

[1] Actually the IV detection threshold was lowered to ≈ 1 MeV in the IV, whereas the self-triggering threshold of the IV is around 4 MeV. This could be achieved by considering events recorded by an ID trigger.

	correlated backgrounds [cpd]				
period	**1st analysis [55]**	**2nd analysis [56]**		**reactor off-off [129]**	
selection	**DC I**	**DC I**	**DC II**	**DC I**	**DC II**
FN/SM total	0.83 ± 0.38	0.93 ± 0.26	0.67 ± 0.20	N/A	N/A
FN	N/A	N/A	0.30 ± 0.14	0.33 ± 0.16	0.23 ± 0.18
βn	2.3 ± 1.2	N/A	$2.05^{+0.62}_{-0.52}$	1.7 ± 0.9	1.1 ± 0.8

Table 7.1: Comparison of different measurements of FN and βn-emitter backgrounds, utilizing two different selections as quoted in [55, 56] and different data samples. Namely the data set with reactors on of the first and second analysis period and the off-off data sample , where both reactors at the Chooz site where shutdown for maintenance. The rates obtained from the latter will be used as input values for the scaling presented in this chapter.

spacial cut on the distance of closest approach of the IBD like coincidence to the muon track, $d_{\mu\nu} < 80\,\text{cm}$, was applied. In the low energy region below 275 MeV, also using a spacial cut, only muons crossing the buffer or the rim of the GC are selected. Combining the different energy regimes, the overall rate of βn-decay events can be measured.

For the combined reactor shutdown periods both selections were used to obtain the correlated backgrounds. This yields a rate of $R_n^{DC\,I} = 0.30 \pm 0.16\,\text{counts per day}$ (**cpd**) or a rate of $R_n^{DC\,II} = 0.23 \pm 0.18\,\text{cpd}$ for the FN background. Regarding the cosmogenic βn-background, a rate of $R_{\beta n}^{DC\,I} = 1.7 \pm 0.9\,\text{cpd}$ was measured for a DC I like selection, and a rate of $R_{\beta n}^{DC\,II} = 1.1 \pm 0.8\,\text{cpd}$ for a DC II like selection. These correlated background rates are summarized in table 7.1 below, where they are also compared to the background rates obtained from the reactor "on" periods, as quoted in [55, 56].

7.2 Determination of the muon flux from the off-off data set

As explained in chapter 5, and in more detail in [129], the determination of the muon rate for a given run can be done by counting the number of events fulfilling the muon threshold conditions and dividing them by the duration of the run. The results of this rate determination and the data taking time for both off-off periods can be found in Table 7.2. The stability of the muon rates during both periods is found to be better than 1%. The difference can be understood, since the first period was in November, where one expects a lower flux due to the atmospheric correlations described in the chapter 6 before. Whereas the second period was in June having higher muon rate values. The average muon rate during both reactor off-off periods was found to be $46.40\,s^{-1}$.

This muon rate, R_μ, measured within a given volume needs to be converted into a muon flux, Φ_μ, in order to compare between different experimental sites. In the following three different

	off-off period 1	**off-off period 2**	**total off-off**
data taking time [d]	0.93	6.60	7.53
muon rate [s^{-1}]	45.99 ± 0.02	46.46 ± 0.01	46.40 ± 0.01

Table 7.2: Data taking time and average muon rates during both reactor off-off periods.

methods to determine the muon flux at the DC far site will be discussed:

Effective area method

In this simple method one divides the muon rate $R_\mu^{\text{ID or IV}}$ by the effective detector area. The effective detector area is defined as the geometrical projection of the detector surface perpendicular to the muon track. For muons coming straight from above this would be the area πR^2, whereas it would be $2RL$ for muons coming from the side. This changes to $2RL\cos\theta$ for muons impinging with zenith-angle θ. Adding up these two contributions and assuming a mean zenith-angle of 45°[2] one ends up with

$$\Phi_\mu^{DC} = \frac{R_\mu^{\text{ID or IV}}}{\pi R^2 + 2RL\cos(45°)}. \tag{7.1}$$

Using the measured rate of $46.40\,s^{-1}$ and the IVs dimensions of $R = 3.25\,\text{m}$ and $L = 7\,\text{m}$ (effective area $65.4\,\text{m}^2$) this conversion yields a flux of $0.71\,\text{s}^{-1}\text{m}^{-2}$.

Sphere method

This method utilizes the muon tracking algorithm to reconstruct muon tracks in the ID. The muon rate is determined for a sub-sample of muon events which are selected by a radial cut R relative to the ID center. By this only muons crossing a sphere of radius R are counted and contribute to the muon flux calculation. In this case, the cross section of the sphere with radius R is simply a disc with an area of πR^2.

In figure 7.2 the resulting muon flux is shown as a function of the chosen radial cut value R. A dependence on R is clearly visible and can be associated to systematic radial shifts of the reconstructed tracks[3]. For very large radii $R > 2.5$m, the rate begins to decrease as the sphere does no longer fit inside the ID volume. Two extreme values are visible, a local minimum at $R = 2.2\,\text{m}$ and a local maximum at $R = 2.4\,\text{m}$ were used to define the lower and upper limits for the muon flux [130]. The corresponding result of $\Phi_\mu = 0.72 \pm 0.01\,\text{m}^{-2}\text{s}^{-1}$ is in very good agreement with the effective-area approach discussed before.

Track length method

In the third method, also relying on muon track reconstruction, the muon flux, Φ_μ, can be determined within a given volume. One can calculate the flux from the rate of muons passing this volume (R_μ/V in $\text{s}^{-1}\text{m}^{-3}$) and from the mean path length of the muons within the volume according to

$$\Phi_\mu = R_\mu/V\langle L_\mu\rangle. \tag{7.2}$$

This approach has the advantage that it is not necessary to compute an effective cross section as the rate can be directly computed from the muons detected and the tracks reconstructed

[2]Private communication with A. Tonazzo.

[3]This effect is expected, because of the slightly distorted impact parameter distributions of muon tracking reconstruction algorithm RecoMuHam.

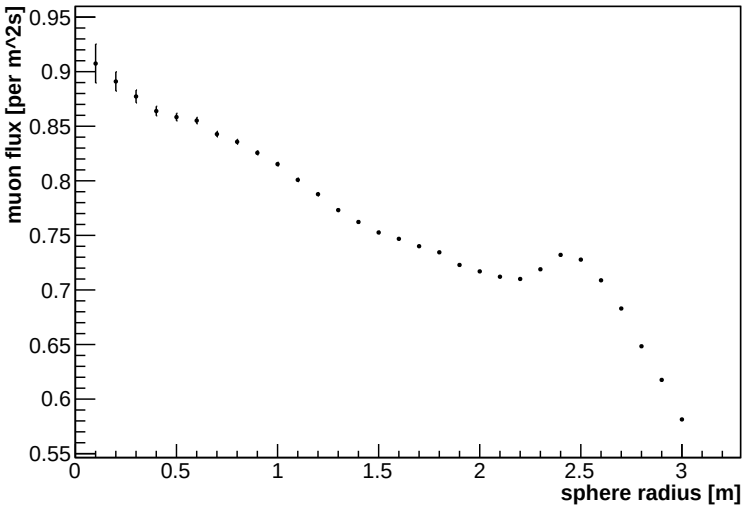

Figure 7.1: Muon flux determination with the sphere method. The plot shows the muon flux as function of the maximum cut radius R. Only muons having a track inside the sphere contribute to the muon flux determination. Plot taken from [130]

within the detector. On the other hand, also this method suffers from systematic shifts in the muon reconstruction. Table 7.2 shows the values utilized the calculation of the muon flux taking the NT or NT+GC as reference volumes. The total ID volume cannot be used due to the muon detection/tracking threshold applied in the ID. The fluxes determined in this way are high compared to the first two methods. However, this is expected as figure 7.2 clearly shows an inward-shift of the reconstructed muon tracks close to the detector center [130].

vessel		**NT**	**GC**
Muon rate	$[s^{-1}]$	4.88	10.2
Volume	$[m^2]$	10.3	33.6
Mean length	[m]	1.65	2.42
Muon flux	$[m^{-2}s^{-1}]$	0.79	0.74

Table 7.3: Track length method: muon flux determined by multiplying the measured muon rate within a given detector volume with the average track length of a muon within this volume.

Comparison

The values of these three methods are compared in table 7.4, where also the results of a dedicated Monte Carlo simulation for the DC far site using the MUSIC code [91], a numerical calculation [96] and an unpublished measurement done during the first Chooz experiment are listed. The discrepancy between extrapolation and the measured flux can be explained due to the fact that, for the extrapolation, a flat overburden is assumed. Therefore the 300 m.w.e. are the minimal shielding, whereas this is true in reality only for muons coming from the river site, where the rock overburden descends towards the meuse river. Muons coming from

muon flux Φ_μ^{DC} [$m^{-2}s^{-1}$]			
DC far measurement	**Extrapolation**	**MUSIC simulation**	**Chooz measurement**
0.71/0.72/0.79/0.74	0.8±0.1	0.75±0.06	0.4

Table 7.4: Comparison of different muon fluxes Φ_μ. For the DC far measurement, the first value comes from the effective area method, the second from the sphere method the last two from the track length method either applied for the NT or the GC volume. The extrapolation value is from [96], the MUSIC simulation value from [91, 94] and the value of the Chooz measurement can be found in [132].

other directions have to traverse more material and are therefore more suppressed, leading to a somewhat smaller flux.

The MUSIC simulation and the Chooz measurement are compatible once taking into account the acceptance of the detector and the slightly different definitions of muon flux used in the simulation and in the measurement of this data[4] [132]. In addition, for the Chooz measurement the errors on the measurement are not known. As the track length method suffers from systematic shifts of the reconstructed muon tracks, the muon flux values obtained by this method are considered as upper limit. This is because the inward shift at low R is clearly increasing the result of the muon flux. As the dimensions of the ID and the GC are within the 1500 mm region where the inward shift is present, the mean path method is overestimating the flux[5]. The values of the effective area and sphere method agree very well, therefore the average of these two flux values was chosen as input to the scaling, where the systematic error is given by the difference between those two methods and the MUSIC simulation:

$$\Phi_\mu^{DC} = (0.72 \pm 0.04)\,\mathrm{m}^{-2}\mathrm{s}^{-1} \tag{7.3}$$

7.3 Scaling of muon flux and mean muon energy

This section will now focus on the derivation of equations of muon flux and muon mean energy related to a given depth h underground. The goal is to find formulas which enable the extrapolation of the DC far muon flux and mean energy at 300 m.w.e. to the depths of the Daya Bay and RENO experiments.

To find such relations, one has to consider the energy loss of muons in matter. The energy loss mechanisms are ionization, creation of electron-positron pairs, bremsstrahlung and nuclear interactions. While the ionization loss at high muon energies is constant, the relative strength of other processes increase linearly with muon energy:

$$\frac{dE_\mu}{dx} = a(E_\mu) + b(E_\mu)E_\mu \tag{7.4}$$

[4] In the Chooz measurement the muon flux was measured through a horizontal surface, whereas the normal surface is used in the MUSIC simulation.

[5] This is consistent with the result of the sphere method.

Assuming the parameters a and b to be independent of energy, which is justified because both are slowly varying function of energy, one can use eq. 7.4 above to workout the range of muons in matter by integration [5]

$$h = \int_{E_{th}}^{0} \frac{dE_\mu}{dx} dE_\mu = \frac{1}{b} \ln\left(1 + \frac{b}{a} E_{th}\right), \tag{7.5}$$

with the definition $\epsilon = b/a$. In addition 7.4 can be used to calculate the relation between the initial energy $E_{\mu,0}$ at production and its average energy E_μ after traveling a distance h through rock

$$\langle E_\mu \rangle = E_{\mu,0} - E_{th} = (E_{\mu,0} + \epsilon) e^{-bh} - \epsilon. \tag{7.6}$$

With the knowledge of the sea-level muon spectrum and the energy-loss mechanisms one is able to calculate the depth-intensity relation for muons using 7.6 above. Approximating the integral sea-level muon spectrum by a power law $N_\mu = A E_\mu^{-\gamma}$ and discriminating between two energy-depth regimes, the first for shallow depths $h << b^{-1} \approx 2.5\,\text{km.w.e.}$ and the second $h >> b^{-1}$ results in

$$N_\mu(h, E > E_{th}) = \begin{cases} A(E_\mu + ah)^{-\gamma}, & \text{if } h << b^{-1} \\ A(E_\mu + \epsilon)^{-\gamma} e^{-\gamma b h}, & \text{if } h >> b^{-1} \end{cases} \tag{7.7}$$

In principle, relations 7.6 and 7.7 allow to calculate the muon intensity and muon mean energy at any given depth h. However, especially at high muon energies the assumption of a and b being constant in energy does not hold any more and fluctuations in energy loss become important. Therefore an accurate calculation, which is needed for the subsequent scaling of the background rates requires a simulation that accounts correctly for stochastic energy-loss processes of muons. In addition the parameters a, b are sensitive to the chemical composition[6] of the rock surrounding the experimental sites making an analytical calculation impossible. Thus empirical formulas and numerical calculations will be used in the following to obtain the muon flux and mean energy at a given depth h underground.

7.3.1 Scaling the muon flux with depth

Several empirical parametrization for the dependency of muon intensity I_μ and depth underground h and elaborate numerical calculations can be found in literature. The numerical calculation of Bugaev in [96] agrees well with the compilation of underground muon measurements that can be found in Crouchs 1987 "World Survey" [133]. This can be seen in figure 7.2 where the intensity for wide range of depths $(30 - 9000\,\text{m.w.e.})$ is shown. The start of the numerical calculation is the production of pions and kaons in the upper atmosphere taking into account the logarithmic growth of the inelastic cross section for their production processes with energy as well as the generation of pions, kaons and nuclei in pion-nucleus collisions. The calculated muon spectra were the input to the muon transport equation, which

[6] Radiative energy losses of muons are proportional to the ratio of the square of the mean atomic number to the mean atomic weight $\langle Z \rangle^2 / \langle A \rangle$, whereas ionization losses are proportional to the ratio $\langle Z \rangle / \langle A \rangle$ for a given chemical rock composition.

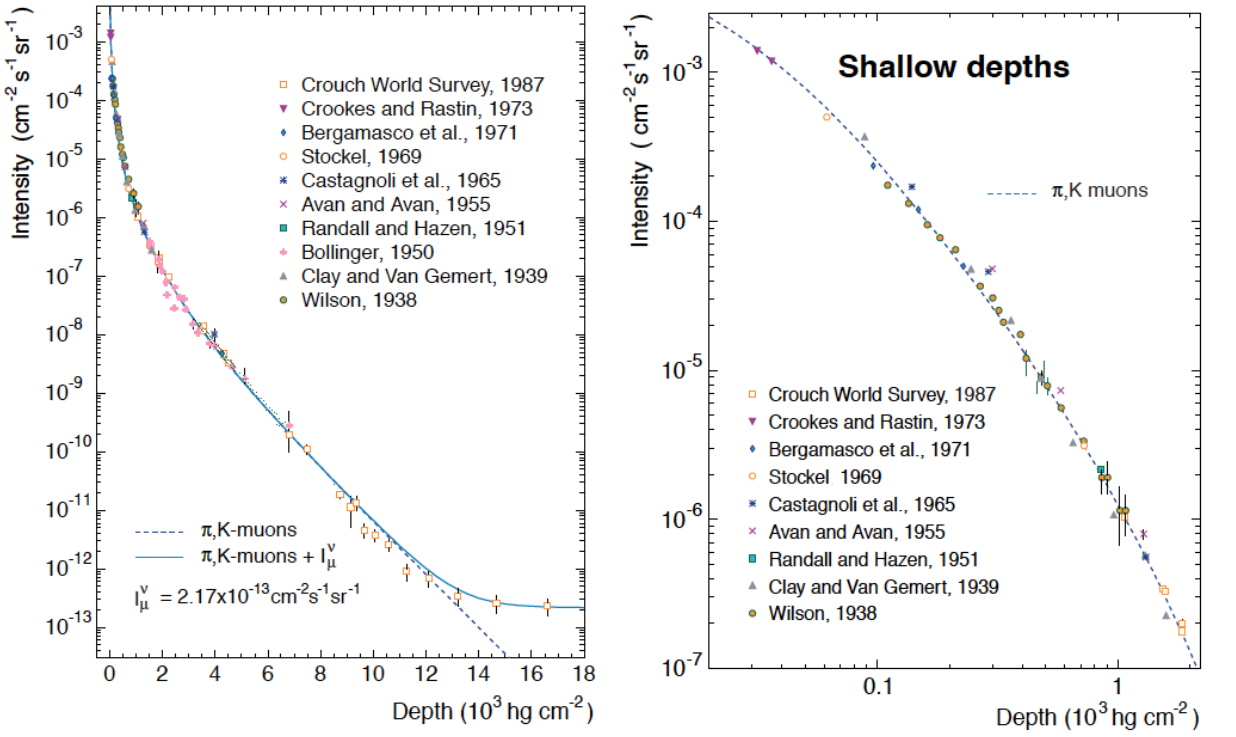

Figure 7.2: Muon intensity versus depth underground. The left plot shows the depth range up to 18 k.m.w. (1 hg/cm^2 correspond to 1 m.w.e.), whereas the right plot only shows the data for shallow depths underground. The dashed curve is numerically calculated by Bugaev in [96], while the solid line represents the same values plus a neutrino induced muon contribution as given by Crouch. Plots taken from [96].

was solved numerically to obtain the muon intensity at a given depth of a homogeneous medium.

In [122] Reichenbacher numerically computed the propagation of a muon of given energy through standard rock considering its energy loss mechanisms[7]. They used the standard Gaisser approximation, as derived in Eq. 4.18, for the surface muon spectrum to work out the muon intensity underground as a function of slant depth in standard rock.

Now, having formulas or numerical calculations for muon intensities underground, the measured flux Φ_μ^{DC} at the DC far site can now be used as a normalization or anchor point for the muon fluxes Φ_μ^X at a given site X with depth h. They are calculated by multiplying the DC far anchor point with the intensity ratios $I_\mu^X(h)/I_\mu^{DC}$

$$\Phi_\mu^X = \frac{I_\mu^X(h)}{I_\mu^{DC}} \times \Phi_\mu^{DC} \equiv f_\mu^\Phi \times \Phi_\mu^{DC}, \tag{7.8}$$

where the flux scaling factor f_μ^Φ was defined. The results of the muon flux scaling can be found in table 7.5 and the results are also visualized in figure 7.3. Comparing the two numer-

[7]Ionization loss and radiative energy loss processes: Bremsstrahlung, pair production and photo nuclear interactions.

		muon flux Φ_μ [$s^{-1}m^{-2}$]		
detector	**depth [m.w.e.]**	**measured**	**Bugaev**	**Reichenbacher**
RENO near	120	N/A	5.47±0.30	4.84±0.27
DC near	150	N/A	3.74±0.21	3.12±0.17
DB EH1	250	1.27	1.18±0.07	1.08±0.06
DB EH2	265	0.95	1.01±0.06	0.95±0.05
DC far	300	0.72±0.04	Φ_μ^{DC}	Φ_μ^{DC}
RENO far	450	N/A	0.32±0.02	0.28±0.02
DB EH3	860	0.056	0.06±0.01	0.05±0.01

Table 7.5: Scaling of muon fluxes Φ_μ for different intensity-depth relations and comparison with measured values from [57, 58]. The errors listed in this table are obtained by scaling the DC far error on the muon flux to the specific depth with the relations presented before.

detector	**depth [m.w.e.]**	f_μ^Φ	**flux Φ_μ [$s^{-1}m^{-2}$]**
RENO near	120	6.73±0.87	4.84±0.68
DC near	150	4.34±0.86	3.12±0.64
DB EH1	250	1.50±0.14	1.08±0.12
DB EH2	265	1.32±0.08	0.95±0.08
RENO far	450	0.39±0.05	0.28±0.04
DB EH3	860	0.07±0.01	0.05±0.01

Table 7.6: Scaling results for muon flux using the Reichenbacher numerical calculation [122]. The error quoted in the table is the squared sum of the scaled flux error from our measurement $\Delta\Phi_\mu^{DC}$ of $0.04\,s^{-1}m^{-2}$ plus the squared difference between each Bugaev and Reichenbacher data point Δf_μ^Φ.

ical methods of Bugaev and Reichenbacher, they both fit all DB data points well. One should note that the intensity values in the Bugaev case were taken from the plot in figure 7.2 of [96] by reading the approximate value for each specific depth. The numerical parametrization of Reichenbacher is chosen for the further scaling attempts, as the calculated intensity values were kindly provided in the range 1 m.w.e. up to 1000 m.w.e. by J. Reichenbacher.

One can attribute an systematic error to the muon flux scaling by taking the difference between the Bugaev and Reichenbacher values for each scaled data point, $\Delta f_\mu^\Phi = |f_\mu^{Bug} - f_\mu^{Rei}|$. The overall error is calculated as the quadratic sum of this scaling uncertainty plus the scaled DC far site muon flux error Φ_μ^{DC}

$$\Delta\Phi_\mu^X = \Phi_\mu^X \sqrt{\left(\frac{\Delta f_\mu^\Phi}{f_\mu^\Phi}\right)^2 + \left(\frac{\Delta\Phi_\mu^{DC}}{\Phi_\mu^{DC}}\right)^2}. \tag{7.9}$$

The resulting muon flux values that later will be taken as input for the spallation neutron and βn-emitter scaling, can be found in table 7.6 with their associated errors.

7.3.2 Scaling the mean muon energy with depth

In order to scale the mean muon energy, a parametrization with depth h underground is needed. The first one considered is given by Ambrosio et. al. in [95], where the energy loss

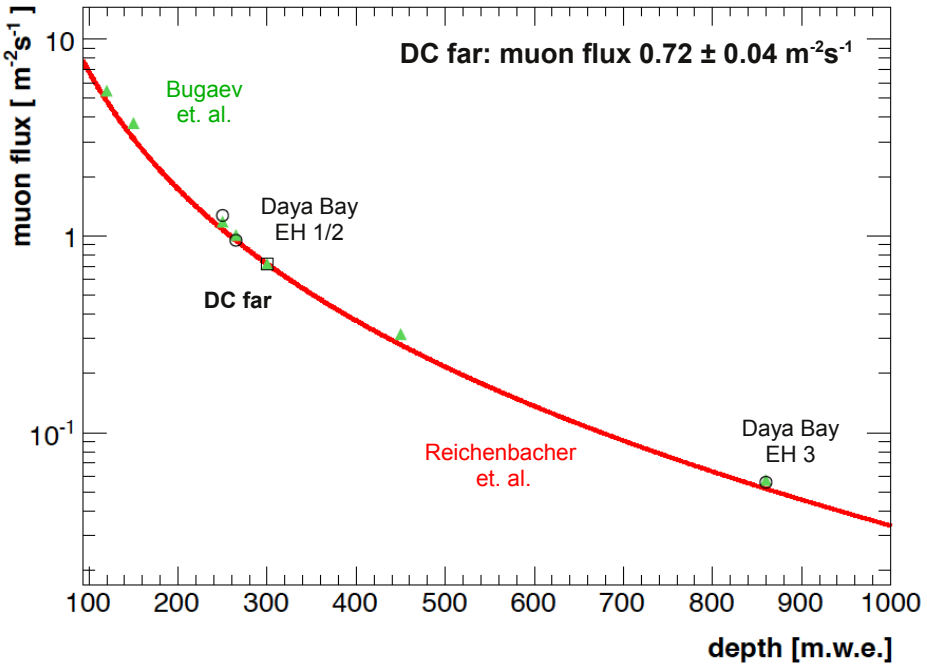

Figure 7.3: Scaling of muon flux with the DC far value Φ_μ^{DC} of $0.72\,\mathrm{s}^{-1}\mathrm{m}^{-2}$ as anchor point using the numerical calculations of Bugaev (green points) and Reichenbacher (red curve).

parameter ϵ of muons in matter is assumed being constant[8]:

$$\langle E_\mu \rangle(h) = \frac{\epsilon(1 - e^{-\beta h})}{\alpha - 2} \tag{7.10}$$

Here the asymptotic value for very large depths is given by $\epsilon/(\alpha - 2)$. The used parameters are $\epsilon = 620\,\mathrm{GeV}$, $\beta = 0.383 \times 10^{-5}\,\mathrm{cm}^2\mathrm{g}^{-1}$ and $\alpha = 3.7$. However this yields a mean energy of $\approx 40\,\mathrm{GeV}$ for the DC far site, whereas a dedicated MUSIC simulation of the DC far underground site [91,94] yields a value of $(63.7 \pm 0.8)\,\mathrm{GeV}$. Again, as for the muon flux scaling discussed before, the extrapolation by Ambrosio et. al. considers a flat rock overburden. This is a good approximation for great depths, but being shallow underground the topology of the overburden get more and more important. In addition, a different approximation of $\langle E_\mu \rangle(h)$ as in [122] given by Reichenbacher is considered

$$\langle E_\mu \rangle(h) = \frac{e^{h/p_0} - p_1}{p_2}. \tag{7.11}$$

The parameter values are $p_0 = 2298.2\,\mathrm{m.w.e.}$, $p_1 = 0.99809\,\mathrm{GeV}^{-1}$ and $p_2 = 0.00192$. Calculating the mean muon energy for the DC far site with this approximation yields a value

[8]The assumption is, that the energy loss parameters a and b, defining $\epsilon = a/b$,only change slightly with energy in the considered energy range.

of $\approx 74\,\mathrm{GeV}$, resembling the $\approx 64\,\mathrm{GeV}$ MUSIC simulation value much better. However, one should note that the energy values calculated by Reichenbacher et. al. resemble the minimum energy at surface, that a muon must have to reach the detector site a given depth h. Formula 7.11 simply reflects the energy-range relation of muons and is therefore not directly comparable to eq. 7.10 calculating the mean muon energy. Nevertheless it can be used for comparison.

By taking the ratio of calculated mean energies and multiplying this with the DC far site value one gets a extrapolation for the different experiments X depths h:

$$\langle E_\mu^X \rangle = \frac{\langle E_\mu \rangle(h)}{\langle E_\mu \rangle(300)} \times \langle E_\mu^{DC} \rangle \equiv f_\mu^E \times \langle E_\mu^{DC} \rangle, \tag{7.12}$$

where the muon energy scaling factor f_μ^E was defined. The results of this empirical muon energy scaling can be found in table 7.7. The results are visualized in figure 7.4. The given error is simply the scaled one, obtained using the error on mean energy $\Delta\langle E_\mu^{DC} \rangle$ of the DC far site being $0.8\,\mathrm{GeV}$.

		mean energy $\langle E_\mu \rangle$ [GeV]		
detector	**depth [m.w.e.]**	**measured**	**Ambrosio**	**Reichenbacher**
RENO near	120	N/A	26.4±0.3	25.0±0.3
DC near	150	N/A	32.8±0.4	31.3±0.4
DB EH1	250	57	53.6±0.7	52.6±0.7
DB EH2	265	58	56.6±0.7	55.9±0.7
DC far	300	63.7±0.8	$\langle E_\mu^{DC} \rangle$	$\langle E_\mu^{DC} \rangle$
RENO far	450	N/A	92.9±1.2	98.3±1.2
DB EH3	860	137	164.7±2.1	205.4±2.6

Table 7.7: Scaling of mean muon energy $\langle E_\mu \rangle$ and comparison with quoted values.

Empirical scaling conclusion

Both empirical formulas considered yield results compatible with the quoted DB EH1 and EH2 muon energy values, were the difference in depth to the DC far site is not that much. However they diverge from each other a greater depths, were the Reichenbacher parametrization yields much higher mean energies than the Ambrosio one. With respect to the muon energy value of DB EH3, the Ambrosio parametrization seems to better fit the data points. In addition these parametrization reaches an asymptotic limit whereas the Reichenbacher one seems to increase indefinitely. This is maybe related to the fact that with Ambrosio one calculates the mean muon energy underground, whereas the Reichenbacher calculation yields the minimum surface energy a muon must have to reach the underground site with depth h. Therefore these results should be handled with care and are not trust able to use in the scaling. In order to clarify the situation dedicated simulations have been done using two different muon simulation and transportation codes as will be explained in the next section.

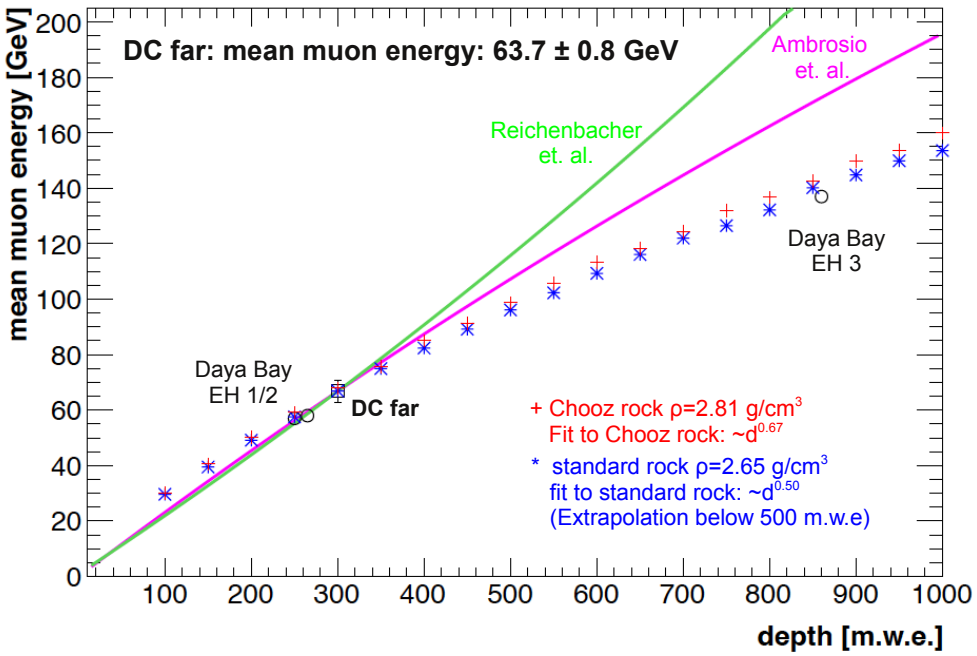

Figure 7.4: Scaling of mean muon energy using the empirical parametrization of muon energy with depth by Ambrosio (green) and Reichenbacher (magenta). The scaling uses the DC far muon mean energy value of $\langle E_\mu^{DC} \rangle = 63.7 \pm 0.8\,\text{GeV}$ (MUSIC result from [91, 94]) as anchor point. The values from the MUSIC and MUSUN simulations are shown in red, for Chooz rock, and in blue for "standard rock". Simulation data taken from [134].

7.3.3 Mean muon energy from MUSIC and MUSUN simulation

This subsection describes a simulation that was done in [130, 134] to obtain the mean muon energy at a given depth underground. The codes utilized are MUSIC (MUon Simulation Code) [135–137] and MUSUN (MUon Simulations UNderground) [137]. In [134] a total number of 10^5 muons with surface energies up to 100 TeV were simulated. As the muon interaction cross sections depend on the chemical composition of the matter through, the type of rock affects the the mean muon energy at a given depth. Therefore calculations for "standard rock" and Chooz rock were done. Regarding the energy loss, rock is characterized by its mean atomic number $\langle Z \rangle$ and its mean atomic weight $\langle A \rangle$. The relevant characteristic parameters for standard rock and Chooz rock are shown in Table 7.8. The differences in the mean muon energy values are less than 3.5% for standard rock to Chooz rock. Power law fits were performed to obtain the following scaling relations:

$$\langle E_\mu \rangle(h) = -8.34 + 1.90\, h^{0.64} \qquad \text{Chooz rock} \qquad (7.13)$$

$$\langle E_\mu \rangle(h) = -6.86 + 1.72\, h^{0.66} \qquad \text{standard rock} \qquad (7.14)$$

type of rock	$\langle Z \rangle$	$\langle A \rangle$	$\langle Z \rangle / \langle A \rangle$	$\langle Z \rangle^2 / \langle A \rangle$	ρ[g/cm^3]
standard	11	22	0.50	5.50	2.65
Chooz	11.8	24.1	0.49	5.78	2.81

Table 7.8: Parameters describing standard or Chooz rock composition.

Effect of hill profile at the DC far site

In order to quantify the effect of the hill profile at the DC far site, the simulation was performed for a flat overburden of 300 m.w.e. and with the Chooz hill profile as shown in figure 4.9 in chapter 4. The flat overburden simulation gives a mean muon energy of 66.8 GeV, whereas the full simulation yields 62.3 GeV. The two values are within 7.2% of each other, thus the uncertainty in the mean muon energy due to the detailed profile of the hill is taken to be half that value, being 3.6%.

Calculation of the Mean Muon Energy at Daya Bay and RENO depths

Considering a flat overburden at the corresponding depth, the simulation was performed for DB and RENO. Because of the limited information about the rock composition at these sites[9], the simulations were performed taking standard rock or Chooz rock composition. Table 7.9 lists the simulation results. The results for DB are between (2.0-5.3)% off for Chooz rock and less than 7.6% off for standard rock from the quoted values. Thus, the mean muon energy values used in the further scaling relations will be the ones obtained from the simulation with Chooz rock.

		mean muon energy [GeV]		
detector	**depth [m.w.e.]**	**quoted**	**Chooz rock**	**standard rock**
RENO near	120	N/A	33.3 ± 2.0	34.1 ± 2.1
DC near	150	N/A	39.7 ± 2.4	40.6 ± 2.5
Daya Bay EH1	250	57	58.5 ± 3.6	59.8 ± 3.6
Daya Bay EH2	265	58	61.0 ± 3.7	62.4 ± 3.8
DC far	300	66.8 ± 4.1	68.3 ± 4.2	
RENO far	450	N/A	89.3 ± 5.4	91.5 ± 5.6
Daya Bay EH3	860	137	139.8 ± 8.5	144.2 ± 8.8

Table 7.9: Mean muon energies from MUSIC and MUSUN simulations. In the simulations for the the Daya Bay and RENO sites a flat overburden was assumed and were calculated for two different rock types, standard rock and Chooz rock.

Uncertainty in the simulations

In [130] a detailed discussion on the overall uncertainty of the simulation is presented. As explained before, there is a 3.6% error due to the lack of knowledge of the hill profile and an error of 3.5% due to the unknown rock composition for the DB and RENO sites. The simulation uncertainty itself is 3.5% due to the numerical method used, the limited knowledge of the muon surface flux and muon energy loss processes as well due to the stochastic

[9] Without the values of $\langle Z \rangle$ and $\langle A \rangle$ one is not able to accurately model the muon energy losses.

character of the muon energy loss. Adding those errors up in quadrature, the total error of the simulation is 6.1%.

7.3.4 Summary of muon related observables

This subsection now summarises the muon related observables, flux Φ_μ and mean energy $\langle E_\mu \rangle$. As discussed in detail before, the numerical calculation of Reichenbacher is used to obtain the flux values at a given depth. As the values calculated by Bugaev are not far off one can trust this parametrization and the errors are given by the difference between the two parametrization. Regarding the mean energy, a dedicated simulation was performed in [134] that rejected the empirical formula discussed as energy parametrization before. The values utilized come from a MUSIC and MUSUN simulation for Chooz rock composition and a flat overburden, where the error is taking into account the uncertainty in the rock composition, the unknown profiles of the hill overburdens and the simulations uncertainty in modeling the muon energy loss process. The results are given and summarized in table 7.10.

		muon flux [$\mathbf{m^{-2}s^{-1}}$]	**mean Muon Energy [GeV]**
detector	**depth [m.w.e.]**	**Reichenbacher**	**Chooz rock, flat overb.**
RENO near	120	4.84±0.27	33.3 ± 2.0
DC near	150	3.12±0.17	39.7 ± 2.4
Daya Bay EH1	250	1.08±0.06	58.5 ± 3.6
Daya Bay EH2	265	0.95±0.05	61.0 ± 3.7
DC far	300	0.72±0.04	66.8 ± 4.1
RENO far	450	0.28±0.02	89.3 ± 5.4
Daya Bay EH3	860	0.05±0.01	139.8 ± 8.5

Table 7.10: Muon related observables, flux Φ_μ and mean energy $\langle E_\mu \rangle$, used in the scaling.

7.4 General scaling relations

Having derived the input values of muon flux and mean energy, this section follows a description given in an internal collaboration note [138] and aims to derive the general scaling equations used to scale a given background rate produced by muons from one experimental site to another. In organic liquid scintillators muons predominately interact with ^{12}C, the most abundant nucleus after ^{1}H, hydrogen, via electromagnetic or hadronic processes creating cosmogenic isotopes. Regarding reactor neutrino experiments, the following production process is of interest

$$\mu + {}^{12}\mathrm{C} \rightarrow {}^{9}\mathrm{Li} + X. \tag{7.15}$$

Fast neutrons on the other hand are mainly produced outside the detector in the surrounding rock of the detectors vicinity. They are detected by scattering off protons,

$$n + p \rightarrow n + p + E_{recoil}, \tag{7.16}$$

variable	description	dimension
N_B	count of B	[B]
N_{B_μ}	number of B per μ	$[B/\mu]$
n_B	number density of B per volume	$[B/L^3]$
$\lambda_{B/\mu}$	number linear density of B	$[(B/\mu)^{-1}]$
Y_{B_μ}	specific(mass) yield of B per μ	$[B/\mu L^2/kg]$
$\alpha_{X\to Y}$	cross section for process $X \to Y$	$[l^2 Y/X]$
m_b	molar mass of substance B	$[g/mole]$
m_X	total detector mass of X	$[kg]$
ρ_X	density of X	$[g/L^3]$
R_b	total production rate of B	$[B/s]$
r_b	specific production rate of B per Y	$[B/(Ys)]$
N_A	Avogadro's number	$[mole^{-1}]$

Table 7.11: List of variables used in the derivation of the scaling relations with a short description and their dimensions. The dimensions are length [L], volume [L^3], mass [g] or [kg], time [s]. From [138].

which in turn deposit their recoil energy in the LS. Recoils happen until the neutrons are finally slowed down and get captured on hydrogen or gadolinium nuclei. Thus in the following the observable B will be either one or multiple neutron or ^{9}Li. Table 7.11 summarizes the different variables that will be used in the derivation of the general scaling formula.

7.4.1 Derivation of scaling relation

First, the number density n_C of carbon in a given liquid scintillator (LS) is calculated via the number of carbon atoms per LS molecule $N_{C/LS}$ according to

$$n_C = N_A N_{C/LS} \frac{\rho_{LS}}{m_{LS}}. \tag{7.17}$$

Now it is possible to calculate the linear density of B per μ initiating a reaction in LS. This number is given by the product of the number density and the cross-section for the process creating B

$$\Lambda_{B/\mu} = n_C \sigma. \tag{7.18}$$

Thus, the number of B produced per μ with an average track length $\langle L_\mu \rangle$ in LS is

$$N_{B/\mu} = \Lambda_{B/\mu} \langle L_\mu \rangle. \tag{7.19}$$

The specific yield of B per μ can be calculated according to

$$Y_B = \frac{\lambda_{B/\mu}}{\rho_{LS}} = \frac{N_C \sigma}{\rho_{LS}} = N_A \frac{N_{C/LS}}{m_{LS}} \sigma. \tag{7.20}$$

Taking the ratio of yields for an unknown site X with depth h and the DC far site yield results in the relation

$$\frac{Y^X(h)}{Y^{DC}} = \left(\frac{N^x_{C/LS}}{N^{DC}_{C/LS}}\right)\left(\frac{m^x_{LS}}{m^{DC}_{LS}}\right)^{-1}\left(\frac{\sigma^x}{\sigma^{DC}}\right). \tag{7.21}$$

The cross-sections for the processes creating neutrons or cosmogenic isotopes are assumed to scale with the average muon energy to the power of some constant like $\sigma \propto E^\alpha$ [139]. Using relation 7.21 above, one is able to establish a relation for $N_{B/\mu}$, the number of B produced per muon by multiplying the yields with the average track length of a muon $\langle L_\mu \rangle$ in the experiments LS and the LS density ρ_{LS}

$$\begin{aligned}\frac{N^X_{B/\mu}}{N^{DC}_{B/\mu}} &= \left(\frac{Y^X(h)}{Y^{DC}}\right)\left(\frac{\rho^X_{LS}}{\rho^{DC}_{LS}}\right)\left(\frac{\langle L^X_\mu\rangle}{\langle L^{DC}_\mu\rangle}\right) \\ &= \left(\frac{N^X_{Y/LS}}{N^{DC}_{Y/LS}}\right)\left(\frac{m^X_{LS}}{m^{DC}_{LS}}\right)^{-1}\left(\frac{\langle E^x_\mu\rangle(h)}{\langle E^{DC}_\mu\rangle}\right)^\alpha\left(\frac{\rho^X_{LS}\langle L^x_\mu\rangle}{\rho^{DC}_{LS}\langle L^{DC}_\mu\rangle}\right).\end{aligned} \tag{7.22}$$

This in turn can now be used to calculate the specific production rate $R_B = N_{B/\mu}R_\mu$ per muon

$$\frac{R^X_B}{R^{DC}_B} = \left(\frac{N^X_{Y/LS}}{N^{DC}_{Y/LS}}\right)\left(\frac{m^X_{LS}}{m^{DC}_{LS}}\right)^{-1}\left(\frac{\langle E^x_\mu\rangle(h)}{\langle E^{DC}_\mu\rangle}\right)^\alpha\left(\frac{\rho^X_{LS}\langle L^X_\mu\rangle}{\rho^{DC}_{LS}\langle L^{DC}_\mu\rangle}\right)\left(\frac{R^X_\mu}{R^{DC}_\mu}\right). \tag{7.23}$$

The muon rate R_μ that is measured within a given detector volume can be related to the muon flux via

$$\Phi_\mu = R_\mu\langle L_\mu\rangle \times \frac{\rho_{LS}}{m_{det}}. \tag{7.24}$$

Multiplying the ratio with $1 = (m^X_{det}/m^{DC}_{det})(m^{DC}_{det}/m^X_{det})$, making use of the muon flux definition and separating the ratio into factors regarding muon quantities and scintillator properties results in

$$\frac{R^X_B}{R^{DC}_B} = \left(\frac{m^X_{det}}{m^{DC}_{det}}\frac{N^X_{C/LS}}{N^{DC}_{C/LS}}\right)\left(\frac{m^X_{LS}}{m^{DC}_{LS}}\right)^{-1} \times \left(\frac{\langle E^X_\mu\rangle(h)}{\langle E^{DC}_\mu\rangle}\right)^\alpha\left(\frac{\Phi^X_\mu}{\Phi^{DC}_\mu}\right). \tag{7.25}$$

Rearranging expression 7.25 and solving it for the specific R^X_b of detector X at depth h yields

$$R^x_B = \left(\frac{m^X_{det}}{m^{DC}_{det}}\frac{N^X_{C/LS}}{N^{DC}_{C/LS}}\right)\left(\frac{m^X_{LS}}{m^{DC}_{LS}}\right)^{-1}\left(\frac{\Phi^X_\mu}{\Phi^{DC}_\mu}\right)\left(\frac{\langle E^X_\mu\rangle}{\langle E_\mu\rangle^{DC}}\right)^\alpha \times R^{DC}_B. \tag{7.26}$$

The detector mass divided by the molar mass is simply the number of LS molecules N_{LS}. Multiplying this with Avogadro's constant[10] N_A and the number of carbon atoms per LS molecule $N_{C/LS}$ yields the number of carbon atoms in the experiment, thus

[10] Avogadro's constant is defined as the ratio of the number of particles in sample to the amount of the substance and given by $N_A = 6.022 \cdot 10^{23}$ particles per mole.

Double Chooz	**KamLAND**	**Daya Bay**	**RENO**
Dodecane(80%)	Dodecane(80%)	LAB	LAB
$[CH_3(CH_2)_{10}CH_3]$	$[CH_3(CH_2)_{10}CH_3]$	$[C_6H_5C_NH_{2N+1}]$	$[C_6H_5C_NH_{2N+1}]$
O-PXE(20%)	Pseudocumene(20%)		
$[C_{16}H_{18}]$	$[C_9H_{12}]$		

Table 7.12: Chemical compositions of the various scintillators. The scintillators for Daya Bay and RENO have been assumed to be pure LAB based with N=12. From [57, 58, 97].

experiment	$N_{C_{LS}}$	$N_{H_{LS}}$	N_C [10^{29} C]	N_H [10^{29} H]	m_{LS} [g/mol]	M [tons]
Double Chooz	12.67	24.56	3.587	6.747	176.53	8.3
KamLAND	11.21	22.87	398.941	813.898	158.52	936.8
Daya Bay	18	30	8.804	14.673	246.24	20.0
RENO	18	30	7.263	12.106	246.24	16.5

Table 7.13: Different scintillator properties calculated from the values in table 7.12 where a density of $\rho = 8\,\mathrm{g/cm^3}$ was used for all liquid scintillators. The results are in close agreement with values given in [54]. The proton number in the DC far detector was not calculated, but the measured value from [140] is taken.

$$N_C = \frac{m_{det}}{m_{LS}} N_{C/LS} N_A. \tag{7.27}$$

From this follows the final scaling equation

$$R_B^x = \left(\frac{N_C^X}{N_C^{DC}}\right)\left(\frac{\Phi_\mu^X}{\Phi_\mu^{DC}}\right)\left(\frac{\langle E_\mu^X\rangle}{\langle E_\mu\rangle^{DC}}\right)^\alpha \times R_B^{DC} \equiv f_B \times R_B^{DC}, \tag{7.28}$$

where the scaling factor f_B was defined. This equation, apart from the power law dependency, is the well-known textbook result of a process $a + b \to c + d$, where the reaction rate is given by the product of flux Φ_a and number of target particles N_b times the cross section of the reaction, resulting in $R_b = N_B \Phi_a \sigma_b$. As a last step, one needs to calculate the number of hydrogen or carbon atoms for a given experiment X.

The different scintillator compositions of the various experiments considered (DC, RENO, Daya Bay and KamLAND) can be found in table 7.12. From the listed numbers the number of carbon or hydrogen atoms is calculated and can be found in table 7.13.

7.4.2 Error on the scaling

The error for this scaling attempt can be computed as the quadratic sum of all independent error sources, being either the error of the muon flux scaling f_μ^Φ, the mean muon energy $\langle E_\mu\rangle$, the power law parameter α or the anchor point rate R_B^{DC} as measured at the DC far site during the reactor off-off periods. The DC far muon flux measurement Φ_μ^{DC} cancels out and its error does not contribute to the overall error on the scaling. Calculating the different error terms and quadratically summing them yields the overall error to the scaling factor Δf_n:

$$\Delta f_B = f_B \sqrt{\left(\frac{\Delta f_\mu^\Phi}{f_\mu^\Phi}\right)^2 + \left(\alpha \frac{\Delta\langle E_\mu^x\rangle}{\langle E_\mu^x\rangle}\right)^2 + \left(\alpha \frac{\Delta\langle E_\mu^{DC}\rangle}{\langle E_\mu^{DC}\rangle}\right)^2 + \left(log\left(\frac{\langle E_\mu\rangle}{\langle E_\mu^{DC}\rangle}\right)\Delta\alpha\right)^2}.$$

Including the error for the DC far off-off anchor point yields the overall error on the scaled rate R_B^X:

$$\Delta R_B^X = R_B^X \times \sqrt{\Delta f_B^2 + \left(\frac{\Delta R_B^{DC}}{R_B^{DC}}\right)^2}.$$

With theses definitions one is able to distinguish errors induced through the scaling relation from errors coming from the measurement of the DC far off-off anchor point.

7.5 Scaling of fast neutron background

As shown in [141, 142], the rate of fast neutrons produced by spallation can be calculated according to

$$R_n^X = 4.14 \cdot 10^{-6} n/(\mu \mathrm{gcm}^{-2}) \times m_{det} \cdot \Phi_\mu \cdot \langle E_\mu\rangle^\alpha, \tag{7.29}$$

where the power law parameter α was found to be 0.74. Using the general relations derived in the section before, considering the detailed scintillator compositions, one can relate the rate in experiment X to the DC far measurement/anchor point R_n^{DC}

$$R_n^X = \left(\frac{N_H^X}{N_H^{DC}}\right)\left(\frac{\Phi_\mu^x}{\Phi_\mu^{DC}}\right)\left(\frac{\langle E_\mu^x\rangle(h)}{\langle E_\mu^{DC}\rangle}\right)^{0.74} \times R_n^{DC} \equiv f_n \times R_n^{DC}. \tag{7.30}$$

The extrapolation depends on the number of free protons, as the neutrons were mainly detected as they scatter off the protons in the scintillator. This assumption suggests a volume effect[11], not considering the finite interaction length of neutrons. The neutrons measured at the DC far site have a interaction length of $\approx 1\,\mathrm{m}$, smaller than the size of the detector and thus a scaling with the volume is a first order approximation. To correct for this in second order, acceptance factors for each detectors would be needed accounting for the finite interacting length of neutrons and the fact that those neutrons do not "see" the full volume of the detectors but rather a surface density of hydrogen atoms as they can not fully enter the detector. But these acceptance factors depend on the details of each detector geometry and thus a full detector MC for each site would be needed to quantify this effect. Hence, in the first order approximation used, the scaling is valid for DC far like detectors placed at the given depth h of the experiment considered.

DC far: For the DC far detector the numbers are $\Phi_\mu^{DC} = (0.72 \pm 0.04)\,\mathrm{m}^{-2}\mathrm{s}^1{-}1$ and $\langle E_\mu^{DC}\rangle = (66.8 \pm 4.1)\,\mathrm{GeV}$. The number of hydrogen atoms in the target scintillator is $N_H^{DC} = 6.747{\cdot}10^{29}$ [140]. The DC anchor point FN measurements are $R_n^{DC} = (0.23{\pm}0.18)\,\mathrm{cpd}$

[11] Bigger volume also means more hydrogen target atoms and thus more interaction and higher detectable rate

for a DC I like analysis, where the OV was used as veto and (0.33 ± 0.16) cpd for a DC II like analysis where the OV was used as a veto. Both rates were scaled, because the DC I like rate is comparable to RENO, where no veto was used to measure the neutron rates. On the other hand for DB, the big water pools surrounding the detectors were used to create distinct veto conditions and thus the neutron rate measured is a reduced one and more comparable to the rate obtained using the OV as a veto as done in the DC II like analysis. As last input parameter in the eq. 7.30 above, a α-parameter of 0.74 ± 0.05 was utilized for the scaling of muon energies in the following.

Other sites: The values of Φ_μ and $\langle E_\mu \rangle$ were taken from table 7.10, where the scaled flux values were chosen from the Reichenbacher calculation and the mean muon energies from the MUSIC and MUSUN simulations. The number of hydrogen atoms was taken from table 7.13. It should be noted that this scaling attempt assumes DC far like detectors with a flat overburden and Chooz rock composition.

The FN rates scaled with the formula in eq. 7.30 and the measured rates from [57, 58] can be found in table 7.14. The error was computed as the quadratic sum for all error sources, being either the flux Φ, the mean energy $\langle E_\mu \rangle$, the power law parameter α or the DC far spallation neutron rate R_n^{DC}.

DC I like (0.33 ± 0.16) **cpd**							
detector	**depth**	R_n^X **[cpd]**		R_n^X $[(\mathbf{d}\,10^{30}\mathbf{H}^{-1}]$	f_n	$\Delta f_n/f_n$	$\Delta R_n/R_n$
	[m.w.e.]	**measured**	**scaled**	**scaled**	[%]	[%]	
RENO Near	120	5.00±0.13	2.31±1.17	1.97±1.00	6.99±1.01	14.50	50.61
DC near	150	N/A	0.97±0.51	1.44±0.76	2.95±0.62	20.85	52.78
DB EH1	250	0.84±0.28	0.98±0.49	0.67±0.33	2.95±0.33	11.31	49.79
DB EH2	265	0.74±0.44	0.89±0.44	0.60±0.30	2.68±0.24	8.80	49.28
DC Far	300	0.23±0.18	0.33±0.16	0.49±0.24	1	–	48.48
RENO Far	450	0.97±0.06	0.28±0.14	0.24±0.12	0.84±0.12	14.34	50.56
DB EH3	860	0.04±0.04	0.09±0.04	0.06±0.03	0.26±0.04	15.73	50.97
DC II like (0.23 ± 0.18) **cpd**							
detector	**depth**	R_n^X **[cpd]**		R_n^X $[(\mathbf{d}\,10^{30}\mathbf{H}^{-1}]$	f_n	$\Delta f_n/f_n$	$\Delta R_n/R_n$
	[m.w.e.]	**measured**	**scaled**	**scaled**	[%]	[%]	
RENO Near	120	5.00±0.13	1.61±1.28	1.37±1.09	6.99±1.01	14.50	79.59
DC near	150	N/A	0.68±0.55	1.01±0.82	2.95±0.62	20.85	80.99
DB EH1	250	0.84±0.28	0.68±0.54	0.46±0.37	2.95±0.33	11.31	79.07
DB EH2	265	0.74±0.44	0.62±0.49	0.42±0.33	2.68±0.24	8.80	78.75
DC Far	300	0.23±0.18	0.23±0.18	0.34±0.27	1	–	78.26
RENO Far	450	0.97±0.06	0.19±0.15	0.16±0.13	0.84±0.12	14.34	79.56
DB EH3	860	0.04±0.04	0.06±0.05	0.04±0.03	0.26±0.04	15.73	79.83

Table 7.14: Scaling of expected FN events and comparison with quoted values [57,58]. Upper table gives the number scaling the DC anchor point measured not using the OV as a veto, whereas the lower table uses the anchor point measured using the OV as a veto. Column 3 lists the quoted measurements, whereas column 4 and 5 give the results of the scaling either as neutrons per day or per day and normalised to the number of hydrogen atoms in the considered experiment. The last columns show the scaling factor with its associated relative error and the relative error on the scaling itself.

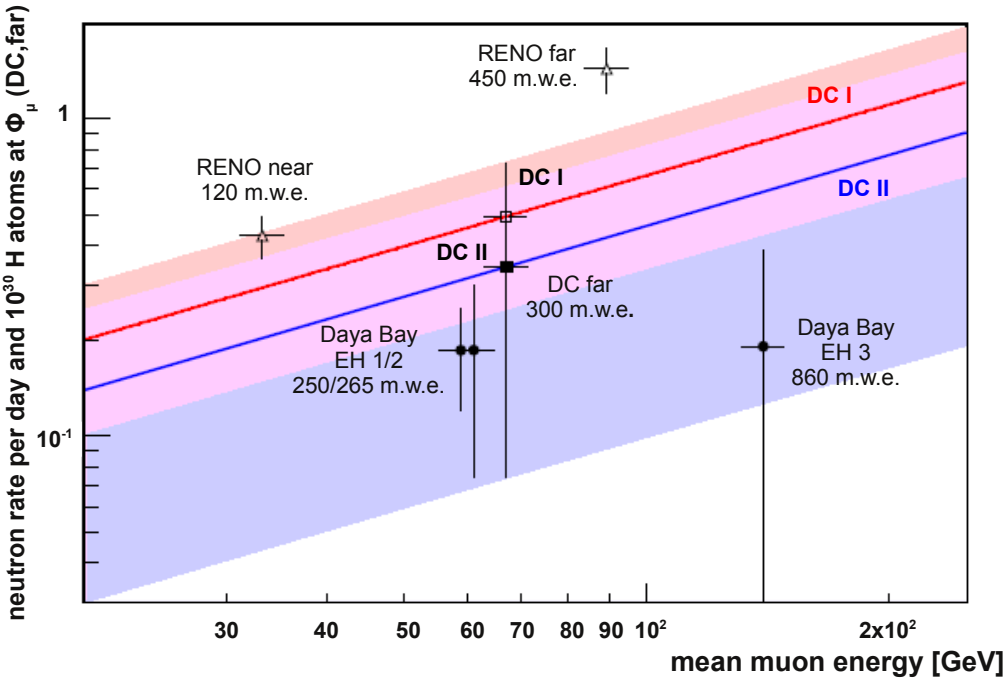

Figure 7.5: Visualization of the FN scaling. The quoted neutron rates R_n^X were rescaled (multiplied by $(\Phi_\mu^{DC}/\Phi_\mu^X)(N_H^{DC}/N_H^X)$) in order to normalize to muon flux and proton number at the DC far site. The red line corresponds to the expected energy scaling for the DC far off-off measurement not using the OV, whereas the blue line corresponds to the anchor point using the OV as a veto detector. The shaded regions enclose the uncertainty range for this scaling attempt.

In general the scaling yield values not far off from the measured values. The errors in this scaling are mainly given by the DC far measurement of FN during the reactor off-off. The relative error of this measurement yields around 78 % for the DC II like measurement, or around 48 % if the OV is not used as a veto detector as done in the DC I like analysis. This attributes the biggest part to the overall error on the scaling $\Delta r_n/r_n$. Thus the scaling is not limited by errors on the input parameters of the scaling relation, but rather by the DC far FN measurement's error. Thus increased statistics of an enlarged off-off data set would help to reduce this error.

Figure 7.5 shows a visualization of the scaling. Here the measured rates R_n^X were rescaled to match muon flux and the proton number at the DC far site. Two things are obvious, first the rescaled RENO rates are higher than the extrapolation in opposite to the DB rate values that are lower than the extrapolation. For DB this is easy to understand as the scaling assumes a DC far like detector, so assuming the same shielding situation, which is not true for DB. Here the detectors are surrounded by 1200 t/1950 t of water in the case of the far and the Near detector sites respectively. As this shielding is not taken into account the extrapolation yields somewhat higher rates. For RENO the situation is less clear, the discrepancy could be due to rock composition or the hill profile of the rock overburden. Another, more drastic,

assumption would be, that the quoted values are not only FN. So in principle one could argue that there is a contamination of events different from neutrons, which leads to a higher rate.

7.6 Scaling of cosmogenic produced βn-emitters

As stated before, for FN created by cosmic muons, the rate of cosmogenic radioisotopes can be scaled according to an empirical law depending on the number of carbon atoms contained in the detector volume, the muon flux Φ_μ and mean energy $\langle E_\mu \rangle$ at a given site [139]. This section summarizes the studies done in [130,143,144] to scale the DC far off-off measurement to any other reactor neutrino experiment X in a given depth h underground. In principle, this is the same scaling law as for FN, but the power-law parameter α has a different value and one considers the amount of carbon instead of hydrogen atoms:

$$R^X_{\beta n} = \left(\frac{N^X_C}{N^{DC}_C}\right)\left(\frac{\Phi^X_\mu}{\Phi^{DC}_\mu}\right)\left(\frac{\langle E^X_\mu\rangle}{\langle E^{DC}_\mu\rangle}\right)^\alpha \times R^{DC}_{\beta n} \equiv f_{\beta n} \times R^{DC}_{\beta n}. \tag{7.31}$$

DC far: The number of carbon atoms $N^{DC}_C = 3.58 \times 10^{29}$, the muon flux $\Phi^{DC}_\mu = (0.72 \pm 0.04)\,\mathrm{m^{-2}s^{-1}}$, mean muon energy $\langle E^{DC}_\mu\rangle = (66.8 \pm 4.1)\,\mathrm{GeV}$ and the off-off measurement yield a rate of $R^{DCI}_{\beta n} = 1.7 \pm 0.9\,\mathrm{cpd}$ for a DC I like analysis and a rate of $R^{DCII}_{\beta n} = 1.1 \pm 0.8\,\mathrm{cpd}$ for a DC II like analysis are chosen as input values.

Other sites: Like for the neutron scaling, the values of Φ_μ and $\langle E_\mu\rangle$ were taken from table 7.10. However, now the most uncertain component of the scaling law is the power-law parameter α, as this value has never been measured experimentally.

Hagner et. al. measured the combined rate of ^{9}Li and ^{8}He[12] produced by muons in a liquid scintillator target at a single energy of 190 GeV in the CERN NA54 muon beam experiment [139]. They used values of $\alpha = 0.50 - 0.93(\pm 0.20)$ to extrapolate their measurement to KamLAND and Borexino muon energies. Another value of $\alpha = 0.801 \pm 0.026$ is given by KamLAND, where they studied the production of radioactive isotopes through cosmic muon spallation [97]. They used a FLUKA simulation considering different muon energies to extract the value of α. A similar GEANT4 based simulation is described in [145] where the resulting value is $\alpha = 1.06$. To account for this uncertainty in the power-law parameter, a value in the range from the lower 1σ bound of the CERN experiment, $\alpha = 0.63$, to the result of [145], $\alpha = 1.06$, or $\alpha = 0.84 \pm 0.22$ was chosen [130].

The scaled rates and the computed scaling factors can be found in table 7.15 with their corresponding errors. For both DB near sites, EH1 and EH2, the uncertainty in the extrapolation is below 15 % as Φ_μ is well known and the difference in energy to DC far is low. However, the extrapolation to both RENO detectors and DC Near suffers from the large uncertainty in α. The relative uncertainty for the scaling factor f_{Li} is in the order of 20- %. Finally, the rather large uncertainty on the extrapolated value of Φ_μ for DB EH3 causes a even larger error for

[12] Due to the low contribution of ^{8}He to the βn-emitter rate, only ^{9}Li is considered here.

DC I like (1.7 ± 0.9) **cpd**							
detector	**depth**	$R^X_{\beta n}$ **[cpd]**		$R^X_{\beta n}$ $[(\mathbf{d}\,10^{30}\mathbf{C})^{-1}]$	$f_{\beta n}$	$\Delta f_{\beta n}/f_{\beta n}$	$\Delta R_{\beta n}/R_{\beta n}$
	[m.w.e.]	**measured**	**scaled**	**scaled**		(%)	(%)
RENO near	120	12.45±5.93	12.73±6.99	18.08±9.94	7.49	14.50	54.89
DC near	150	N/A	4.77±2.71	13.52±7.69	2.80	20.85	56.90
DB EH1	250	3.10±1.60	5.69±3.08	6.47±3.50	3.35	11.31	54.14
DB EH2	265	1.80±1.10	5.19±2.78	5.90±3.17	3.05	8.08	53.67
DC far	300	1.70±0.90	1.70±0.90	4.82±2.55	1	-	52.94
RENO far	450	2.59±0.75	1.69±0.93	2.40±1.32	0.99	14.34	55.85
DB EH3	860	0.16±0.11	0.55±0.30	0.63±0.35	0.32	15.74	55.23
DC II like(1.1 ± 0.8) **cpd**							
detector	**depth**	$R^X_{\beta n}$ **[cpd]**		$R^X_{\beta n}$ $[(\mathbf{d}\,10^{30}\mathbf{C})^{-1}]$	$f_{\beta n}$	$\Delta f_{\beta n}/f_{\beta n}$	$\Delta R_{\beta n}/R_{\beta n}$
	[m.w.e.]	**measured**	**scaled**	**scaled**		(%)	(%)
RENO near	120	12.45±5.93	8.24±6.11	11.70±8.68	7.49	14.50	74.16
DC near	150	N/A	3.08±2.33	8.75±6.62	2.80	20.85	75.66
DB EH1	250	3.10±1.60	3.68±2.71	4.19±3.08	3.35	11.31	73.60
DB EH2	265	1.80±1.10	3.36±2.46	3.82±2.80	3.05	8.08	73.26
DC far	300	1.10±0.80	1.10±0.80	3.12±2.27	1	-	73.73
RENO far	450	2.59±0.75	1.09±0.81	1.55±1.15	0.99	14.34	74.13
DB EH3	860	0.16±0.11	0.36±0.27	0.41±0.30	0.32	15.74	74.41

Table 7.15: Scaling of βn cosmogenic background, mainly constituted by the isotope ^{9}Li, computed according to eq. 7.31 and resulting scaling factors $f_{\beta \mathrm{n}}$ for the DC I and DC II like anchor points of the off-off measurement. An exponent $\alpha = 0.84 \pm 0.22$ has been used for the computation. The upper table lists the scaling for the DC I like measurement, whereas the lower table lists the scaling for the DC II like measurement. In both cases Column 3 lists the measurements of [57, 58], whereas column 4 gives the results of the scaling. Column 5 shows the results normalized to the number of carbon atoms in the considered experiment and enables an easier comparison between the experiments. The last columns show the scaling factor with its associated relative error and the relative error on the scaling.

f_{Li}. Looking at the overall uncertainty in the scaled rates, one observes that it is dominated by the uncertainty in the DC-off-off measurement of the βn-rate of more than 50 %, like it is the case for neutrons.

Finally, to allow for a graphical comparison, the βn-rates of other sites are scaled to DC far muon flux Φ_μ^{DC} and the number of carbon atoms N_C^{DC}. Figure 7.6 visualizes the scaling, for this the βn-decay rates (^{9}Li+^{8}He) were normalized by the number of carbon atoms in the considered experiment and given in units of 10^{30} carbon atoms. The RENO data points are within the expectation of the DC I like scaling, not utilizing the OV to reduced the number of ^{9}Li events. This DC I like analysis is comparable to the method utilized by RENO, where no distinct veto conditions are used to reduced ^{9}Li. This is opposite to DB, which give rates that are already reduced in terms of ^{9}Li as distinct conditions of the water Cherenkov veto are used to reject some cosmogenic events. Thus this rate is reduced in terms of ^{9}Li as is more comparable to the rate obtained using the DC II like method. Indeed, the DB data points are within this scaling expectation. In addition, measurements of the KamLAND and NA54 experiments are included in figure 7.6. In [97], the results of a combined ^{8}He and ^{9}Li measurement are given as $R(^8\mathrm{He}) = 1.0 \pm 0.5$ and $R(^9\mathrm{Li}) = 2.8 \pm 0.2$ per kiloton and day. Considering the branching ratios $\Gamma_{\beta n}(^8\mathrm{He}) = 16 \pm 1\,\%$ and $\Gamma_{\beta n}(^9\mathrm{Li}) = 50.8 \pm 0.9\,\%$ yields a βn-decay rate

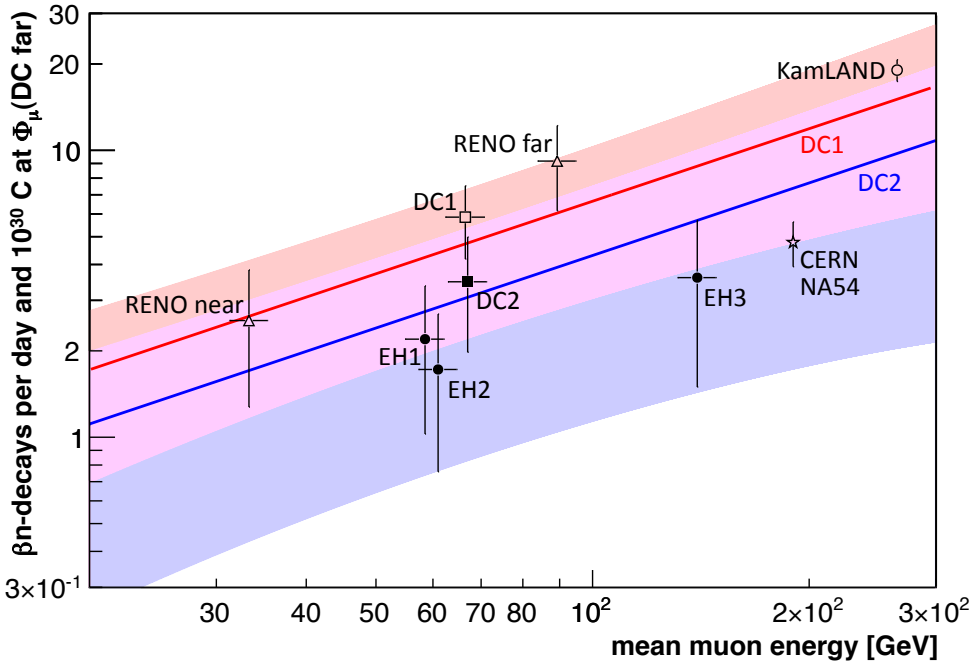

Figure 7.6: Expectation for cosmogenic βn-emitter rate scaled from DC I like (red) and DC II like (blue) off-off measurements. The lines correspond to the expected energy scaling and the shaded regions give the uncertainty range for α. RENO, CERN NA54 and KamLAND measurements are taken from [58,97,139] and were rescaled to the muon flux and the number of carbon atoms at DC far. In addition the DC far reactor on-on measurements of the first and second analysis periods are plotted. Plot taken from [130].

that is comparable to DC, DB and RENO. The result is $R_{\beta n} = 1.58 \pm 0.13\,(\mathrm{d} \cdot \mathrm{kt})^{-1}$. The NA54 muon beam experiment [139] measured the combined production rate of ^{9}Li and ^{8}He at a single energy of 190 GeV. This rate needs to be rescaled to compare it with the measurements of reactor neutrino experiments. This is done by scaling with the number of carbon atoms, the muon flux, the branching ratios and a correction factor $\beta = 0.87 \pm 0.03$ that takes into account the energy spectrum of cosmic muons [130].

7.7 Conclusion

In this chapter, the correlated background rates of fast neutrons and cosmogenic βn-emitters, measured by the Double Chooz far detector during two reactor "shutdown periods", were scaled to the depths of the two other reactor neutrino experiments, Daya Bay and RENO. First, the analysis steps for a direct measurement of the fast neutron and cosmogenic βn-emitter ^{9}Li were presented and the values from the overall reactor shutdown time of 7.53 days were quoted:

$$R_n^{DC\,I} = 0.33 \pm 0.16\,\text{cpd} \qquad R_n^{DC\,II} = 0.23 \pm 0.18\,\text{cpd}$$
$$R_{\beta n}^{DC\,I} = 1.7 \pm 0.9\,\text{cpd} \qquad R_{\beta n}^{DC\,II} = 1.1 \pm 0.8\,\text{cpd}$$

These values correspond to the different analysis strategies utilized in either [55] or [56] and were used as DC far "anchorpoints" in the scaling. As these backgrounds are produced by cosmic muons, the muon flux Φ_μ and mean muon energy $\langle E_\mu \rangle$ at the DC far site were estimated. The muon rate of around $46\,\text{s}^{-1}$, measured during both off-off periods, was converted to a flux value of $0.72 \pm 0.04\,\text{m}^{-2}\text{s}^{-1}$ using three different methods. Several ways to calculate the mean muon energy at the DC far site were presented. The DC far mean muon energy value of $63.7 \pm 0.8\,\text{GeV}$ was calculated using MUSIC/MUSUN simulation code. The influence of the hill profile at the DC far site and the uncertainty due to rock composition were taken into account and effect the mean energy by less than 6.1 %.

Empirical formula and dedicated simulations have been used to predict the values of muon flux and muon mean energy for different depths of interest, namely the depths of the Daya Bay and RENO experimental sites. A general background scaling relation, $R_{n,\beta-n}(h) \propto \Phi_\mu(h)\langle E_\mu^\alpha \rangle$, was derived. Utilizing the approximation of similar scintillator compositions the background rates of fast neutrons and cosmogenic ^{9}Li were extrapolated. It was shown, that this approximation affects the results by no more than 3 %. The extrapolation, as presented in this chapter, constitutes the second part of a dedicated paper [131] on the background measurements performed during both reactor off-off periods.

In future, increasing statistics with further data taken during a shutdown of both detectors will be useful to better constrain the background rates. In addition, the presented scaling would profit from this, as the errors on the DC far anchorpoints would be reduced in turn reducing the errors on the predicted background rates.

As the power law dependency of the cross section with muon energy, $\sigma \propto E_\mu^\alpha$, is poorly known for the cosmogenic βn-emitter ^{9}Li, the data presented in this chapter could be used to determine this parameter. Instead of fixing the parameter like it was done in the extrapolation, it can be fitted to the different experimental data. This could be done using the measured rates of all experiments, obtained at different depths and therefore different parent muon energies.

"All science is either physics or stamp collecting."

Ernest Rutherford (1871-1937)

8

Monitoring and calibration with cosmic ray muons

Cosmic ray muons provide an excellent possibility to monitor changes in the detector response with time. In addition, via their decay, they are a natural calibration source. This chapter will focus on both points making use of muons for detector surveillance and calibration.

First the energy scale of the ID will be introduced. This is followed by an explanation of two different methods that will be used to examine the detector response in the high energy regime. The discussion starts with the ratio of muon rates in ID and IV, R_μ^{IV}/R_μ^{ID}, which can give hints on unstable detector conditions on a very low-level, being easy and fast to access. After this, the energy loss per track length (Δ/X) of muons is used to monitor the overall detector response and the stability of the energy scale. Whereas such a monitoring is already done utilizing neutron capture on hydrogen or gadolinium in the low energy regime, the methods that will be presented in the following enable a monitoring in the high energy regime.

The use of muon decay for calibration purposes will be the last item of this chapter. In contrast to muons passing through the detector setup, muons stopping and decaying inside can be used as a well defined calibration source. Stopping muons leave an energy deposition in the detector which is proportional to their track length. This is followed by an energy deposition of the subsequent decay into a electron. The resulting energy distribution of the decay has an endpoint of 53 MeV and a mean of 35 MeV. As the range of such an electron in the scintillator is in the order of a few cm's, the energy of the decay is well contained within the detector volume rendering these decay electrons as natural calibration sources. Another benefit is, that muon decay does not only happen in the ID, but also in the IV yielding a calibration opportunity in both sub detectors.

8.1 The energy scale of the Inner Detector

As this chapters focus is on monitoring and calibration, this first section will introduce the utilized energy scale of the ID [56] according to [146, 147] in more detail. The visible energy, E_{vis}, is defined as the total number of gain-calibrated photoelectrons per trigger defined as

$$E_{vis} = PE(\rho, z, t) \times f_{\text{uniformity}}(\rho, z) \times f_{\text{stability}}(t) \times f_{MeV}. \tag{8.1}$$

It is the calorimetric estimator of the deposited energy per trigger, being linear, independent of time and position inside the ID. The different factors used in the visible energy definition

will now be explained in some detail. The detector response in photoelectrons is position dependent, in addition it varies in time (for example after power cuts) and it is different for data and MC. The total number of PEs is the sum over the collected raw charge per channel divided by the gain g_i of this channel, resulting in $PE = \sum_i q_i/g_i(q_i)$. In this calculation the raw charge is estimated from the waveform of each PMT by the RecoPulse charge reconstruction algorithm using a sliding time window. The function g_i corrects charge non-linearities for single photoelectrons per Channel i and is measured weekly by using dedicated IDLI runs.

In order to account for the non-uniformity of the Detector the capture of neutrons on H is used. The gamma lines released after a n-H capture are used to characterize the response variation across the ID volume. The factor $f_{\text{uniformity}}$ converts the detector response at any given position (ρ, z) inside the ID into one at the detector center $(\rho = 0, z = 0)$. This correction factor is defined in the following way:

$$f_{uniformity} = \frac{\text{Response(nH)}(\rho = 0, z = 0)}{\text{Response(nH)}(\rho, z)}$$

The third factor, $f_{\text{stability}}$, corrects possible variation in the detector response over time. These variations or drift could have two possible causes, first variations in the gain of PMTs or in the readout electronics or changes in the scintillator response. A 2.2 % monotonic increase of the detector response was measured, utilizing the response of a neutron capture on gadolinium. Correcting for this with $f_{\text{stability}}$ leaves a relative instability of 0.61 % of the root mean square (**RMS**) values for the data taking period considered in this thesis.

The forth and last factor, f_{MeV}, gives the overall MeV energy scale. During the calibration campaign in August 2011 the following calibration sources, sealed in miniature capsules, have been deployed: ^{137}Cs (0.662 MeV gamma rays), ^{68}Ge (2×0.511 keV annihilation gamma rays) and ^{60}Co (1.173 MeV and 1.333 MeV gamma rays). Up to know the neutron capture on hydrogen is defining the absolute MeV scale. These neutrons arise from the deployment of a ^{253}Cf-source at detector center. The neutrons of this source get captured on hydrogen, which subsequently releases an energy of 2.223 MeV. It should be noted that these calibration measurements define the time zero of the stability calibration (August 2011), as the detectors response changes due to power cuts and electronics issues for some channels before and after the calibration period.

8.2 Monitoring using the muon rate ratio IV/ID

A simple way to monitor the stability of the detector is given by the ratio of muon rates in ID and IV, R_μ^{IV}/R_μ^{ID}. This ratio should stay constant in time and any change reflects a difference in the detector response in the ID or the IV, which could be due to changes in gain or in threshold. In addition there can be an increase of light noise in the ID causing deviations. This can be seen in the following, as the muon rate can be calculated via integration of the muon flux over the detector area, $R_\mu = \int d\vec{A} \cdot \Phi_\mu$. The muon flux Φ_μ at the detector location is the same for ID and IV, apart from differences in the effective surface area A of both sub detector systems. Of course, the ratio will be a function of the applied cut values in E_{vis} and Q_{IV}, but the essential fact that the ratio is a constant over time remains.

As leading order approximation for cylindrical DC far detector, one can use an effective surface parametrization like $A = 2rL\sin(45°) + \pi r^2$, which corresponds to the geometrical projection of the detector surface perpendicular to the muon track, as defined in chapter 7. Using the detector dimensions[1] without applying any cut on the ID energy and the IV charge one expects a ratio of:

$$R \equiv \frac{R_\mu^{IV}}{R^{ID}} = \frac{2R_{IV}L_{IV}\cos(\pi/4) + \pi R_{IV}^2}{2R_{ID}L_{ID}\cos(\pi/4) + \pi R_{ID}^2} = \frac{65.36\,\mathrm{m}^2}{19.40\,\mathrm{m}^2} = 3.37. \tag{8.2}$$

The upper panel of figure 8.1 shows the measured average muon rates per day in ID (blue) and IV (red), the lower panel shows the muon rate ratio obtained from the rate values shown in the panel above. The average muon rates per day follow a sinusoidal pattern connected to seasonal variations in the effective temperature of the atmosphere as derived in chapter 6. The muon rate ratio however should be constant. The RMS value of the rate ratio is 3.51 and the variation is found to be around $1\,\%_{rms}$. It is known, that there are still light noise events with energies of $> 30\,\mathrm{MeV}$ in the ID. These events can lead to a deviation from the expected value. To check this, the muon rates were re-evaluated using a higher cut value of 100 MeV on the muon energy for the ID. The average muon rates per day and the resulting ratio utilizing this higher cut value can be seen in figure 8.2.

After the application of this higher cut value, the muon rates in ID and IV match each other better compared to the lower ID cut value of 30 MeV. In addition the ratio is flatter and it's RMS value is found to be 4.06. The variation of the ratio is around 0.01 and corresponds to fractional changes of the energy scale of $0.2\,\%_{rms}$, being compatible with the variation at the n-H capture peak of around $0.61\,\%_{rms}$ [56]. This again confirms the assumption, that some high energy events are actually caused by light emitting PMTs, not caused by muons. Still, there are small discrepancies between the ID and IV muon rates resulting in a decrease of the ratio ratio within the first two months of the measurement and at the end of the data taking period.

The decrease at the start of the data set could be due to change in gain of the PMTs with time, as the gain itself is a dependent on high voltage, temperature and humidity. Environmental conditions in the lab within the first days after commissioning of the detector might not have been stabilized, causing the gain to change until the conditions are stable. However, the reason for the decrease at the end of the data set is unknown. Further data will show if the ratio is further decreasing or stabilizing or even rising back to the expected value. Nevertheless this monitoring approach proved to be useful, as for the large middle period of the considered data set a stable muon rate ratio was found, indicating stable detector conditions in the high energy regime of both sub-detectors, the ID and the IV.

[1] $r_{ID} = 1808\,\mathrm{mm}$, $L_{ID} = 3572\,\mathrm{mm}$ and $R_{IV} = 3250\,\mathrm{mm}$, $L_{IV} = 7000\,\mathrm{mm}$, from technical drawing of the far detector A.2.

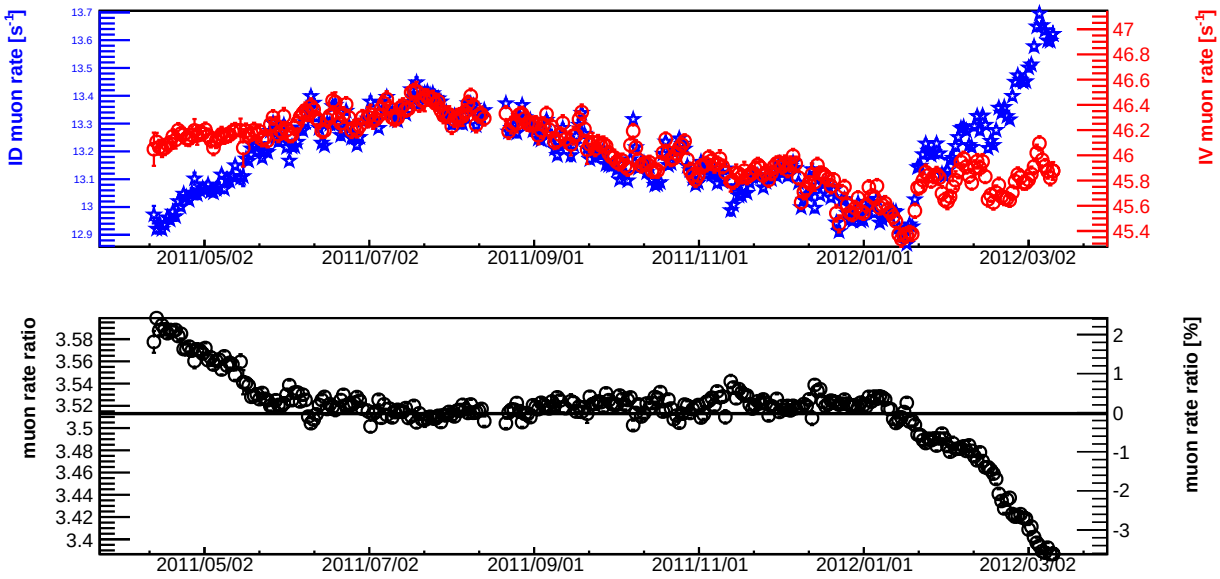

Figure 8.1: Upper panel: Muon rate stability in ID and IV for the whole data taking period from 2011/04/13 till 2012/02/29 for the nominal muon thresholds of 30 MeV for the ID and 10 kDUQ for the IV. Lower panel: Ratio of muon rates in ID and IV R_μ^{IV}/R_μ^{ID}. The RMS value of the ratio is indicated by the black solid line.

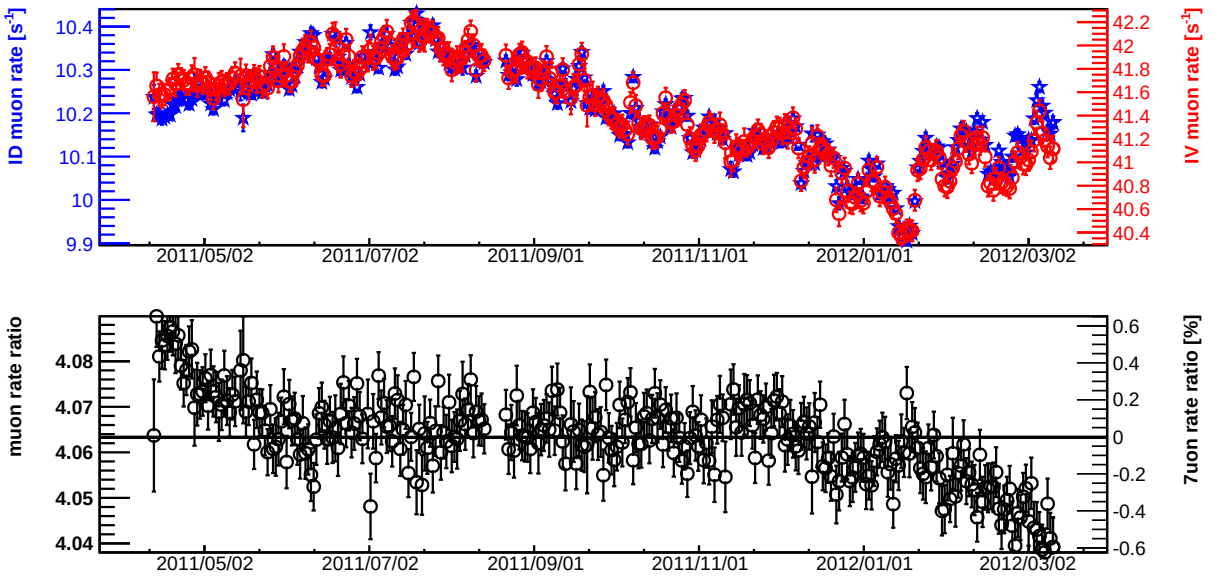

Figure 8.2: Upper panel: Muon rate stability in ID and IV ratio of muon rates for a higher energy cut value of 100 MeV for the ID and 40 kDUQ for the IV. The daily muon rates of ID and IV behave very similar having a small relative deviation from each other. Lower panel: The rate ratio is more flat compared to the ratio with the nominal muon threshold. The RMS value is found to be 4.06, the deviation is around 0.2 $\%_{rms}$.

8.3 Monitoring using muon energy loss

The energy loss of muons per track length, $(\Delta E/X)$, can be used to check the overall stability of the scintillator and to identify possible artefacts created by the readout electronics. The general idea behind this monitoring is that the energy loss should not vary in time and any variation, especially step like behaviors reflects changes in the PMTs or electronics gain, changes in the scintillator light yield or changes in the performance of the track reconstruction algorithm. Before the method will be introduced, a short overview on energy loss in general will be given leading to the question how to describe the energy loss of muons in LS.

8.3.1 Bethe and Landau energy loss

Following the comprehensive approaches of [148] and [64], the energy loss Δ of a muon traversing a material of thickness x is given by the sum of N individual collisions δE_n : $\Delta = \sum_{n=1}^{N} \delta E_n$. The Central Limit Theorem of statistics states that the sum of N random variables, all following the same statistical distribution, approach a Gaussian distributed variable in the limit of $N \to \infty$. One makes the assumption, that the energy loss δE_n in each collision n is such, that the velocity of the muon is not altered. Thus the velocity dependent cross-section of the collision processes stays constant. For relatively thick absorbers the number of collisions N is high and a mono-energetic beam of muons traversing a material of thickness x will show a Gaussian energy loss distribution:

$$f(\Delta, \beta\gamma, x) \approx exp\left(- \frac{(\Delta/x - \bar{\Delta}/x)^2}{2\sigma^2} \right). \tag{8.3}$$

Δ is the energy loss in the absorbing material, $\bar{\Delta}$ is the mean energy loss as given by Bethe and σ is the width of the Gaussian distribution as defined below.

$$\bar{\Delta} = 2z^2\xi\left(\frac{1}{2} \ln \frac{2mc^2\beta^2\gamma^2 T_{max}}{I^2} - \beta^2 - \frac{\delta(\beta\gamma)}{2} \right) \tag{8.4}$$

$$\sigma = 2\xi\beta^2 \tag{8.5}$$

$$T_{max} = \frac{2m_e c^2\beta^2\gamma^2}{1 + 2\gamma m_e/M + (m_e/M)^2} \tag{8.6}$$

The value ξ is defined as $(K/2)\langle Z/A\rangle x/\beta^2$ in MeV for a detector with a thickness of x measured in g/cm^2. T_{max} is the maximum energy transfer from the incident material to a free electron in the absorber material within a single collision δE_n. The constants Z and A are the atomic mass and the atomic number of the absorbing material, $\beta = v/c$ being a measure of the particles velocity and $\gamma = 1/\sqrt{1-\beta^2}$ it's Lorentz factor. The ratio K/A can be numerically calculated to be $0.307075\,\mathrm{MeV\,g^{-1}\,cm^2}$ if one measures A in $\mathrm{g\,mol^{-1}}$. The function $\delta(\beta\gamma)$ in eq. 8.5 above accounts for density effects corrections to the ionization loss.

In contrast to the thick absorber case discussed before, LSs have a comparably low density ($\approx 0.8\,\mathrm{g/cm^3}$) being a relatively thin absorber for GeV muons. The number of collisions N is

not sufficient for the Central Limit Theorem to hold. The energy loss probability distribution $f(\Delta, \beta\gamma, x)$ is given by the highly-skewed Landau-distribution[2]

$$f(\Delta, \beta\gamma, x) \approx \frac{1}{2} exp\Bigg(-\frac{1}{2}\frac{\Delta/x - a\Delta_p/x}{\xi} + e^{-\frac{\Delta/x - a\Delta_p/x}{\xi}} \Bigg), \tag{8.7}$$

where the most probable energy loss can be calculated according to

$$\Delta_p = \xi \Bigg[\ln \frac{2mc^2\beta^2\gamma^2}{I} + ln\frac{\xi}{I} + j - \beta^2 - \delta(\beta\gamma) \Bigg]. \tag{8.8}$$

The high energy behavior of the density effect parameter δ is such, that the most probable energy loss δ_p reaches a Fermi plateau

$$\Delta_p \xrightarrow[\beta\gamma>100]{\xi} \left(\frac{2mc^2\xi}{(\hbar\omega_p)^2} + j \right) = \xi \Bigg(\frac{2mc^2\xi}{(28.816\sqrt{\rho\langle Z/A\rangle})^2} + j \Bigg), \tag{8.9}$$

with the plasma frequency $(\hbar\omega_p)^2$. This frequency can be expressed as $(28.816\sqrt{\rho\langle Z/A\rangle})^2$ using material constants. The distribution in eq. 8.9 is highly asymmetric, having a tail extending to higher energy losses. These very rare high energy transfer collisions drive the mean of the distribution into its tail. As high energy collisions are rather rare, the mean of the distribution usually consists of a few hundred events and shows a large spread. Therefore the mean of the energy loss $\bar{\Delta}$, as given by the Bethe equation fails to describe the energy deposition of this single muon and is ill-defined experimentally and the most probable energy loss δ_p is used instead [64]. A comparison of the distributions for both cases: thick absorbers (Gaussian distribution) and thin absorbers (Landau distribution) is shown in figure 8.3.

8.3.2 Calculation of expected energy loss

In this section the most probable energy loss for the different scintillating volumes will be calculated. As shown in chapter 4, the mean muon energy at the DC far site is $\langle E_\mu \rangle = 63.7\,\mathrm{GeV}$. The resulting value of $\beta\gamma \approx 578$ justifies the use of the high energy approximation of the most probable energy loss Δ_p. In the calculation, the plasma frequency $(\hbar\omega_p)^2$ was computed using material constants $(28.816\sqrt{\rho\langle Z/A\rangle})^2$. Therefore one only needs to know the values of Z and A and the density ρ of the scintillating liquids. These scintillator properties can be found in table 3.6 in chapter 3.

For the NT scintillator one has n-dodecane ($Z = 98$, $A = 170.33\,\mathrm{g\,mol^{-1}}$) and PXE ($Z = 114$, $A = 210.31\,\mathrm{g\,mol^{-1}}$) as main components. Calculating a weighted average of Z and A according to volume fractions. One obtains an atomic mass number of $A = 178.32\,\mathrm{g\,mol^{-1}}$ and an atomic charge number of $Z = 101.2$. The corresponding value of $\langle Z/A\rangle$ is 0.5675 which leads to a ξ of 20.627 MeV (0.105 MeV/cm). Incorporating these values into eq. 8.8 for the most probable energy loss one obtains a value of Δ_p^{NT} around 1.17 MeV/cm.

[2]Quoted in an approximation given by Moyal, that can be found in [149].

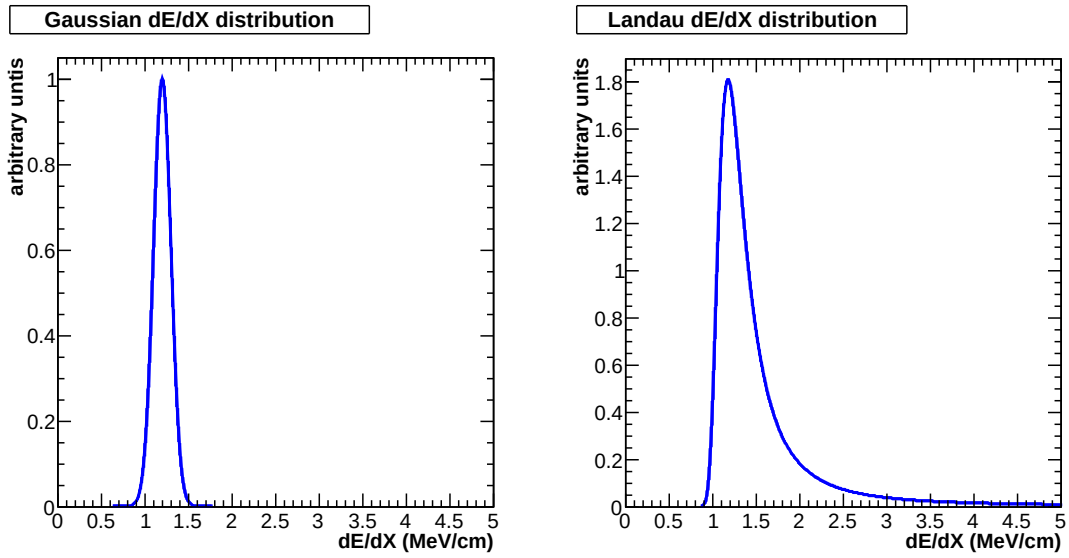

Figure 8.3: Theoretical distributions of the energy loss in thick (left plot, Gaussian distribution) and in thin (right plot, Landau distribution) absorbers.

The main components of the IV's LS are LAB ($Z = 133$, $A = 246.43\,\mathrm{g\,mol^{-1}}$) and n-dodecane. Similar to the ID, a weighted average is calculated resulting in $Z = 125.25$, $A = 212.11\,\mathrm{g\,mol^{-1}}$ and $\langle Z/A \rangle = 0.5904$. This corresponding values of ξ is 11.89 MeV (0.1081 MeV/cm) and the expected most probable energy loss for the IV is found to be Δ_p^{IV} is 1.14 MeV/cm.

8.3.3 Muon track reconstruction

To perform a measurement of the muon energy loss per track length, $\Delta E/X$, a proper reconstruction of the muon entry and exit points is needed to calculate the muon track length. The **RecoMuonHam** software[3] [150] was used for this. The basic principle behind the method is, that a muon traveling through the scintillator emits a spherical light front along its track, which is superimposed with a Cherenkov light cone.

Using the reconstructed entry and exit points, the track in the ID can be calculated. The actually used track length is corrected for the muon track length inside the buffer volume, X_B, thus the track length utilized in the calculation corresponds to the one through the volumes of GC and T

$$X_{TGC} = \sqrt{\sum_{i=x,y,z} (EP_i^{ID} - XP_i^{ID})^2} - X_B. \tag{8.10}$$

To calculate the muon track length for the IV the entry and exit points, EP and XP, on the buffer surface are extrapolated to the surface of IV vessel. Thus the RecoMuonHam algorithm can be used to reconstruct the track of muons in the IV, if they cross the ID as

[3]More details on this software package and the utilized algorithm can be found in chapter 3.

well. Then the track length can be calculated from the extrapolated IV entry and exit points and is corrected for the track length in the ID afterwards

$$X_{IV} = \sqrt{\sum_{i=x,y,z} (EP_{\alpha}^{IV} - XP_{i}^{IV})^2} - X_{TGC}. \tag{8.11}$$

8.3.4 Measurement of muon energy loss

To account for the finite energy resolution of the detector, the expected Landau distribution L_τ of muon energy loss has to be smeared with a Gaussian distribution G_σ resembling the energy resolution of the detector. This is done by the convolution of both functions, $L \oplus G$, and is defined as follows:

$$L \oplus G = \int L_\tau(x - \Delta_p) G_\sigma(\bar{\Delta} - x) dx \tag{8.12}$$

$$G_\sigma(x) = \frac{1}{\sqrt{2\pi}\sigma} e^{-x^2/\sigma^2} \tag{8.13}$$

$$L_\tau(x) = \frac{1}{\pi\tau} \int_0^\infty e^{-t \ln t - t \cdot x/\tau} \cdot \sin(\pi t) dt \tag{8.14}$$

The parameters are $\bar{\Delta}$, the Bethe energy loss, Δ_p, the most probable energy loss, σ, the energy resolution and τ, the Landau width. The most probable energy loss is extracted from data by dividing the deposited energy ΔE by the reconstructed track length X of the muon. The resulting distribution is then fitted with the Landau-Gaussian convolute $L \oplus G$ and the most probable value for the energy loss, $\Delta E_p/X$, is extracted.

Fits performed on an exemplary run can be seen in figures 8.4 and 8.5 for the ID and the IV respectively. For the ID, the asymmetric Landau distribution is obvious, the energy loss has a clear extension to higher energies. For the IV this is less obvious, but the logarithmic scale in figure 8.5 shows a contribution of higher energy losses. The energy loss distribution of the IV seems to miss entries in the tail extending to high energy losses. An explanation for this could be that due to the high light-level in the IV, the PMTs in the upper IV saturate. This would restrict the maximum charge that can be measured and consequently drain the high energy loss tail. In order to avoid contaminations of high energetic light noise, the logical *and* threshold combination ID∧IV is used to select muons. The most probable muon energy loss is estimated per run from the fit-function $L \oplus G$ presented above. A weighted average of all runs taken at one specific day was calculated, where the weight was given as the inverse of the statistical error.

This averaging allows for a daily stability check of the detector response in the high energy regime. Figures 8.6, 8.7 and 8.8 show the stability of the most probable muon energy loss Δ_p/X in the ID versus the days of measurement for the uncalibrated response, Q_{ID}, simply the raw charge collected by the PMTs divided by track length. It shows the gain-calibrated response in photoelectrons, $PE(\rho, z, t) \times f_{\text{uniformity}}(\rho, z)$, and at last, the fully calibrated response in E_{vis}. In all plots, the grey band indicates a deviation from the weighted mean value

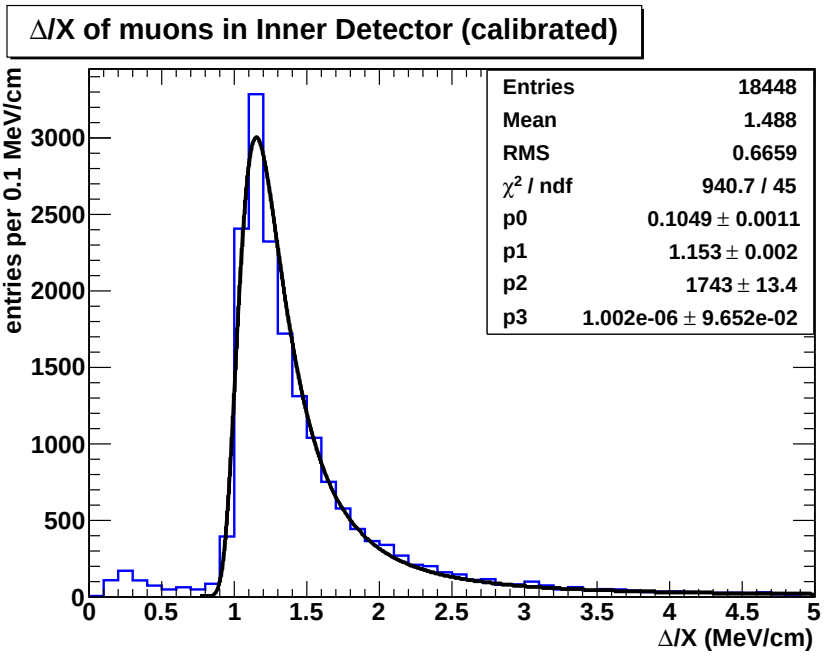

Figure 8.4: Muon energy loss Δ/X in the ID for a specific run. Shown is the fully calibrated response in E_{vis} over reconstructed track length. For this exemplary run the most probable energy loss is $\Delta_p/X = 1.15\,\mathrm{MeV/cm}$, the width of the Landau distribution is found to be $\sigma_{(\Delta_p/X)} = 0.10\,\mathrm{MeV/cm}$.

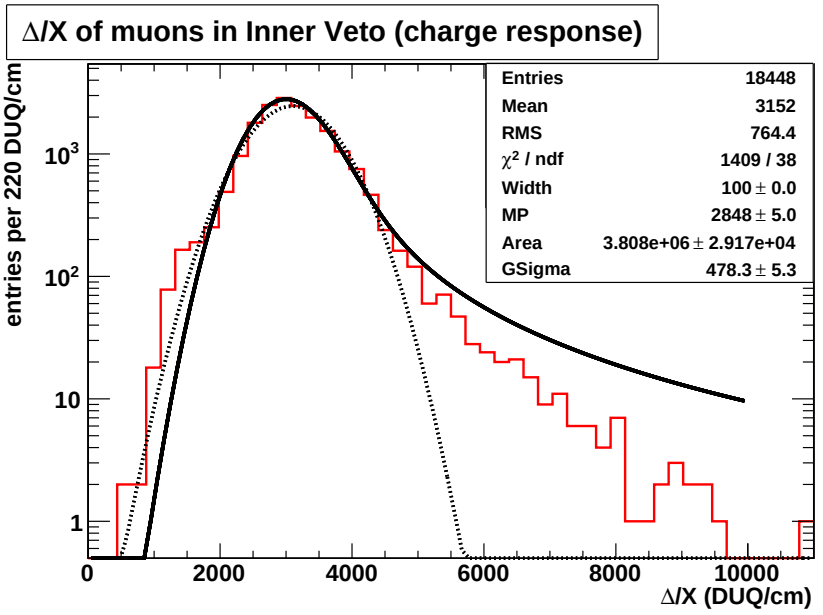

Figure 8.5: Muon energy loss Δ/X in the IV, shown in logarithmic scale. One can see that there are a few events with high energy loss in the tail, indeed indicating a deviation from the Gaussian distribution (dotted black line) for higher energy losses. However, the distribution misses entries in the tail extending to high energy losses that is expected due to the fitted Landau fit (black solid line). Nevertheless, the most probable energy loss was found to be $\Delta_p/X = 2848\,\mathrm{DUQ/cm}$ in contrast to Bethe value of $\bar{\Delta}/X = 3107\,\mathrm{DUQ/cm}$ .The width of the Landau distribution was $\sigma_{(\Delta_p/X)} = 100\,\mathrm{DUQ/cm}$ for this exemplary run.

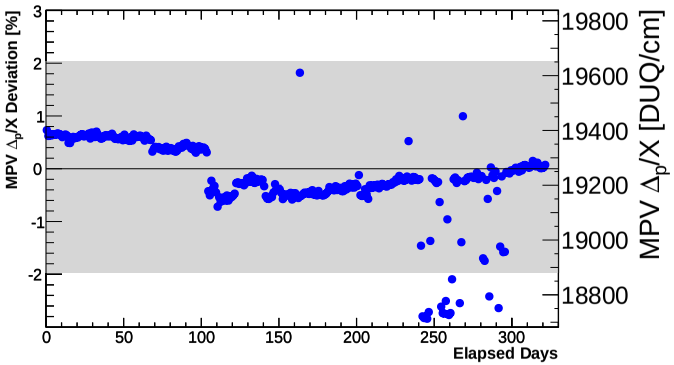

Figure 8.6: ID: most probable muon energy loss Δ/X vs time. Shown is the uncalibrated charge response in Q_{ID} per cm, thus no gain correction is applied.

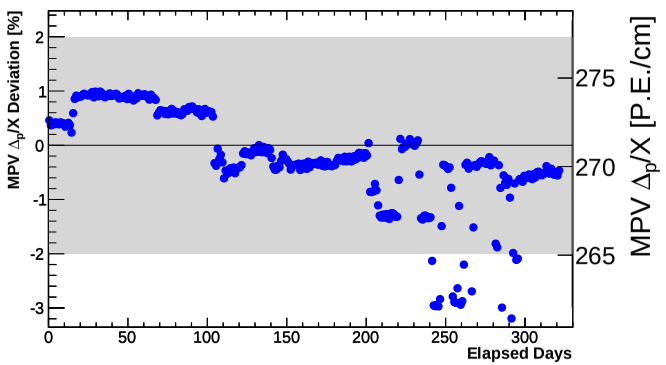

Figure 8.7: ID: most probable muon energy loss Δ_p/X vs time. Shown is the gain-calibrated response measured in photoelectrons PE per cm.

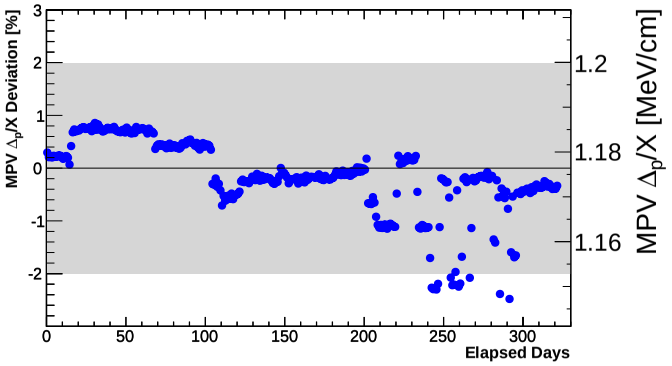

Figure 8.8: ID: specific muon energy loss Δ_p/X vs time. Shown is the fully calibrated response in E_{vis} per cm.

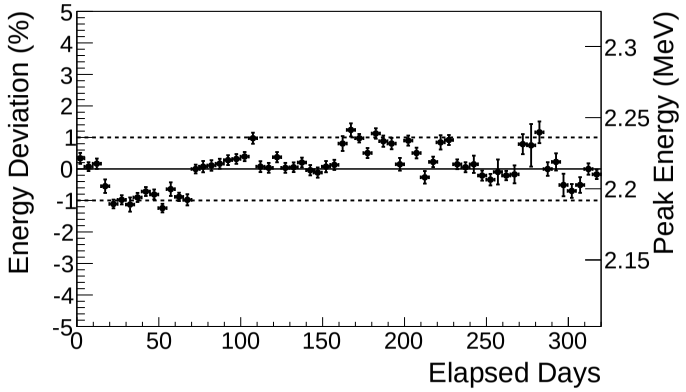

Figure 8.9: Stability of neutron capture peak on hydrogen.

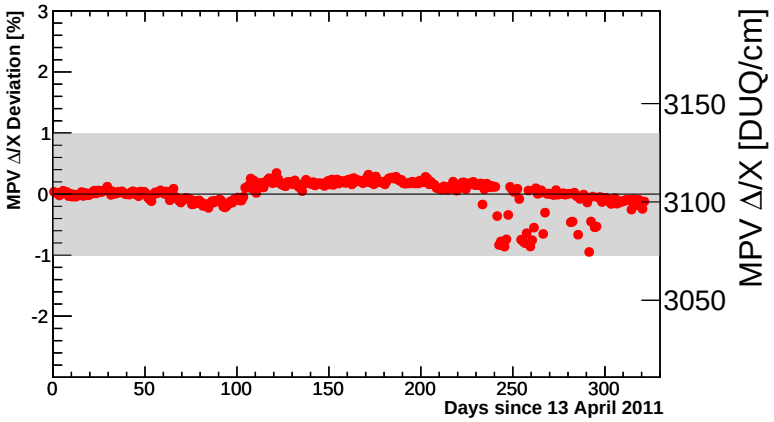

Figure 8.10: IV: most probable muon energy loss Δ_p/X vs time. Shown is the uncalibrated charge response Q_{IV}, therefore no Gain correction applied. Again, like the response in the ID, a period of strong fluctuations in response can be observed starting around day 250 and ending around day 300.

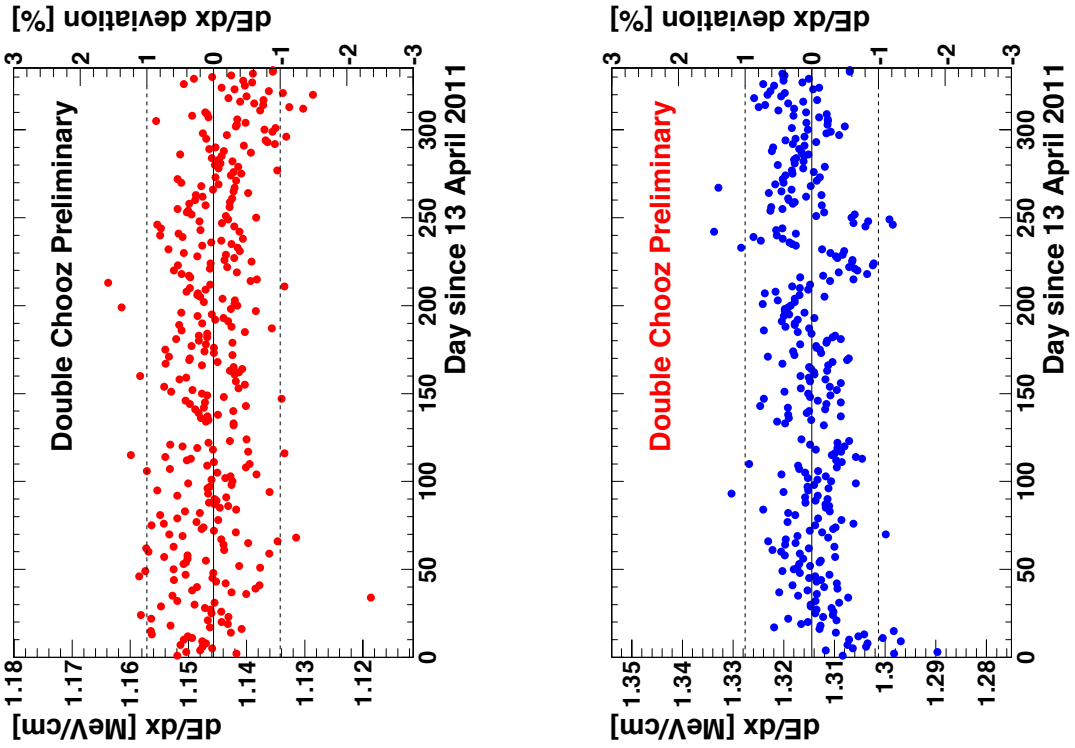

Figure 8.11: Most probable muon energy loss Δ_p/X vs time, obtained from a muon track reconstruction in the IV, not RecoMuonHam utilizing the ID. The left plot shows the charge response of the IV given by a rough DUQ to MeV conversion, where as the right plot shows the E_{vis} response of the ID. Due to the limited spatial resolution one can achieve in the IV, the spread is rather big compared to the plots obtained from the ID muon track reconstruction. However, still no step at day 100 is present, justifying the conclusion that these steps originate from a bug in the ID algorithm. Plot from S. Shimojima, private communication.

of 2 %. These plots give some insight on the response in the different calibration stages. The raw charge response in Q_{ID} basically stays flat except for a big step around day 100, which is introduced due to a bug fix in the RecoMuonHam track reconstruction package [151]. The small steps and the variations present in the data correspond to known shutdowns and restarts of the DAQ electronics, so called "power cycles". However, the origin of the rather big variation from days 250 to 300 is unknown.

Focusing on the plots of the response in PE and E_{vis}, the small steps corresponding to power cycles are further amplified. After each electronics power cycle the baseline of each channel changes, leading to a slightly different gain and thus different response. The gain calibration takes care to correct this, however, the applied correction is optimized in the low energy regime and seems to over-correct in the high energy regime. This becomes clear by comparing these stability plots to the stability of the neutron capture on H, thus the stability in the low energy regime. Figure 8.9 exhibits the same step-like behavior in the mean energy of n-H capture. But the steps are in the opposite direction, being an evidence for the over-correction in the high energy regime of muons.

The calculated RMS values and variances for the whole data set can be found in table 8.1. The overall instability is found to be on the level of $0.70\,\%_{rms}$ considering the E_{vis} energy scale compatible to the value of $0.61\,\%_{rms}$ obtained from neutron capture on hydrogen [56] in the low-energy regime. In addition, the RMS value of 1.17 MeV/cm matches the theoretical expectation calculated in the section before.

Focusing now on the specific energy loss of muons in the IV, as shown in figure 8.10, the steps caused by power cycles are not visible. This can be understood, as currently only the IV charge response in Q_{IV} is used and no gain calibration to correct for this power cycles is applied. However, there is an exception to the flat behavior around day 100 like in the ID, which is caused by the track reconstruction algorithm. As for the ID, a large variation is visible in the period of days from 250 to 300. Calculating the rms value of the specific energy loss in the IV and it's associated variance, see table 8.1, a relative instability of $0.22\,\%_{rms}$ was found, being smaller compared to the ID.

The specific muon energy loss in the IV can be cross-checked utilizing another track reconstruction algorithm. In [85] an algorithm for the IV is discussed and first results of it's performance were presented in [152]. Utilizing this reconstruction, there is no dependence on the ID and the step around day 100 is gone, as can be seen from the left plot (red) in figure 8.11. This justifies that the step is introduced by the use of the ID reconstruction algorithm. For this IV analysis, a rough conversion from IV charge to energy is applied, resulting in a specific energy loss of around 1.14 MeV/cm matching the prediction as well. The right plot (blue) in figure 8.11 shows the specific energy loss of the ID, were the track inside the ID was calculated from the reconstructed entry and exit points of the IV. It should be noted, that due to the limited position resolution one can achieve in the IV, the spread in the specific muon energy loss is rather big compared to the one utilizing the ID track reconstruction.

	ID response			IV response
item	Q_{ID} **[DUQ/cm]**	PE_{ID} **[PE/cm]**	E_{vis} **[MeV/cm]**	Q_{IV} **[DUQ/cm]**
$\langle \Delta_p/X \rangle_{RMS}$	19230	270.58	1.17	3104
$\sigma_{\langle \Delta_p/X \rangle}$	142.69	2.43	0.01	7.02
relative instability error [%]				
$(\Delta_p/X)/\langle \Delta_p/X \rangle_{RMS}$	0.74	0.90	0.70	0.22

Table 8.1: RMS values of most probable muon energy loss Δ_p/X in ID and IV for the considered data taking period. The relative response instability in the high energy regime is found to be $0.70\,\%_{rms}$ comparable to the one in the low energy regime of $0.61\,\%_{rms}$. The relative instability of the IV response is rather small, a value of $0.22\,\%_{rms}$ was found.

8.4 Muon decay and calibration

After the surveillance of the detector via muons, this section will concentrate on the use of muons for the calibration purposes. The currently used calibration sources (^{60}Co, ^{68}Ge, ^{137}Cs and ^{252}Cf) provide energies well below 10 MeV. Another calibration source at higher energy would be useful to check the linearity of the energy scale at higher energies and would provide an additional charge to energy conversion value. The decay of the cosmic muon inside the detector provides an excellent source for calibration at higher energies. It comes in high quantity and without any dead time due to source deployment. Another benefit is, that muon decay does not only happen in the ID, but also in the IV providing an conversion value there as well. This section starts with some theoretical explanation regarding muon decay, afterwards it will focus on the selection technique and the applied cuts to select electrons originating from muon decay in the ID and the IV. The section ends discussing the results and presents an attempt to fit the obtained muon decay spectra.

8.4.1 Muon decay

As stated in chapter 4 muons are not stable elementary particles, but decay via weak interaction

$$\mu^- \rightarrow e^- + \bar{\nu}_e + \nu_\mu\,, \quad \mu^+ \rightarrow e^+ + \nu_e + \bar{\nu}_\mu\,.$$

For a muon that stops and decays at rest, the mean lifetime is $2.197\,\mu$s [64]. However, it should be noted that for negative muons μ^-, the capture on carbon, $\mu^- + \mathrm{C} \rightarrow \mathrm{B} + \nu_\mu$, forming boron is a competing process. As positive and negative muons have not the same abundance their charge ratio $\rho = N_+/N_-$ of 1.268 has to be considered. Noting that μ^+ and μ^- independently contribute to the number of observed decays one finds

$$N(t) \;=\; N_{bkg} + N_+ e^{-\lambda_+ t} + N_- e^{-(\lambda_- + \lambda_c)t}, \tag{8.15}$$

assuming a constant number of background events N_{bgk}. Taking into account the capture rate $\lambda_c = 3.76 \cdot 10^4\,\mathrm{s}^{-1}$ [153] of negative muons, considering the total decay rate to be $N_0 = N_+ + N_-$ and assuming $\lambda_+ = \lambda_- \equiv \lambda$, thus equality of charged muon lifetimes, the decay rate is given by

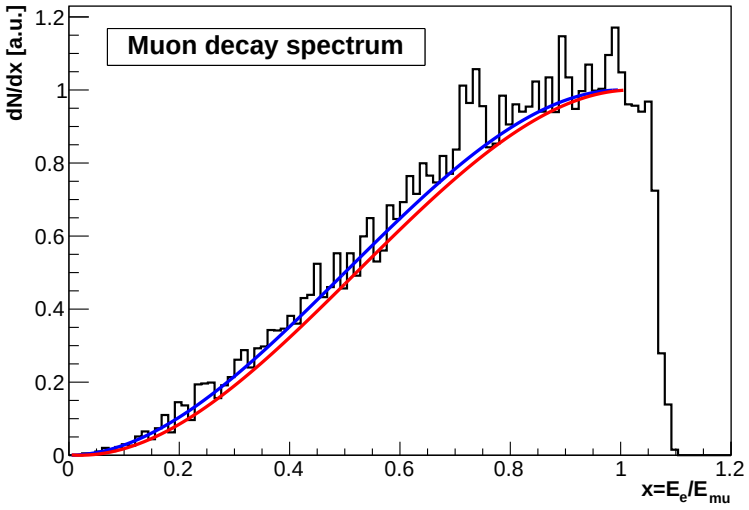

Figure 8.12: Theoretical muon decay spectrum calculated for μ^- in blue with a sharp cut-off at 52.82 MeV. Superimposed in red is the spectrum for μ^+ with a cut-off at 53.92 MeV. Due to quantum electrodynamic corrections the cut-off is not that sharp and is even further smoothed taking into account a finite detector resolution as indicated by the black histogram obtained from a simple MC.

$$N(t) = N_{bkg} + \frac{N}{1+\rho} e^{-\lambda t} \left\{ \lambda(\rho + e^{-\lambda_c t}) + \lambda_c e^{-\lambda_c t} \right\}. \tag{8.16}$$

In muon decay, the rest-mass of the muon 105.65 MeV is transferred into the mass of the electron/positron [4] and into the kinetic energy of the the three resulting particles. The electron (positron) gets on average $105/3 \approx 30$ MeV, whereas the whole decay spectrum is continuously from 0 up to 52.8 MeV for kinematic reasons. The electron/positron created in these decay is frequently named **Michel** electron, after Louis Michel who did first investigations into this weak process. The energy distribution of those michel electrons can be calculated being

$$dN = \frac{G_f^2 m_\mu c^2}{192\pi^3}(3-2x)x^2 dx, \tag{8.17}$$

with the Fermi constant G_F, the reduced energy $x = E_e/E_{max}$. The maximum energy $E_{max} = m_\mu c^2/2 = 52.82$ MeV is given by the endpoint of the spectrum. In comparison to μ^-, the spectrum of the μ^+-decay is shifted to higher energies by 2×511 keV because of the positron annihilation. Figure 8.12 shows the theoretical μ^-/μ^+ decay spectrum in blue/red superimposed to a Monte Carlo of muon decay smeared with a Gaussian energy resolution being $\Delta E/E = \alpha/\sqrt{E}$ with $\alpha = 10\,\%$.

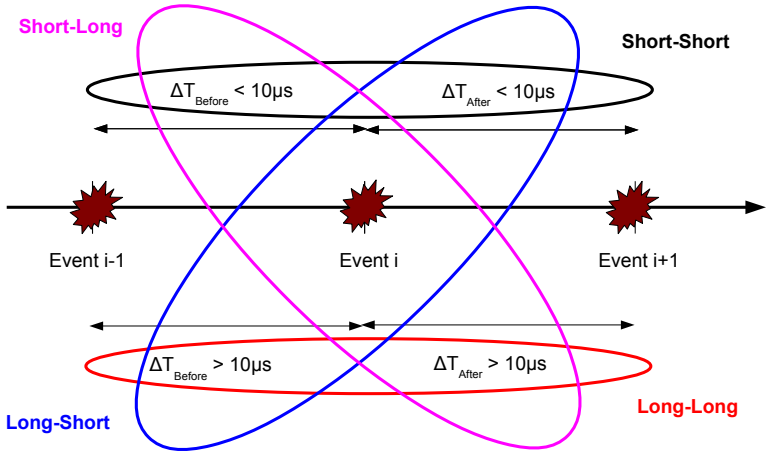

Figure 8.13: Scheme of applied selection method. For the current event i the time difference to the preceding event $i-1$ is ΔT_{before} and to the following event $i+1$ is ΔT_{after}. A classification is applied regarding whether the time differences are bigger or smaller than $10\,\mu$s, which leads to four categories indicated by the different coloring.

8.4.2 Time series analysis to select stopping muons and michel electrons

In the following the analysis method to select SM and subsequent michel electrons in the ID and the IV will be presented. This method was first used in [107] and was originally developed for the analysis of neutron capture efficiencies of ^{256}Cf and AmBe sources [154]. The basic idea is a classification of events by their timing: one considers the time differences to the preceding and following event. For a given event i the time difference to the preceding event $i-1$ is defined as ΔT_{before} and the time difference to the following event $i+1$ is defined as ΔT_{after}. The basic time unit of this classification is $10\,\mu$s. This value was chosen because if a SM is identified, most of these muons should have been decayed and an michel electron should be observed within the considered $10\,\mu$s
.
The classification scheme is visualized in figure 8.13. After the rejection of light noise and external triggers, this scheme applied to all ID events with $E_{vis} > 4.5\,$MeV and to all IV events $Q_{IV} > 10\,$kDUQ. The applied energy and charge threshold was chosen to suppress natural radioactivity. This leads to four categories depending whether the time differences ΔT are longer or short than the basic time unit:

- Long-Long: both time differences ΔT_{before} and ΔT_{after} are longer than $10\,\mu$s. This category should be dominated by muons, as the mean muon rates are around tens of Hz, which leads to average times between two different muons of around hundred μs.
- Long-Short: the time difference ΔT_{before} is longer and the difference ΔT_{after} is shorter

[4]It is safe to neglect the very small neutrino masses in this calculation.

than 10 μs. SM are expected to dominate this category, as most of the decays happens within the 10 μs. Some PMT and electronic effects are present, because after the big energy deposition of a muon the baseline restores only slowly, which leads to additional fake triggers.

- Short-Long: the time difference ΔT_{before} is shorter and the difference ΔT_{after} is longer than 10 μs. This category is filled with events correlated to a muon. This can be michel electrons from muon decay, FN created by the muon or fake triggers.
- Short-Short: both time differences ΔT_{before} and ΔT_{after} are both shorter than 10 μs. This category of events is expected to be dominated by burst-like light noise events, directly happening after each other.

Figures 8.14 (Long-Long), 8.15 (Long-Short), 8.16 (Short-Long) and 8.17 (Short-Short) show the distributions in the plane of E_{vis} in ID versus Q_{IV} in IV for the four different event categories. Figures 8.18 and 8.19 show the spectra of the four different event categories for ID and IV separately. It can be seen that muons dominate the L-L and L-S event categories, extending up to 800 MeV in the ID and having the characteristics of muons passing the IV. This is supported by the peaks of around 200 kDUQ and 500 kDUQ corresponding to muons passing the IV once or twice. For the L-S category the peak at 200 kDUQ is more prominent, indicating a larger contribution of SM in this sample than through going muons compared to the L-L category.

The S-L category extends up to 800 MeV in the ID indicating a contribution of muons coming short in time after another event. Mainly populated is the region of $E_{vis} < 100$ MeV in the ID and $Q_{IV} < 200$ kDUQ in the IV, were FN and michel electrons should dominate. Also the S-S category shows some events extending up to 800 MeV in the ID which could either be due to several muons coming close in time to each other ($\approx 10\,\mu$s) or due to fake triggers cause by high energetic muons. Again the region extending up to 300 MeV in the ID, being below 200 kDUQ in the IV is more populated. These events that create less light in the IV, but a considerable amount of energy in the ID are compatible with FN depositing energy via proton recoil or with fake triggers caused by the huge energy deposition of the previous muon.

8.4.3 Michel electron selection cuts

As motivated before, the michel electron being created in the decay of a SM should be in a candidate pair of events of type LS-SL. This can be translated into the following condition; a SM candidate event and michel candidate event must have a smaller time difference than 10 μs and have to be isolated in time to the preceding and following event by more than 10 μs as visualized in figure 8.20. The individual energy and charge spectra of ID and IV will now be considered in more detail to search for SM and michel electron candidates.

ID michel electron cuts

In addition to the timing cuts expressed through the selection of SM and michel candidate events out of the categories L-S and S-L respectively, cuts on energy and charge in ID and

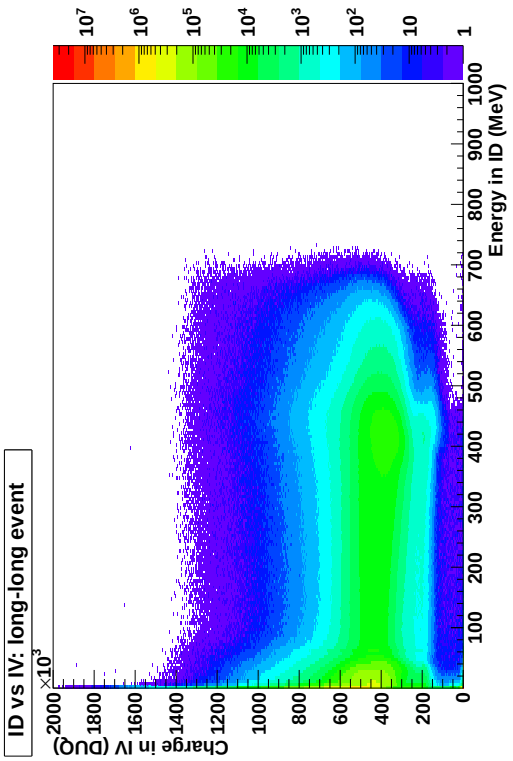

Figure 8.14: Plane ID energy vs IV charge for events in L-L category.

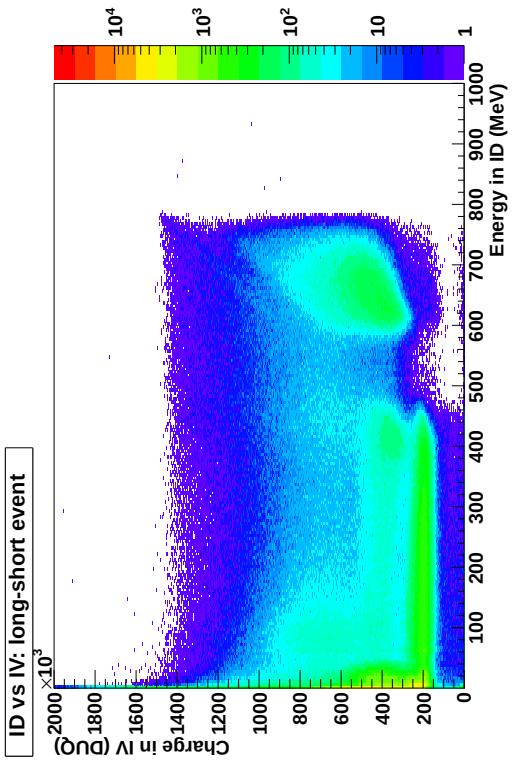

Figure 8.15: Plane ID energy vs IV charge for events in L-S category.

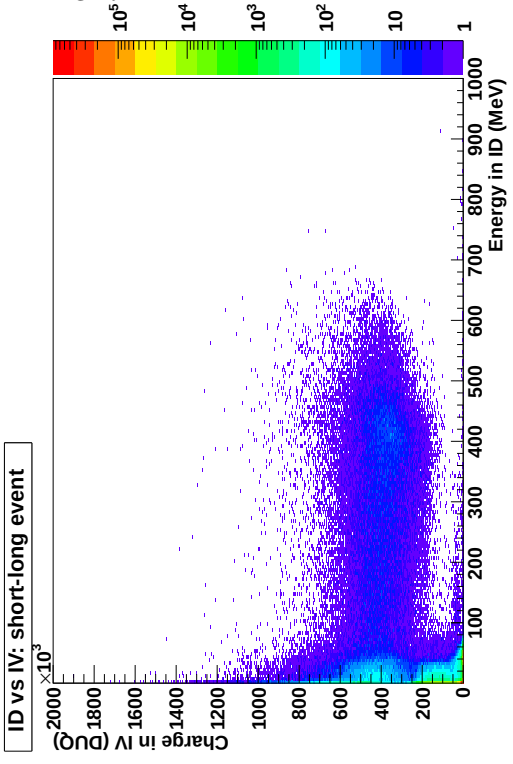

Figure 8.16: Plane ID energy vs IV charge for events in S-L category.

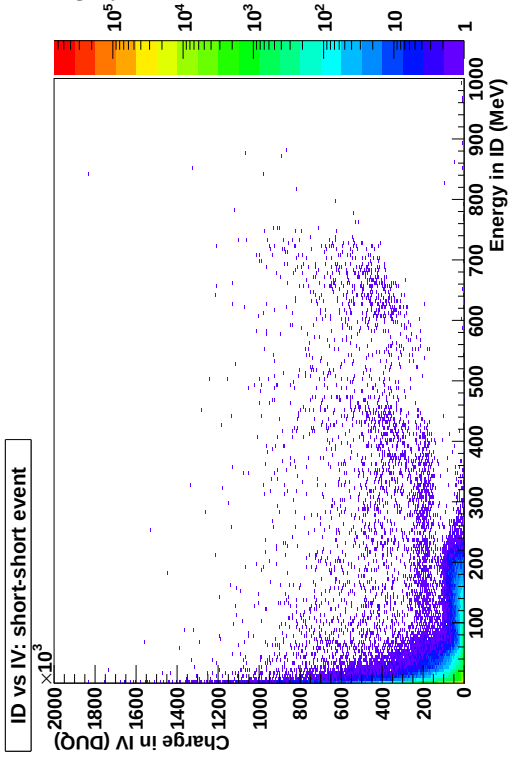

Figure 8.17: Plane ID energy vs IV charge for events in S-S category.

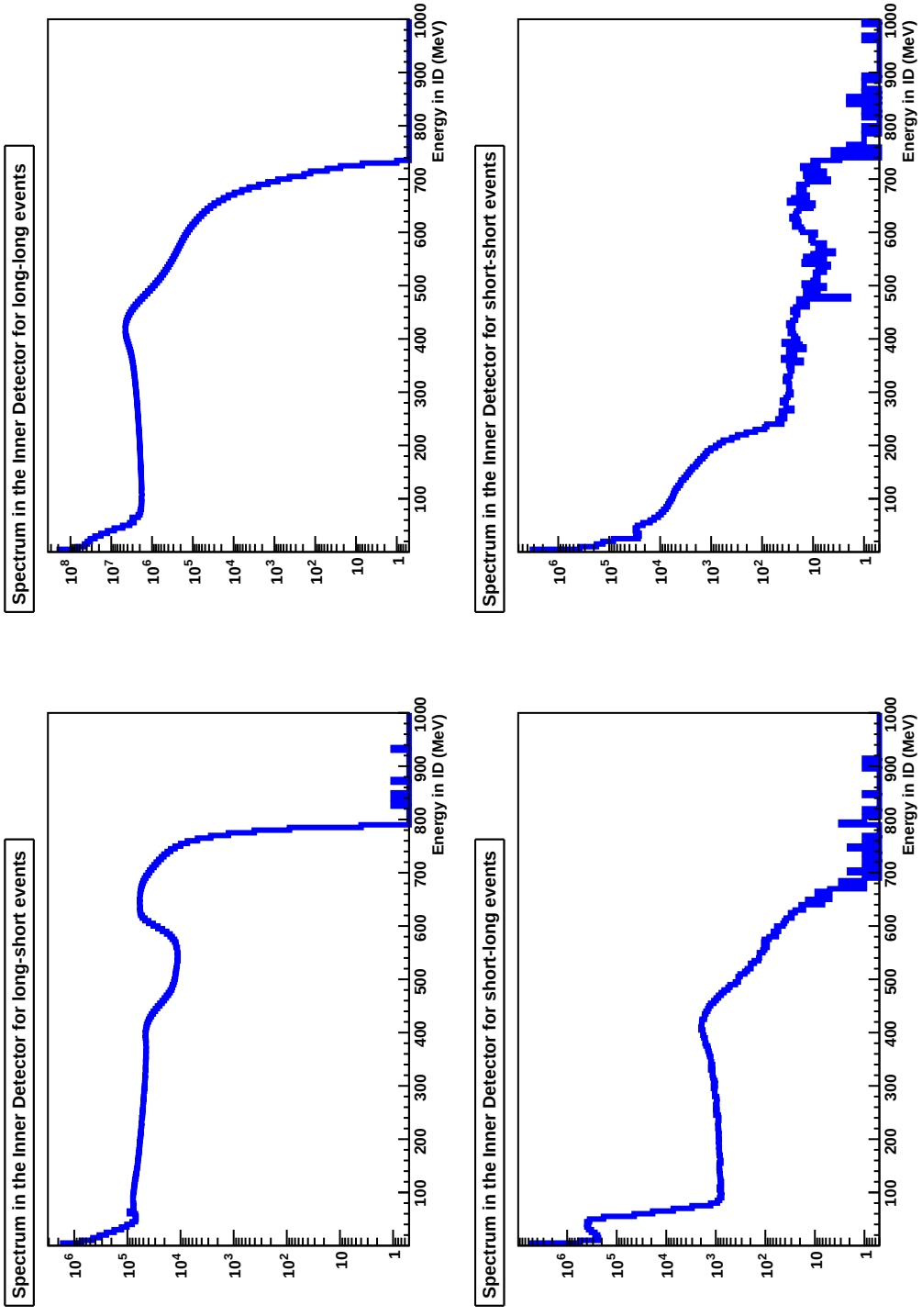

Figure 8.18: Energy spectra in the ID for the four different event categories being Short-Long, Long-Long, Long-Short and Short-Short depending on the basic time unit of 10 μs.

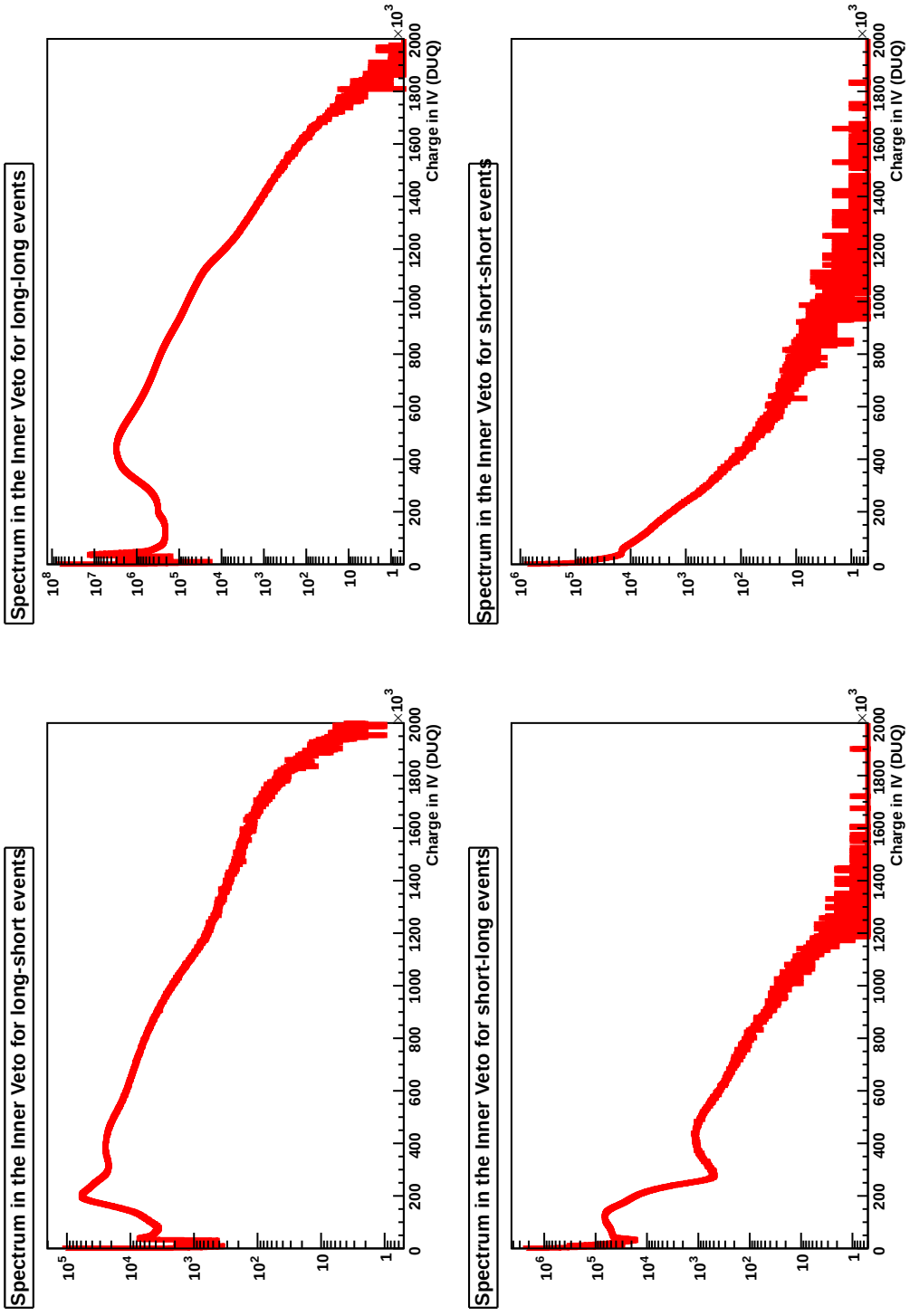

Figure 8.19: Charge spectra in the IV for the four different event categories being Short-Long, Long-Long, Long-Short and Short-Short depending on the basic time unit of 10 μs.

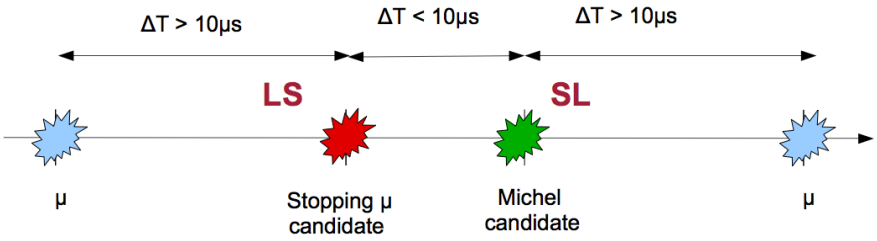

Figure 8.20: Visualization of coincidence condition for stopping muon and michel electron candidates. A valid candidate pair should be isolated in time by more than 10 μs to the previous and following event, hence not in a burst of events. In addition the SM and michel electron candidate have to be separated in time by less than 10 μs..

IV have to be used to select them. The expected pattern for a SM with subsequent decay is having a muon been identified by the IV, depositing around 200 kDUQ [5] and a high amount of energy in the ID. Predominantly these muons should enter the top of the IV, cross its volume and enter the ID. The biggest amount of detectable light should be created in the upper part of the IV, whereas less or no light at all is detected by the PMTs at the IV bottom. Thus one can request that the IV is not self-triggered by the 42 PMTs mounted at the bottom of the IV vessel. In addition, for runs taken later than July 2011 the OV is available and can be used for the selection as well. This is done by requesting a hit in the OV plastic scintillator panels, selecting muons coming from above.

The subsequent decay of these muons happens within the next 10 μs and releases an energy up to 60 MeV in the ID, whereas there should be no energy deposition in the IV and no hit detected in the OV at the same time. Specifying this considerations into proper cuts values for the SM yields

- ID: $E_{vis} > 30\,\text{MeV}$
- IV: $Q_{bot} < 10\,\text{kDUQ}$
- OV: hit (only applied if OV data available)

and for the subsequent event, which should be the decay into a michel electron

- ID: $4.5\,\text{MeV} < E_{vis} < 70\,\text{MeV}$
- IV: $Q_{IV} < 10\,\text{kDUQ}$
- OV: no hit (only applied if OV data available)

The application of these cuts selects 1,047,282 SM and michel electron candidate pairs in 322 days of data taking corresponding to a rate of around 3252 counts per day (**cpd**). Figures 8.21 show the energy and charge spectra of SM candidates in ID and IV. The cut on the charge collected in the IV bottom selects mainly SM extending up to 500 MeV. This is compatible with the maximum track length[6] of $\sqrt{2} \cdot 3598\,\text{mm}$ in the NT+GC vessel or $\sqrt{2} \cdot 2458\,\text{mm}$ for

[5] Corresponding to around 65 cm's of track length in the IV utilizing the muon energy loss value of 3104 DUQ/cm obtained in the section before.

[6] Calculate as $\sqrt{2}$ times the height of the NT or GC vessel, being the diagonal.

the T vessel only, corresponding to energies of 605 MeV in the first and to 410 MeV in the second case. In the IV charge spectrum the 200 kDUQ peak is very pronounced, as expected for stopping and decaying muons which cross the IV only once.

Figure 8.22 shows these distributions for michel electron candidates. The charge spectrum of the selected michel electron events in the IV resembles a exponential shape compatible with radioactivity events having a change in shape around 2 kDUQ. The energy spectrum of the ID resembles the shape expected from muon decay having a mean value of around 35 MeV matching the kinematics expectation of 105 MeV/3 perfectly.

In the following the event vertices of the michel candidates in the ID[7] and the time difference $\Delta T_{\mu e}$ between the previous SM and michel candidate will be investigated.

Focusing on the event vertices, their distribution in the x-y plane can be seen in the left part of figure 8.23 and in the plane height h versus radius squared ρ^2 in the right part of the same figure. The second distribution shows that most of the michel electron candidates were reconstructed in the upper part of the detector, matching the expectation that these events are created by the decay of muons that reach the detector from above. For the first distribution in the x-y plane, it can be seen that the events are well localized within the target, being rotational symmetric with the exception of the +y direction. This can be understood as this is the direction towards the flank of the hill, thus having less overburden according to the hill profile, Fig 4.9, that can be found in chapter 4. As muons travel through the rock overburden they loose energy therefore being less energetic as they reach the detector, increasing the chance to stop and decay. However muons traveling through the flank of the hill, loose less energy as they have to pass less matter having a smaller chance to stop and decay inside the detector.

The left plot in figure 8.24 visualizes the time difference $\Delta T_{\mu e}$ between michel electron candidate and the preceding SM. This distribution shows the expected exponential behavior between $1 - 5\,\mu$s, but detector issues compromise this behavior for shorter and longer time differences. Investigations into this [155] showed that the energy of the parent SM has an impact on the ΔT distribution, being compromised for SM energies above 100 MeV and recovering for energies below. It is thought that the cut-off's at 1 MeV and 5 MeV are due to instrumental effects caused by a high energy deposition of the previous muon leading to after-pulsing of the PMT, a long recovery time of the PMT baseline and additional, fake triggers as well as some inefficiency in the trigger system. Fitting the distribution with the expected exponential behavior of eq. 8.15 in the range of 1 to 5 μs yields a decay time of 2.27 μs ($\chi^2/ndf = 1971/11$), while fixing the positive to negative ratio ρ and the capture rate of negative muons λ_c. This value is higher than the muon lifetime τ_μ of around 2.20 μs by 3 %. The right plot in figure 8.24 shows the time differences $\Delta T_{\mu e}$ versus E_{vis}, the energy of the parent SM candidate.

[7] Reconstructed utilizing the RecoBama vertex reconstruction algorithm.

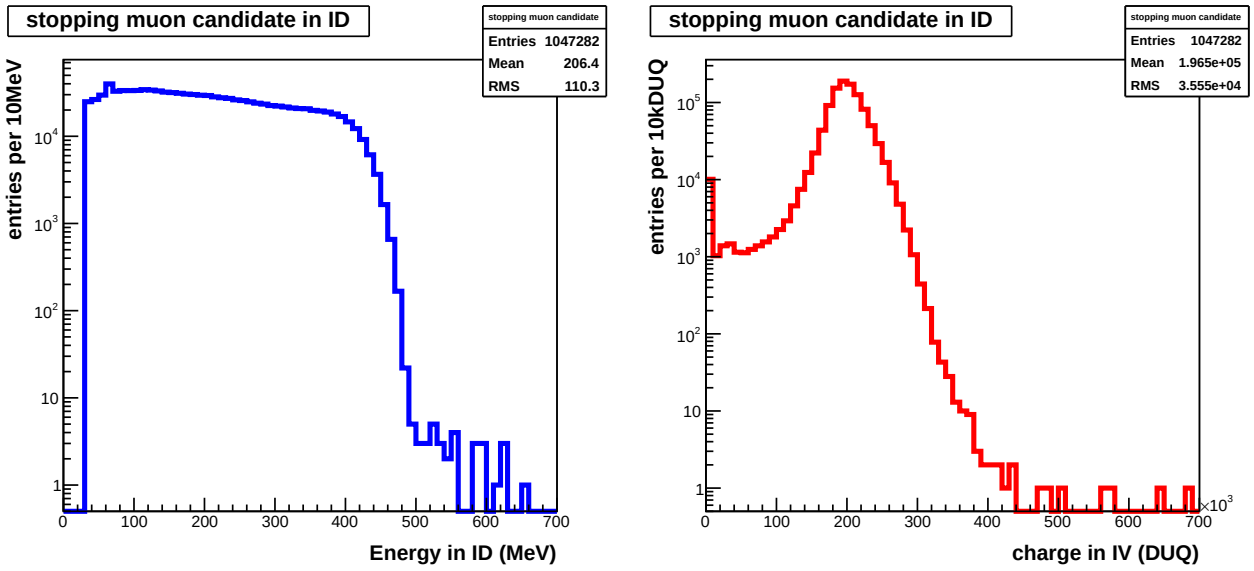

Figure 8.21: Stopping muon in the ID: Shown in the left plot is the distribution of deposited energy in the ID reaching up to 500 MeV corresponding to track lengths of up to 4.2 m. This is less than the maximal track in the ID being compatible with muons stopping inside the detector and passing through it. The plot on the left side visualizes the charge response of the IV, where the peak corresponding to muons passing the IV once is clearly visible.

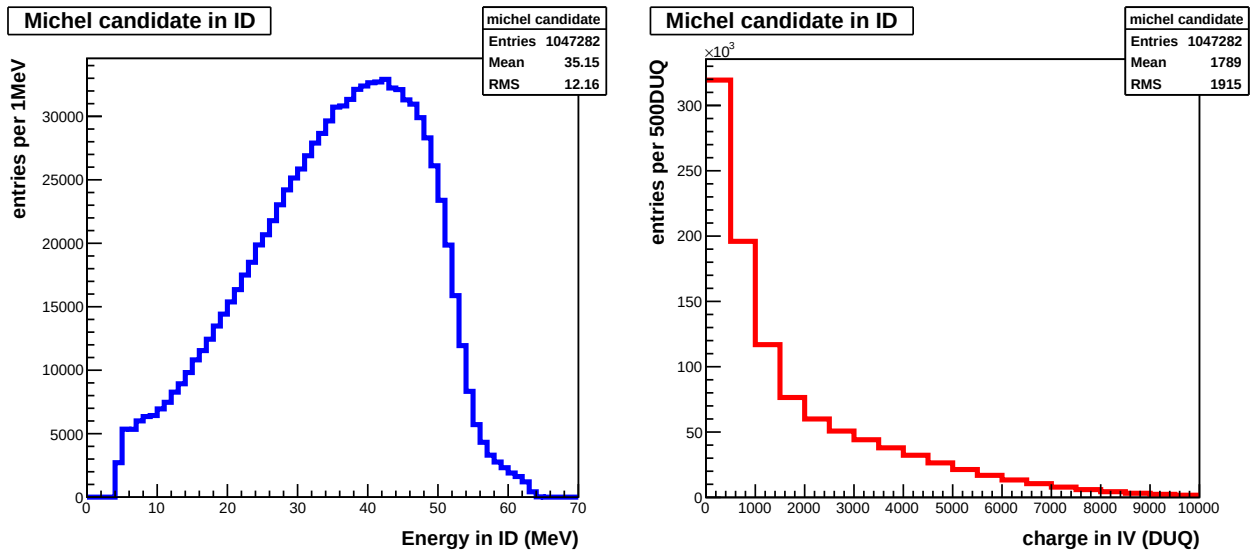

Figure 8.22: Michel electrons in ID: shown on the left side is the energy spectrum of muon decay within the ID and on the right side the corresponding charge response of the IV for these events. The spectrum in the ID clearly resembles the shape expected from muon decay, whereas the spectrum in the IV is compatible with radioactivity events being accidentally in coincidence with a muon decay.

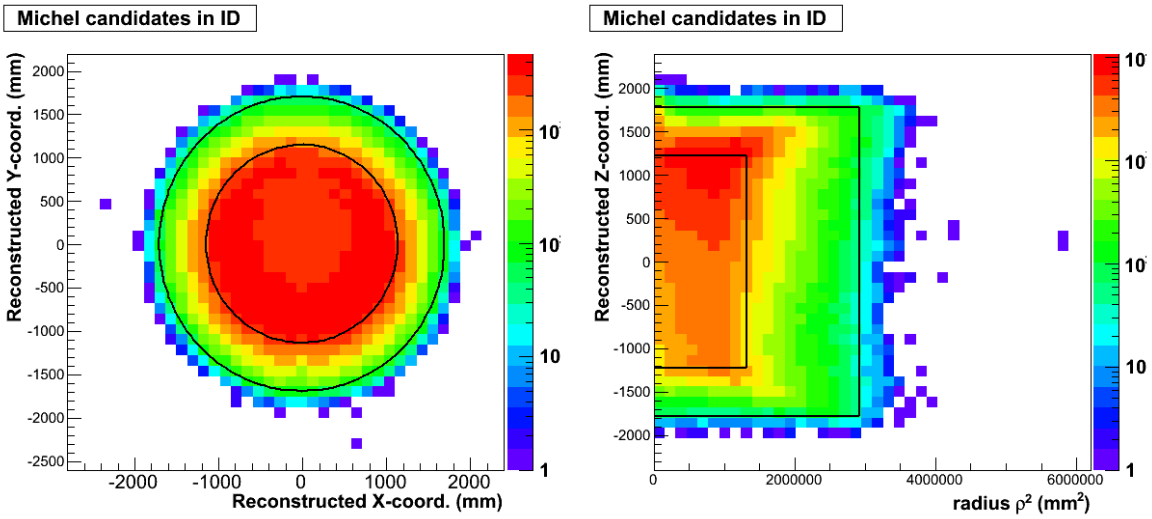

Figure 8.23: Event vertices of michel electrons in ID: left figure shows the reconstructed event vertices in x-y plane, whereas the right figure shows the in the plane height versus radius squared ρ^2. The solid black correspond either to the T acrylic vessel or the GC acrylic vessel.

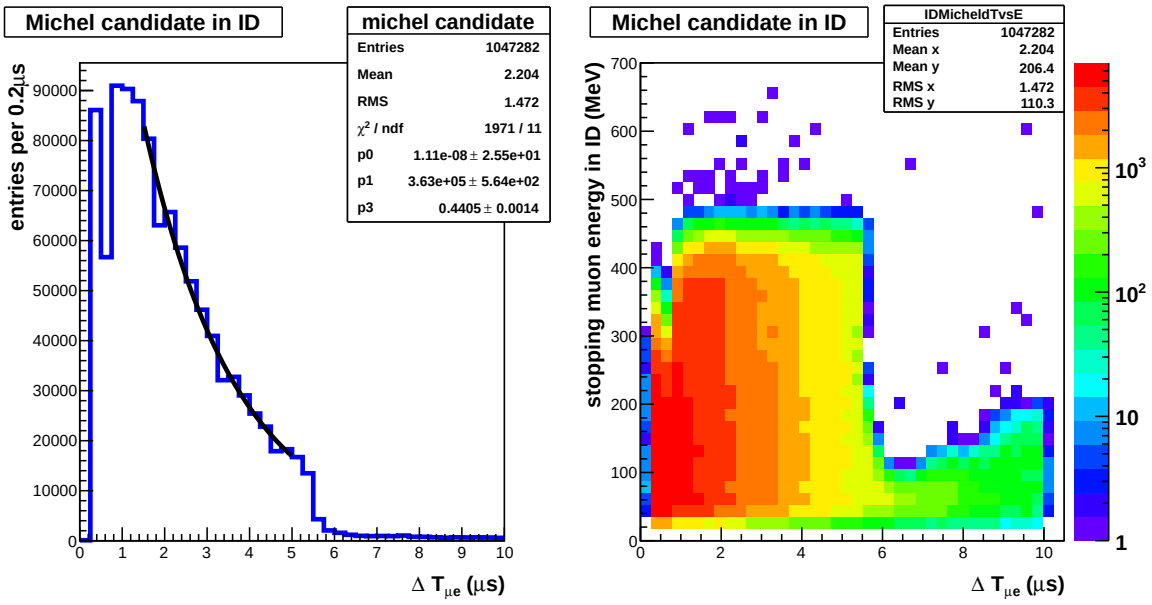

Figure 8.24: Distribution of time difference between stopping muon and michel electron candidate in the ID: right side shows the time difference distribution $\Delta T_{\mu e}$, whereas the left side shows this distribution versus the energy of the previous stopping muon candidate in the ID. It can be seen, that the energy of the parent stopping muon has a strong impact on the $\Delta T_{\mu e}$ distribution. A cut-off due to electronic effects in the time difference at around 5 μs is visible. The extracted muon lifetime is 2.27 μs (χ^2/ndf= 1971/11).

IV michel electron cuts

The expected SM and michel electron pattern in the IV is different from the one in the ID. A SM in the IV should have a high energy deposition within the IV volume and no energy deposition in the ID, because it should not enter the ID volume at all. As muons are expected to enter the IV vessel from above, the majority of light should be detected by the upper IV PMTs. Thus less collected charge for the bottom PMTs and like it was the case for the ID a valid hit in the OV. The subsequent muon decay happens within the IV as well, therefore there should not be any significant energy deposition in the ID and no valid hit in the OV. To express this expectation in selection conditions one gets

- ID: $E_{vis} < 4.5\,\mathrm{MeV}$
- IV: $Q_{IV} > 100\,\mathrm{kDUQ}$
- IV: $Q_{IV,bot} < 10\,\mathrm{kDUQ}$
- OV: hit (only if OV data were available)

for the stopping muon candidate and

- ID: $E_{vis} < 4.5\,\mathrm{MeV}$
- IV: $10\,\mathrm{kDUQ} < Q_{IV} < 200\,\mathrm{kDUQ}$
- OV: no hit (only applied if OV data available)

for a subsequent muon decay.

The application of these cuts selects $1,006,456$ events in 322 days corresponding to a rate of 3125 cpd being around 4 % lower then the ID selection. Figures 8.25 and 8.26 show the energy and charge spectra of ID and IV for SM and michel electron candidates. The energy spectrum of SM in the ID shows an exponential sharper for energies below 5 MeV being an inflection point where the slope of the spectrum changes decreasing monotonically to higher energies. The IV charge spectrum goes up to 600 kDUQ corresponding to track lengths of up to 2 m. Longer track lengths in the IV are excluded because of the restriction on the charge of the bottom PMTs.

The ID energy distribution of the michel candidates resembles an exponential shape indicating radioactivity events being randomly coincident with the michel event in the IV. Considering the IV, the charge spectrum resembles the expected shape of the michel spectrum having a mean of 120 kDUQ taking into account the cut-off at low charges, corresponding to around 34 MeV not far away from the kinematic expectation.

As there is no vertex reconstruction for the IV at the moment, the following paragraph will focus on the time difference between SM and michel electron candidate which should reflect the muon lifetime. The right side of figure 8.27 shows the distribution of time differences $\Delta T_{\mu e}$, whereas the left side shows this time difference versus the energy of the preceding SM candidate like in the ID case.

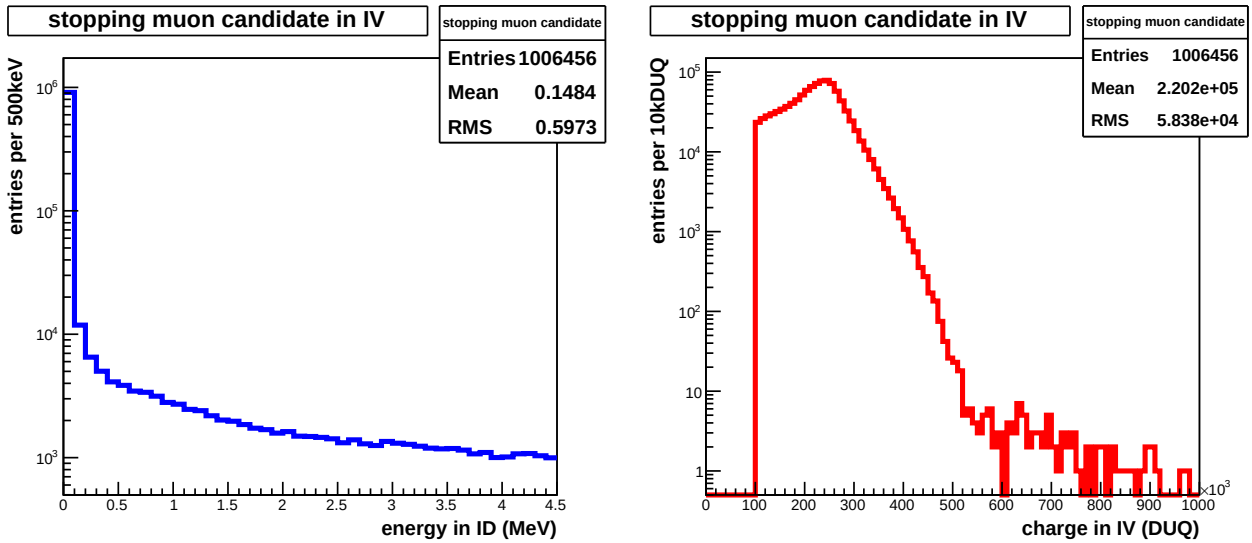

Figure 8.25: Stopping muon in the IV: Shown in the left plot is the deposited energy in the ID and on the left plot is the charge response of the IV for stopping muons. The energy spectrum in the ID exhibits an exponential shape as expected from random coincidences of natural radioactivity events in the ID and a SM in the IV.

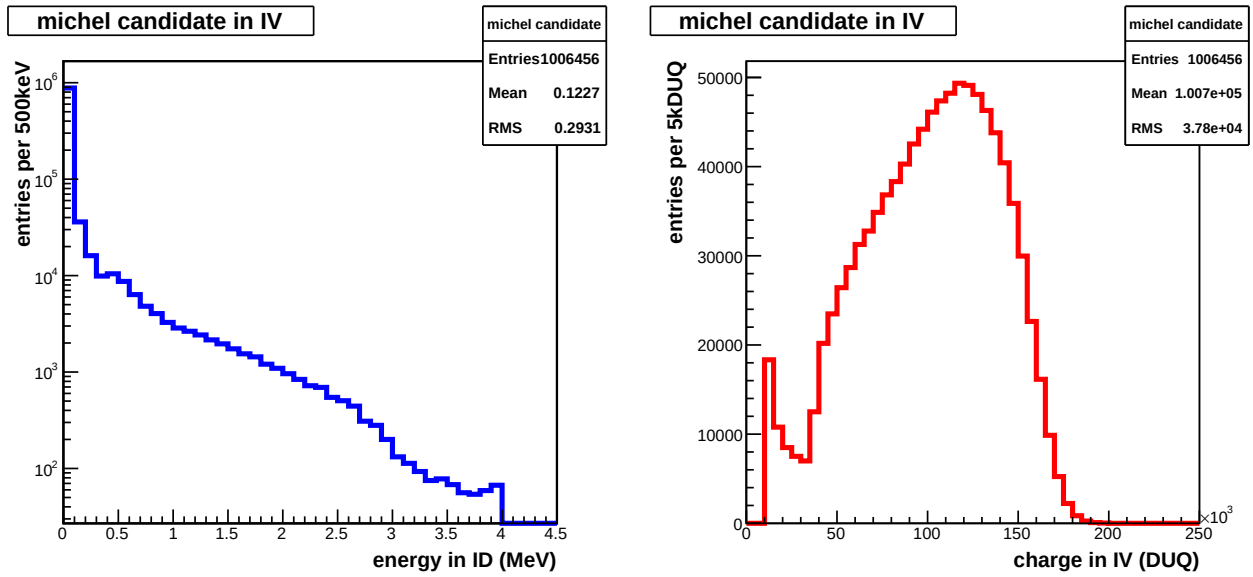

Figure 8.26: Michel electrons in the IV: shown on the right plot is the charge spectrum of muon decay within the IV and on the left plot the corresponding energy response of the ID for these events. Apart from a peak at around 15 kDUQ the charge spectrum in the IV resembles the shape expected from muon decay, whereas the energy spectrum in the ID is compatible with accidental coincident radioactivity events.

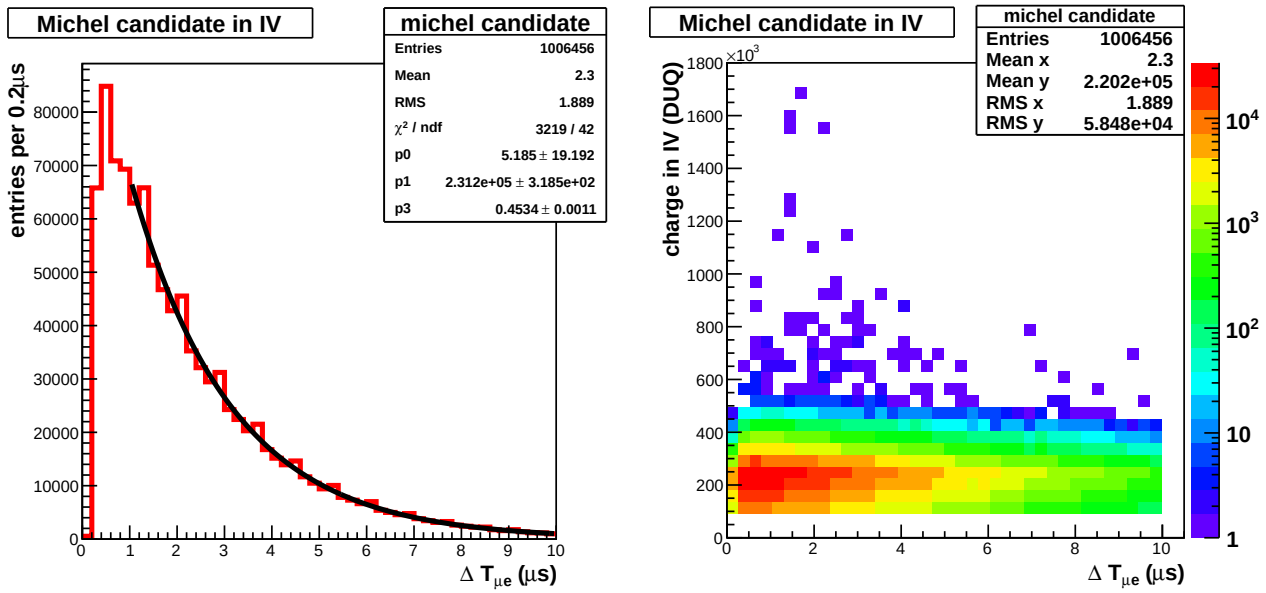

Figure 8.27: Distribution of time difference $\Delta T_{\mu e}$ between stopping muon and michel electron candidate in the IV. In opposite to the ID, now the full range from 1 to 10 μs shows an exponential behavior. The extracted muon lifetime is 2.21 μs ($\chi^2 = 3219/42$) matching the theoretical expectation of around 2.20 μs much better compared to the value extracted from the same distribution in the ID.

Compared to the time distribution $\Delta T_{\mu e}$ in the ID, the distribution for the IV resembles the expected exponential behavior up to 10 μs after the preceding SM. Fitting this distribution with the exponential described in eq. 8.15, while fixing the the parameters ρ and λ_c as it was done in the ID case, yields a lifetime of 2.21 μs ($\chi^2/ndf = 3219/42$) matching the literature lifetime of $\tau_\mu \approx 2.20\,\mu$s better.

8.4.4 Determination of the endpoint of the michel spectrum

After the selection of michel electron candidates was presented, this subsection will focus on the attempt to extract the decay spectrum endpoint. A fit to the measured data is done by numerical convolution of the decay spectrum described by Eq. 8.17 and a Gaussian function resembling the finite energy resolution of the detector. Figures 8.28 and 8.29 show this fit attempts to the michel spectra measured in the ID and the IV respectively. The utilized selection cuts are the ones discussed in the previous subsection. However, fitting the spectrum is not straight forward and fits do not converge for several reasons connected to the detector response after a huge muon energy deposition, as already noticed in the timing distribution $\Delta T_{\mu e}$ for the ID.

In figure 8.28 the upper plot shows the measured michel spectrum in blue, whereas the applied fit is colored yellow. The lower plot visualizes the difference between data and the fit, indicating several strong deviations from the expectation. It can be seen that data and fit do not agree in the range from 4.5 MeV to 40 MeV and in the range from 50 MeV to 60 MeV. Regarding the IV, the upper plot of figure 8.29 shows the measured spectrum in red, the

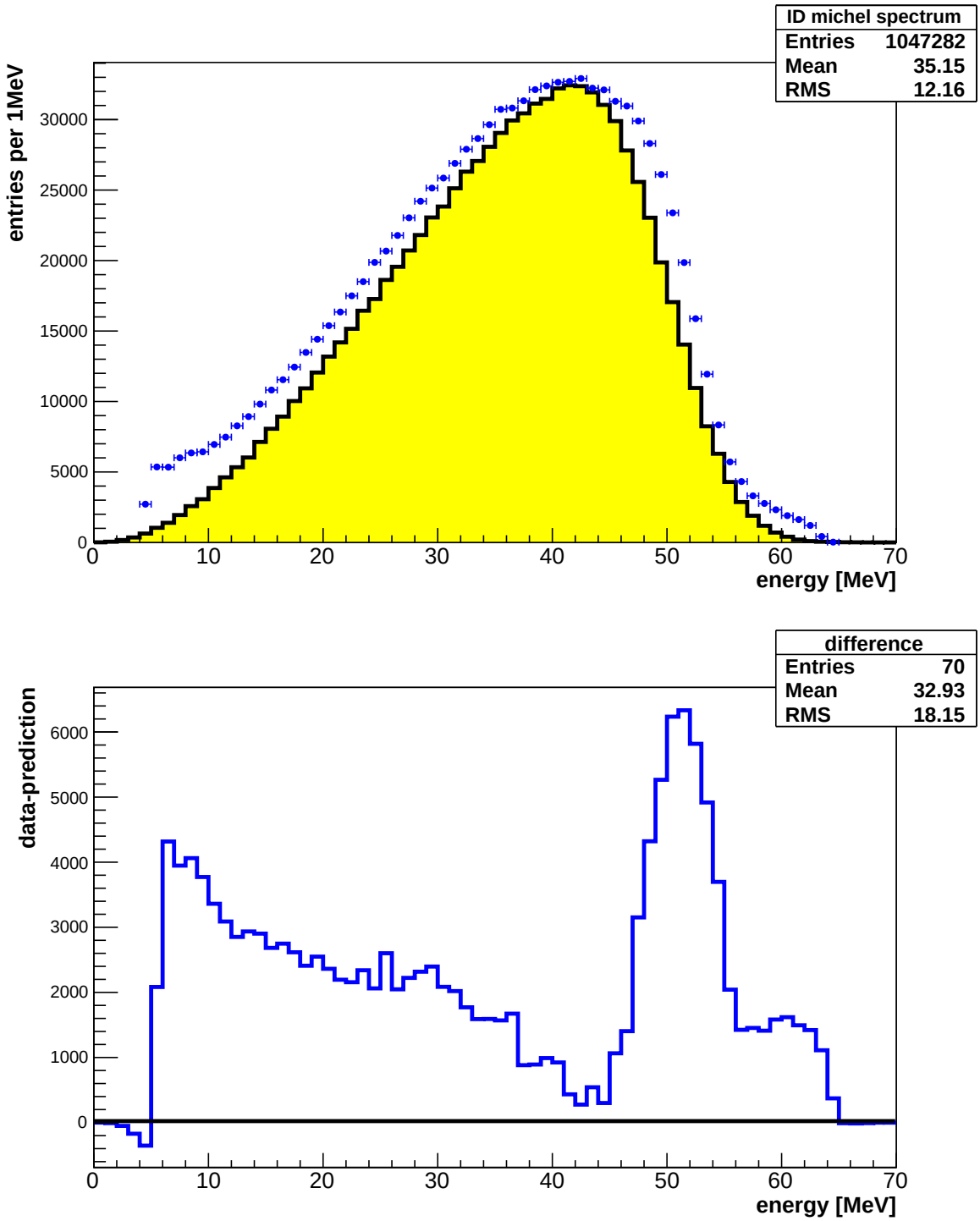

Figure 8.28: Fitting the michel spectrum in the ID. The upper plot shows the measured spectrum in blue, the fit is shown by the superimposed histogram colored yellow. The lower plot visualizes the difference between data and the fit prediction. Two energy regions with discrepancies are visible, the first, 4.5 MeV $< E_{vis} <$ 40 MeV and the second extending from 50 MeV to 60 MeV.

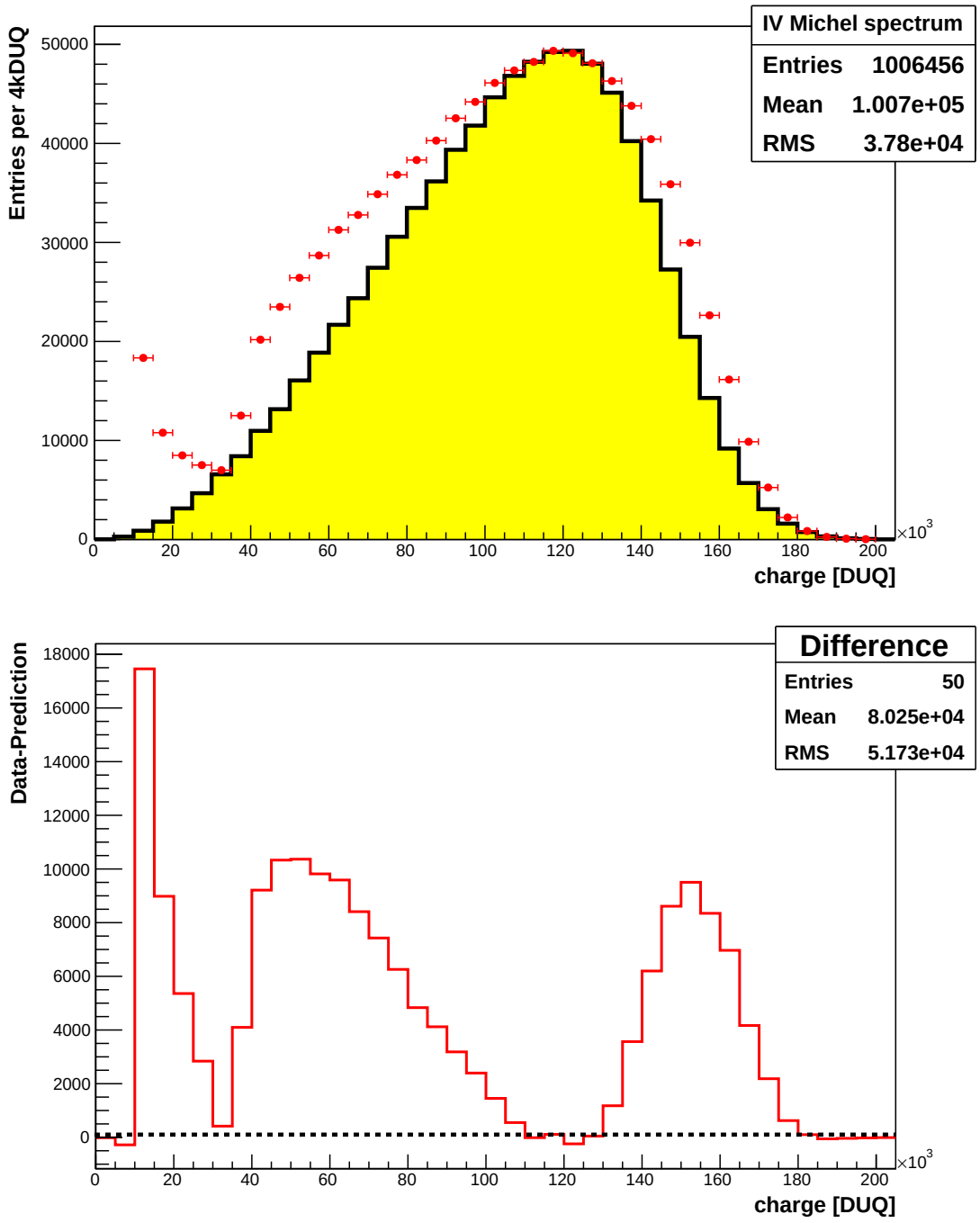

Figure 8.29: Fitting the michel electron spectrum in the IV. The upper plot shows the measured spectrum in red, the fit is shown by the histogram colored yellow. The lower plot visualizes the difference between data and the fit. The structure around 15 kDUQ in data does not correspond to the expected michel spectrum, also the range from 40 to 100 kDUQ as well as the range $140 - 180$ kDUQ.

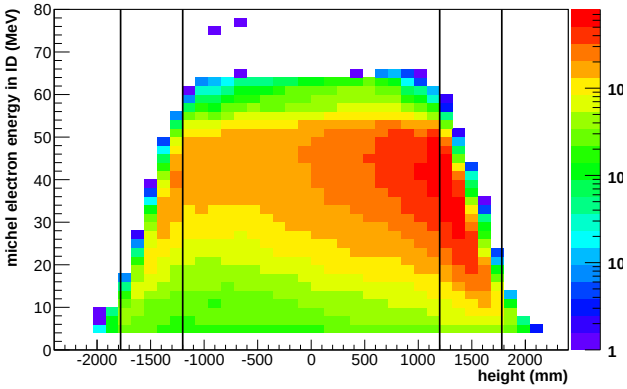

Figure 8.30: Energy of a michel electron candidate versus z-coordinate in the ID. The black line at ±1200 mm and ±1780 mm correspond either to the top or bottom of the T or the GC acrylic vessels.

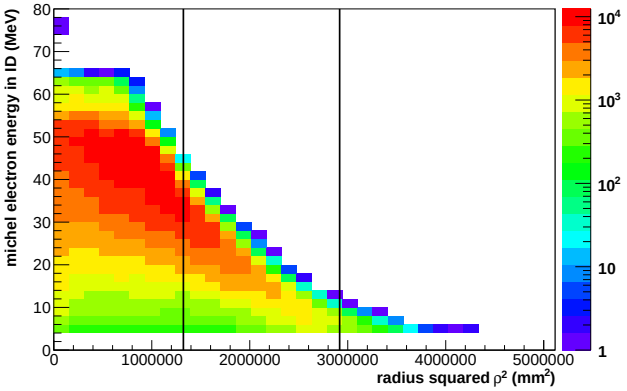

Figure 8.31: Energy of michel electron candidates versus squared radius ρ^2 in the ID. The black lines at $(1150\,\text{mm})^2$ and $(1708\,\text{mm})^2$ correspond to the borders of the T and the GC acrylic vessels respectively.

fitted spectrum is colored yellow. The lower plot visualizes the difference between data and prediction indicating strong deviations around 15 kDUQ and in the range 40 to 100 kDUQ, as well as the range 140 to 180 kDUQ.

The following subsections will explain observations regarding different dependencies (position and energy of previous SM) of the michel spectra in ID and IV which could explain the observed deviations to some extent.

Michel electrons in the ID

In the ID the michel spectrum exhibits a strong position dependence, as close to the NT borders the energy of the decay is not fully detectable. As a consequence of this, the mean of the spectrum shifts, being a position dependent function in radius ρ and height z in the NT. This shift can be seen in figures 8.30 and 8.31 showing the michel electron spectrum as a function of reconstructed z-coordinate or as a function of squared radius ρ^2 respectively. In both cases, near the boundary of the GC high energies seem to be missing.

The reason for this could be that the michel electron produced in the muon decay next to the wall of the GC acrylics vessel spills into the buffer volume. There, without any scintillator it creates less light via the Cherenkov effect. To handle this, fiducial volume cuts need to be applied, restricting the michel candidate events to the ones reconstructed inside the T. But the effect of such a cut needs to be studied carefully, as this does not only alter the number of selected events, but changes the shape of the spectrum as well.

This is visualized in figure 8.32 for several fiducial volume cuts compared to the nominal selection shown in black. The restriction in the z-coordinate (red) of the ID to be within the T acrylics vessel, $z < 1200\,\text{mm}$, shifts the mean of the spectrum to higher energies as the michel electrons now deposit their energy with the T scintillator. The opposite happens

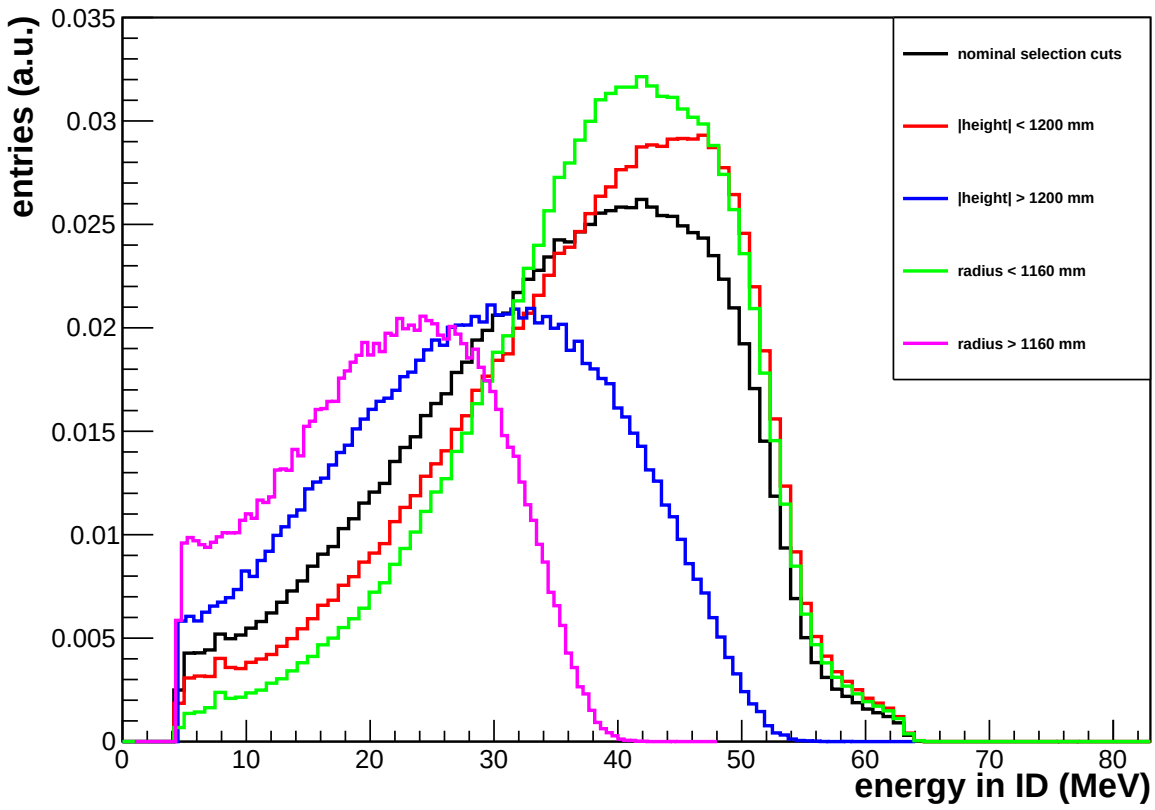

Figure 8.32: This plot visualizes the position dependence of the michel candidate spectrum in the ID. The black histogram is the spectrum obtained from the nominal cuts described in Sec. 8.4.3 before. The red and blue histogram show the michel spectrum by restricting the z-coordinate of the decay event to be inside the T or outside respectively. The same is shown for the radial direction, in red events inside the T, in green outside the T. It can be seen, that the michel energy spectrum is distorted in the boundary regions of the T and in the GC vessel.

for $z > 1200\,\text{mm}$, thus requesting the reconstructed event to be outside the T vessel. The spectrum is much broader and compared to the nominal selection, the mean is shifted to lower energies. The same observations hold for restricting the event to be inside the T or outside in radial direction. Requesting, $\rho < 1160\,\text{mm}$ shifts the mean to higher energies, whereas for $\rho > 1160\,\text{mm}$ the spectrum gets broader and the mean shifts to lower energies.

Actually the effect can be quantified utilizing a dedicated MC simulation, homogeneously generating electrons/positrons in the michel electron energy range. Calculating the ratio of measured and deposited energy, E_{meas}/E_{dep}, dependend on position in the detector one should obtain similar plots like 8.30 and 8.31 for MC data. Detector regions where the full deposited energy cannot be measured would be indicated by a ratio smaller than one.

In addition, for the ID there is a strong correlation between the energy of a michel candidate and the energy of the parent SM, distorting the spectrum for high SM energies. This is

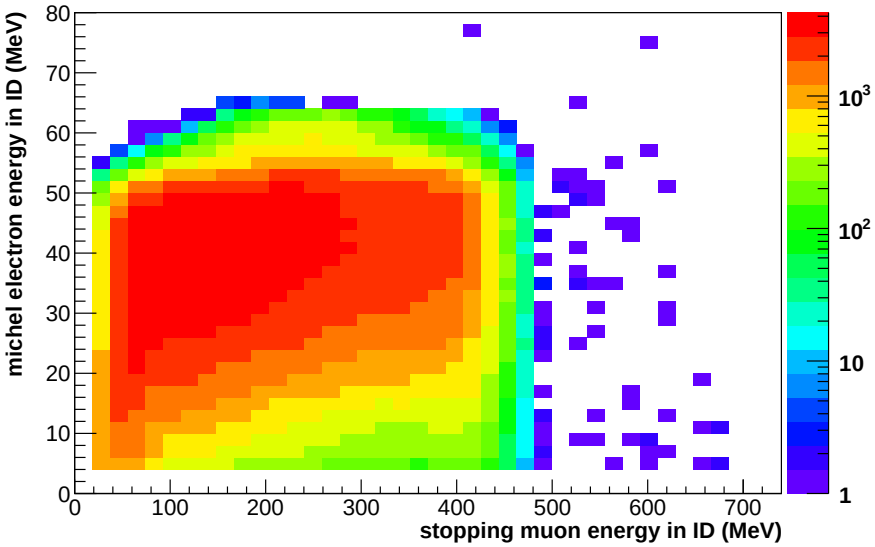

Figure 8.33: Michel candidate energy versus SM energy in the ID. A strong correlation is observable, with higher SM energy the michel energy increases. After high muon energy depositions the PMT baseline overshoots and needs some time to recover faking higher charge and therefore higher energies for a second PMT pulse coming shortly afterwards.

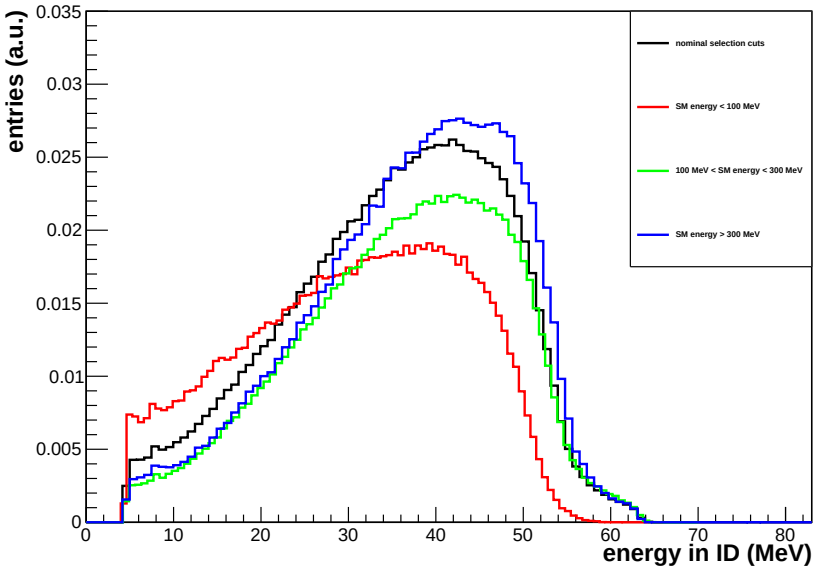

Figure 8.34: Dependence of michel energy spectrum on stopping muon energy in the ID. Compared to the spectrum selected with the nominal cuts, the shape of the spectrum changes by varying the parent SM energy. For SM energies higher than 300 MeV the mean of the spectrum moves to higher energies, whereas for SM energies below 100 MeV it shifts to lower energies.

because after a high energy depositions the PMT baseline overshoots and needs some time to recover resulting in a misleadingly high charge that is faking higher energies for a second PMT pulse coming shortly afterwards. This can be seen in figure 8.33 showing the plane of SM energy versus michel candidate energy. In figure 8.34 the michel spectrum obtained with the nominal cuts (mean value 35 MeV) is compared to the ones obtained using three different ranges of parent SM energies. First, in red the region below 100 MeV in SM energy, where the mean of the spectrum is shifted to lower energy by 11 %, being 31 MeV, compared to the nominal selection in black. In green an intermediate SM energy range, 100 MeV$< E_{vis} <$ 300 MeV, is shown. Here the mean is shifted to higher energy by 3 % to 36 MeV. In blue the region of high SM energies, being above 300 MeV is shown. Compared to the nominal selection, the blue spectrum's mean of 37 MeV is shifted to higher energy by 6 %.

Michel electrons in the IV

In the following only the correlation between SM charge and michel spectrum in the IV will be observed, as there is currently no position reconstruction which could enable a check for any position dependence. Figure 8.35 shows the plane of SM charge versus michel electron charge in the IV. Most of the michel candidates populate the region below SM charges of 500 kDUQ and michel charge below 200 kDUQ resembling the individual spectra. Within this region no strong change of michel charge with SM charge is visible, in opposite to the situation in the ID. This will be further checked in figure 8.36 by comparing different selections in SM charge to the michel candidate selection utilizing the nominal cuts. Like for the ID, the nominal selection is given by the black histogram. Selecting only SM-michel pairs where the SM created less than 100 kDUQ in the IV shifts the mean to higher charges, as shown by the red histogram. Selecting an inter mediated charge region, 100 kDUQ $< Q_{IV}^{SM} <$ 200 kDUQ, slightly shifts the mean of the spectrum to lower charges, as can be seen from the green histogram. The blue histogram shows michel-SM candidate pairs for a selection of $Q_{IV}^{SM} >$ 200 kDUQ, compared to the nominal selection the mean of the blue spectrum is shifted to lower charges and the spectrum is much broader. In addition, an additional peak around 12 kDUQ shows up more strongly.

8.5 Summary

This chapter demonstrated that muons provide an excellent opportunity to monitor the response of the ID and the IV at high energies. The ratio of muon rates in ID and IV, R_μ^{IV}/R_μ^{ID}, was analyzed and found to be stable except for decreases in the first and the last two months of the data taking period under consideration. The measured ratio of 3.51 is compatible with the expectation of 3.37. Applying a "stricter" muon cut value in the ID ($E_{vis} >$ 100 MeV) changed to ratio to 4.01, also resulting in a flatter muon rate ratio over time. This yielded the conclusion that high energy light noise events are contaminating the muon event sample selected by the nominal muon threshold in the ID ($E_{vis} >$ 30 MeV). The fractional variation in the muon rate ratio with time was found to be around 0.20 $\%_{rms}$ consistent with the relative variation of the n-H capture peak of around 0.61 $\%_{rms}$ in the low energy region.

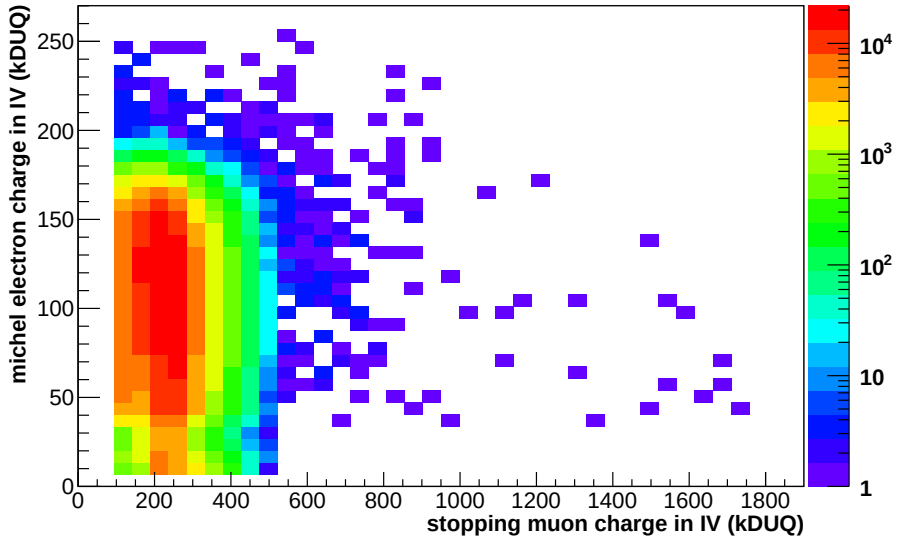

Figure 8.35: Michel candidate charge versus SM charge in the IV. In opposite to the same plot for the ID, no strong increase of michel candidate charge with SM charge is visible.

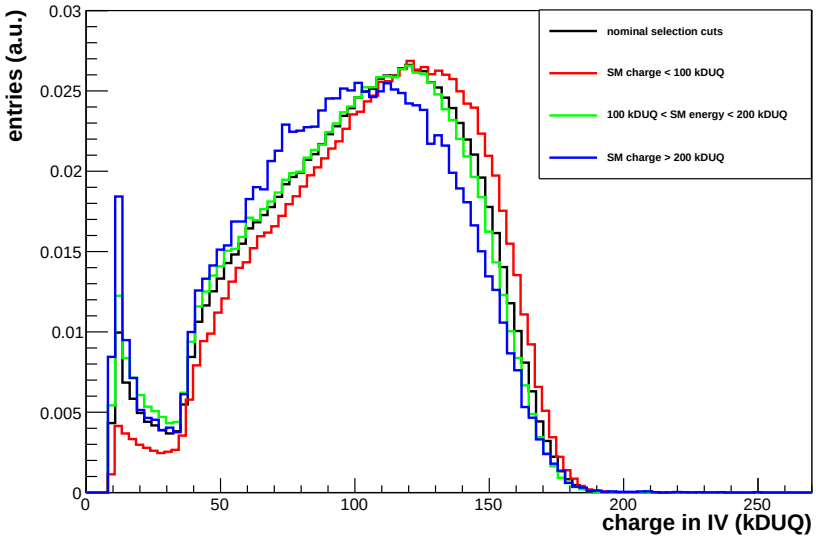

Figure 8.36: Dependence of the michel charge spectrum on the stopping muon charge in the IV. The spectrum obtained from the nominal selection cuts is shown in back, superimposed are spectra with different cuts on SM charge. First in red the charge region below 100 kDUQ, in green, 100 kDUQ $< Q_{IV}^{SM} <$ 200 kDUQ and the charge region above 200 kDUQ in blue. The higher the collected SM charge, the more the michel charge spectrum gets broader and the mean shifts to smaller charges. In addition the peak at 15 kDUQ is more pronounced.

In addition, utilizing track reconstruction algorithms, the energy loss of muons enabled the monitoring of the energy scale at high energies. The most probable muon energy loss was found to be

$$\begin{aligned} \text{ID} &: \quad \langle \Delta_p / X \rangle = (1.17 \pm 0.01)\,\text{MeV/cm} \\ \text{IV} &: \quad \langle \Delta_p / X \rangle = (3104 \pm 7)\,\text{DUQ/cm} \end{aligned}$$

Measuring these values daily, a relative instability of the detector response of $0.70\,\%_{rms}$ was found in the ID, compatible with the value $0.61\,\%_{rms}$ in the low energy range. For the IV, were no calibration procedure is applied yet, an overall instability of $0.22\,\%_{rms}$ for the considered data taking period was found.

This result hints that the relative instability of the ID response is nearly the same in the low neutrino energy range and in the high muon energy range. The value found for the IV, together with the time behavior of the muon rate ratio suggests that the relative instability in response is even better than the one achieved in the ID.

The usefulness of muon decay in the detector was stressed, a selection technique was introduced and the applied cuts were motivated. The spectra of stopping muons and michel electrons were discussed and the dependencies of the michel spectrum on reconstructed event position and parent stopping muon energy were presented. However, due to electronic effects and PMT saturation after the huge energy deposition of muons, it was not possible to reconstruct the endpoint of the michel electron spectrum. Nevertheless, the mean of the michel energy spectrum, 35 MeV, in the ID matches the theoretical expectation of $105/3\,\text{MeV}$ for the three-body decay of the muons. This indicates a good linearity of the E_{vis} energy scale even at high muon energies. In order to achieve the goal of utilizing muon decay as a calibration tool, the detector/photomultiplier effects after huge muon energy depositions have to be understood and should be the main interest of future studies.

Conclusion and outlook

Together with the Daya Bay experiment in China and the RENO experiment in South Korea, the Double Chooz reactor neutrino experiment achieved its goal of a measurement of the third neutrino mixing angle θ_{13}. With the main focus shifted from the analysis of reactor neutrino oscillations to cosmic ray muons, the data taken and published so far was analyzed in this thesis. Different analysis topics regarding the cosmic ray muon background were studied and discussed:

Identification and rejection of cosmic ray muons

The analysis of this thesis started with the means to identify and reduce muons. Different cut values to identify muons were compared. The muon rejection utilized in the neutrino selection was developed, being $E_{vis} > 30\,\mathrm{MeV}$ in the ID and $Q_{IV} > 10\,\mathrm{kDUQ}$ in the IV, and motivation for these specific values was given. The muon veto time window was introduced and the decision for the specific value of $100\,\mu\mathrm{s}$ was explained. It was shown, that the use of this muon selection identifies and rejects the majority of muon events very reliably. Using these cut values the muon rates of $13\,\mathrm{s}^{-1}$ in the ID and $46\,\mathrm{s}^{-1}$ have been determined.

The muon rejection efficiency of the Inner Muon Veto was determined and found to be 98.71 %. However, the identified and rejected sample of muons contains some contribution of high energetic light noise. These events lead to high rates in the Inner Detector faking muon events. This implies, that stricter cuts have to be applied in order to select pure muon samples. Requesting a hit in the Outer Muon Veto in addition to muon cuts introduced before rejects most of the high energy light noise. The data set obtained with this selection was used to estimate the muon rejection efficiency neglecting the influence of the high energy light noise. The efficiency of the Inner Muon Veto for this data set was estimated to be 99.98 % compatible with the result of a dedicated Monte Carlo simulation.

Currently new muon selection cuts are under consideration [100], aiming to reduce the wrong identification of high energy light noise events as muons, which causes unnecessary dead time. In addition, the OV could be used to identify muons that miss the ID or IV but could create fast neutrons entering the detector setup. Taking these consideration into account, the muon veto time could be dependent on reconstructed muon energy and X-Y position reconstructed in the OV.

Seasonal modulation of the measured muon rates

Checking the stability of the measured muon rates lead to the observation of a seasonal modulation. This modulation was analyzed in much detail, the connection between muon rate and atmospheric conditions was presented. A significant correlation with the effective temperature of the atmosphere ($C = 0.96$) and with surface pressure ($C = -0.44$) was found.

The parameters quantifying the connection between the muon rate and effective temperature or barometric pressure, the effective temperature coefficient α_t or the barometric pressure coefficient β_p, were determined and found to be $\alpha_T = 0.39 \pm 0.01(stat.) \pm 0.02(syst.)$ and $\beta_p = -0.59 \pm 0.20(stat.) \pm 0.10(syst.)$ ‰/mbar. This study enabled the measurement of the

atmospheric kaon to pion ratio, which was found to be $r(K/\pi) = 0.14 \pm 0.06$ compatible with the theoretical expectation of 0.15 ± 0.06. After having developed a good understanding of these effects, the muon rate measured at the DC far site was corrected for these effects and the remaining modulation was found to be around $0.5\,\%_{rms}$.

Extrapolation of the backgrounds from DC far to DB and RENO

During the course of this thesis a good understanding of the muon rate and spectra at the DC far shallow underground site was developed. Empirical models and Monte Carlo simulations were used to calculate muon flux and mean muon energy as a function of depth underground. The motivation for this was the extrapolation of the measured muon flux and energy values from the DC far site to the depths of the two other reactor neutrino experiments RENO and Daya Bay.

In the end, this was used to extrapolate the correlated background rates of fast neutrons and cosmogenic βn-emitters that were measured during a period when both reactors at the Chooz site were shut down. The steps to reach this extrapolation, presented in this thesis was worked out in a dedicated collaboration working group. The work done in the context of this thesis was summarized in an internal technical note [130]. Together with a part focusing on the background analysis of the reactor "shutdown" data, this ultimately lead to a paper published in Physical Review D [131].

Muons and their use for monitoring and calibration

At last, two different approaches to use cosmic ray muons as detector monitoring tools were presented. Using the ratio of muon rates in IV and ID, R_μ^{IV}/R_μ^{ID}, and the energy loss of muons in the detector gives an indication on the relative instability of the energy scale. It was found to be around $0.70\,\%_{rms}$ for the ID and around $0.22\,\%_{rms}$ for the IV. This can be compared with the instability of $0.61\,\%_{rms}$ that was found at around 2 MeV in the ID, originating from the neutron capture on hydrogen. It is compatible with the value determined from muon energy loss.

Finally, a technique to select and analyse stopping muons and their subsequent decay into Michel electrons was presented and utilized in the ID and for the first time also in the IV. The resulting Michel electron candidate samples in ID and IV are well compatible with the expectations from muon decay. However, due to DAQ electronic effects and PMT saturation distorting the spectral shape, it was not possible to extract the endpoint of the Michel electron spectrum. In the future, studies of the PMT saturation and readout effects after a high muon energy deposition should help to correct for the observed effects. Nevertheless, the mean energy of the Michel spectrum in the ID, 35 MeV, fits the theoretical expectation of 103/3 MeV indicating a good linearity of the energy scale up to muon energies.

Outlook

The DC experiment continues to take data with the far detector only. The second, near detector is currently under construction and the start of data taking in the two detector configuration is expected to begin in 2014 aiming for a relative, more precise θ_{13} measurement.

Muons continue to play an important role as the expected muon rate in the Near detector will be 10 times higher compared to the rate measured in the far detector. This implies a higher rate of correlated background events, further stressing the necessity of a good understanding of muon rate and spectra at this detector site. In future dedicated studies have to be performed to optimise the muon identification potential in order to reject high energetic light noise events and to include the OV in the overall muon identification and rejection scheme.

Currently having nearly two years of measurement time, the statistical uncertainties for the barometric and effective temperature coefficients will decrease, resulting in more precise measurements of these coefficients and the atmospheric kaon to pion ratio. In addition, a dedicated MUSIC simulation should be performed taking into account the actual hill profile at the DC far site to calculate the muon threshold energy more precisely. Then it is planned to incorporate these results in a dedicated collaboration paper on muon measurements performed with the DC far detector, once an enlarged data set is available.

In addition, the scaling presented in this thesis would profit from an enlarged data set of reactor "shutdown" time, as the scaling is currently limited by the statistical error of the background measurements. These errors are two times larger as the ones measured during the periods when both reactors were "on" and an increase from the current one week data set to a four week data set would increase predictive power of the extrapolation.

Acknowledgements/Danksagung

The 3 years being a phd student gave me the opportunity to meet and work with many interesting people all around the world. I am thankful to the Double Chooz Collaboration for the warm welcome and the chance to work in such a interesting international scientific project. Thanks also to the EU++ analysis cluster for the chance to present my work nearly every meeting (thanks for endurance) and the encouraging work environment. I had the chance to participate, I received many hints, new ideas and insights concerning this work and profited a lot from the meetings and discussions.

Thanks also to the following organizations providing the environmental data used in this thesis: The NASA AIRS data used in this effort were acquired as part of the activities of NASA's Science Mission Directorate, and are archived and distributed by the Goddard Earth Sciences (GES) Data and Information Services Center (DISC). The ECMWF Interim Reanalysis data used in this study have been obtained from the ECMWF Data Server. The surface pressure data use in this study have been obtained from the National Oceanic and Atmospheric Administration (NOAA) National Climatic Data Center NCDC server.

And switching to German, ist es Zeit an dieser Stelle Danke zu sagen für all die Unterstüzung und Hilfe die ich in den drei Jahren meiner Doktorarbeit erfahren habe. Zuerst möchte ich Prof. Josef Jochum und Prof. Tobias Lachenmaier für die Vergabe dieser interessanten Doktorarbeit und die Betreuung danken. Danke für die freundliche Aufnahme ins Team, die Möglichkeit internationale Konferenzen und Schulen zu besuchen. Danke für die vielen Ratschläge und Hinweise, vorallem für die konstruktive Kritik und die hilfreichen Kommentare gegen Ende dieser Arbeit.

Ebenso möchte ich meinen Tübinger Double Chooz Kollegen Markus Röhling und Lee Stokes für ihre Unterstüzung, die Hilfe beim Korrekturlesen und vorallem für die lockere und gute Atmosphäre im Büro und unseren Konferenzen danken. Ebenso allen anderen Diplomanden und Doktoranden am Lehrstuhl die mit dem ein- oder anderen Hinweis zum Gelingen dieser Arbeit beigetragen haben, oder in Zeiten geringer Motivation gemeinsam mit mir gelitten haben: Christian Strandhagen, Gerhard Deuter, Kai Freund, Christopher Schmitt, Katharina von Sturm, Raphael Falkenstein, Klemens Rottler, Ann-Kathrin Schütz, Rainer Schmidt und Eduard Friske.

Einen besonderen Dank an Christof Sailer der immer ein offenes Ohr für mich hatte und an Martin Uffinger der vorbildlich bei jedem meiner Skype "Kaffee-Aufrufe" zur Stelle war, um meinen Kaffeedurst zu stillen. Danke auch an die Ehemaligen, die zumindest den Anfang meiner Arbeit mit getragen und ertragen haben: Florian Ritter und Daniel Greiner.

Danke auch an meine Kommilitonen Stephan Hartmann, Tobias Müller und Johannes von Keler die "bereitwillig" meinen Geschichten und meinem Klagen in der Mensa lauschten, wenn wir uns wieder einmal mittwochs zum Essen getroffen haben, nachdem wir eine "nicht genehmigte Rundenmail" erhalten hatten.

Zuletzt noch ein Dankeschön an Wolfram Brodowski, der mir Lust auf Physik gemacht hat und mich zum Studium motivierte. Ganz am Ende geht ein "dickes" Danke an meine Familie,

meine Frau Larissa, meinen Sohn Jonah und an meine Freunde Thorsten und Franzsika Diehl, die vorallem in der letzten Phase dieser Promotion einige Launen und etliche demotivierte Tage ertragen mussten.

Abbreviations

- $\mathcal{SM}$ Standard model of particle physics
- **CP** Charge-parity (symmetry)
- **CKM** Cabibo-Kobayashi-Maskava (quark mixing matrix)
- **SNU** Solar neutrino unit
- **IBD** Inverse beta decay
- **POT** Protons on target
- **DC** Double Chooz
- **DB** Daya Bay
- **RENO** Reactor Experiment for Neutrino Oscillation
- **m.w.e.** Meter water equivalent
- **PWR** Pressureized water reactor
- **EDF** Electricite de France
- **PMT** Photomultipliertube
- **NT** Neutrino Target
- **GC** Gamma-Catcher
- **ID** Inner Detector
- **IV** Inner Muon Veto
- **OV** Outer Muon Veto
- **LS** Liquid scintillator
- **LAB** Linear Alkl Benzne
- **PXE** Phenyl-xylyl-ethane
- **PPO** 2,5-Diphenyloxazole
- **bis-MSB** 1,4-bis(2-methylstyryl)benzene
- **IDLI,IVLI** Inner Detector/Inner Veto Light Injection
- **DAQ** Data Aquisition System
- **FEE** Front End Electronics
- **DUQ** Digital units of charge
- **DOGS** Double Chooz offline group software
- **FN** Fast neutron

- **SM** Stopping muon
- E_{vis} calorimetric energy variable in the ID
- Q_{IV} uncalibrated raw charge in the Inner Muon Veto

"Charlie Chaplin to Albert Einstein:
People applaude me, because everybody understands me,
they applaud to you, because nobody understands you."
Charlie Chaplin (1889-1977)

A Extraction of IV time offsets

As small differences in readout electronics and in signal cable length of the PMTs could lead to different signal transit times, one needs to measure those timing differences and needs to correct for them. This is important because otherwise an event would be recorded by different PMTs at different times, in the worst case causing fake triggers. In addition a systematic deviation in the PMT timing behavior would limit the accuracy and performance of any position or track reconstruction where the PMT timing is needed.

Measurements of PMT timing and gain was foreseen regularly and the IVLI system was designed for this, but the measurement gained more importance after problems with the IV PMTs were observed during commissioning. Due to an material incompatibility the encapsulated PMTs of the IV had to be replaced [156]. Inside the IV vessel the cables were cut close to the capsules and the encapsulated PMTs were taken out of the vessel and replaced by new ones having a design correcting for this problem. As during this procedure the cables were cut roughly at the same length, small differences in cable length and thus in turn in the relative timing arise.

The correction constants, or time offsets are extracted using the IDLI or IVLI system that have already been described in Chapter 3. During the data taking period, the IVLI system was utilized once a week to perform a measurement of the PMT gains and the relative timing between the PMTs[1]. The extraction of the relative offsets between the IV PMTs was done regularly each week as a part of this thesis. These constants were uploaded to a database and were applied to the regular physics data to correct for any timing offset. A dedicated software package for DOGS was written to perform this task [157]. The basic idea, the applied algorithm, the results for the analysis period and some explanation about how to use this software package will be given in the following.

A.1 Inner Veto Light Injection system

A schematic illustration of the IVLI system is shown in Figure A.1. The heart of the IVLI system is contained in a metal box outside the IV vessel, see Figure A.2. This light tight box contains all light injection LEDs with electronic drivers mounted inside on a circuit board. The utilized matrix of LEDs consists of 8×12 LEDs, having 6 UV (375 nm) and 90 blue (475 nm) LEDs. Wave length shifting fibers capture the light emitted from the

[1] Gain measurements are performed with low LED intensity, D19 configuration, whereas the D20 high LED intensity configuration is used to measure the timing behavior.

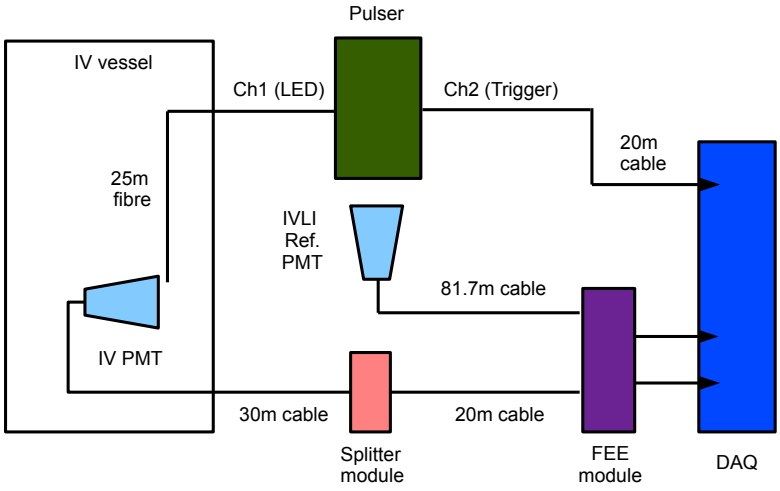

Figure A.1: The Inner Veto Light Injection system. Per run, one LED is pulsed and via an optical fiber one IV PMT is illuminated. The timing of this PMT is than compared to the timing of the IV reference PMT and the t0 offset can than be extracted.

LEDs and transport it to a reference PMT mounted in a separate dark box inside the IVLI box. Ordinary Quartz fibers transport the light to the PMTs mounted inside the IV vessel. This is shown in Figure A.3, and in Figure A.4 showing an encapsulated IV PMT with attached fibers. For timing and attenuation reasons all fibers have the same length. Because of different distances between the external IVLI box and the PMTs, some extra fiber was added, resulting in a length of 25 m for all fibers. Additional cable is added to the IVLI reference PMT to have the same light arrival time than for the PMTs inside the IV vessel illuminated by a LED of the IVLI system.

A.2 Algorithms applied

The basic idea for the timing measurement is to pulse one LED of the LED matrix at a given time, which is illuminating a single PMT via the quartz fiber. For this PMT the start time of the resulting pulse is measured. The start time is defined as the time, when the PMT pulse is reaching 50% of its maximum amplitude. This time can than be compared to the external reference, which is the start time t_{Ref} of the reference PMT located in the dark box outside the IV vessel. As said before, the cable length of the reference PMT was tuned to match the length of the IV PMT cables and electronic processing times in order to have the same signal transit time. Thus the timing offset for a given IV PMT i can be obtained by comparison to the reference PMT

$$t_{0,i} = t_{Ref} - t_i. \tag{A.1}$$

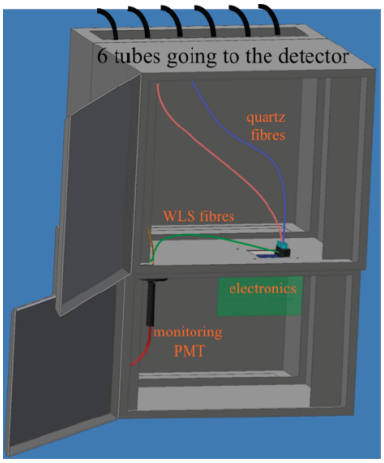

Figure A.2: IVLI external box.

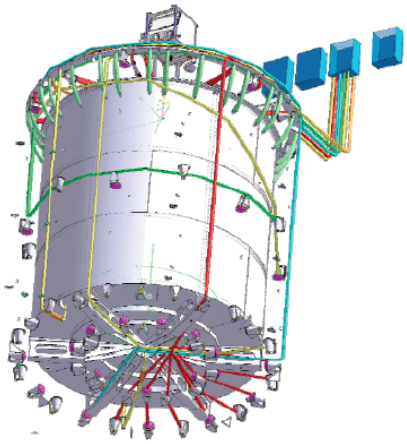

Figure A.3: Distribution of fibres inside the IV vessel.

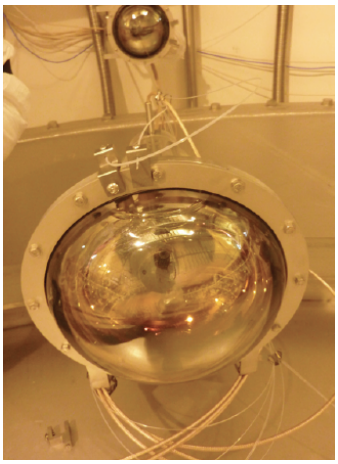

Figure A.4: PMT with two fibers oriented in opposite directions.

A time difference $t_{0,i} > 0$ indicates that PMT i is detecting the emitted light earlier then the reference PMT in opposite to $t_{0,i} < 0$, where PMT i detects light later than the reference PMT. Having measured these offsets for each PMT i a correction in software can be applied according to

$$t_i^{cor} = t_i^{uncor} + t_{0,i}. \tag{A.2}$$

In total 96 fibers enter the IV vessel which are attached to 78 IV PMTs, corresponding to readout channels 1000-1078, where the channel 1015 is reserved for the IVLI reference PMT. The used DAQ configuration for the timing measurement with the IVLI system is named DAQ configuration D20, were the LED intensity is high compared to the second IVLI D19 configuration having a low intensity is low creating only single photoelectrons in the IV PMTs. This in turn is used to measure the PMT gains. In each run of the DAQ a single LED is pulsed illuminating one PMT, thus a IVLI data set of configuration D20 contains 96 separate runs. The runs interesting for the timing measurements are the ones from D20_6 to D20_96 leaving out the UV LEDs.

Some IV PMT channels have two fibers, one pointing in forward and one in backward direction to illuminate another PMT. During the replacement of the encapsulated PMTs in the IV vessel some of the backward pointing fibers were mistakenly put in the forward direction during the replacement. This breaks up the original allocation of PMTs and fibers. In order to handle this and to have a new allocation of fiber and PMT, dedicated test runs with the IVLI system were made leading to a new table of PMT and fiber allocation [158]. For this reason three different methods have to be used, as there are PMTs not illuminated by the originally foreseen fiber:

- For 68 PMTs the timing can be extracted by simply taking the pulse start time and comparing it to the pulse start time of the reference PMT following the basic idea presented before. This could be done for PMTs, were the optical fiber illuminating this PMT is attached to this very PMT.

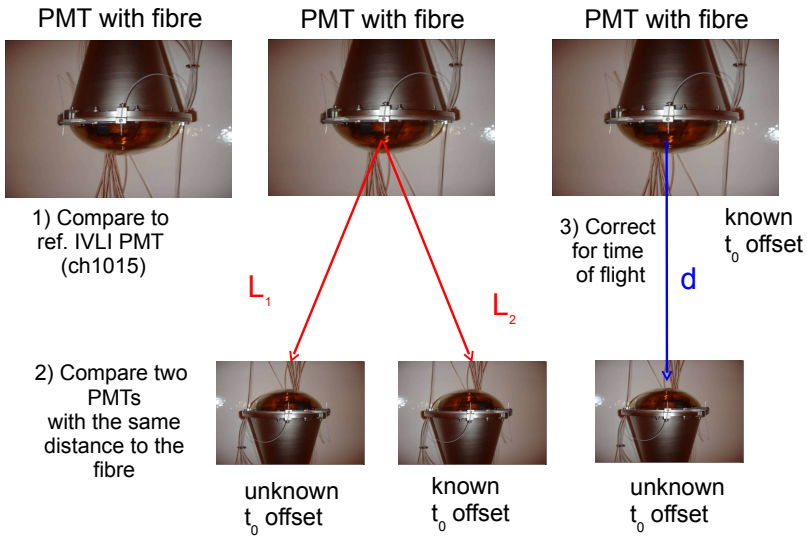

Figure A.5: Three different methods used to extract the timing offsets of the IV PMTs. Utilizing method 1), one can simply compare the measured start time of the PMT with the start time of the reference PMT. Where this was not possible, in 2) pairs of PMTs were chosen having the same distance to a illuminating fiber and the relative timing between the PMTs was measured being in turn compared to the reference PMT. In 3) two PMTs facing each other were chosen and the relative timing was measured being corrected for the photon time of flight and in turn compared to the reference PMT.

$$t_0 = t_{Ref} - t_{PMT} \tag{A.3}$$

- For 6 other PMTs (channels 1060, 1024, 1052, 1043, 1023 and 1042) another method has to be used as no fiber illuminating the PMT itself is attached to these PMTs. To extract their timing offsets, another PMT was chosen, were the t_0 offset was measured with the method described before. These six PMT pairs have the same distance from a pulsed fiber for a given run. The timing of both PMTs is compared with each other and corrected for the known t_2 of the second PMTs, which was measured by comparing the pulse start time with the IVLI reference PMT.

$$t_0 = (t_2 + t_{0,2}) - t_{PMT} \tag{A.4}$$

- For two PMTs none of the other methods mentioned worked. This are two lateral PMTs (channels 1013 and 1011) facing downwards. Here the PMT, with known time offset t_2, directly below the PMTs being in their field of view is used to extract the time of flight corrected t_0 offset.

$$t_0 = (t_2 + t_{0,2}) - \left(t_{PMT} - \frac{d \cdot n}{c}\right) \tag{A.5}$$

These three different methods to extract the IV timing offsets are schematically visualised in Figure A.5.

T0 offsets for the data taking period

The analysis period from 2011/04/13 to 2012/03/11 covers 41 IVLI data sets in D20 configuration being:

13825-13912, 2011-05-07	14604-14691, 2011-05-15	15216-15303, 2011-05-21
15971-16058, 2011-05-29	16651-16738, 2011-06-05	17869-17956, 2011-06-19
18640-18726, 2011-06-26	19324-19411, 2011-07-03	20069-20156, 2011-07-10
21380-21469, 2011-07-25	22360-22447, 2011-07-31	23070-23157, 2011-08-07
23712-23800, 2011-08-15	24207-24294, 2011-08-21	24744-24831, 2011-08-28
25243-25330, 2011-09-04	25758-25871, 2011-09-11	26332-26419, 2011-09-18
26826-26913, 2011-09-21	27940-28027, 2011-10-09	28401-28489, 2011-10-16
29180-29268, 2011-10-30	29656-29746, 2011-11-06	30209-30300, 2011-11-14
30554-30643, 2011-11-17	31144-31232, 2011-11-30	31631-31719, 2011-12-04
32327-32407, 2011-12-14	32681-32769, 2011-12-18	33376-33464, 2011-12-25
33889-33997, 2012-01-01	34361-34449, 2012-01-08	34880-34968, 2012-01-15
35398-35486, 2012-01-22	35870-35958, 2012-01-29	36645-36733, 2012-02-05
37160-37248, 2012-02-12	37664-37752, 2012-02-19	38135-38223, 2012-02-26
38605-38694, 2012-03-04	39354-39442, 2012-03-15	

The upper plot in Figure A.6 shows the distribution of the mean t_0 for the analysis period, whereas the lower plot shows the mean t_0 offset versus the channel number of IV PMTs. The mean t_0 shown in these Figures in the simple average of the 41 measurements performed during the analysis period. The mean timing offset t_0 is around -2 ns indicating that the majority of IV PMTs detects the light from the LED earlier than the reference PMT indicating a shorter cable length than the originally foreseen before the replacement. The overall channel to channel spread is around 6 ns being uniformly distributed on the channels not indicating any systematic time offset for a group of IV PMTs. Most channels show offsets around 0, but several channel have offsets around 10 ns and there is one outlying channel with more 20 ns difference to the reference PMT. This differences correspond to 2 m additional or less cable length for the 10 ns deviation and around 4 m for the 20 ns outsider. However that amount of cable should not have been cut during the replacement, thus the reason for this big time deviation is still unknown.

Nevertheless the time offsets are applied to the physics data used in the neutrino analysis. A future muon track reconstruction software utilizing the IV as well could be used to verify the measured offsets. Without any correction the reconstruction is expected to perform a crude track reconstruction leading for example to a broad Landau distribution in the muon energy loss Δ/X. Applying the offsets the reconstruction is expected to perform better decreasing the width of this energy loss distribution. This is the case for RecoMuonHam and the measured time offsets of the ID. Thus such a comparison between time calibrated and time un-calibrated Δ/X distribution in the IV would verify the correctness of the extracted offsets.

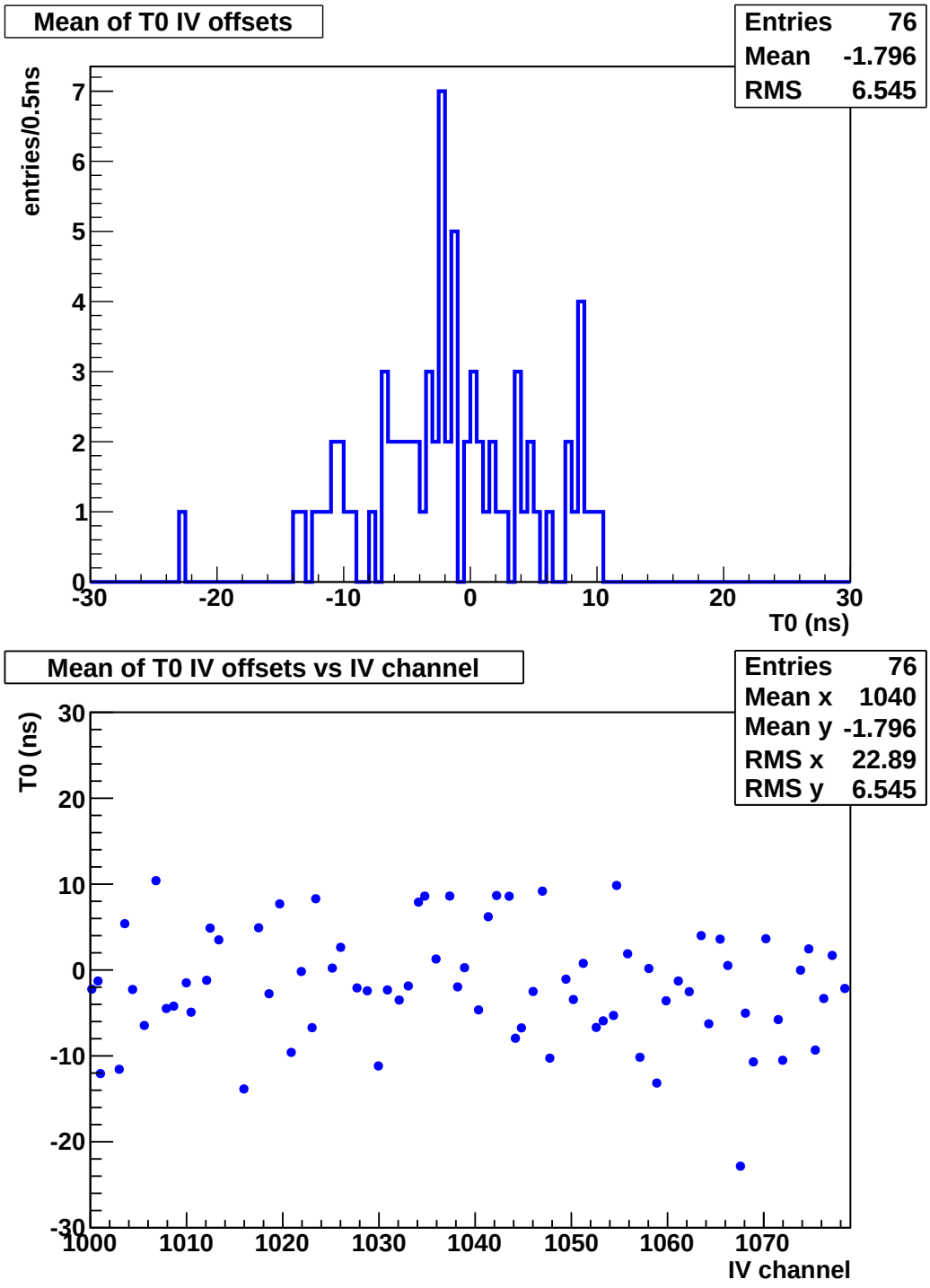

Figure A.6: Upper plot: Distribution of extracted t_0 offsets. Lower plot shows extracted t_0 offsets versus the channel number of IV PMTs.

The stability of the extracted timing offsets can be seen in Figure A.7. Most of the measured t_0 offsets are stable not deviating much in the considered period. All deviations found are smaller than the overall channel to channel spread in the timing offsets indicating the stability of the used methods.

The DCToffsetsIVLI package

This section will be more technical, describing the software written to perform the t_0 offset measurement. This code can be found in the DCCalibAna repository of the DOGS software package *$DOGS_PATH/DCCalibAna* used within DC. There one can find an Action Unit *DCToffsetsIVLI* written in C++ together with a template ROOT-script *runToffsetsIVLI.C* in the mac repository to run the Action Unit. In order to run the Analysis on a given set of D20 IVLI runs a python script is provided in the scripts repository *$DOGS_PATH/DCCalibAna/scripts*. This python script *runToffsetsIVLIJobs.py* is used to submit several analysis jobs (one root job per PMT) to the GE batch system. One has to start the script specifying the IVLI data set which should be used, for example:

```
[ddiet@ccage013 scripts]$ python runToffsetsIVLIJobs.py 13825 13912
```

These run numbers can be looked up via the Detector Run Info web page[2]. One can start the job submission by typing python runToffsetsIVLIJobs.py in the shell. Each job consists of a batch of 5 IVLI runs, where the script puts together the right LED and corresponding channel numbers to extract the timing. Starting the script creates the following output:

```
[ddiet@ccage013 scripts]$ python runToffsetsIVLIJobs.py
Starting batch job Nr 0
Your job 8326097 ("ToffsetsIVLI0") has been submitted
Starting batch job Nr 1
Your job 8326098 ("ToffsetsIVLI1") has been submitted
Starting batch job Nr 2
Your job 8326099 ("ToffsetsIVLI2") has been submitted
. . .
. . .
. . .
Starting last batch job!
Your job 8326112 ("ToffsetsIVLIS2") has been submitted
```

Per run a root file is created in *$DOGS_PATH/DATA/*, where the naming scheme is *ToffsetsIVLI-RUNNUMBER.root*. These root files contain several histograms:

[2] *http://dcmonitor.in2p3.fr/QualityControl/RunInfo/*

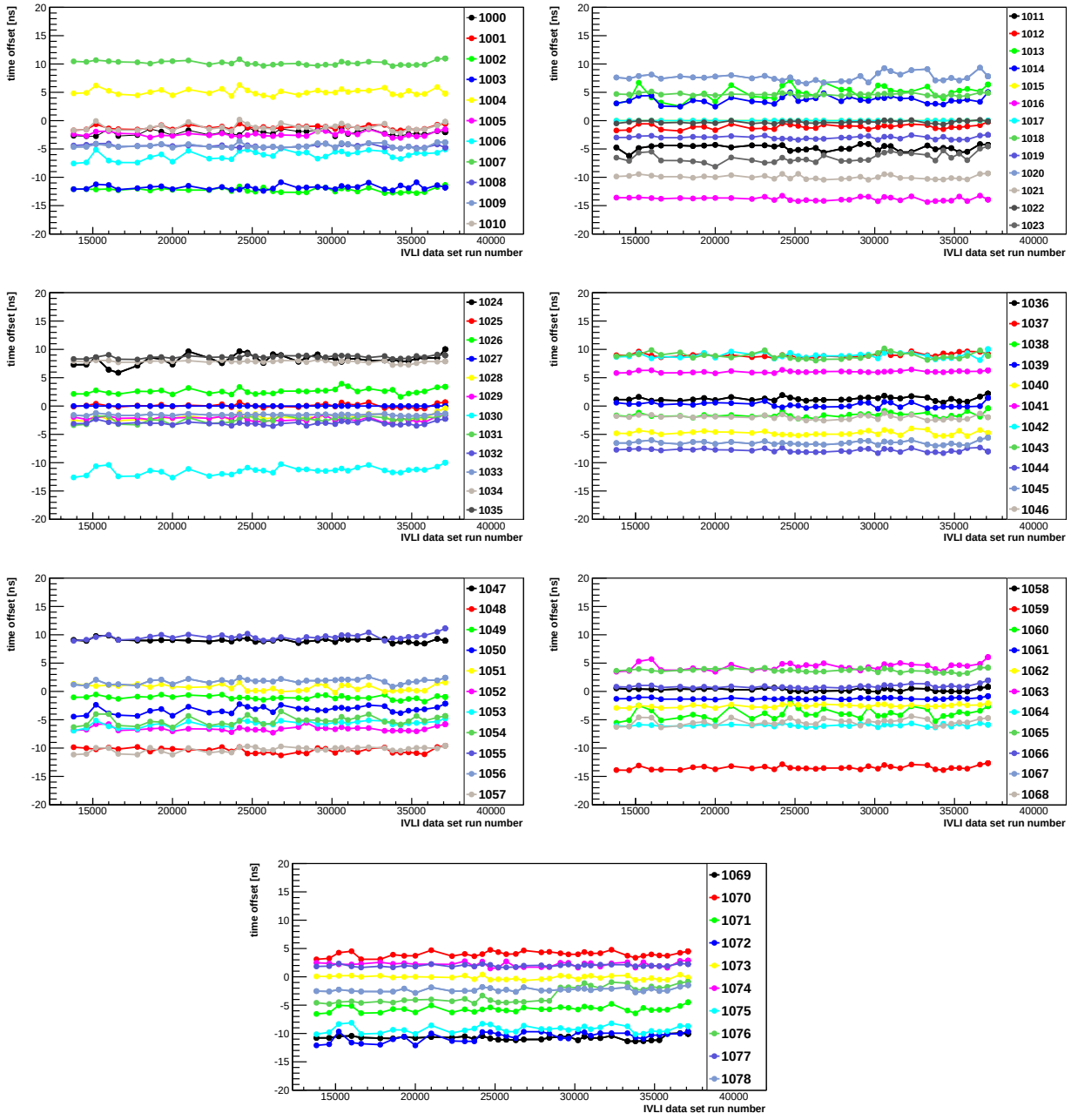

Figure A.7: Stability of extracted t_0 offsets for the considered analysis period from 2011/04/13 till 2012/03/11 corresponding to 41 IVLI runs, the first beeing 13825 to 38694.

```
Attaching file ToffsetsIVLI-13826.root as _file0...
root [1] .ls
TFile**         ToffsetsIVLI-13826.root
 TFile*         ToffsetsIVLI-13826.root
  KEY: TH1F     PMT404;1
  KEY: TH1F     HalfMPMT404;1
  KEY: TH1F     PMT408;1
  KEY: TH1F     HalfMPMT408;1
  KEY: TH1F     PMT412;1
  KEY: TH1F     HalfMPMT412;1
  KEY: TH1F     PMT1015;1
  KEY: TH1F     HalfMPMT1015;1
  KEY: TH1F     HalfMComp2RefPMT;1
  KEY: TH1F     PMT1079;2
  KEY: TH1F     PMT1079;1
  KEY: TH1F     HalfMPMT1079;1
  KEY: TH1F     HalfMComp2IVTrig;1
  KEY: TCanvas  c_AddedPF;1     Added PulseForms
  KEY: THStack  AddedPF;1       Added Pulseforms of Wished PMTs
  KEY: TLegend  TPave;1 Legend of markers/lines/boxes to represent obj's
  KEY: TTree    Histograms;2    Histograms
  KEY: TTree    Histograms;1    Histograms
  KEY: TH1F     HalfMComp;1
root [2]
```

First, the summed waveforms for three PMTs labeled *PMTXXX* (first and second PMT have the same distance to the pulsed fiber and the third PMT is the one, to which the fiber is attached). Also included are the distributions of the extracted times @50% of the maximum pulse height for each of this PMTs, labeled *HalfMPMTXXX*. Also one finds the added waveforms for the reference PMT and the external trigger (labeled *PMT1005* and *PMT1079*), as well as their timing distributions.

There are in addition histograms where the extracted times of the last PMT (the one to which the fiber is attached) is compared to the extracted timing of the reference PMT or the external trigger (*HalfMComp2RefPMT* or *HalfMComp2IVTrig*).

At last a canvas created, which shows the summed waveforms of the three considered PMTs, the reference PMT and the external trigger. Also a ASCII file is created, the naming scheme is *ToffsetsIVLIData.txt*, where the output for the whole IVLI data set is stored. See the following example:

```
...
...
...
13826   8       404     69.6478
```

```
13826   8       408     75.7554
13826   8       412     57.0062
13826   8       1015    63.1108 5.58434
13826   8       1079    215.977 159.341
...
...
...
```

The output is per run: run number, LED number followed by the PMT number and the mean of the extracted time of 50% of the pulse maximum. The last two rows for each run contain the IV reference PMT (ch. 1015) and the IV external trigger (ch. 1079). Here the last column is the time difference from the last PMT (the one with the fiber) to the reference PMT or to the external trigger is listed. This time difference is the the mean of the timing difference per pulse for PMT j.

$$t_{o,j} = \frac{1}{N}\sum_{i=0}^{N}(t_{Ref,i} - t_{PMT,i})$$

After the batch jobs have been completed, With the python script *AnalysisToffsetsIVLIJobs.py* in the script repository the Analysis can be done. This script extracts the t0 offsets from the data file *ToffsetsIVLIData.txt* for the 68 normal PMTs by taking the time difference between the third PMT and the IV reference PMT. For the special 6 PMTs the timing difference for the first two PMTs will be taken and corrected for the known t0 offset. In the third case the timing of the examined PMT is corrected for the time of flight and will be compared with one PMT directly below, where the t0 offset is known and is corrected as well. The output of this script is as follows; first row is channel number and second row is the extracted t0 offset:

```
[ddiet@ccage015 scripts]$ python AnalysisToffsetsIVLIJobs.py
1053 -6.93018
1012 -1.73364
1044 -7.73314
...
...
...
```

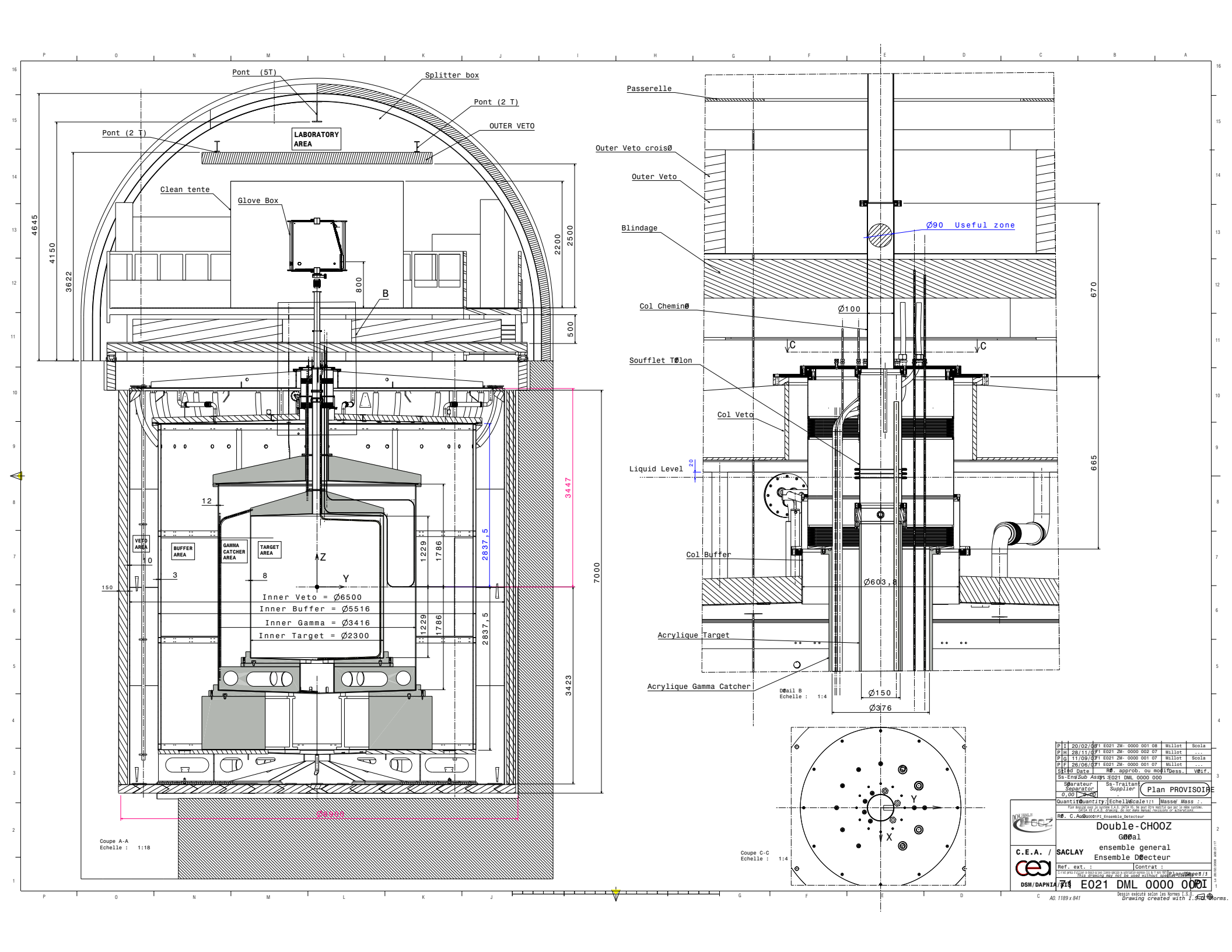

P I	20/02/08	E021 ZM- 0000 001 08	Millot	Scola	
P H	28/11/07	E021 ZM- 0000 002 07	Millot	...	
P G	11/09/07	E021 ZM- 0000 001 07	Millot	Scola	
P F	26/06/07	E021 ZM- 0000 001 07	Millot	...	
Sld	Date	Rø. approb. ou modif.	Dess.	Vérif.	

Ss-Ens. / Sub Assy. : E021 DML 0000 000

Séparateur / Separator: 0,00 | Ss-Traitant / Supplier: . | Plan PROVISOIRE

Quantité / Quantity: | Echelle / Scale: 1:1 | Masse / Mass :

Rø. C.Aug. 0000 PI Ensemble Détecteur

Double-CHOOZ

Général

ensemble general

Ensemble Détecteur

C.E.A. / SACLAY

DSM/DAPNIA/SPP

Ref. ext. :

Contrat :

Planche 1 / 1

E021 DML 0000 0001

AO. 1189 x 841

Dessin exécuté selon les Normes [.S.O. / Drawing created with I.S.O. norms.

Bibliography

[1] ETH Institute for particle physics. Particle Physics: Probing the fundamental interactions of elementary particles, http://www.ipp.phys.ethz.ch/aboutus/?file=institut.

[2] N. Schmitz. *Neutrinophysik*. Vieweg Teubner, Kln, 1997. aufl. edition, 1997.

[3] H.V. Klapdor-Kleingrothaus and K. Zuber. *Teilchenastrophysik*. Teubner-Studienbücher: Physik. Teubner, 1997.

[4] M. Kobayashi and T. Maskawa. CP-violation in the Renormalizable Theory of Weak Interaction. *Progress of Theoretical Physics*, 49(2):652–657, 1973.

[5] C. Grupen, G. Cowan, S. Eidelman, and T. Stroh. *Astroparticle physics*. Springer, Berlin, 1. aufl. edition, 2005.

[6] S.L. Glashow. Partial Symmetries of Weak Interactions. *Nucl. Phys.*, 22:579–588, 1961.

[7] S. Weinberg. A Model of Leptons. *Phys. Rev. Lett.*, 19:1264–1266, Nov 1967.

[8] A. Salam. Proc. of the 8th Nobel Symposium on Elementary particle theory, relativistic groups and analyticity. 1969.

[9] C. Giunti and M. Laveder. Neutrino Mixing, 2003.

[10] B. Kayser. Neutrino Oscillations, Lecture given at the International Neutrino Summer School, Yokohama, Japan. 2010.

[11] T. Yanagida. Horizontal Symmetry and Masses of Neutrinos. Technical Report TU-80-208, Tohoku Univ., Sendai, May 1980.

[12] J. Schechter and J.W.F. Valle. Neutrino masses in SU(2) $\bigotimes$ U(1) theories. *Phys. Rev. D*, 22:2227–2235, Nov 1980.

[13] R.N. Mohapatra and G. Senjanović. Neutrino Mass and Spontaneous Parity Nonconservation. *Phys. Rev. Lett.*, 44:912–915, Apr 1980.

[14] L. Wolfenstein. Neutrino oscillations in matter. *Phys. Rev. D*, 17:2369–2374, May 1978.

[15] J. Jenkins A. de Gouvêa and B. Kayser. Neutrino mass hierarchy, vacuum oscillations, and vanishing $|U_{e3}|$. *Phys. Rev. D*, 71:113009, Jun 2005.

[16] K. Nakamura et al. Review of particle physics. *J. Phys.*, G37:075021, 2010.

[17] F. Close. *Neutrino*. Oxford University Press, 2010.

[18] J. Learned and S. Pakvasa. A NEUTRINO TIMELINE, (2005), $http://www.phys.hawaii.edu/\sim jgl/nu\_timeline.html$.

[19] E. Fermi. *Note e memorie: Collected papers. Vol. 2: United States, 1939-1945*. University of Chicago Press, 1965.

[20] E. Fermi. Tentativo di una teoria della emissione di raggi beta, 1962-1965.

[21] E. Fermi. Versuch einer Theorie der β-Strahlen. *Zeitschrift für Physik A Hadrons and Nuclei*, 88:161–177, 1934. 10.1007/BF01351864.

[22] C.L. Cowan et.al. Detection of a free neutrino: A Confirmation, Science 124, 1956.

[23] M. Goldhaber et.al. Helicity of Neutrinos. *Phys. Rev.*, 109:1015–1017, Feb 1958.

[24] R.E. Marshak et.al. *Theory of weak interactions in particle physics*. Interscience monographs and texts in physics and astronomy. Wiley-Interscience, 1969.

[25] C. Wu et.al. Experimental Test of Parity Conservation in Beta Decay. *Phys. Rev.*, 105:1413–1415, Feb 1957.

[26] G. Danby et.al. Observation of High-Energy Neutrino Reactions and the Existence of two kinds of neutrinos. *Phys. Rev. Lett.*, 9:36–44, Jul 1962.

[27] M.L. Perl et.al. Evidence for Anomalous Lepton Production in $e^+ - e^-$ Annihilation. *Phys. Rev. Lett.*, 35:1489–1492, Dec 1975.

[28] J. Ellis and K.A. Olive. Constraints on light particles from supernova SN 1987A. *Physics Letters B*, 193(4):525 – 530, 1987.

[29] D. Buskulic et.al. Inclusive pi+-, K+- and (p, anti-p) differential cross-sections at the Z resonance. *Z.Phys.*, C66:355–366, 1995.

[30] P. Abreu et.al. Improved measurements of cross sections and asymmetries at the Z^0 resonance. *Nuclear Physics B*, 418:403–427, 1994. CERN PPE 9431,LAL 94-24,ISN 9448,LPC 9407.

[31] M. Acciarri et al. Measurements of cross sections and forward-backward asymmetries at the z resonance and determination of electroweak parameters. *The European Physical Journal C - Particles and Fields*, 16:1–40, 2000. 10.1007/s100520050001.

[32] R. Akers et al. Improved measurements of the neutral current from hadron and lepton production at lep. *Zeitschrift fr Physik C Particles and Fields*, 61:19–34, 1994. 10.1007/BF01641883.

[33] C.J. Hogan et.al. A Bayesian Estimate of the Primordial Helium Abundance. *The Astrophysical Journal Letters*, 489(2):L119, 1997.

[34] K. Kodama et.al. (DONUT Collaboration). Observation of tau neutrino interactions. *Physics Letters B*, 504(3):218 – 224, 2001.

[35] D. Szam. Wikipedia, *http : //en.wikipedia.org/wiki/file : proton_proton_cycle.png*. 2006.

[36] R.M. Bionta et.al. Contained neutrino interactions in an underground water detector. *Phys. Rev. D*, 38:768–775, Aug 1988.

[37] K.S. Hirata et.al. Experimental study of the atmospheric neutrino flux. *Physics Letters B*, 205(2A3):416 – 420, 1988.

[38] Y. Fukuda et.al. (Super-Kamiokande Collaboration). Evidence for Oscillation of Atmospheric Neutrinos. *Phys. Rev. Lett.*, 81:1562–1567, Aug 1998.

[39] Y. Ashie et.al. Measurement of atmospheric neutrino oscillation parameters by Super-Kamiokande I. *Phys. Rev. D*, 71:112005, Jun 2005.

[40] M.H. Ahn et.al. Indications of Neutrino Oscillation in a 250 km Long-Baseline Experiment. *Phys. Rev. Lett.*, 90:041801, Jan 2003.

[41] P. Adamson et.al. (MINOS Collaboration). Measurement of Neutrino Oscillations with the MINOS Detectors in the NuMI Beam. *Phys. Rev. Lett.*, 101:131802, Sep 2008.

[42] N. Agafonova et.al. Observation of a first ν candidate event in the OPERA experiment in the CNGS beam. *Physics Letters B*, 691:138–145, July 2010.

[43] The OPERA Collaboration. Search for $\nu_\mu \rightarrow \nu_\tau$ oscillation with the OPERA experiment in the CNGS beam. *ArXiv e-prints*, July 2011.

[44] S. Parke H. Nunokawa and J.W.F. Valle. CP violation and neutrino oscillations. *Progress in Particle and Nuclear Physics*, 60(2):338–402, April 2008.

[45] K. Abe et.al. (T2K Collaboration). Indication of Electron Neutrino Appearance from an Accelerator-Produced Off-Axis Muon Neutrino Beam. *Phys. Rev. Lett.*, 107:041801, Jul 2011.

[46] P. Adamson et.al. (MINOS Collaboration). Active to Sterile Neutrino Mixing Limits from Neutral-Current Interactions in Minos. *Phys. Rev. Lett.*, 107:011802, Jun 2011.

[47] P.H. Frampton and P. Vogel. Massive neutrinos. *Physics Reports*, 82(6):339 – 388, 1982.

[48] P. Adamson et.al. (MINOS Collaboration). Measurement of the Neutrino Mass Splitting and Flavor Mixing by MINOS. *Phys. Rev. Lett.*, 106:181801, May 2011.

[49] S. Abe et.al. (The KamLAND Collaboration). Precision Measurement of Neutrino Oscillation Parameters with KamLAND. *Phys. Rev. Lett.*, 100:221803, Jun 2008.

[50] M. Apollonio et.al. Search for neutrino oscillations on a long base-line at the CHOOZ nuclear power station. *Eur. Phys. J.*, C27:331–374, 2003.

[51] F. Ardellier et.al. Letter of Intent for Double-CHOOZ: a Search for the Mixing Angle θ_{13}. *ArXiv High Energy Physics - Experiment e-prints*, May 2004.

[52] J.K. Ahn et.al. RENO: An Experiment for Neutrino Oscillation Parameter θ_{13}3 Using Reactor Neutrinos at Yonggwang. Technical Report arXiv:1003.1391, Mar 2010. Comments: 126 pages, Technical Design Report.

[53] X. Guo et.al. A Precision Measurement of the Neutrino Mixing Angle θ_{13} using Reactor Antineutrinos at Daya Bay. Technical Report hep-ex/0701029. BNL-77369-2006-IR. LBNL-62137. TUHEP-EX-06-003, Brookhaven Nat. Lab., Upton, NY, Jan 2007.

[54] G. Mention. A unified analysis of the reactor neutrino program towards the measurement of the θ_{13} mixing angle. *Journal of Physics: Conference Series*, 110(8):082013, 2008.

[55] Y. Abe et.al. Indication of Reactor $\overline{\nu}_e$ Disappearance in the Double Chooz experiment. *Phys. Rev. Lett.*, 108:131801, Mar 2012.

[56] Y. Abe et.al. Reactor ν_e disappearance in the Double Chooz experiment. *Physical Review Letters D*, 86(5):052008, September 2012.

[57] F.P. Ahn et.al. Observation of Electron-Antineutrino Disappearance at Daya Bay. *Phys. Rev. Lett.*, 108:171803, Apr 2012.

[58] J.K. Ahn et.al. Observation of Reactor Electron Antineutrinos Disappearance in the RENO Experiment. *Phys. Rev. Lett.*, 108:191802, May 2012.

[59] K. Schreckenbach et.al. Determination of the anti-neutrino spectrum from U-235 thermal neutron fission products up to 9.5-MeV. *Phys. Lett.*, B160:325–330, 1985.

[60] Th. A. Mueller et.al. Improved Predictions of Reactor Antineutrino Spectra. Technical Report arXiv:1101.2663. IRFU-10-280, Jan 2011. Comments: 17 pages, 12 figures. Submitted to Phys. Rev. C.

[61] P. Huber. On the determination of anti-neutrino spectra from nuclear reactors. *PHYS.REV.C*, 84:024617, 2011.

[62] G. Mention et.al. The Reactor Antineutrino Anomaly. *Phys.Rev.*, D83:073006, 2011.

[63] K.N. Abazajian et.al. Light Sterile Neutrinos: A white paper. apr 2012.

[64] J. Beringer et.al. (Particle Data Group). Review of Particle Physics. *Phys. Rev. D*, 86:010001, 2012.

[65] G.L. Fogli et.al. Evidence of $\theta_{13} \geq 0$ from global neutrino data analysis. *Phys. Rev. D*, 84:053007, Sep 2011.

[66] P. Machado, H. Minakata, H. Nunokawa, and R. Funchal. Combining accelerator and reactor measurements of θ_{13}: the first result. *Journal of High Energy Physics*, 2012:1–13, 2012. 10.1007/JHEP05(2012)023.

[67] K. Nakamura and Particle Data Group. Review of Particle Physics. *Journal of Physics G: Nuclear and Particle Physics*, 37(7A):075021, 2010.

[68] Z. Djurcic. Review of Reactor Antineutrino Experiments. Technical Report arXiv:1201.1522, Jan 2012. 2011, XIIIth InternationalWorkshop on Neutrino Factories, Super beams and Beta beams, CERN/UNIGE, Geneva, Switzerland, August 1-6, 2011.

[69] R.R.G. Marleau and A.Hebert, Tech. Rep. IGE-157, 1994.

[70] Mcnp utility for reactor evolution: couples monte-carlo transport with fuel burnup calculations MURE. Url http://www.nea.fr/tools/ abstract/detail/nea-1845, 2009.

[71] O. Meplan, Tech. Rep. LPSC 0912 and IPNO-09-01, 2009.

[72] D. Lhuillier. Reactor plots and macros. *DocDB-3373*, 2011.

[73] A. Onillon and M. Fallot. Reactor plots UNDER REVIEW. *DocDB-3377*, 2011.

[74] V. Kopeikin et.al. Reactor as a Source of Antineutrinos: Thermal Fission Energy. *PHYS.ATOM.NUCL.*, 67:1892, 2004.

[75] Jeff and eff projects. Url http://www.oecd-nea.org/dbdata/jeff/.

[76] P. Huber and T. Schwetz. Precision spectroscopy with reactor anti-neutrinos. *Physical Review D*, 70:053011, 10 2004.

[77] A.A. Hahn et.al. Antineutrino spectra from ^{241}Pu and ^{239}Pu thermal neutron fission products. *Physics Letters B*, 218(3):365 – 368, 1989.

[78] Y. Declais et.al. Study of reactor anti-neutrino interaction with proton at Bugey nuclear power plant. *Phys. Lett.*, B338:383–389, 1994.

[79] K. Zbiri. Note on Drexel tests of the IMB R1408 PMTs used in the inner veto of both far and near detectors of the Double Chooz experiment. 2011.

[80] C. Buck at.al. Large scale Gd-beta-diketonate based organic liquid scintillator production for antineutrino detection. *ArXiv e-prints*, December 2011.

[81] C. Aberle. Optimization, simulation and analysis of the scintillation signals in the Double Chooz experiment. *Thesis*, 2012.

[82] A. Cabrera. DC-I Readout Diagram. *DocDB-4126*, 2012.

[83] D. Greiner. Design und Aufbau des Double Chooz Myonen Veto. *Thesis under preparation*, 2013.

[84] P. Novella. RecoPulse: Software and algorithms for pulse reconstruction. *DocDB-649*, 2012.

[85] M. Wurm. Muon ID and tracking summary talk. *DocDB 3826*, 2012.

[86] C. Amsler et.al. (Particle Data Group). The Review of Particle Physics. *Physics Letters B667*, 2008.

[87] L.I. Dorman. *Cosmic rays in the earth's atmosphere and underground*. Astrophysics and space science library. Kluwer Academic Publishers, 2004.

[88] P.H. Barrett et.al. Interpretation of Cosmic-Ray Measurements Far Underground. *Rev. Mod. Phys.*, 24:133–178, Jul 1952.

[89] S. Cecchini and M. Sioli. Cosmic Ray Muon Physics. *ArXiv High Energy Physics - Experiment e-prints*, February 2000.

[90] T.K. Gaisser. *Cosmic rays and particle physics*. Cambridge University Press, 1990.

[91] A. Tang et.al. Muon simulations for Super-Kamiokande, KamLAND, and CHOOZ. *Phys. Rev. D*, 74:053007, Sep 2006.

[92] T.K. Gaisser and T. Stanev. Cosmic Rays. *Review of Particle Physics, edited by L. Alvarez-Gaumè et al., Physics Letters, B592, 228*, 2004.

[93] J.C. Barton and C.T. Stockel. A study of muons deep underground. II. The rate of energy loss. *Journal of Physics A: General Physics*, 2(6):650–657, 1969.

[94] A. Tang. Music simulation of the DC far site. *DocDB-4225*, 2007.

[95] M. Ambrosio et.al. Measurement of the residual energy of muons in the Gran Sasso underground Laboratories. *Astropart. Phys.*, 19(hep-ex/0207043):313–328. 28 p, Jul 2002.

[96] E.V. Bugaev et.al. Atmospheric muon flux at sea level, underground, and underwater. *Phys. Rev. D*, 58:054001, Jul 1998.

[97] S. Abe et.al. Production of radioactive isotopes through cosmic muon spallation in KamLAND. *Phys. Rev. C*, 81:025807, Feb 2010.

[98] EU++ Analysis Cluster. EU++ results for second comparison stage. *DocDB-3199*, 2011.

[99] M. Röhling. IV Trigger Studies. *DocDB-3769*, 2011.

[100] A. Cabrera et.al. DC-III Muon Tagging Thoughts. *DocDB-4533*, 2013.

[101] A. Remoto. Muon identification: synthesis and EU++ proposal. *DocDB-3210*, 2011.

[102] A. Cabrera. Correlated background analysis for DC 1st Pub. *DocDB-3471*, 2011.

[103] D. Shresta M. D'Agostino. Fast neutrons in Cluster United. *DocDB-3254*, 2011.

[104] K. Nakajima. Technical note and spectrum of a stop muon and fast neutron analysis at 1st publication stage. *DocDB-3631*, 2012.

[105] K. Nakajima. Summary of Stop Muon and Fast Neutron Analysis. *DocDB-3475*, 2011.

[106] A. Remoto. Muon dead time plot. *DocDB-3336*, 2011.

[107] United Cluster. Cluster United Summary of First Analysis Comparision. *DocDB 2779*, 2011.

[108] L. Kalousis. Towards the muon signature. *DocDB 3998*, 2012.

[109] D. Dietrich et.al. Monte Carlo aided design of the inner muon veto detectors for the Double Chooz experiment. *Journal of Instrumentation*, 7:8012, August 2012.

[110] D. Greiner. High energy light noise. *DocDB-2511*, 2011.

[111] M. Toups. OVDAQ-NuDAQ status and merging. *DocDB-3245*, 2011.

[112] S. Tilav et.al. (For The Icecube Collaboration). Atmospheric variations as observed by icecube. *Arxiv preprint arXiv10010776*, page 4, 2010.

[113] G. Bellini et. al. Cosmic-muon flux and annual modulation in Borexino at 3800 m water-equivalent depth. *jcap*, 5:15, may 2012.

[114] N.R. Lomb. Least-squares frequency analysis of unequally spaced data. *apss*, 39:447–462, feb 1976.

[115] J. D. Scargle. Studies in astronomical time series analysis. II - Statistical aspects of spectral analysis of unevenly spaced data. *apj*, 263:835–853, dec 1982.

[116] B. Aharmim et. al. Search for periodicities in the ^{8}B solar neutrino flux measured by the Sudbury Neutrino Observatory. *prd*, 72(5):052010, September 2005.

[117] S. Sagisaka. Atmospheric effects on cosmic-ray muon intensities at deep underground depths. *Nuovo Cimento C Geophysics Space Physics C*, 9:809–828, August 1986.

[118] D. Pham et.al. Depdencene of the Cosmic Muon Flux on Atmospheric Pressure and Temperature. *Communications in Physics*, 14(1), 2007.

[119] S. Sagisaka et.al. Atmospheric Effect on Muon Intensity for Observations at Various Atmospheric and Underground Depths. *16th ICRC, Vol. 4, p.235*, 1979.

[120] E.W. Grashorn et.al. The atmospheric charged kaon/pion ratio using seasonal variation methods. *Astroparticle Physics*, 33(3):140 – 145, 2010.

[121] P. Adamson et.al. (MINOS Collaboration). Observation of muon intensity variations by season with the MINOS far detector. 2010.

[122] J. Reichenbacher et.al. Calculation of the underground muon intensity crouch curve from a parameterization of the flux at surface. 2007.

[123] K.A. Semendjajew. *Taschenbuch der Mathematik*. Deutsch, 2008.

[124] The IceCube Collaboration. The IceCube Neutrino Observatory III: Cosmic Rays. *ArXiv e-prints*, November 2011.

[125] T. Alexopoulos et.al. Mass-identified particle production in proton-antiproton collisions at $/sqrts$ =300, 540, 1000, and 1800 GeV. *Physical Review D*, 48:984–997, August 1993.

[126] M.M. Aggarwal et.al. Pion freeze-out time in Pb+Pb collisions at 158 AGeV/c studied via π^-/π^+ and K^-/K^+ ratios. *European Physical Journal C*, 48:343–352, November 2006.

[127] S.V. Afanasiev et.al. Energy dependence of pion and kaon production in central Pb+Pb collisions. *Physical Review C*, 66(5):054902, November 2002.

[128] C. Adler et.al. Kaon production and kaon to pion ratio in Au + Au collisions at $/sqrts_{NN}$=130 GeV. *Physics Letters B*, 595:143–150, August 2004.

[129] D. Dietrich et.al. Background measuremt from reactor-off data. *DocDB 4166*, 2012.

[130] D. Dietrich et.al. Off-Off background scaling Technote. *DocDB 4163*, 2012.

[131] Y. Abe et.al. Direct measurement of backgrounds using reactor-off data in Double Chooz. *Phys. Rev. D*, 87:011102, Jan 2013.

[132] A. Tonazzo. Muon rate. *DocDB-2103*, 2010.

[133] M. Crouch. An Improved World Survey Expression for Cosmic Ray Vertical Intensity VS. Depth in Standard Rock. In *International Cosmic Ray Conference*, volume 6 of *ICRC*, page 165, 1987.

[134] L. Goodenough. Mean Muon Energy Scaling with Depth - MUSIC Simulation. *DocDB-4220*, 2012.

[135] P. Antonioli et.al. A three-dimensional code for muon propagation through the rock: MUSIC. *Astroparticle Physics*, 7(4):357 – 368, 1997.

[136] V. Kudryavtsev. Narrow muon bundles from muon pair production in rock. *Physics Letters B*, 471:251–256, December 1999.

[137] V. A. Kudryavtsev. Muon simulation codes MUSIC and MUSUN for underground physics. *Computer Physics Communications*, 180:339–346, March 2009.

[138] G. Horton-Smith D. Shrestha. Scaling KamLAND cosmogenic rates to DC. *DocDB 4142*, 2012.

[139] T. Hagner et.al. Muon-induced production of radioactive isotopes in scintillation detectors. *Astroparticle Physics*, 14(1):33 – 47, 2000.

[140] C. Buck and B. Reinhold. Proton number Technote. *DocDB-4211*, 2012.

[141] G.T. Zatsepin and O.G. Razhskaya. Calculation of neutron production by muons at different depths underground. *Bull. Acad. Sci. USSR Phys. Ser.*, pages p.1779–1782, 1965.

[142] Y.F. Wang et.al. Predicting Neutron Production from Cosmic-ray Muons. *Phys. Rev. D*, 64(hep-ex/0101049):013012, 2001.

[143] M. Wurm. Scaling of Li9 background. *DocDB 4099*, 2012.

[144] M. Wurm. Update on Li-9 scaling. *DocDB 4215*, 2012.

[145] Karim Zbiri. Physics process of cosmogenics Li-9 and He-8 production on muons interactions with carbon target in liquid scintillator. *Nucl.Instrum.Meth.*, A597:219–221, 2008.

[146] A. Cabrera. DC2ndPub Energy Scale FINAL. *DocDB 3960*, 2012.

[147] A. Cabrera (on behalf of the Energy-Scale team). DC2ndPub Energy Scale. *http://doublechooz.in2p3.fr/Private/Working_Groups/Analysis/DC2ndPub/escale.php*, 2012.

[148] W.R. Leo. *Techniques for Nuclear and Particle Physics Experiments: A How-To Approach*. Springer, 1994.

[149] J.E. Moyal. XXX. Theory of ionization fluctuations. *Philosophical Magazine Series 7*, 46(374):263–280, 1955.

[150] M. Wurm. Status of RecoMuonHam. *Private communication*, 2011.

[151] M. Ishitsuka et.al. Shift around days 100. *DocDB 3968*, 2012.

[152] J. Maeda et.al. Li-9 summary talk. *DocDB 3827*, 2012.

[153] N.C. Mukhopadhyay et.al. Inclusive muon capture in light nuclei. *Physics Letters B*, 434(12):7 – 13, 1998.

[154] H. Labranche. Time series analysis for the Cf source in the Sudbury Neutrino Observatory. *M.Sc. Thesis, University of Guelph*, 2003.

[155] C. Maesano. ^{9}Li Production from Stopped Muons in the Double Chooz Detector. *DocDB 4173*, 2012.

[156] D. Greiner. IV nonconformance description. *DocDB 1478*, 2010.

[157] D. Dietrich. Extraction of T0 constants via IVLI. *DocDB 3766*, 2010.

[158] D. Dietrich and M. Röhling. Inner Veto Light Injection: Fiber direction. *DocDB 2786*, 2011.

Slides and reports internal to the DC collaboration are marked with the label **DocDB**. They can be found using the following link:

http://www.dchooz.org/DocDB/cgi-bin/private/DocumentDatabase.

It is expected that this material will be publicly available after the final measurement of the Double Chooz experiment.